DESIGN, SYNTHESIS AND PROPERTIES OF DIINDENO-FUSED ACENES: OPEN-SHELL COMPOUNDS FOR ORGANIC ELECTRONIC APPLICATIONS

by

GABRIEL EDWARD RUDEBUSCH

A DISSERTATION

Presented to the Department of Chemistry and Biochemistry
and the Graduate School of the University of Oregon
in partial fulfillment of the requirements
for the degree of
Doctor of Philosophy

June 2016

DISSERTATION APPROVAL PAGE

Student: Gabriel Edward Rudebusch

Title: Design, Synthesis and Properties of Diindeno-Fused Acenes: Open-Shell Compounds for Organic Electronic Applications

This dissertation has been accepted and approved in partial fulfillment of the requirements for the Doctor of Philosophy degree in the Department of Chemistry and Biochemistry by:

Michael D. Pluth	Chairperson
Michael M. Haley	Advisor
Kenneth M. Doxsee	Core Member
Hans C. Dreyer	Institutional Representative

and

Scott L. Pratt	Dean of the Graduate School

Original approval signatures are on file with the University of Oregon Graduate School.

Degree awarded June 2016

DISSERTATION ABSTRACT

Gabriel Edward Rudebusch

Doctor of Philosophy

Department of Chemistry and Biochemistry

June 2016

Title: Design, Synthesis and Properties of Diindeno-Fused Acenes: Open-Shell Compounds for Organic Electronic Applications

The consequence of free electrons in organic compounds has intrigued chemists for over a century. The fundamental idea of a covalent bond, a pair of electrons in a lasting attraction, and the localized spin of traditional stable free radicals are merged in biradical polycyclic hydrocarbons (PCHs). The field of open-shell PCHs has seen resounding growth over the last decade owing to the development of new synthetic methods, spectroscopic techniques and close collaboration between organic, physical and computational chemists. Previously inaccessible compounds have been shown possess useful electronic properties and the practical application of these new materials is only beginning to be explored. In this thesis I present the design, synthesis and application of the diindeno-fused acene class of biradical PCHs.

In Chapter I recent work in the field of cyclopenta-fused PCHs, including indenofluorenes and diindenothienoacenes, is reviewed. Chapter II represents the first foray into expanding the (hetero)acene core of the diindenoacene family. Chapter III reports the synthesis and properties of an air-stable open-shell diindenoanthracene (DIAn) derivative. Chapter IV examines the redox chemistry of the DIAn system. In Chapter V I report the development and synthesis of a key advanced intermediate in the pursuit of new DIAn derivatives.

This dissertation contains previously published and unpublished coauthored material.

CURRICULUM VITAE

NAME OF AUTHOR: Gabriel Edward Rudebusch

GRADUATE AND UNDERGRADUATE SCHOOLS ATTENDED:

University of Oregon, Eugene
University of Nevada, Reno

DEGREES AWARDED:

Doctor of Philosophy, 2016, University of Oregon
Bachelor of Science, 2010, University of Nevada, Reno

PUBLICATIONS:

Rudebusch, G. E.; Zakharov, L. N.; Liu, S.-Y. Rhodium-Catalyzed Boron Arylation of 1,2-Azaborines. *Angew. Chem. Int. Ed.* **2013**, *52*, 9316–9319.

Liu, S. Y.; Rudebusch, G. E. 1,2-azaborine compounds and synthesis. US patent 2013/049907. Filed 7/10/2013.

Rudebusch, G. E.; Fix, A. G.; Henthorn, H. A.; Vonnegut, C. L.; Zakharov, L. N.; Haley, M. M. Quinoidal Diindenothienoacenes: Synthesis and Properties of New Functional Organic Materials. *Chem. Sci.* **2014**, *5*, 3627–3633.

Haley, M. M.; Fix, A. G.; Rudebusch, G. E. Thieno-containing compounds and processes and uses thereof. US Provisional Patent Application No 61/859,133, filed 7/26/13; PCT Application No PCT/US2014/048262, filed on 7/25/14.

Marshall, J. L.; Rudebusch, G.E.; Zakharov, L. N.; Haley, M. M. Synthesis and Properties of Fully Conjugated Indacenediselenophene and Diindenoselenophene Derivatives. *Tetrahedron Lett.* **2015**, *56*, 3235–3239.

Christensen, M. A.; Rudebusch, G. E.; Parker, C. R.; Andersen, C. L.; Kadziola, A.; Haley, M. M.; Hammerich. O.; Nielsen, M. B. Diindenothienoacene–tetrathiafulvalene redox systems. *RSC Advances* **2015**, *5*, 49748–49751.

Rudebusch, G. E.; Haley, M. M. "Planar Cyclopenta-fused Polycyclic Arenes" in *Polycyclic Arenes and Heteroarenes: Synthesis, Properties, and Applications*. Miao, Q., Ed.; Wiley-VCH: Weinhem, **2015**, pp. 37–60.

Rudebusch, G. E.; Zafra, J. L.; Jorner, K.; Fukuda, K.; Marshall, J. L.; Arrechea-Marcos, I.; Espejo, G. L.; Ortiz, R. P.; Gómez-García, C. J.; Zakharov, L. N.; Nakano, M.; Ottosson, H.; Casado, J.; Haley, M. M. Diindeno-fusion of an anthracene as a design strategy for stable organic biradicals. *Nat. Chem.* [Online early access] DOI: 10.1038/nchem.2518 Published Online: May 23, 2016.

Haley, M. M.; Rudebusch, G. E. Diindenoanthracene and Diindenopentacene. U.S. Provisional Patent Application No. 62/146,086, filed 4/10/15.

ACKNOWLEDGMENTS

I thank Mike Haley for his ceaseless support, advice and energy. I have thoroughly enjoyed research under his guidance and I am lucky to have had an advisor so accepting of new ideas. Over the past six years I've come to appreciate his honesty, passion for organic chemistry and vibrant personality. I would like to thank my previous advisor Shih-Yuan Liu for initial training and my lab-mates Adam Marwitz, Senmiao Xu and Alec Brown for advice and direction in my first three years of graduate school. I thank Lev Zakharov and Mike Strain for their expertise and advice. I thank my committee chair Michael Pluth and committee members Ken Doxsee and Hans Dreyer for guidance and support. Ramesh Jasti and his research group are thanked for their advice on research and illuminating discussions at joint group meetings. I thank previous Haley group members Aaron Fix and Brad Rose for lively discourses on research in science. The National Science Foundation (CHE-1301485) is acknowledged for support of this research.

Spence Bailey, Jon Marshall, Jacob Ishibashi, Evan Darzi, Matthew Hammers, Adam Marwitz and the countless drinks and conversations we've shared have made graduate school enjoyable on an intellectual and personal level. I couldn't have asked for better cohorts during this time.

I am grateful to my parents, Roy and Dixie, and my brother William for their enduring love and support.

To Roy, Dixie and William.

TABLE OF CONTENTS

LIST OF FIGURES

LIST OF TABLES

LIST OF SCHEMES

Scheme Page

CHAPTER I

PLANAR CYCLOPENTA-FUSED POLYCYCLIC ARENES

This chapter was researched and written by Gabriel Rudebusch. Michael M. Haley provided editorial and content advice. It was originally published in *Polycyclic Arenes and Heteroarenes: Synthesis, Properties, and Applications*.

Introduction

The inclusion of five-membered rings in greater polycyclic arenes (PAs) has been studied for over a century. Salient examples include Barth and Lawton's synthesis of corannulene in 1966,[1] and more recently, the bottom-up synthesis of fullerenes,[2] fullerene fragments,[3] and endcaps of carbon nanotubes,[4] where the presence of one or more pentagons accounts for curvature. *Planar* cyclopenta-fused polycyclic arenes (CPPAs) represent a small but growing class of PAs. From planar fullerene subunits to antiaromatic pentalene- and indacene-containing structures, significant progress has been made in the past 15 years on these previously unknown or poorly-characterized molecules. Advances in synthetic methodology, namely Pd-catalyzed cross-coupling, as well as in computational techniques, have allowed researchers to prepare and study new CPPA frameworks, identify structure-property relationships and apply the materials in organic electronics. Compounds that were considered too reactive to synthesize can be investigated. Molecules with open-shell ground states and unprecedented quinoidal structures are now subjects of research programs.

This chapter focuses on three major divisions of CPPAs organized by their defining sub-unit: (1) acenaphthylenes, (2) pentalenes and (3) indacenes (Figure 1.1). Reviews on the history, synthesis, properties and applications of PAs are available.[5-8] Rather, we highlight recent synthetic work in the CPPA field and provide discussion of properties with an eye for potential application as functional materials.

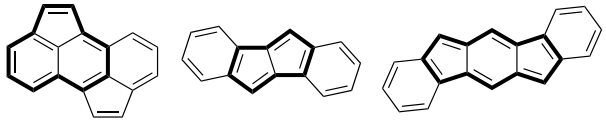

Figure 1.1. Selected cyclopenta-fused polycyclic arenes with sub-unit in bold: cyclopent[*hi*]aceanthrylene (left), dibenzopentalene (middle), indeno[1,2-*b*]fluorene (right).

Acenaphthylenes

One of the smallest non-alternant hydrocarbons is acenaphthylene (Figure 1.2). It can be considered a C_2H_2 unit fused peri to naphthalene, and its first synthesis was just that—in 1867 Berthelot heated naphthalene with acetylene in a tube furnace to provide acenaphthylene. The reactivity of acenaphthylene is dominated by the cyclopenteno-fused ring as the outer double bond readily undergoes halogenation and hydrogenation. The aromaticity of acenaphthylene[9,10] and pyracylene[11-13] has been a source of controversy. The outer conjugated circuits can be considered [11]- or [12]annulenes, translating to non- and anti-aromatic systems, respectively. Taking reactivity into account, however, the two should be viewed as mono- and divinylene-bridged naphthalenes.

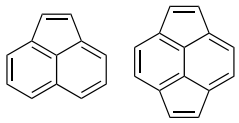

Figure 1.2. Acenaphthylene (left) and pyracyclene (right).

Recent examples featuring acenaphthylene moieties are included in this section. In general, Pd-catalyzed methods of constructing the CPPAs have overtaken traditional annulations and the harsh conditions of flash vacuum pyrolysis. Readily available haloarenes and reliable synthetic procedures have allowed the preparation of these planar fullerene fragments. Study of the compounds has brought to light some of the defining properties of CPPAs and how the desirable traits of fullerenes can be expressed in small molecules.

In 2001 the group of Garcia-Garibay discovered a Pd-catalyzed cyclopentannulation reaction during the routine Sonogashira cross-coupling reaction of 9-bromoanthracene with terminal alkynes (Scheme 1.1).[14] Optimization of the reaction conditions led to a 69% isolated yield of the aceanthrylene derivatives **1** with only trace amounts of alkynylanthracenes. The

identity of the unexpected product was confirmed through single-crystal X-ray diffraction. Attempts to effect a cyclization from the alkynylanthracene byproduct were unsuccessful, suggesting a mechanism distinct from the Sonogashira reaction. In a succeeding article the group expanded the reaction to 9,10-dibromoanthracene.[15] A dual cyclization produced cyclopent[*hi*]aceanthrylene **2a** in 75% yield. Through modification of the reaction conditions, the 9,10-bis(alkynyl)anthracene and half-closed 9-alkynylaceanthrylene could be isolated. The compounds showed a drastic deepening in hue from pale yellow to deep purple with the introduction of five-membered rings. Cyclic voltammetry revealed two reduction events (-1.44 V, -1.86 V vs. SCE) within the range of C_{60} (-1.41 V vs. SCE), alluding to potential materials applications for the C_{70}-fullerene fragment.

Scheme 1.1. Garcia-Garibay's synthesis of (cyclopent[*hi*])aceanthrylene derivatives.

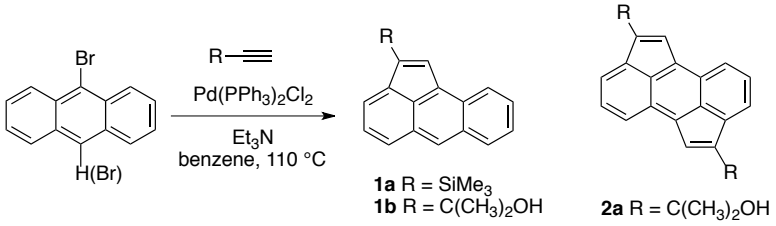

Plunkett and coworkers revisited the Pd-catalyzed cyclopentannulation reaction in 2012 (Figure 1.3).[16] After the cyclization of 9,10-dibromoanthracene and (trimethylsilyl)acetylene, the group moved one step further by converting the silyl groups on the C_2H_2-bridges into dibromo derivative **2b**. The two-step process was successfully applied to 5,11-dibromotetracene, however in reduced yields presumably due to side reactions of the more reactive acene. The authors further note the possible ease of functionalization, unlike fullerene derivatives. Sonogashira cross-coupling of **2b** and **3a** provided π-expanded derivatives **2c** and **3b** with low-energy light absorbing properties and lowered reduction potentials compared to the bare hydrocarbons suggesting potential applications in organic electronics.

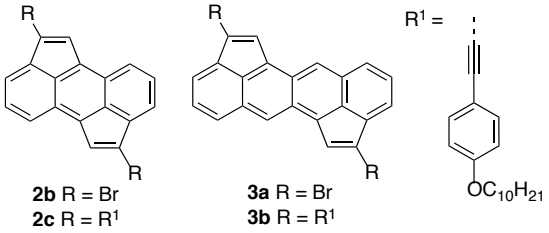

Figure 1.3. Plunkett's cyclopent[*hi*]aceanthrylene (**2b**) and bis(cyclopent)tetracene (**3**) derivatives.

The groups of de Meijere and Scott reported a tandem Suzuki/Heck-type cyclopentannulation in 2003 (Scheme 1.2).[17] The reaction of 2-bromobenzeneboronic acid with 1-bromonaphthalene in the presence of 1,8-diazabicycloundec-7-ene (DBU), Pd(0) and bulky, electron-rich tricyclohexylphosphine provided benzofluoranthene **4** in quantitative yield. No homo-coupling of 2-bromobenzeneboronic acid was observed likely due to its sluggish oxidative addition to Pd. The analogous reaction with the readily available *o*-dibromobenzene and naphthalene-1-boronic acid proceeded in high yield (87%) as well. Indenocorannulene as well as other indeno-annulated PAs were prepared by their method.

Scheme 1.2. Tandem Suzuki/Heck-type cyclopentannulation.

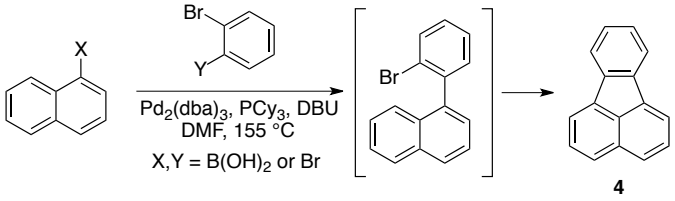

Yao-Ting Wu and colleagues reported the ligand-less Pd-catalyzed formation of benzofluoranthenes **5** (Scheme 1.3).[18] Iodobenzene or diiodonaphthalene served as aryne equivalents in the formal [2+2+2] cycloaddition reaction. Previous methods of constructing extended benzofluoranthenes depended on reactive and difficult to prepare cyclopentadienones or

isobenzofurans. A substrate scope shows the reaction to be general and to provide the fluoranthenes **5a**-**d** in modest yield. Electron-rich and π-expanded aryl iodides were also tolerated. The synthesized compounds were fluorescent with quantum yields as high as 86%. In addition, the Wu group has explored organic light emitting diode (OLED) applications with **5b** and other fluoranthenes.[19,20]

Scheme 1.3. Benzofluoranthenes by Wu's Pd-catalyzed formal [2+2+2] cycloaddition.

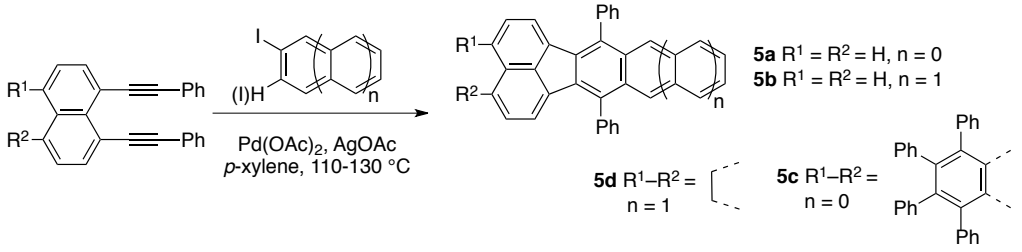

The C_{aryl}–F bond, despite its considerable thermodynamic stability, can be activated by alumina at moderate temperatures.[21] The solid-state reaction provides a high yielding route to large, insoluble PCHs otherwise challenging to prepare by solution chemistry. Presumably, the formation of a strong aluminum–fluorine bond is the driving force for the transformation. Planar benzo[*ghi*]fluoranthene **7** was prepared from the corresponding fluorinated [4]helicene **6** in quantitative yield (Scheme 1.4). Large, spectacularly insoluble fluoroarenes were amenable to the solid-state reaction conditions. The authors found that C–Cl and C–Br bonds remain intact in the reaction, leading to the possibility of orthogonal ring-closures and further derivatization by Pd-catalyzed cross-coupling.

Scheme 1.4. Amsharov's alumina-mediated ring-closure of fluorinated PAs.

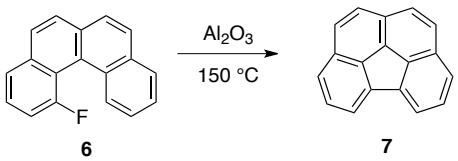

6 **7**

All-carbon copolymers **8a** and **8b** incorporating cyclopent[*hi*]aceanthrylene and a donor repeat unit were recently prepared by the Plunkett group (Figure 1.4).[22] Cross-coupling partner **2b** was polymerized via Sonogashira cross-coupling reaction with the corresponding diethynyl-monomer. Characteristic dual-band features due to the donor-acceptor backbone were evident in the electronic absorption spectra. Optical gaps less than 1.5 eV were deduced from the low-energy absorptions out to 1000 nm. Replacing the weakly donating dialkylfluoren-9-yl unit (**8a**) with a stronger bis(alkoxy)phenylene donor (**8b**) destabilized the HOMO energy levels while the LUMO energy levels remained constant. The electron-accepting capacity of the polymer was investigated by the fluorescence quenching of poly(3-hexyl)thiophene further supporting the fullerene-likeness of the acceptor unit.

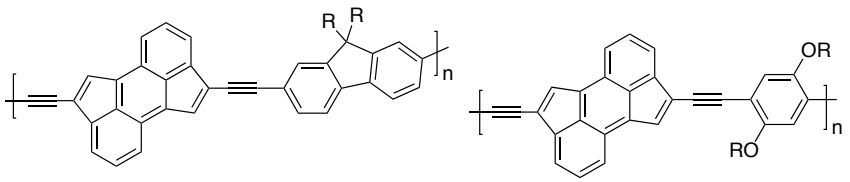

8a R = *n*-dodecyl

8b R = 2-octyldodecyl

Figure 1.4. Plunkett's all-carbon copolymers featuring cyclopent[*hi*]aceanthrylene acceptor units with fluorene or alkoxybenzene donors.

The research group of Miao demonstrated the synthesis and application of a series of cyclopent[*hi*]aceanthrylene compounds in organic field effect transistors (OFETs).[23] Starting from known diketone **9**, nucleophilic attack followed by dehydration gave the fully-conjugated derivatives **2d** and **2e** in 21-31% yield (Scheme 1.5). Compounds **2f** and **2g** were prepared following Müllen's Pd-catalyzed cyclopentannulation protocol.[24] Thin films of the compounds were deposited onto silicon wafers where X-ray diffraction revealed that **2e** arranges into a lamellar structure. Top-contact OFET devices were prepared and measurements showed modest hole (0.05 $cm^2V^{-1}s^{-1}$) and electron (0.07 $cm^2V^{-1}s^{-1}$) mobility for **2e**. OFETs from amorphous films

of tetraphenyl derivative **2g** gave hole mobility up to 0.21 $cm^2V^{-1}s^{-1}$ and electron mobility of 0.07 $cm^2V^{-1}s^{-1}$. However, **2d** also formed amorphous films but exhibited no field effect, most likely due to edge-to-face arrangement in the solid-state and thus poor π-orbital overlap.

Scheme 1.5. Synthesis of cyclopent[*hi*]aceanthrylene derivatives as the active layer in OFETs.

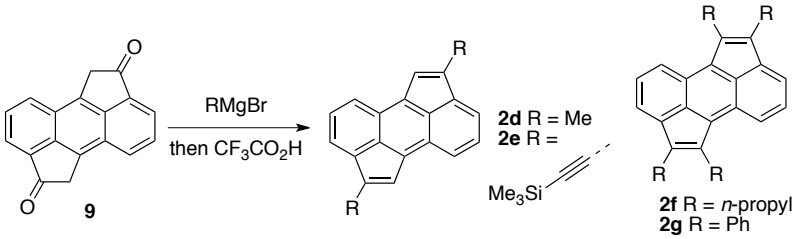

The Plunkett group demonstrated the orthogonal functionalization of the cyclopent[*hi*]aceanthrylene system with a communication in 2013.[25] The 4,9 positions on the anthracene core were borylated by a Ir-catalyzed protocol and subjected to Pd-catalyzed cross-coupling with a thiophene derivative to give **2h**. Bromination of **2h** at the 2,7 positions and further cross-coupling provided tetra-arylated cruciform **2j**. The position of functionalization had a significant impact on the electronic absorption spectra. When the thiophene groups are connected *via* the five-membered rings (**2i**) a strong donor-acceptor band extending to 1000 nm was observed. Linkage through the 4,9 positions (**2i**) gave a larger optical gap of 633 nm. The cruciform **2j** was a balance of the two regioisomers as its absorption extended to 880 nm. Cyclic voltammetry supported this trend as the cyclopenta-functionalized **2i** and **2j** exhibited lower electrochemical gaps (1.48 eV) compared to **2h** (2.13 eV). The authors note the great potential of the orthogonally functionalized cyclopent[*hi*]aceanthrylenes in polymeric and small molecule based organic electronics.

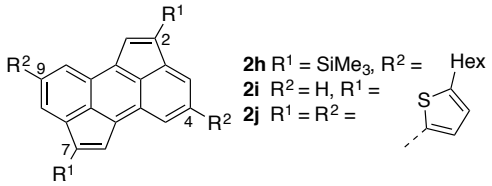

Figure 1.5. Functionalized cyclopent[*hi*]aceanthrylenes accessed by Ir-catalyzed borylation and Pd-catalyzed cross-coupling.

Rubrene (5,6,11,12-tetraphenyltetracene) is widely regarded as a benchmark organic semiconductor.[26,27] Douglas and coworkers reported a rubrene-like diarylindenotetracene **11** as the donor molecule in organic photovoltaic (OPV) cells.[28] Compound **11** could be made in high yield from **10** in a modified Kumada reaction (Scheme 1.6). Substituents at the 2- and 4-positions of the aryl rings were tolerated albeit in reduced yields. The authors noted that no rubrene or diindenotetracene **12** could be detected. Vacuum deposited planar heterojunction OPVs were fabricated with C_{60} as the electron acceptor. The device showed power conversion efficiencies greater than 1.5% with open-circuit voltages from 0.7 to 1.1 V.

Scheme 1.6. Kumada-type arylation for indenotetracene derivatives.

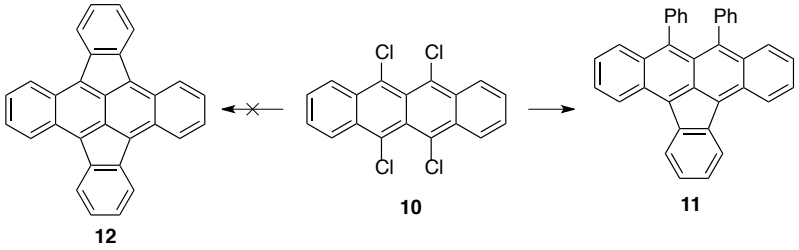

Recently the use of rubicene (**13**) as the active layer in OFETs was described by the Briseno and Wudl groups (Figure 1.6).[29] The planar C_{70} fullerene fragment has been known for a century and is commercially available. Single-crystals of **13** were shown by X-ray diffraction to pack in a staircase structure with close contacts (3.38 Å) between parallel adjacent molecules. Fabricated OFETs exhibited good hole mobilities of 0.20 $cm^2V^{-1}s^{-1}$. Treatment of the gold

contacts with pentafluorobenzenethiol (PFBT) further improved the mobility to 0.32 $cm^2V^{-1}s^{-1}$. Grazing incidence X-ray diffraction (GIXD) of films of **13** deposited on SiO_2 or Gold/SiO_2/PFBT substrates revealed a polycrystalline, edge-on orientation ideal for charge transport devices. The authors suggest potential ambipolar charge transport behavior based on the observed frontier orbital energy levels.

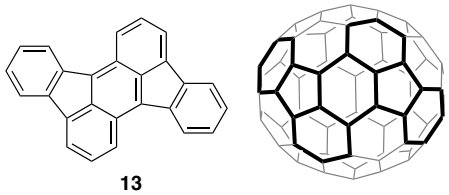

13

Figure 1.6. Planar C_{70} fullerene fragment rubicene.

Dibenzopentalenes

The chemistry of dibenzopentalenes has undergone a significant revival in the past 15 years. Derivatives of the parent compound were studied by Brand in the 1910s[30] and it was finally synthesized by Linstead in 1952.[31] Dibenzopentalene is formally antiaromatic with 16 π-electrons and can be viewed as a bridged cyclooctatetraene.[32] Benzo-fusion and core substituents provide stability to the system as bare pentalene must be generated in Ar matrices and dimerizes when warmed to 80 K.[33] While the synthesis of hexaphenylpentalene[34] and tri-*t*-butylpentalene[35] were considerable feats in their own right, general synthetic entry into this class of CPPAs was not established until recently. This renewed interest in pentalenes can be largely attributed to the advent of transition metal-catalysis and the exploration of new materials for organic electronics.

Early synthetic routes toward the parent dibenzopentalene **14a** begin from 5,10-dihydropentalenes. Blood and Linstead's 1952 synthesis[31] borrowed from Brand's pioneering work and is initiated by chlorination of the known 5,10-diketodibenzopentalene then reduction with Zn metal to yield the 5,10-dihydropentalene (Scheme 1.7). Bromination of the central olefin then elimination of HBr in the presence of AgOAc provides deep red **14a** in good yield (60%). Preliminary reactivity studies showed that **14a** could be ozonolyzed to oxalylbis(benzoic acid) and reduced to the dihydro species via sodium amalgam. Bromination proceeded to an uncharacterized dibromodibenzopentalene. Soon after Linstead's synthesis, Chuen and coworkers

described a new preparation of **14a**.[36] Starting from the 5,10-bis(dimethylamino)dihydro derivative, *N*-alkylation by iodomethane and Hoffman elimination with aqueous NaOH provided **14a** in 30% yield.

Scheme 1.7. Early syntheses of dibenzopentalene.

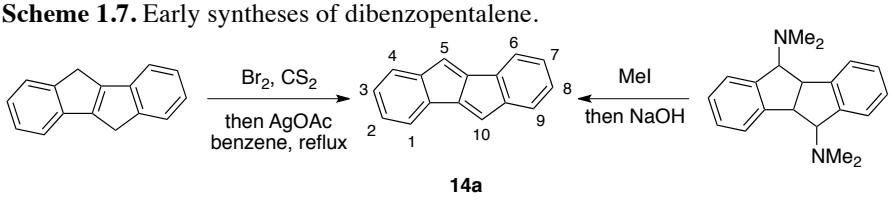

14a

Studies involving **14a** and its derivatives were scarce for the next 40 years. In an attempt to prepare [8]annulene derivative **15a**, Youngs and coworkers discovered a Pd-catalyzed route to dibenzopentalenes (Scheme 1.8).[37] Under standard Sonogashira conditions, **14b** was obtained in 67% yield with desired cyclodimer **15a** in only 10% yield. The unexpected dibenzopentalene **14b** was presumed to arise from an intramolecular cyclization and subsequent hydrogen atom abstraction from the solvent. The lack of trimer and tetramer in the reaction mixture was most likely due to the steric bulk of the flanking *tert*-butyldimethylsilyl groups.

Scheme 1.8. Unexpected formation of dibenzopentalene by Pd-catalyzed arylation/annulation.

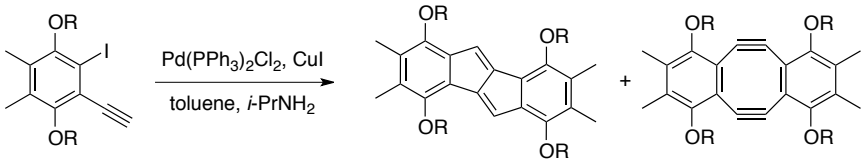

R = Si(*t*-Bu)Me$_2$

14b **15a**

The Otera group reported a new route to dibenzopentalenes by the reaction of dibenzocyclooctadiyne **15b** with alkyllithium reagents (Scheme 1.9).[38] The dibenzopentalenyl anion could be quenched at low temperatures with iodine to provide **14c**. In a later report it was

found that the reaction of I_2 with **15b** could also induce cyclization to diiodide **14d**.[39] Further functionalization was possible by borylation and standard Pd-catalyzed cross-coupling methods to give a range of dibenzopentalene oligomers.

Scheme 1.9. Transannular cyclization initiated by alkyllithium reagents or I_2 to provide dibenzopentalenes and oligomerization by cross-coupling.

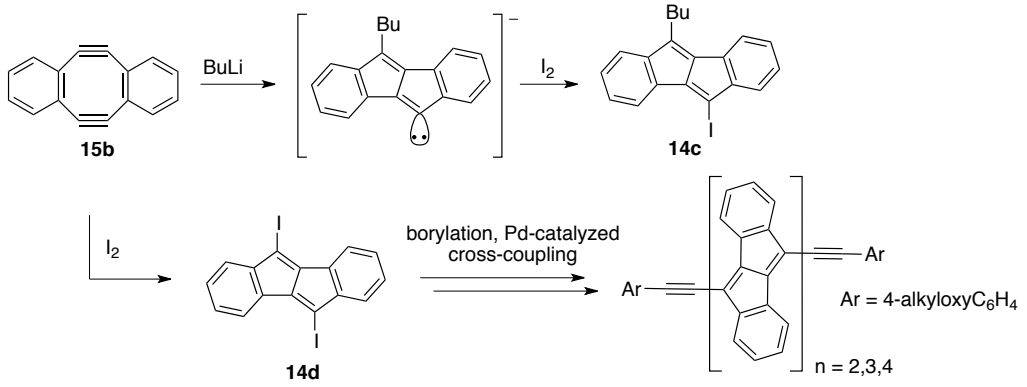

Expanding upon Youngs' discovery, the group of Kawase developed a Ni-mediated reductive cyclization of 2-bromoarylacetylenes (Scheme 1.10).[40] Optimized conditions required one molar equivalent of a Ni(II) complex and excess Zn dust. A variety of substituted dibenzopentalenes **14e**-**h** could be prepared in adequate yields (13-46%), most notably with aryl groups at the 5,10-positions of the pentalene system. The intermediate arylnickel(II) oxidative addition complex could be isolated in the absence of Zn. Upon heating the Ni complex in toluene, the dibenzopentalene derivative was produced in 83% yield. Terminal alkynes and acetylenecarboxylates gave complex mixtures under the reaction conditions.

Scheme 1.10. Ni-mediated reductive cyclization of alkynylaryl bromides.

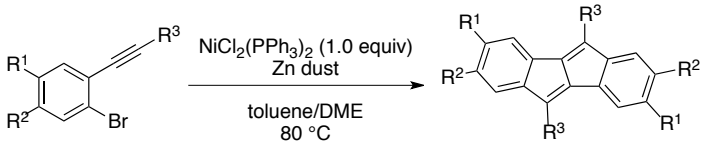

14e $R^1 = R^2 = H$, $R^3 = SiMe_3$
14f $R^1 = R^2 = OMe$, $R^3 = SiMe_3$
14g $R^1 = CO_2Me$, $R^2 = H$, $R^3 = 4\text{-}MeC_6H_4$
14h $R^1 = Me$, $R^2 = H$, $R^3 = 4\text{-}OMeC_6H_4$

The Yamaguchi group at Nagoya University reported the synthesis of dibenzopentalenes from bis(arylcarbonyl)diphenylacetylenes **16** (Scheme 1.11).[41] Excess Li naphthalenide was used to initiate 5-*endo*-dig cyclization onto the central alkyne. Another reduction eliminated Li_2O and gave **14i** in 8-25% yield. The 5,10-diol could be isolated by quenching the intermediate Li alkoxide **17** at -10 °C; further exposure to Li naphthalenide provides **14i** in 49% yield.

Scheme 1.11. Synthesis of diphenyldibenzopentalene **14i** by 5-*endo*-dig cyclizations.

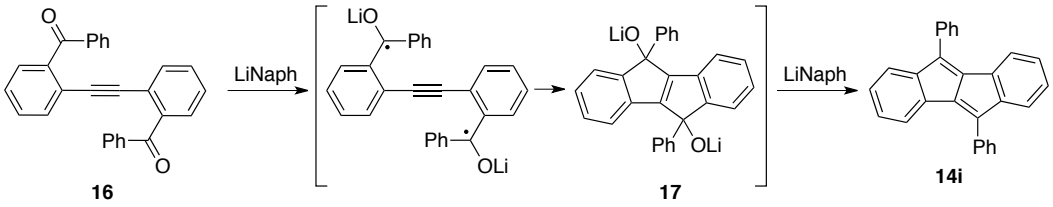

16 **17** **14i**

In an attempt to prepare a 1,4-dilithio-1,3-butadiene derivative, Saito and coworkers observed the unexpected formation of a dilithium dibenzopentalenide **18** (Scheme 1.12).[42,43] Oxidation with iodine gave **14j** in 8% yield over two steps. Interestingly, the larger tri-*tert*-butylsilyl unit led to cleavage of the phenyl group and the smaller *tert*-butyldimethylsilyl gave predominantly 1,4-dilithio-1,3-butadiene. X-ray quality crystals of **18** were obtained and analysis showed nearly identical bond distances (1.444-1.468 Å) in the five-membered rings. Upon oxidation of **18** to neutral **14j** the central bonds displayed remarkable bond length alternation (1.357-1.512 Å) confirming the structural assignment. Recently, the group reported an improved

yield (59%, 2 steps) of **14j** by reduction with K.[44] The range of possible silyl groups was also expanded to include the smaller silyl groups (**14k**, 58%) and (**14e**, 40%).

Scheme 1.12. Alkali metal induced cyclization to provide 5,10-(trialkylsilyl)dibenzopentalenes.

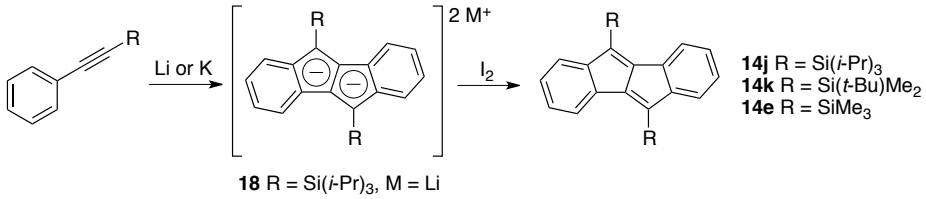

Concurrent with Kawase's Ni-mediated route, the Tilley group reported a preparation of dibenzopentalenes from the Pd-catalyzed homocoupling of haloenynes (Scheme 1.13).[45] High temperature and excess hydroquinone reductant were necessary for the excellent yields in the coupling reaction (55-88%). Thiophenes could also participate in the reaction providing an unprecedented pentalenodithiophene **20**. A perarylated pentalene **19** was prepared from the corresponding iodoenyne in 60% yield. At the time of publication this was the most direct and high yielding route to substituted dibenzopentalenes.

Scheme 1.13. Tilley's Pd-catalyzed reductive homocoupling towards pentalenes.

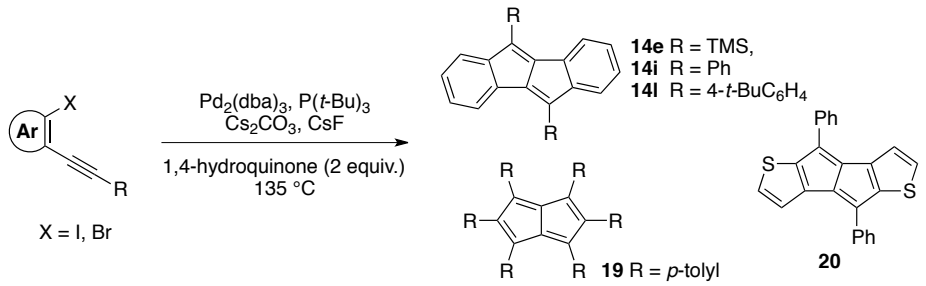

In a succeeding paper, Tilley and Levi took inspiration from a natural product synthesis[46] to prepare large multi-pentalene-containing systems (Scheme 1.14).[47] A Pd-catalyzed annulation of 2-bromostilbenes with symmetrical diarylacetylenes followed by a Lewis-acid mediated

cyclodehydrogenation with $FeCl_3$ provides the dibenzopentalenes. The synthesis could be easily extended to prepare large, fully conjugated, ladder-type molecules. Each symmetrical isomer of dibromodistyrylbenzene was subjected to the two-step reaction sequence providing the dipentalene products **21**-**23**. Cyclic voltammetry revealed that the centrosymmetric **21** was able to accept up to four electrons reversibly.

Scheme 1.14. Preparation of dipentalene-containing systems by stepwise Pd-catalyzed annulation and Lewis-acid cyclodehydrogenation.

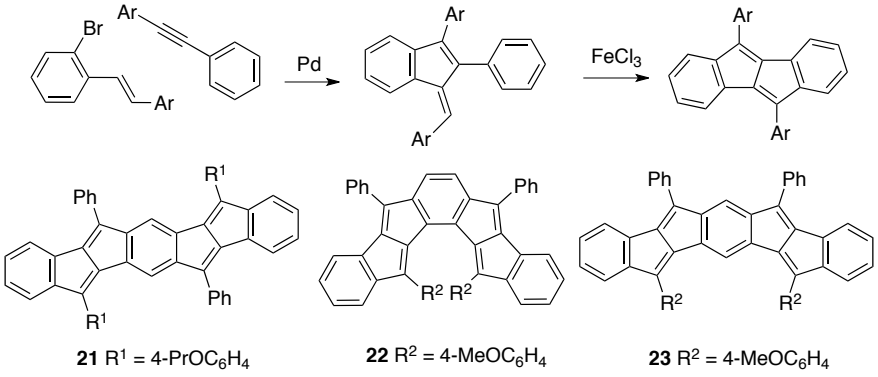

21 R^1 = 4-$PrOC_6H_4$ **22** R^2 = 4-$MeOC_6H_4$ **23** R^2 = 4-$MeOC_6H_4$

Hashmi and coworkers reported a Au(I)-catalyzed synthesis of the parent dibenzopentalene **14a** from diyne precursor **24** (Scheme 1.15).[48] The reaction conditions involved heating **24** in the presence of a *N*-heterocyclic carbene Au(I) catalyst. The reaction, while intolerant of aryl halides and electron-poor substrates, was applied to thiophenes and electron-rich arenes. Experimental evidence supported the intermediacy of a Au-vinylidene **25**. Notably, **14a** was characterized by X-ray diffraction for the first time and was shown to pack in a herringbone arrangement with no sub-van der Waals close contacts.

Scheme 1.15. Gold(I) catalyzed cyclization of a diyne to dibenzopentalene.

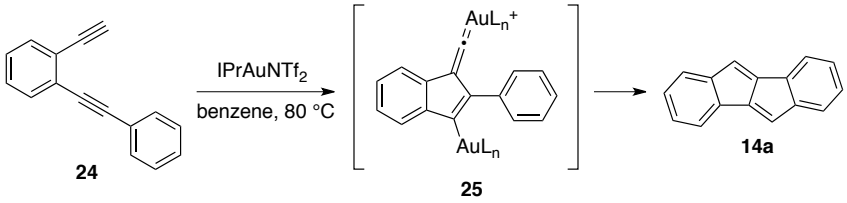

In 2013 a C–H activation route to dibenzopentalenes was discovered by the Itami group (Scheme 1.16).[49] Through a series of electrophilic palladations and insertions the diphenyldibenzopentalene **14i** is constructed in 52% yield. Notably, this method obviates the need for *ortho*-functionalized precursors as in prior examples. Over the course of a mechanistic study, it was found that the first C–H palladation event was sensitive to the electronic nature of the substrate and the subsequent alkyne insertion proceeded without regard. Electron-poor *p*-trifluoromethyl-substituted tolans were excellent substrates (**14m**, 79% yield) and *m*-substituted tolans were decent as well (**14n**, 53% yield; **14o**, 66% yield); however, *p*-methoxy-substituted tolans provided no product.

Scheme 1.16. Dibenzopentalenes by the Pd(II) catalyzed C–H activation of tolans.

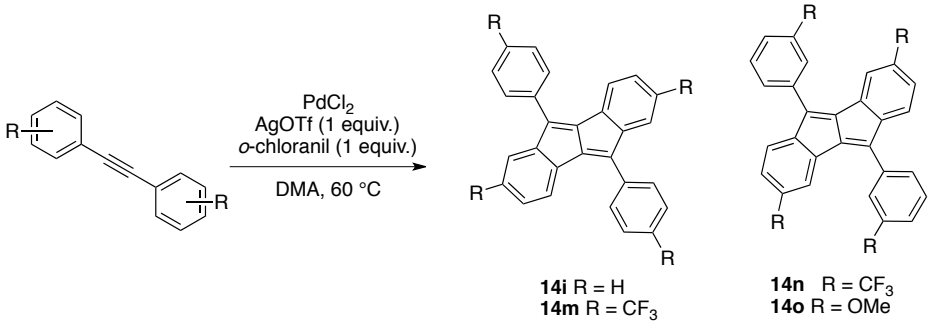

In parallel with Itami's report, the Jin group of Tohoku University published a mechanistically similar approach to dibenzopentalenes.[50] In their work, *o*-alkynylhaloarenes are coupled with diarylacetylenes by the C–H activation mélange of $Pd(OAc)_2$/DBU/CsOPiv

(Scheme 1.17). The substrate scope shows the reaction to be general in contrast to the Itami report; electron-poor (**14o**, **14q**) and electron-rich (**14n**, **14p**) functional groups are tolerated on either substrate and give the dibenzopentalenes in excellent yields (70-89%). Heteroaryl-alkynyl chlorides were also viable substrates as thiophene, benzothiophene and pyridine also participated in the crossover annulation. The authors proposed a mechanism reminiscent of Tilley's and suggested future applications in organic electronics.

Scheme 1.17. Pd-catalyzed crossover annulation towards dibenzopentalenes.

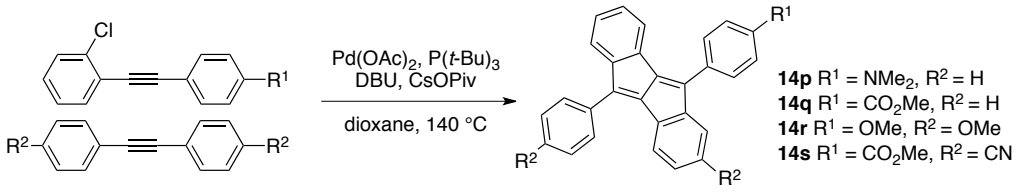

Yi, Zhu and coworkers recently described the Pd-catalyzed synthesis of diacenopentalenes from the homoannulation of 2-iodo(arylethynyl)arenes (Scheme 1.18).[51] The reaction conditions employed $Pd(OAc)_2$ and one equivalent *n*-Bu_4NOAc. According to the authors a Pd(0-II-IV) catalytic cycle is operative with apparent formation of and leaching from Pd nanoparticles. Octacyclic **14t** was prepared in an impressive 80% yield. The compound was shown to pack in slipped stacks with close-contacts just outside van der Waals distances (3.44 Å). In contrast to the non-fluorescent dibenzo- and dinaphthopentalenes also prepared by the authors, the dianthracenopentalene **14t** was emissive at 628 nm ($\Phi = 0.35$).

Scheme 1.18. Preparation of dianthracenopentalene by Pd-catalyzed cyclization.

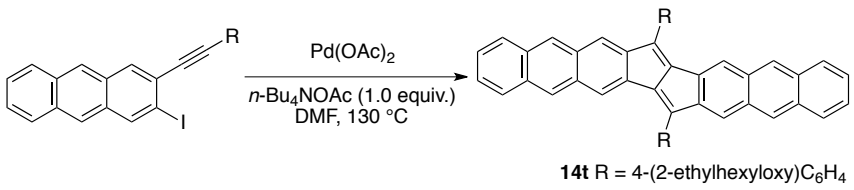

The preparation of large, perfluorinated arenes is an attractive strategy in organic electronics due to the resulting deep LUMO levels and fluoroarene–arene interactions in the solid-state.[52,53] Recently the Xi group reported the preparation of perfluorodinaphtho- and dibenzopentalenes through a C–F cleavage/C–C bond formation promoted by late alkaline earth Grignard reagents (Scheme 1.19).[54] Initially, reaction of the diaryl-diiodobutadiene with *n*-butyllithium only gave trace amounts of the dibenzopentalene **14u**. The use of highly active Rieke Ca, prepared *in situ* by Li biphenylide and CaI_2, at –95 °C provided **14u** in 52% yield. The reaction likely proceeds through formation of a butadienyldicalcium diiodide species and subsequent S_NAr with elimination of a mixed Ca halide. The optimized conditions with Rieke Ca were found to be inadequate for **14v** while lithium-halogen exchange with *n*-butyllithium gave improved yields. LUMO energy levels were estimated by cyclic voltammetry and represent some of the lowest values for pentalene-containing systems (ca. -3.6 eV).

Scheme 1.19. Perfluorinated pentalenes by Rieke-Ca or lithium-halogen exchange initiated C–F bond cleavage.

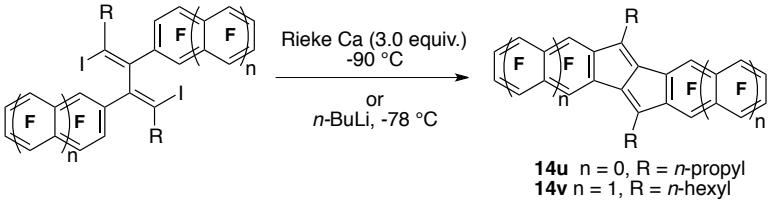

14u n = 0, R = *n*-propyl
14v n = 1, R = *n*-hexyl

The groups of Kawase and Takimiya reported the first OFET device to use a pentalene derivative as the active component.[55] Two isomeric dinaphthopentalenes **14w** and **14x** were prepared via the Kawase route in low yields (Figure 1.7). Single-crystal X-ray diffraction showed the isomers pack in slipped 1D columns, while CV showed two reversible oxidations and two reversible reductions. OFET devices from amorphous films of **14w** and **14x** were fabricated. Linear **14w** gave some hole mobility (1.8×10^{-3} $cm^2V^{-1}s^{-1}$) while **14x** gave a negligible field

effect. Similar behavior was observed with the dinaphthothieno[3,2-*b*]thiophene system: the acene-like (**14w**) isomer showed superior performance in OFETs compared to the phenanthrene-like (**14x**) isomers.[56]

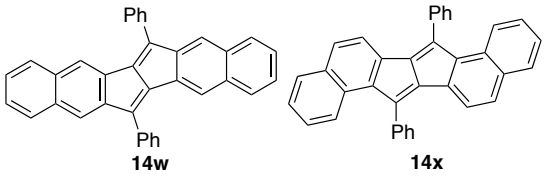

14w **14x**

Figure 1.7. Kawase and Takimiya's diphenyldinaphthopentalenes used in OFETs.

A recent example incorporating dibenzopentalene into conjugated polymers was described by the group of Takimiya (Figure 1.8).[57] Interestingly, the authors noted dissimilar properties depending on the connectivity of the dibenzopentalene moiety within the poly(2,5-thiophene) polymer. Conjugation through the 5,10-positions (**26**) resulted in an electronic structure comparable to an all-donor polymer. The dibenzopentalene in this orientation can be considered a 1,3-butadiene inserted within the polymer. Attachment *via* 2,7-positions (**27**) produced material with significant donor-acceptor character. This was rationalized by the electron-accepting nature of the dibenzopentalene moiety now in direct conjugation with the donor thiophene units and the appearance of a distinctive dual-band electronic absorption. Thin-films of either polymer could be spun-cast from chlorobenzene and exhibited decent OFET device performance (0.1 $cm^2V^{-1}s^{-1}$).

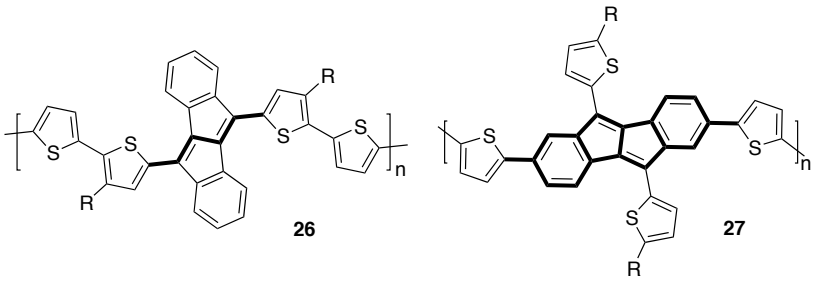

Figure 1.8. Takimiya and coworker's semiconducting polymers with conjugation (bold) through the 5,10 (**26**) or 2,7 (**27**) positions of dibenzopentalene.

Indenofluorenes

Indacene is the core fragment of the third class of CPPAs. In the same vein as pentalene, the parent indacene molecule has an antiaromatic, [12]annulene perimeter around a 5-6-5 ring system. The fusion of benzene rings to the five-membered rings imparts stability to the indacene core and produces the five indenofluorene (IF) isomers (Figure 1.9). Centrosymmetric [1,2-*b*] and axosymmetric [2,1-*a*], [2,1-*b*] and [2,1-*c*] have examples in the literature (vide infra) while the fully-conjugated, asymmetric [1,2-*a*] remains unknown. The syntheses of cross-conjugated indenofluorene derivatives and related structures have been reviewed in detail elsewhere.[58]

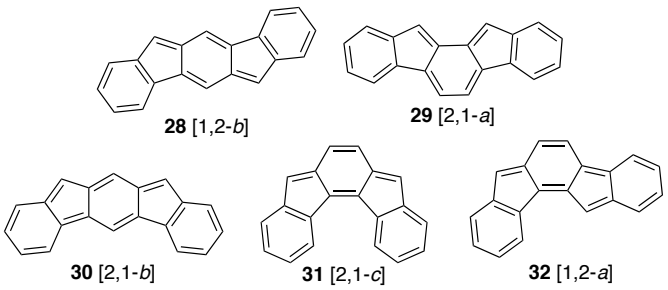

Figure 1.9. Indenofluorene structural isomers and naming scheme.

Indenofluorenes have great potential for use as n-type electron-accepting materials in OFETs and OPVs due to their low-lying LUMO energy levels, 20 π-electron, pro-aromatic backbone and ease of functionalization. While p-type organic semiconductors are commonplace,

the development of stable n-type materials is a major goal in organic electronics.[59-61] Core-expanded indenofluorenes have been predicted to possess ideal energy levels for singlet fission.[62] The low frontier-orbital energy-gap and open-shell character for selected IF derivatives could produce interesting materials for NIR absorption and organic spin-electronics.[63-66]

A communication in early 2011 from the Haley group disclosed the synthesis and characterization of indeno[1,2-*b*]fluorene **28a** (Figure 1.10).[67] Inspiration for the synthesis came from earlier work by the Swager group with their preparation of the unstable tetraiodoindeno[1,2-*b*]fluorene skeleton.[68] The fully conjugated, formally antiaromatic compound was studied by single-crystal X-ray diffraction and was shown to have significant bond alternation in the 5-6-5 tricyclic core that was reminiscent of a *p*-xylylene moiety.

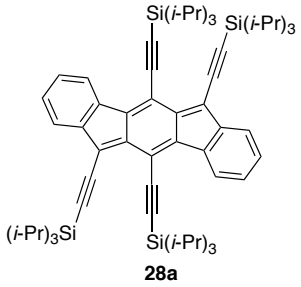

28a

Figure 1.10. Fully-conjugated indeno[1,2-*b*]fluorene derivative.

Haley and coworkers simplified the synthesis and expanded the scope of available fully-conjugated indeno[1,2-*b*]fluorenes in a subsequent report (Scheme 1.20).[69] Easily accessible indeno[1,2-*b*]fluorene-6,12-diones **33** were prepared in three steps. Then, addition of (triisopropylsilyl)ethynyllithium and an acidic work-up provides the diols. Reduction with $SnCl_2$ in toluene yields fully-conjugated derivatives of **28**. The compounds were shown to reversibly accept two electrons at potentials (ca. -0.6V, -1.1V vs. SCE) comparable to the benchmark electron-acceptor material [6,6]-phenyl-C_{61}-butyric acid methyl ester (PCBM). These results were rationalized by the formation of an aromatic 22 π-electron species from the neutral, antiaromatic 20 π-electron system.

Scheme 1.20. Derivitization of indeno[1,2-*b*]fluorene via diones **33**.

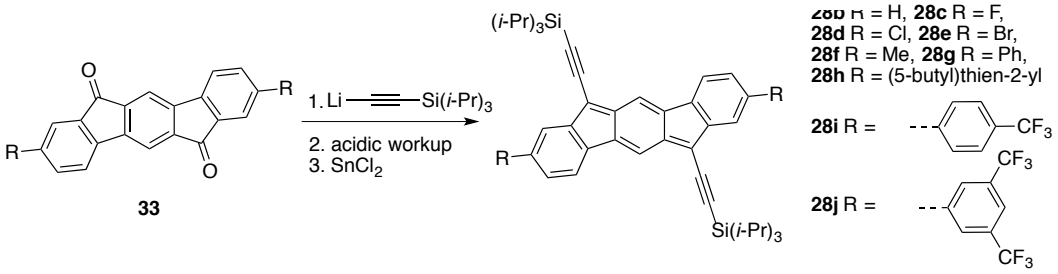

Recognizing the ability of the indenofluorene scaffold to reversibly accept electrons led Haley, Nuckolls and coworkers to report the synthesis of a series of 6,12-diarylindeno[1,2-*b*]fluorenes and the fabrication of an ambipolar OFET (Figure 1.11).[70] The diphenyl derivative **28k** was known from Scherf's work in the 1990s but not thoroughly characterized at that time.[71] A range of derivatives (**28k**-**28t**) were prepared and studied by cyclic voltammetry and electronic absorption spectroscopy. Trends between the electronic character of the aryl group, λ_{max} and E_{red}/E_{ox} were identified: electron-rich aryl groups (**28l**) raised the HOMO and LUMO energy levels while electron-deficient aryl groups (**28n**-**28p**) lowered the energy levels. IFs with fluorinated aryl groups (**28n**-**28p**) exhibited reversible reductions but irreversible oxidations. The amphoteric redox properties were further revealed through device fabrication. Micron-scale single-crystals of **28p** were obtained and used as the active component in an OFET. Although device performance was poor ($\mu_e = 3\times10^{-3}$ cm^{2}V^{-1}s^{-1}, $\mu_h = 7\times10^{-4}$ cm^{2}V^{-1}s^{-1}), this was one of first examples of a small molecule used in an ambipolar OFET.

A concurrent report from the Yamashita group described the synthesis and characterization of 6,12-diarylindeno[1,2-*b*]fluorenes **28k**,**r**-**t**.[72] OFETs fabricated from thin-films of the **28k** exhibited hole transport. The 2,6-difluorophenyl **28r** and 9-anthracenyl **28t** derivatives had deeper LUMO energy levels and as a result showed ambipolar charge transport. The field effect mobility was on the order of 10^{-5} cm^{2}V^{-1}s^{-1} most likely due to the amorphous nature of the thin-films. Further derivatization and device optimization was anticipated to improve performance.

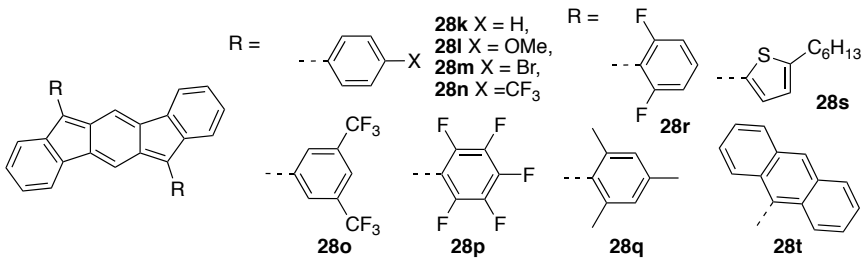

Figure 1.11. 6,12-Diaryl derivatives of indeno[1,2-*b*]fluorene by the groups of Haley(**28k**-**28q**) and Yamashita (**28k**, **28r**-**28t**).

The next isomer in the fully-conjugated indenofluorene family was reported by Tobe and Shimizu in 2011 (Figure 1.12).[73] 11,12-Dimesitylindeno[2,1-*a*]fluorene **29a** was prepared in 40% yield in two steps from a known dione precursor. Analysis of the crystal structure showed bond length alternation (~0.07 Å) in the core confirming the structural assignment. The compound was found to be stable to dienophiles and oxygen considering the reactive *o*-xylylene moiety within the framework. Contribution of a singlet biradical structure to the ground state was proposed based on the elongated methylidyne $C_{sp}{}^2$–$C_{sp}{}^2$ bond and the significant HOMO/LUMO orbital coefficients at the apical positions. Benzannulated analogue **29b** was reported by the same group in 2013 and featured a rare 2,3-naphthoquinodimethane.[74] The compound showed heightened reactivity towards oxygen and greater proclivity to dimerize compared to **29a**. The authors noted a more accessible triplet biradical and smaller HOMO-LUMO energy gap (1.60 eV for **29b** vs. 2.10 eV for **29a**).

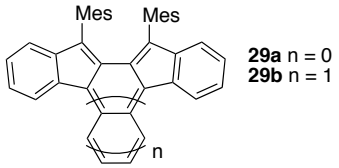

Figure 1.12. Tobe's dimesitylindeno[2,1-*a*]fluorene and benzannulated derivative.

Tobe and coworkers achieved the synthesis of a moderately stable *meta*-quinodimethane containing indeno[2,1-*b*]fluorene **30a** in 2013 (Figure 1.13).[75] The compound was prepared in 59% yield over two steps from the known dione precursor. Characterization by single-crystal X-ray diffraction show slightly delocalized six-membered rings bridged by C(sp^2)–C(sp^3) bonds (~1.43 Å). Combined with the lack of NMR signal at 30 °C, the authors concluded that

indeno[2,1-*b*]fluorene has a substantial singlet biradical contribution to the ground state. The disappearance of EPR signal and appearance of NMR signal upon cooling confirmed the existence of a triplet biradical. The singlet-triplet gap was estimated to be -17.6 kcal mol^{-1} by temperature dependent magnetic susceptibility measurements. Extremely low energy absorption out to 2000 nm (0.62 eV) was observed and the lowest-energy maximum at 1700 nm was assigned to the S_0–S_1 transition by TD-DFT calculations. Indeno[2,1-*b*]fluorene derivatives have potential for low-energy light absorption applications.[65,76]

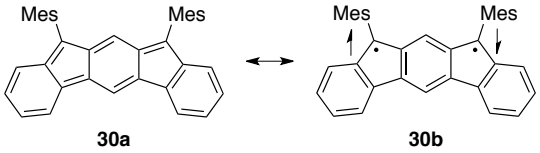

Figure 1.13. Tobe's dimesitylindeno[2,1-*b*]fluorene in Kekulé (left) and open-shell resonance forms.

Haley and coworkers introduced the next member of the fully-conjugated indenofluorene family with their synthesis of indeno[2,1-*c*]fluorenes **31** (Figure 1.14).[77]

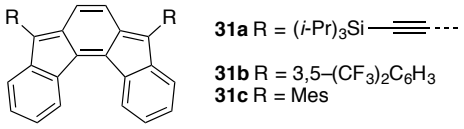

Figure 1.14. Fully conjugated indeno[2,1-*c*]fluorene derivatives featuring an *as*-indacene core.

The compounds are a fragment of C_{60} and contain the rarely explored *as*-indacene motif. This class of compounds was found to be superior electron acceptors to the [1,2-*b*] analogues as the electrochemically derived HOMO-LUMO energy gap was narrowed by 0.14 eV to 2.08 eV (**31c** vs. **28q**). (Triisopropylsilyl)ethynyl (**31a**) and electron-deficient aryl groups (**31b**) were included in the substrate scope to promote solid-state ordering and lower LUMO energy levels, respectively. Also notable is the appearance of a low energy S_0-S_1 transition extending to 850 nm that is formally forbidden in centrosymmetric **28**. The effects of different electron-acceptors on charge photogeneration in bulk heterojunctions was studied by the Ostroverkhova group.[78] The use of **31c** or TIPS-octafluoropentacene as acceptors hampered device results as they disrupted the donor crystallinity. The widely used C_{60} derivative PCBM was used as a comparison.

The effects of extending the indenofluorene core were investigated by the Haley group with their synthesis of fluoreno[4,3-*c*]fluorene **32** in 2012 (Figure 1.15).[79] Scherf and coworkers had previously synthesized the dione precursor for use in ladder-type polymers.[80] Gratifyingly, **32** was isolated in 86% yield over two steps and could be purified by sublimation. The 2,6-naphthoquinodimethane core was surprisingly stable and exhibited no signs of open-shell character by variable temperature EPR/NMR spectroscopy or by analysis of bond distances in a single crystal. A possible explanation is that the lack of radical stabilizing groups (e.g., phenalenyl[81]) enforces a closed shell ground state. The lack of fluorescence in **32** as well as in **31a** and **28b** was explained through transient absorption spectroscopy and computational analysis.[82] Excited state lifetimes on the order of 9-12 ps were obtained, which indicated extremely fast relaxation through nonemissive pathways. The calculations indicate that a potential energy surface crossing between the S_0 and S_1 states, i.e., a conical intersection, is responsible for this phenomenon.

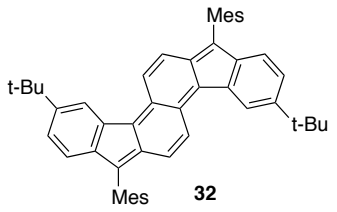

Figure 1.15. Closed shell fluoreno[4,3-*c*]fluorene prepared by the Haley group.

The Fischer and Crommie groups studied the reaction of oligoyne **33** deposited onto metal surfaces.[83] Upon annealing at temperatures greater than 90 °C, a series of enediyne cyclizations and hydride shifts occurred on a Ag surface to give unprecedented indenofluorene containing hydrocarbons **29c** and **31d** (Scheme 1.21). The molecular structures were confirmed through non-contact atomic force microscopy (nc-AFM), which allowed researchers to visualize the individual bonds. The cyclization processes were modeled and supported by DFT computations. Although the products were not further characterized, the design of future surface-supported molecular constructs was alluded to.

Scheme 1.21. Formation of indenofluorene containing molecules by thermal annealing on a Ag(100) surface.

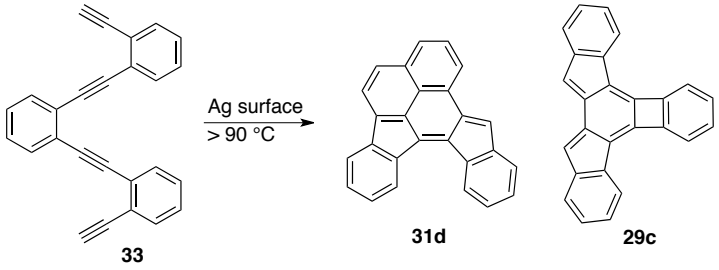

Indacenedithiophenes are a class of molecules that are isoelectronic to the indenofluorene family (Figure 1.16). Incorporation of sulfur into aromatic backbones is an established method to improve processability, stability to ambient conditions and modify electronics.[84-86] Indacenedithiophenes **34a** and **35a** were prepared by the Haley group and exhibited red shifted absorptions and deepened LUMO energy levels compared with **28q**. Benzannulated derivatives **34b** and **35b** were further red-shifted with LUMO energy levels estimated at -4.03 eV and -3.84 eV, respectively. In contrast to the preparation of pentacene analogue anthradithiophene[87,88], both regioisomers (e.g. **34a** "syn" vs. **34b** "anti") could be independently and easily prepared. All compounds were characterized by single-crystal X-ray diffraction and showed a *p*-xylylene core but with more homogenous bond distances than **28q** indicating increased paratropicity of the indacene unit. Also notable is a short contact (3.35 Å) between the five-membered rings of **35a** and an adjacent sulfur atom.

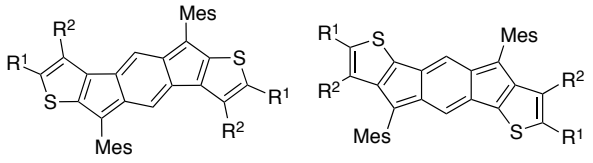

34a $R^1 = R^2 = H$
34b $R^1–R^2 = C_4H_4$

35a $R^1 = R^2 = H$
35b $R^1–R^2 = C_4H_4$

Figure 1.16. Fully-conjugated indacenedi(benzo)thiophenes prepared by the Haley group.

Reports from the Haley[89] and Chi[90] groups described the synthesis and characterization of quinoidal diindenothienoacenes (DI[*n*]Ts) **36**–**39** (Figure 1.17). The family of compounds can be considered analogues of **31** as the bridging C_2H_2 unit is exchanged with an isoelectronic sulfur atom. Motivation for this research stemmed from the ubiquity of thiophenes throughout organic electronics and the increased stability of thienoacenes compared to acenes. Whereas **36**–**38** are stable, isolation and characterization of **39** proved challenging as Chi and coworkers cited moderate biradical character ($y_0 = 0.20$) with a thermally accessible triplet state. The DI[*n*]Ts reversibly accept two electrons at increasingly positive potentials as the core (*n*) expands. The electrochemically derived HOMO-LUMO energy gap decreases from 1.93 (**36**) to 1.60 eV (**38**) coincident with red-shifting of the electronic absorption edge.

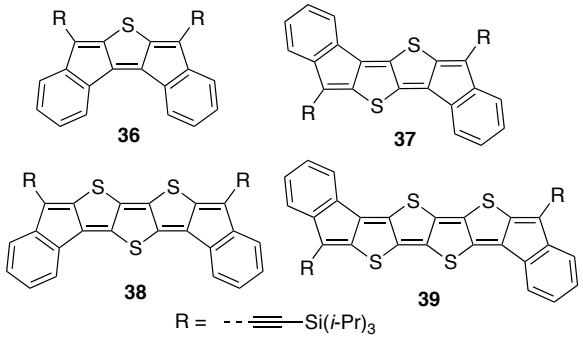

Figure 1.17. Quinoidal diindenothienoacenes (DI[*n*]Ts) prepared by the groups of Haley and Chi.

The DI[*n*]Ts solid-state structure was determined through single-crystal X-ray diffraction and confirms the quinoidal assignment. The compounds were found to arrange into 1-D slipped stacks with the lateral slip between molecules decreasing as *n* increases (Figure 1.18). For **36**, tuning of the solid-state packing by modification of the trialkylsilyl group to the smaller triethylsilyl was shown. From their favorable solid-state packing, electron-accepting properties and intense NIR absorption, DI[*n*]Ts show potential as organic materials for use in OFETs and OPVs.

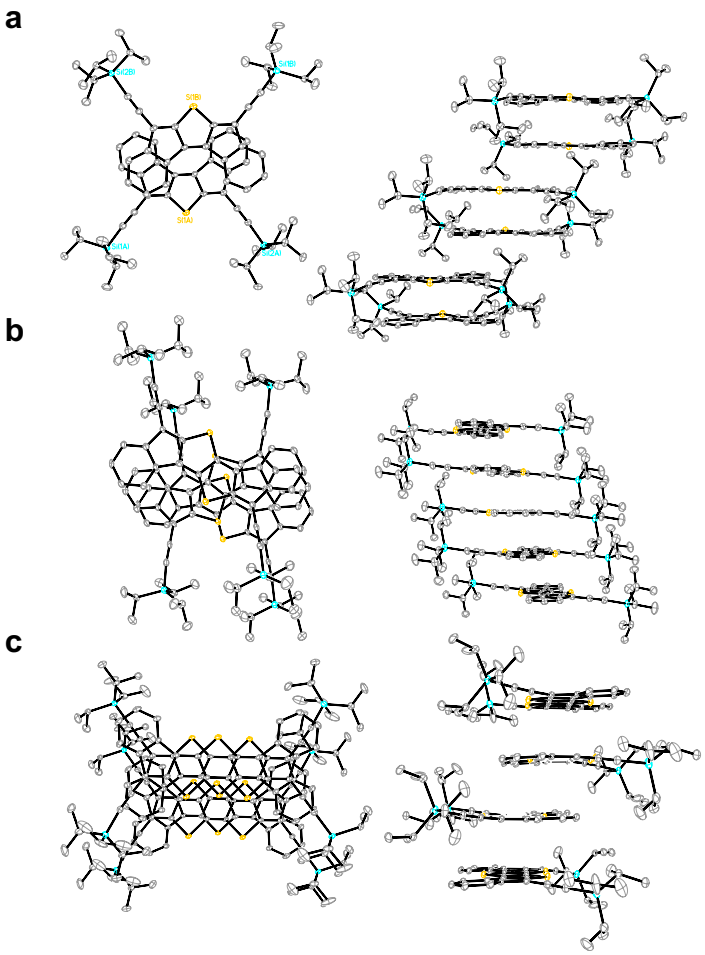

Figure 1.18. Solid-state packing for DI[*n*]Ts a) **36**, b) **37** and c) **38**. The compounds exhibit slip-stacked through column-like arrangements.

Conclusion

We have surveyed the emerging class of planar cyclopenta-fused polycyclic arenes. Recent examples of acenaphthylene-, pentalene- and indacene-containing compounds demonstrate the breadth of synthetic work. The discovery of unusual reaction products followed by methods development is a central theme in the field. Resoundingly, Pd-catalysis has led to a multitude of new strategies for PA synthesis. Collaborative studies applying CPPAs in devices such as OFETs and OPVs has exploited the favorable properties of the compounds and

establishes a foundation for further investigations. Molecules with reactive, antiaromatic cores are now viable platforms for researchers to apply in carbon-based materials.

Bridge to Chapter II

Chapter I serves as an introduction to the recent chemistry and historical context of cyclopenta-fused polycyclic hydrocarbons. Chapter II represents some of our early work in exploring the effects of expanding the core of the indenofluorene scaffold with fused heterocycles.

CHAPTER II

QUINOIDAL DIINDENOTHIENOACENES: SYNTHESIS AND PROPERTIES OF NEW FUNCTIONAL ORGANIC MATERIALS

This chapter was written by Gabriel Rudebusch. Aaron G. Fix developed an initial synthetic route, Hillary A. Henthorn performed calculations and the EPR studies, Chris L. Vonnegut performed electrochemical measurements. Michael M. Haley provided editorial and material support. This work was originally published in *Chemical Science*.

Introduction

We report the preparation and characterization of a new class of quinoidal thienoacenes. The synthetic route is efficient, high-yielding and scalable with the potential for further functionalization. Single crystal X-ray diffraction reveals that, as size increases, the molecules pack in progressively closer 1D arrangements. The title compounds are shown to have amphoteric redox behaviour by cyclic voltammetry. The anion radicals are studied by ESR spectrometry and by computations. The electron-accepting nature, strong NIR absorption and the low-lying LUMO energies (ca. –4.0 eV) allude to potential use in materials applications.

Quinoidal oligothiophenes (QOTs) and quinoidal thienoacenes (QTAs) have attracted significant interest as functional organic materials (Figure 2.1). Initially, the preparation of thiophene oligomers and study of their reduced and oxidized forms provided models for the doped portions of polythiophene.[1] One of the first small molecules to exhibit ambipolar character in an OFET was based on a terthienoquinoidal core (**1**).[2] Thorough understanding of the stability of the reduced

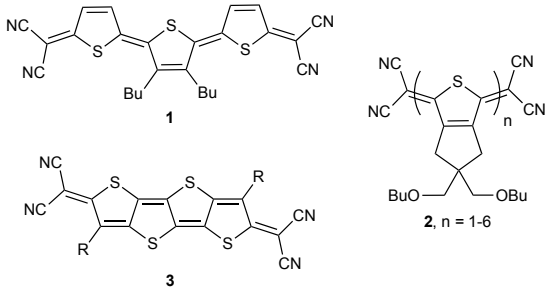

Figure 2.1. Examples of quinoidal oligothiophenes (1, 2) and thienoacenes (3) reported in the literature; R = solubilizing alkyl group.

and oxidized states of **1** led to increased OFET performance and the discovery of ambipolar transport characteristics.3 Otsubo, Aso and co-workers accomplished the synthesis of the largest family of QOTs (**2**).[4] Solubility issues of the larger QOTs were solved by fusion of a solubilizing bis(butoxymethyl)-cyclopentane group to the thiophene core. The longest members (n = 5, 6) featured open-shell ground states and low-energy absorptions to 1400 nm.[5] A terthiophene derivative of **2** as the active layer in OFETs was also described.[6] Recently, Zhu et al. reported n-channel behaviour in thin films of QTA **3**.[7] As noted by the authors, isomerization issues inherent in QOTs are eliminated by moving to the fused QTA core. Lastly, the QTA scaffolds are promising for nonlinear optics due to their rigidity and symmetry.[8] Large alternant polycyclic hydrocarbons possessing low energy triplet excited states and multiphoton absorption properties are of interest for singlet exciton fission.[9]

Our group has initiated studies on a seldom explored class of quinoidal molecules based on the indenofluorene skeleton.[10] While most of our work has focused on indeno[1,2-*b*]fluorenes,[11] we have reported derivatives of indeno[2,1-*c*]fluorene **4**[12] and fluoreno[4,3-*c*]fluorene **5**[13] (Figure 2.2), which exhibit interesting absorption profiles and amphoteric redox behaviour. Very recently we reported the fully conjugated indacenedithiophenes,[14] where thiophenes replaced the outer benzene rings of indeno[1,2-*b*]fluorenes. In analogy, exchange of the bridging sp^2 carbon units in **4** and **5** with isoelectronic sulfur atoms to provide **6** and **7** is an attractive and straightforward approach to further tune the quinoidal core of indenofluorenes. Sulfur incorporation into the framework of polycyclic hydrocarbons is a versatile method to promote good solid-state ordering and improve stability at ambient conditions.[15]

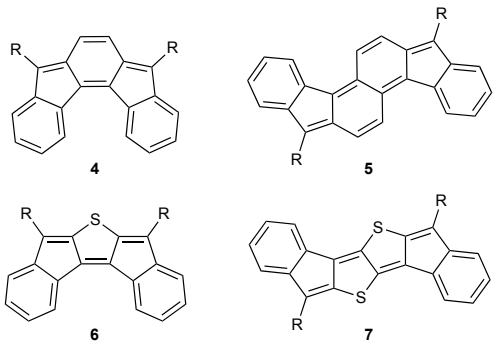

Figure 2.2. Previously reported indenofluorene **4** and fluorenofluorene **5** and their DI[*n*]T analogues **6** and **7**.

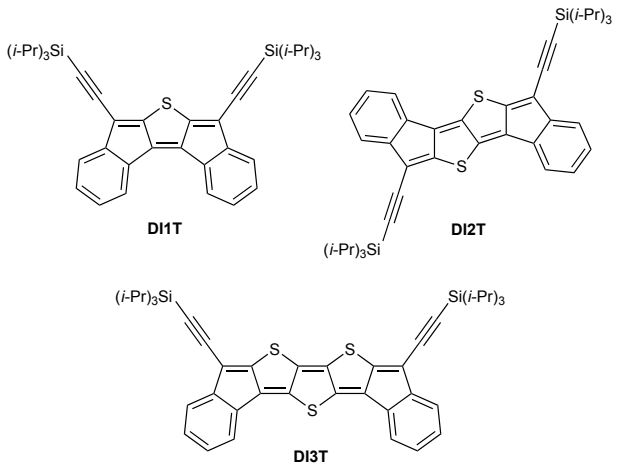

Figure 2.3. Structures of diindeno(thieno)thiophenes (DI[*n*]Ts).

Herein we describe the synthesis and characterization of a series of quinoidal diindeno(thieno)thiophenes (DI[*n*]Ts) (Figure 2.3). This work represents a new approach to quinoidal thienoacenes through the fusion of electron-accepting indene fragments to a thienoacene core. The ease of thiophene synthesis and anticipated stability of the final quinoidal molecules are appealing features of this strategy. Possible substituents include (trialkylsilyl)ethynyl groups to favour solid-state order[16] and aryl groups to tune the electronics[11b,c] of the architecture.

Results and Discussion

Synthesis

Synthesis is initiated with the Suzuki-Miyaura cross-coupling of 3,4-dibromothiophene and commercially available 2-ethoxycarbonylbenzeneboronic acid (Scheme 2.1). Use of Buchwald's SPhos ligand was critical for efficient coupling of the electron-rich bromothiophene with the electron-poor arylboronic acid.[17] Next, saponification of diester **8** followed by formation of the acid chloride and Friedel-Crafts acylation provides dione **9** in good yield. Gratifyingly, we found that 3,4-dibromothiophene could be mono-acylated to give **10** in 92% yield. Condensation

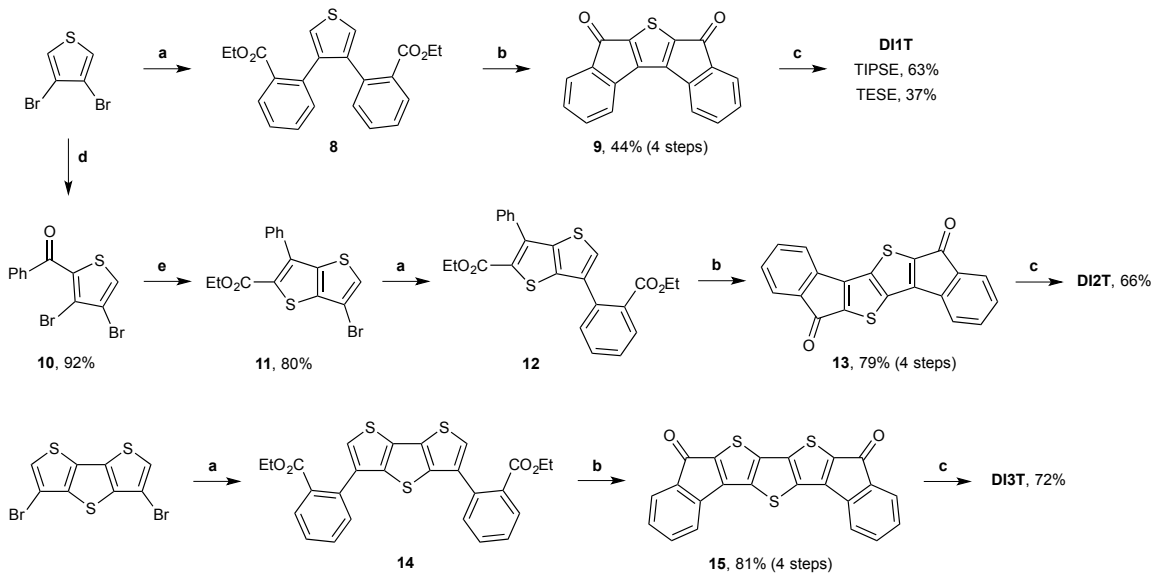

Scheme 2.1. Synthesis of **DI1T**, **DI2T** and **DI3T**; Reagent and conditions: (a) 2-ethoxycarbonylbenzeneboronic acid, Pd_2dba_3, SPhos, K_3PO_4, toluene, 100 °C; (b) i) KOH, EtOH, reflux; ii) oxalyl chloride, DMF, CH_2Cl_2, rt; iii) $AlCl_3$, CH_2Cl_2, 0 °C to rt; (c) i) (trialkylsilyl)ethynyllithium, 0 °C, then sat. NH_4Cl; ii) $SnCl_2$, toluene, rt; (d) benzoyl chloride, $AlCl_3$, 0 °C to rt; (e) ethyl thioglycolate, K_2CO_3, DMF, 60 °C.

with ethyl thioglycolate in the presence of potassium carbonate furnishes thienothiophene **11** in 80% yield. This route avoids the preparation of unsubstituted thieno[3,2-*b*]thiophene either through traditional methods[18] or the improved Matzger route.[19] Suzuki-Miyaura cross-coupling gives diester **12** in quantitative yield. Elaboration to **13** proceeds in 79% yield over four steps. Dione **15** was prepared in an analogous manner via diester **14** starting from 3,5-dibromodithieno[3,2-*b*:2',3'-*d*]thiophene. Notably, the synthesis of diones **9**, **13** and **15** can be performed on multi-gram scale with no silica gel chromatography. Nucleophilic addition of (trialkylsilyl)ethynyllithium proceeds quantitatively despite poor solubility of the dione starting materials. Reduction of the respective diols by anhydrous $SnCl_2$ in toluene gives the quinoidal DI[*n*]Ts in modest to very good yield. Interestingly, the reduction to **DI3T** is complete within minutes while the reduction to **DI1T** and **DI2T** requires several hours to reach full conversion. The final compounds were stable toward silica gel and ambient conditions. No measures to protect the compounds from air or water were taken and no significant decomposition was observed in the solid-state or in solution.

Solid-State State Structure from X-ray Diffraction

Single crystals of DI[*n*]Ts sufficient for characterization by X-ray diffraction were obtained by slow evaporation from CH_2Cl_2. **DI1T-TIPSE** arranges into a pairwise slipped stacks with distances between average planes of 3.30 Å within the pair and 3.37 Å between adjacent pairs (Figure 2.4, left and Table 2.1). Lateral (short-axis) slip of the core was found to be 1.06 Å in the pair and 5.82 Å between pairs. **DI1T-TESE** also packs in pairwise slipped stacks with the distance between average planes of the molecules of 3.43 Å in the pair and 3.34 Å between pairs (Figure 2.4, right). The smaller trialkylsilyl group altered the lateral slip to 2.52 Å in the pair and 2.55 Å between pairs. **DI2T** forms an alternating 1D structure rather than the dimers seen with **DI1T** due to its centrosymmetry (Figure 2.5, top). The distance between the average planes is 3.41 Å with a lateral slip of 1.46 Å between cores of the molecules. Spacing between neighbouring 1D stacks was greater than van der Waals distance. **DI3T** shows strong overlapping of the quinoidal cores with inter-planar distance of 3.46 Å and lateral slip of 1.79 Å and 1.23 Å (Figure 2.5, bottom). The 1D columns are essentially insulated from adjacent columns by the (triisopropylsilyl)ethynyl groups.

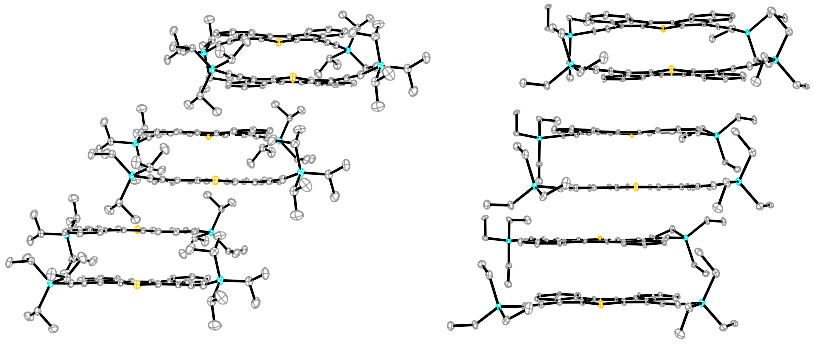

Figure 2.4. Solid-state packing of **DI1T-TIPSE** (left) and **DI1T-TESE** (right).

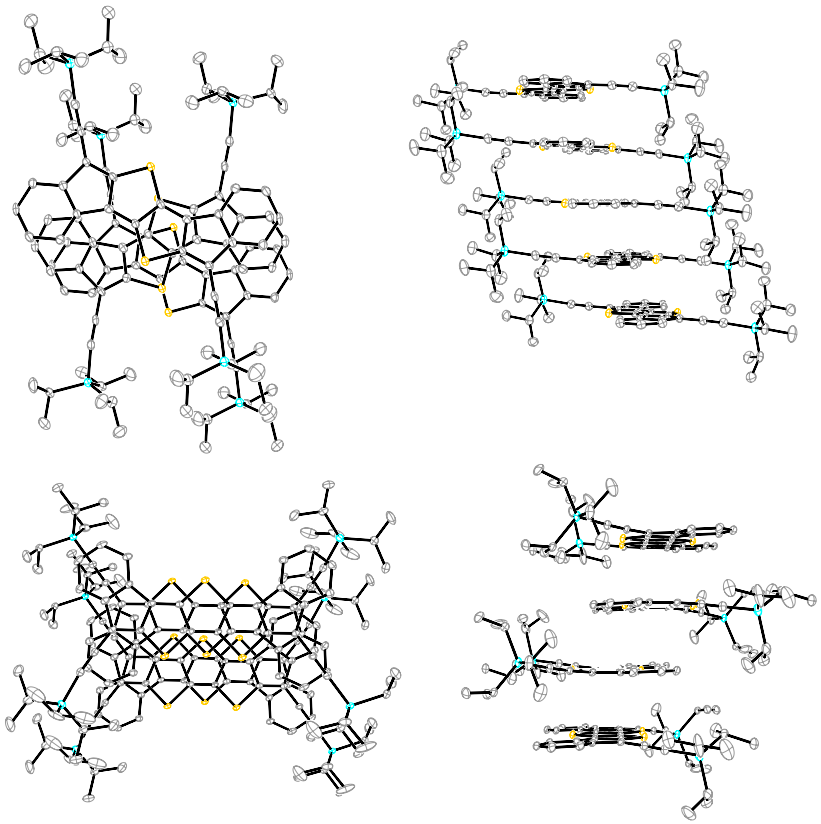

Figure 2.5. Solid-state packing of DI2T (top) and DI3T (bottom).

Table 2.1. Solid-state packing and bond distances of the DI[*n*]T family[a]

	DI1T-TIPSE	DI1T-TESE	DI2T	DI3T
Interplanar distance[b]	3.30, 3.37	3.43, 3.34	3.41	3.46
Lateral slip[b]	1.06, 5.82	2.52, 2.55	1.46	1.23, 1.79
RMS deviation from planarity[b]	0.042	0.026	0.013	0.026
C(1)–C(2)	1.365(3)	1.364(12)[c]	1.373(5)	1.368(4)[c]
C(2)–C(3)	1.454(2)[c]	1.454(12)[c]	1.447(5)	1.439(4)[c]
C(3)–C(3a/4)	1.359(3)	1.358(11)[c]	1.366(5)	1.367(4)[c]
C(4)–C(4a/5)	–	–	1.440(7)	1.437(4)[c]
C(5)–C(5a)	–	–	–	1.366(4)[c]

[a] All distances in Å; atom numbering is shown below. [b] (trialkylsilyl)ethynyl groups are omitted from the calculations. [c] Average value due to asymmetry in the solved crystal structure or crystallographically independent molecules.

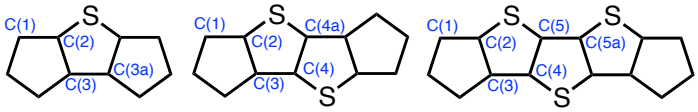

The bond distances in the thienoacene core of the DI[*n*]T family are summarized in Table 2.1. Distinct bond alternation is seen in all three molecules, with the "double" bonds averaging 1.36-1.37 Å and "single" bonds 1.44-1.45 Å, thus fully supporting the proposed quinoidal structures. These values are also in good agreement with those observed in their purely hydrocarbon analogues.[12,13] The peripheral benzene rings in the DI[*n*]Ts have an average bond distance of 1.390 Å with a standard deviation of 0.006 Å. The molecules are essentially planar, as the root-mean-square (RMS) deviation from the average molecular plane is negligible; **DI1T-TIPSE** showed the greatest RMS deviation of only 0.042 Å.*

In addition to the DI[*n*]Ts, we were able to obtain single crystals suitable for X-ray diffraction of diones **9** and **13** from $CHCl_3$/cyclohexane and upon slow cooling from refluxing nitrobenzene, respectively (Figure 2.6). Dione **9** alternates its orientation within the 1D stack such that the molecular arrangement would result in a net dipole; however, the dipole of the neighbouring stack balances the opposing dipole (see Appendix A). Dione **13** shows a more ordered 1D arrangement due to its centrosymmetry. The distance between the average planes of **9** and **13** are nearly identical at 3.39 Å and 3.38 Å, respectively. Dione **9** has a significant RMS deviation from planarity of 0.079 Å while **13** is nearly planar at 0.027 Å. This is likely due to the

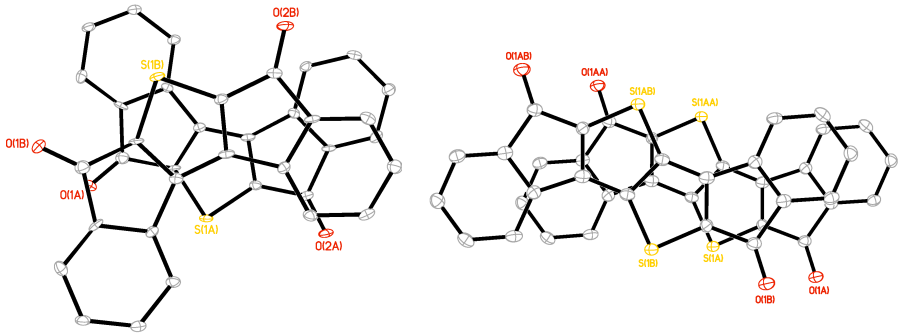

Figure 2.6. Solid-state packing of DI[*n*]T diones **9** (left) and **13** (right).

* RMS deviation from planarity for the dimesityl derivative of **4** is 0.094 Å and 0.186 Å for the two crystallographically independent molecules; see ref 12.

steric crowding of the hydrogens in the bay region of **9**. Interestingly, the carbonyl oxygens of **9** and **13** show a strong interaction with the bay carbons of adjacent stacks with distances of 3.25 Å for **9** and 3.28 Å for **13**.

Electronic Absorption Spectroscopy

The DI[*n*]Ts were characterized further by absorption spectroscopy (Figure 2.7). All compounds exhibit strong, acene-like vibronic features from 350-600 nm and low energy absorptions reaching into the NIR (800-925 nm). The absorption edges are staggered, possibly as a result of the family's alternating axo-/centro-symmetry and the assignment of the lowest energy absorption. Interestingly, **DI1T** and **DI2T** exhibit similar absorbance profiles to the related indeno[2,1-*c*]fluorene and fluoreno[4,3-*c*]fluorene derivatives (see Appendix A). For the DI[*n*]Ts, the high energy bands red shift by ca. 50-70 nm and the low energy bands blue shift by ca. 25-35

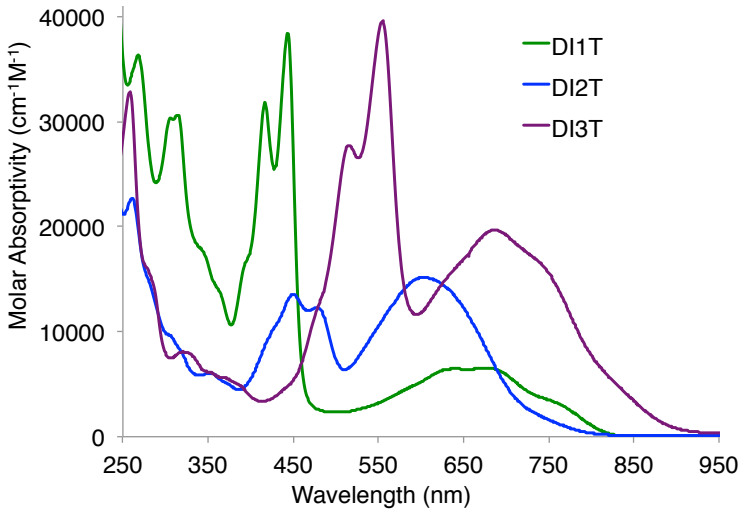

Figure 2.7. Electronic absorption spectra of DI[n]Ts (n=1-3) in CH_2Cl_2.

nm. Analogous to derivatives of **4** and **5**, the DI[*n*]Ts are non-emissive.

Cyclic Voltammetry

DI[*n*]Ts exhibit two reversible one electron reductions in solution as examined by cyclic voltammetry (Figure 2.8, Table 2.2). **DI1T** shows a reversible oxidation while the oxidation of **DI2T** and **DI3T** are essentially irreversible. The difference between E_{red}^{1} and E_{red}^{2} decreases by ca. 0.1 V upon sequential expansion of the quinoidal core. This is most likely due to the mitigation of Coulombic repulsion in the doubly reduced species.[21] The values for E_{ox} appear to approach a constant, indicating that incorporation of additional thiophene units does not alter the ionization potential to a large degree. LUMO and HOMO energy levels were derived from the E_{red}^{1} and E_{ox} values, respectively. E_{gap} decreases over the series in nonlinear fashion.

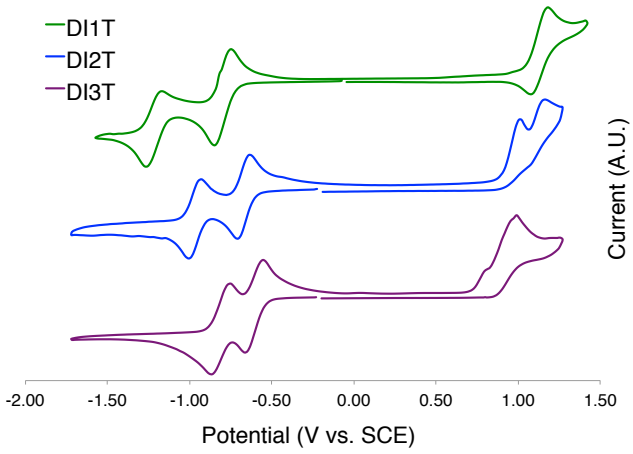

Figure 2.8. Cyclic voltammograms of DI[n]Ts (n=1-3).

Table 2.2. Electrochemical data for DI[n]Ts (n=1-3)[a]

	E_{red}^{1}	E_{red}^{2}	E_{ox}	LUMO	HOMO	E_{gap}
DI1T	–0.80	–1.22	1.13	–3.84	–5.77	1.93
DI2T	–0.67	–0.97	1.02	–3.97	–5.66	1.69
DI3T	–0.61	–0.81	0.99	–4.03	–5.63	1.60

[a]Values reported as the half-wave potential (vs SCE) using the Fc/Fc^{+} couple (0.46 V) as an internal standard. HOMO and LUMO energy levels in eV were approximated using SCE = –4.68 eV vs. vacuum (see ref. 20) and $E_{1/2}$ values for reversible processes or E_p values for irreversible processes; E_{gap} = LUMO–HOMO.

EPR Experiments

The DI[n]T anion radicals were obtained by reduction of the neutral species with potassium metal in THF. The EPR spectrum of **DI1T**$^{\bullet-}$ is shown in Figure 2.9 (see Appendix A for the EPR spectra of **DI2T**$^{\bullet-}$ and **DI3T**$^{\bullet-}$).The hyperfine coupling constants (HFCCs) of the spin active nuclei were determined and experimental carbon spin densities (ϱ_c) were calculated by the McConnell equation (Tables 2.3 and see Appendix A). Due to the lack of spin active nuclei on the core of DI[*n*]T, ϱ_c could not be directly calculated. Very little spin density is contained within the fused benzene rings (0.004-0.044), with more contained in the ethynyl group (0.094-0.112). The approximate spin densities remaining in the core for **DI1T**, **DI2T**, and **DI3T** are 0.59, 0.64, and 0.66, respectively, indicating that a majority of the spin density resides in the thienoacene unit.

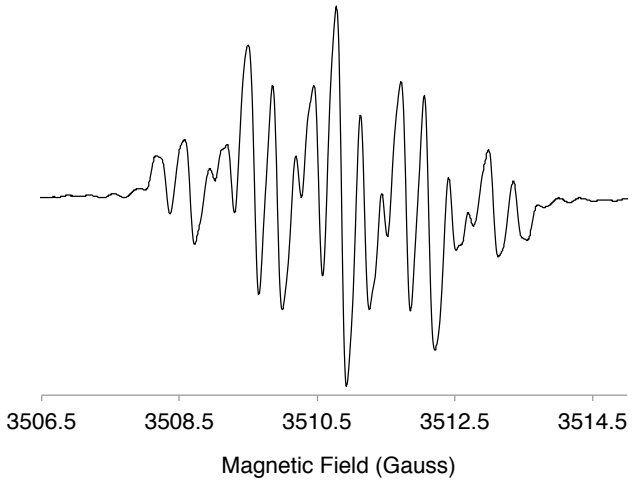

Figure 2.9. EPR spectrum of the radical anion of **DI1T**.

Table 2.3. Carbon spin densities (ϱ_c)[a]

position	**DI1T**	**DI2T**	**DI3T**
A	0.034	0.022	0.024
B	0.012	0.016	0.014
C	0.044	0.029	0.028
D	0.004	0.010	0.010
E	0.112	0.103	0.094
remainder	0.59	0.64	0.66

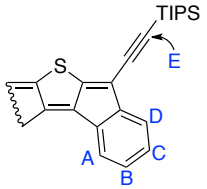

[a]See Appendix A for full details; labeling scheme on right

Computations

DFT calculations were performed to predict the geometry of the neutral, radical anion and dianion states of the DI[*n*]Ts. For computational ease, trimethylsilyl was used in place of the larger TIPS/TES groups. Bond distances in the core of **DI2T** are shown in Figure 2.10. Upon one electron reduction, the quinoidal bonds begin to homogenize as the unpaired electron is delocalized over the system. The dianion shows a reversal of the quinoidal pattern, indicating rearomatization of the central thienothiophene moiety. In accord with the CV experiments, the dianionic, fully aromatic species is stabilized with respect to the neutral state.[22]

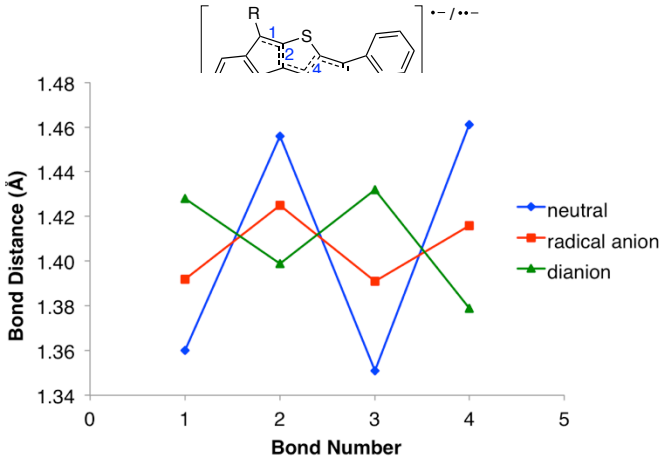

Figure 2.10. DFT calculated **DI2T** bond distances upon reduction (R = (trimethylsilyl)ethynyl); performed at UCAM-B3LYP/6-31G(d,p) (neutral) and UCAM-B3LYP/6-31++G(d,p) (radical anion/dianion) level of theory.

Conclusions

In summary, the synthesis and characterization of a new class of quinoidal thienoacenes has been reported. The synthetic route is shown to be rapid and amenable to scale. X-ray

crystallography corroborates the presence of distinct quinoidal motifs and reveals that the title compounds pack in progressively closer pairwise 1D arrangements. Analysis of the reduced states by EPR spectra and DFT calculations indicate stable anionic species. The large degree of π-orbital overlap, NIR absorption and favourable electrochemical properties suggest great potential for application in organic electronics. Future work will consist of further derivatization and expansion of the DI[*n*]T structures in addition to testing their performance as organic semiconductors.

Experimental Section

Diethyl 2,2'-(thiophene-3,4-diyl)dibenzoate (Compound 8)

In a dry glass pressure vessel, 2-ethoxycarbonylbenzeneboronic acid (6.0 g, 31 mmol), Pd_2dba_3 (120 mg, 0.124 mmol), SPhos (100 mg, 0.248 mmol), anhydrous K_3PO_4 (10.5 g, 49.6 mmol) and toluene (35 mL) were combined. The mixture was sparged with nitrogen (10 min) then 3,4-dibromothiophene (3.0 g, 12.4 mmol) was added via syringe. The vessel was sealed and brought to 100 ºC for 16 h. Upon cooling to rt, the reaction was diluted with CH_2Cl_2 then filtered. The organics were washed with brine then dried over $MgSO_4$. Volatiles were removed under reduced pressure to give an orange oil in quantitative yield. This material can be used directly or purified by silica gel chromatography (20% EtOAc/hexanes) (v/v). ^{1}H NMR (500 MHz, $CDCl_3$) δ 7.70 (dd, *J* = 7.7, 1.5 Hz, 2H), 7.35 (td, *J* = 7.5, 1.5 Hz, 2H), 7.30 (td, *J* = 7.6, 1.5 Hz, 2H), 7.26 (dd, *J* = 7.5, 1.4 Hz, 2H), 7.20 (s, 2H), 4.08 (q, *J* = 7.2 Hz, 4H), 1.12 (t, *J* = 7.1 Hz, 6H); ^{13}C NMR (126 MHz, $CDCl_3$) δ 167.92, 141.38, 136.60, 131.98, 131.74, 130.87, 129.40, 127.11, 122.62, 60.84, 13.84. HRMS (ES+) calcd for $C_{22}H_{21}O_4S$ $(M+H)^+$ 381.1161, found 381.1168.

Diindeno[2,1-b:1',2'-d]thiophene-5,7-dione (Compound 9)

To a solution of the crude diester **8** (4.4 g) in ethanol (100 mL) was added aqueous potassium hydroxide (115 mmol, 5 M). The reaction was heated at reflux for 16 h then cooled to

rt. The volume was reduced *in vacuo* (30 mL) and acidified with concentrated hydrochloric acid. The diacid was collected, washed with water and dried. To a suspension of the diacid in CH_2Cl_2 (100 mL) was added 5 drops DMF. Oxalyl chloride (4.0 mL, 46 mmol) was added drop wise via syringe. The reaction was stirred at rt for 3 h then the volatiles were removed *in vacuo*. Dichloromethane (100 mL) was added and the flask was cooled to 0 ºC. Aluminum chloride (9.25 g, 69 mmol) was added and the reaction was stirred at 0 ºC for 16 h. The dark solution was poured onto ice and the precipitate was collected by filtration then washed with water. Recrystallization from $CHCl_3$ (1.5 L) provided the title compound as orange needles (1.71 g, 46% from 3,4-dibromothiophene). ^{1}H NMR (600 MHz, $CDCl_3$) δ 7.64 (d, J = 7.2 Hz, 2H), 7.54 (t, J = 7.5 Hz, 2H), 7.46 (d, J = 7.3 Hz, 2H), 7.34 (t, J = 7.5 Hz, 2H). Limited solubility of the title compound hindered acquisition of ^{13}C NMR spectra.

DIIT-TIPSE

In a dry two-neck flask, (triisopropylsilyl)acetylene (0.8mL, 3.45 mmol) was added to THF (5 mL) and cooled to 0 ºC. A solution of *n*-butyllithium (3.1 mmol, 1.6 M) was added dropwise then stirred for 5 min. In a second flask, dione **9** (200 mg, 0.69 mmol) was suspended in THF (25 mL) and cooled to 0 ºC. The (triisopropylsilyl)ethynyllithium solution was transferred via syringe to the dione suspension and stirred for 30 min. The reaction was quenched with saturated ammonium chloride (50 mL). The organics were extracted with EtOAc (2 x 50 mL), washed with brine and dried over $MgSO_4$. The volatiles were removed under reduced pressure then the crude material was passed through a short plug of silica, eluting first with hexanes then EtOAc. The polar fractions were combined and reduced *in vacuo*. Toluene (15 mL) was added and the solution was degassed thoroughly under dynamic vacuum. Finely ground tin(II) chloride (400 mg, 10.4 mmol) was added then further degassed under dynamic vacuum. The slurry was stirred for 3 h at rt then poured onto a plug of silica and eluted with 1:1 CH_2Cl_2/hexanes. Removal of the volatiles under reduced pressure provided the title compound (270 mg, 63%). ^{1}H NMR

(500 MHz, $CDCl_3$) δ 7.51 (d, *J* = 7.3 Hz, 2H), 7.20 (td, *J* = 7.5, 1.0 Hz, 2H), 7.13 (d, *J* = 7.3 Hz, 2H), 7.07 (td, *J* = 7.5, 1.2 Hz, 2H), 1.17 (s, 42H); ^{13}C NMR (126 MHz, $CDCl_3$) δ 153.77, 148.89, 144.03, 130.77, 130.19, 125.78, 124.37, 120.68, 116.32, 105.90, 99.70, 18.73, 11.28; HRMS (ES+) calcd for $C_{40}H_{51}SSi_2$ $(M+H)^+$ 619.3250, found 619.3243.

DI1T-TESE

The procedure for **DI1T-TIPSE** was adapted with (triethylsilyl)acetylene (521 mg, 3.71 mmol), n-butyllithium (3.34 mmol, 1.6 M) and **9** (214 mg, 0.74 mmol) to provide the title compound as a green solid (147 mg, 37%). ^1H NMR (500 MHz, $CDCl_3$) δ 7.47 (d, *J* = 7.3 Hz, 2H), 7.19 (td, *J* = 7.5, 1.0 Hz, 2H), 7.11 (d, *J* = 7.4 Hz, 2H), 7.06 (td, *J* = 7.5, 1.1 Hz, 2H), 1.14 (t, *J* = 7.9 Hz, 18H), 0.77 (q, *J* = 7.9 Hz, 12H); ^{13}C NMR (126 MHz, $CDCl_3$) δ 153.79, 148.73, 144.01, 130.66, 130.11, 125.80, 124.35, 120.62, 116.17, 106.53, 99.06, 7.63, 4.48; HRMS (ES+) calcd for $C_{34}H_{38}SSi_2$ (M^+) 534.22328, found 534.22079.

2-Benzoyl-3,4-dibromothiophene (Compound 10)

Aluminum chloride (15 g, 125 mmol) was added in three portions to a stirred solution of 3,4-dibromothiophene (10.0 g, 41.3 mmol) and benzoyl chloride (8.7 g, 62 mmol) in CH_2Cl_2 (100 mL) at 0 ºC. The cooling bath was removed and the reaction was stirred for 16 h. The dark solution was poured onto ice, diluted with CH_2Cl_2 (100 mL) and washed successively with aqueous sodium hydroxide (1 M) and brine. The organic phases were combined and dried over $MgSO_4$. Removal of volatiles by reduced pressure provided the title compound (13.13 g, 92%). ^1H NMR (500 MHz, $CDCl_3$) δ 7.88–7.84 (m, 2H), 7.67–7.63 (m, 2H), 7.52 (dd, J = 8.5, 7.1 Hz, 2H); ^{13}C NMR (126 MHz, $CDCl_3$) δ 187.38, 136.87, 136.82, 133.42, 129.86, 128.56, 128.08, 118.19, 116.67; HRMS (ES+) calcd for $C_{11}H_6SBr_2$ (M^+), 343.85064 found 343.85212.

Compound 11

To a solution of **10** (13.13 g, 37.9 mmol) in DMF (50 mL) was added potassium carbonate (15.7 g, 113.8 mmol) and the reaction was rigorously degassed under dynamic vacuum. With stirring, ethyl thioglycolate (4.79 g, 39.8 mmol) was added dropwise via syringe. The reaction was brought to 60 ºC for 1 d after which the flask was allowed to cool and the contents were poured into water (100 mL). The solids were collected and washed with water. Recrystallization from ethanol (500 mL) provided **11** (11.2 g, 80%). ^{1}H NMR (500 MHz, $CDCl_3$) δ 7.60–7.55 (m, 2H), 7.53–7.45 (m, 4H), 4.30 (q, *J* = 7.1 Hz, 2H), 1.29 (t, *J* = 7.1, 3H); ^{13}C NMR (126 MHz, $CDCl_3$) δ 162.08, 141.75, 141.14, 140.77, 133.72, 129.21, 129.05, 128.82, 128.30, 128.17, 103.14, 61.36, 14.08; HRMS (ES+) calcd for $C_{15}H_{12}S_2O_2Br$ $(M+H)^+$ 366.9462, found 366.9454.

Compound 12

In a dry glass pressure vessel, 2-ethoxycarbonylbenzene boronic acid (581 mg, 2.99 mmol), Pd_2dba_3 (25 mg, 0.027 mmol), SPhos (22 mg, 0.054 mmol), anhydrous K_3PO_4 (1.15 g, 5.44 mmol), **11** (1.00 g, 2.72 mmol) and toluene (10 mL) were combined. The mixture was sparged with nitrogen (10 min). The vessel was sealed and brought to 100 ºC for 16 h. Upon cooling to rt the reaction was diluted with CH_2Cl_2 then filtered. The organics were washed with brine and dried over $MgSO_4$. Removal of volatiles under reduced pressure provides the title compound in quantitative yield. This material can be used directly or purified by silica gel chromatography (20% EtOAc/hexanes) (v/v). ^{1}H NMR (500 MHz, $CDCl_3$) δ 8.01 (dd, *J* = 7.8, 1.4 Hz, 1H), 7.66–7.63 (m, 2H), 7.61 (dd, *J* = 7.4, 1.4 Hz, 1H), 7.57 (dd, *J* = 7.6, 1.5 Hz, 1H), 7.55–7.47 (m, 4H), 7.45 (s, 1H), 4.26 (q, *J* = 7.1 Hz, 2H), 4.18 (q, *J* = 7.1 Hz, 2H), 1.25 (t, *J* = 7.1 Hz, 3H), 1.06 (t, *J* = 7.1 Hz, 3H); ^{13}C NMR (126 MHz, $CDCl_3$) δ 167.58, 162.35, 141.73, 141.01, 140.94, 134.82, 134.78, 134.28, 131.91, 131.07, 130.61, 130.55, 129.17, 128.61, 128.44, 128.21, 127.88, 127.84, 61.23, 61.09, 14.10, 13.71; HRMS (ES+) calcd for $C_{24}H_{21}S_2O_4$ $(M+H)^+$ 437.0881, found 437.0875.

Compound 13

To a solution of **12** (0.98 g, 2.25 mmol) in ethanol (100 mL) was added aqueous potassium hydroxide (12 mmol, 1.5 M). The reaction was heated at reflux for 16 h then cooled to rt. The volume was reduced *in vacuo* (to 20 mL) and acidified with concentrated hydrochloric acid. The diacid was collected, washed with water and dried. To a suspension of the diacid in CH_2Cl_2 (100 mL) was added DMF (5 drops). Oxalyl chloride (1.0 mL, 11.2 mmol) was added dropwise via syringe. The reaction was stirred at rt for 3 h then the volatiles were removed *in vacuo*. CH_2Cl_2 (50 mL) was added and the flask was cooled to 0 ºC. Aluminum chloride (3.0 g, 22.3 mmol) was added as a solid. The reaction was allowed to warm to rt and stir for 16 h. The dark solution was poured onto ice and the precipitate was collected by filtration. Successive washes with water and acetone gave the title compound as a magenta solid. (630 mg, 79%). Limited solubility hindered acquisition of NMR spectra.

DI2T-TIPSE

To a solution of (triisopropylsilyl)acetylene (527 mg, 2.9 mmol) in THF (5 mL) at 0 ºC was added *n*-butyllithium (2.6 mmol, 1.6 M in hexanes) dropwise. In a separate flask, **13** (200 mg, 0.58 mmol) was suspended in THF (25 mL) and cooled to 0 ºC. The (triisopropylsilyl)ethynyllithium solution was transferred to the dione suspension via syringe then sonicated for 10 min. After quenching with a saturated NH_4Cl solution, the organics were extracted with diethyl ether and dried over $MgSO_4$. The volume was reduced *in vacuo* and passed through a short plug of silica, eluting with EtOAc. Volatiles were removed under reduced pressure. Toluene (15 mL) was added and the flask was rigorously degassed under dynamic vacuum. Finely ground tin(II) chloride (250 mg, 1.25 mmol) was added and the reaction was stirred for 3h. The mixture was passed through a plug of silica (CH_2Cl_2/hexanes). Evaporation of

the volatiles provided the title compound as a dark blue solid (260 mg, 66%). ^{1}H NMR (500 MHz, $CDCl_3$) δ 7.36 (d, *J* = 7.3 Hz, 2H), 7.28–7.24 (m, 2H), 7.22 (dd, *J* = 7.5, 1.1 Hz, 2H), 7.12 (td, *J* = 7.3, 1.4 Hz, 2H), 1.21 (s, 42H); ^{13}C NMR (126 MHz, $CDCl_3$) δ 150.07, 147.30, 146.98, 139.43, 129.62, 128.82, 125.51, 122.65, 120.76, 114.77, 105.47, 99.95, 18.76, 11.30; HRMS (ES+) calcd for $C_{42}H_{50}S_2Si_2$ (M^+) 674.28926, found 674.28917.

3,5-Dibromodithieno[3,2-b:2',3'-d]thiophene

In a 3-neck flask, tetrabromodithieno[3,2-*b*:2',3'-*d*]thiophene[23] (2.7 g, 5.3 mmol) in glacial acetic acid (150 mL) was brought to reflux. Zinc powder (3.44 g, 53 mmol) was added to the suspension. The reaction was refluxed for a further 30 min and then hot filtered through a fritted funnel. The solution was allowed to cool to rt then the crude product was precipitated by the addition of water. The solids were collected by filtration. Recrystallization from chloroform provided the title compound as colorless needles (450 mg, 24%). ^{1}H NMR (500 MHz, $CDCl_3/CS_2$) δ 7.31 (s); ^{13}C NMR (126 MHz, $CDCl_3/CS_2$) δ 142.74, 130.84, 123.16, 103.90. These spectroscopic data correspond to previously reported data.[24]

Compound 14

In a dry glass pressure vessel, 3,5-dibromodithieno[3,2-*b*:2',3'-*d*]thiophene (450 mg, 1.27 mmol), 2-ethoxycarbonylbenzene boronic acid (754 mg, 3.18 mmol), Pd_2dba_3 (12 mg, 0.013 mmol), SPhos (24 mg, 0.05 mmol), anhydrous K_3PO_4 (1.0 g, 5.1 mmol) and toluene (15 mL) were combined and sparged with nitrogen (10 min). The vessel was sealed and brought to 100 ºC for 24 h. Upon cooling to rt the reaction was diluted with CH_2Cl_2 then filtered. The organics were washed with brine and dried over $MgSO_4$. Removal of volatiles under reduced pressure provided the title compound in quantitative yield. This material can be used directly or purified by silica gel chromatography (20% EtOAc/hexanes) (v/v). ^{1}H NMR (500 MHz, $CDCl_3$) δ 7.94 (d, *J* = 7.8 Hz, 2H), 7.54 (m, 4H), 7.46 (m, 2H), 7.23 (s, 2H), 4.12 (q, *J* = 7.2 Hz, 4H), 1.01 (t, *J* = 7.2 Hz,

6H); ^{13}C NMR (126 MHz, $CDCl_3$) δ 167.76, 142.24, 135.53, 135.00, 131.73, 131.27, 130.42, 130.40, 130.18, 128.25, 122.45, 61.13, 13.75; HRMS (ES+) calcd for $C_{26}H_{21}S_3O_4$ $(M+H)^+$ 493.0602, found 493.0601.

Diindenodithieno[3,2-b:2',3'-d]thiophene-3,13-dione (Compound 15)

To a solution of **14** (0.50 g, 2.25 mmol) in ethanol (100 mL) was added aqueous potassium hydroxide (14.3 mmol, 1.4 M). The reaction was heated at reflux for 16 h then cooled to rt. The volume was reduced *in vacuo* (to 15 mL) and acidified with concentrated hydrochloric acid. The diacid was collected, washed with water and dried. To a suspension of the diacid in CH_2Cl_2 (100 mL) was added DMF (5 drops). Oxalyl chloride (0.35 mL, 11.2 mmol) was added dropwise via syringe. The reaction was stirred at rt for 3 h then the volatiles were removed *in vacuo*. CH_2Cl_2 (50 mL) was added and the flask was cooled to 0 ºC. Aluminum chloride (1.0 g, 22.3 mmol) was added as a solid. The reaction was stirred for 1 h. The dark solution was poured onto ice and the precipitate was collected by filtration. Successive washes with water and acetone gave the title compound as a red solid. (328 mg, 81%). Limited solubility hindered acquisition of NMR spectra.

DI3T-TIPSE

To a solution of (triisopropylsilyl)acetylene (227 mg, 1.25 mmol) in THF (5 mL) at 0 ºC was added *n*-butyllithium (1.12 mmol, 1.5 M in hexanes) dropwise. In a separate flask, **15** (100 mg, 0.25 mmol) was suspended in THF (25 mL) and cooled to 0 ºC. The (triisopropylsilyl)ethynyllithium solution was transferred to the dione suspension via syringe then sonicated for 10 min. After quenching with a saturated NH_4Cl solution, the organics were extracted with diethyl ether and dried over $MgSO_4$. The volume was reduced *in vacuo* and passed through a short plug of silica, eluting with EtOAc. Volatiles were removed under reduced pressure. Toluene (15 mL) was added and the flask was rigorously degassed under dynamic

vacuum. Finely ground tin(II) chloride (250 mg, 1.25 mmol) was added and the reaction was stirred for 10 min. The mixture was passed through a plug of silica (CH_2Cl_2/hexanes). Evaporation of the volatiles provided the title compound as a deep purple solid (131 mg, 72%). ^{1}H NMR (500 MHz, $CDCl_3$) δ 7.31 (d, *J* = 7.3 Hz, 2H), 7.25 (d, *J* = 7.4 Hz, 2H), 7.19 (t, *J* = 7.5 Hz, 2H), 7.07 (t, *J* = 7.5 Hz, 2H), 1.21 (s, 42H); ^{13}C NMR (126 MHz, $CDCl_3$) δ 148.91, 146.56, 143.92, 142.96, 138.51, 129.20, 128.52, 125.08, 122.04, 120.72, 113.17, 105.36, 100.45, 18.78, 11.34; HRMS (ES+) calcd for $C_{44}H_{51}S_3Si_2$ $(M+H)^+$ 731.2691, found 731.2711.

Bridge to Chapter III

Chapter II detailed some of our work in exploring the effects of expanding the core of the indenofluorene scaffold with fused heterocycles. Chapter III looks at introducing anthracene as the core unit and the consequences it has on biradical character and electronic properties.

CHAPTER III

DIINDENO-FUSION OF AN ANTHRACENE AS A DESIGN STRATEGY FOR STABLE ORGANIC BIRADICALS

This chapter was written by Gabriel Rudebusch with contributions from several research groups. José L. Zafra performed the Raman spectroscopic measurements. Jonathan L. Marshall acquired and analysed the CV data. Iratxe Arrechea-Marcos, Guzmán L. Espejo and Rocío Ponce Ortiz obtained the OFET data. Carlos J. Gómez-García performed the SQUID experiments. Lev N. Zakharov acquired and analysed the x-ray crystallographic data. Masayoshi Nakano and Kotaro Fukuda performed the calculation and discussion on the geometry optimization, the open-shell character and the singlet-triplet gaps. Henrik Ottosson and Kjell Jorner performed the ACID and NICS-XY DFT calculations and analyzed the data from these computations. Juan Casado interpreted magnetic and spectroscopic data and co-wrote the paper. Michael M. Haley played a critical role in discussion of the experimental design, project direction, experiments and results, and preparation of the manuscript. This work was originally published in *Nature Chemistry*.

Introduction

The consequence of unpaired electrons in organic molecules has fascinated and confounded chemists for over a century. The study of open-shell molecules has been rekindled in recent years as new synthetic methods, improved spectroscopic techniques, and powerful computational tools have been brought to bear on this field. Nonetheless, it is the intrinsic instability of the biradical species that limits the practicality of this research. Herein we report the synthesis and characterization of a molecule based on the diindeno[*b,i*]anthracene framework that exhibits pronounced open-shell character yet possesses remarkable stability. The synthetic route is rapid, efficient and possible on the gram-scale. The molecular structure was confirmed through single-crystal X-ray diffraction. From variable-temperature Raman spectroscopy and magnetic

susceptibility measurements a thermally accessible triplet excited state was found. Organic field-effect transistor device data shows ambipolar performance with balanced electron and hole mobilities. Our results demonstrate the rational design and synthesis of an air- and temperature-stable biradical compound.

Biradical compounds push the covalent π–bond to the limit of dissociation, yielding highly reactive products. Due to the strong π–electron correlation in these systems, new perspectives on the nature of the chemical bond are revealed and offer unique opportunities to investigate fundamental rules and concepts in chemistry. Organic compounds exhibiting biradical character have been known since the early twentieth century. A classic example is Tschitschibabin's hydrocarbon, first synthesized in 1907 (Figure 3.1a)[1]. The compound features two linked dearomatized benzene rings. At the expense of a C–C double bond, the center rings regain aromaticity, leading to an open-shell biradical structure that is in resonance with the closed-shell quinoidal structure[2]. The contribution of the open-shell resonance form to the overall ground state structure is described by the biradical character index, y, which is derived from the natural orbital occupation number (NOON) of the lowest unoccupied natural orbital (LUNO)[3,4]. The index ranges from pure biradical, y = 1, to pure closed-shell, y = 0 (Figure 3.1b). The interacting pair of electrons in open-shell polycyclic hydrocarbons (PCHs) can be in a spin paired singlet state (S=0), or a spin parallel triplet state (S=1)[5]. Due to the double spin polarization effect, most biradical PCHs have singlet ground states and low-lying triplet excited states[6]. Recent reports of compounds with quinoidal motifs and low-lying triplet states are illustrated in Figure 3.1c[7-10]. Although represented with closed-shell bonding patterns, the compounds exhibit significant open-shell character (y = 0.50–0.74; calculated at the PUHF level to permit comparison) with thermally accessible triplet states ($\Delta E(S_0–T_1)$ = 3.8–4.9 kcal mol^{-1}) (See Appendix B for details). This class of molecules has been shown to possess desirable properties such as narrow frontier orbital energy gaps[11], strong absorption in the visible spectrum, redox

amphoterism, multicenter bonding, large second hyperpolarizabilities[12-15] and substantial two-photon absorption cross-sections[16,17]. There has been an effort towards taking advantage of biradical PCHs in non-linear optics[15], molecular spintronics[18], and singlet fission sensitized organic photovoltaic devices[19-21].

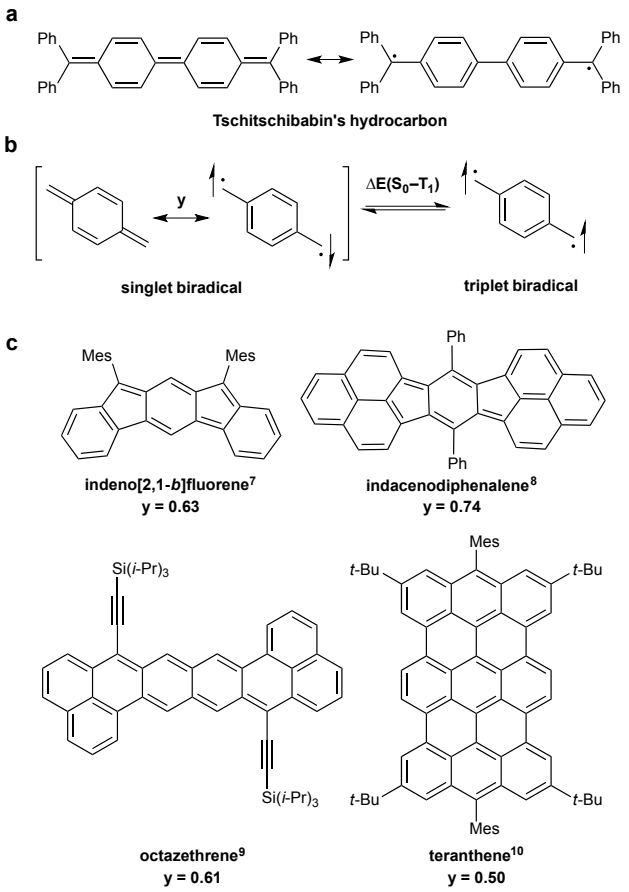

Figure 3.1. Polycyclic hydrocarbons with open-shell character. (a) Molecular structure of Tschitschibabin's hydrocarbon. (b) The electronic structure of open-shell PCHs is described by the biradical character index, y, and $\Delta E(S_0–T_1)$. (c) Recent examples of compounds with significant open-shell character and thermally accessible triplet states.

The practical application of open-shell PCHs has been hampered by the lack of stable and easily accessible materials. Indeed, the design and synthesis of stable open-shell organic compounds is challenging due to the reactivity associated with biradical character and the

inherent thermodynamic instability of pro-aromatic fragments. A survey of the literature is illustrative; recent examples of biradical PCHs suffer from protracted, low-yielding syntheses, decomposition under ambient conditions and insufficient characterization. Herein we report the synthesis, characterization and properties of a new biradical polycyclic hydrocarbon, diindeno[*b*,*i*]anthracene (**DIAn**). The synthesis is concise and possible on the gram-scale. Our results are underlined by the remarkable stability of **DIAn** under ambient conditions and at elevated temperatures, and by the investigation of a low-lying triplet excited state through variable temperature techniques. We offer a design strategy towards building biradical PCHs that approach the open-shell character of large acenes[22] but retain chemical stability. This work introduces new perspectives on the accessibility of high-spin organic materials with a view towards potential materials applications.

Results and Discussion

Synthesis

Our approach to the synthesis of a stable diindenoanthracene derivative blocks anticipated sites of high-spin with bulky mesityl (Mes) groups. The introduction of (triisopropylsilyl)ethynyl groups from the outset provides solubility, steric bulk and resistance towards oxidation[23,24]. The synthesis is initiated by the palladium-catalysed Suzuki-Miyaura cross-coupling of known dibromoanthracene **1**[25] and 2-formylbenzeneboronic acid (Scheme 3.1). The use of Buchwald's SPhos ligand allows access to dialdehyde **2** in near quantitative yield. Addition of mesitylmagnesium bromide provides the secondary alcohol in high yield, which is carried forward without purification. Formation of the heptacyclic core of **3** was achieved through a Friedel-Crafts alkylation mediated by boron trifluoride etherate in 79% yield. Gratifyingly, selective closure to the C(3) and C(7) positions was observed due to the steric clash between the bulky Mes and Si(*i*-Pr)$_3$ groups that block electrophilic substitution at the more activated C(1) and

C(5) positions. Oxidation of the tertiary C–H bonds in **3** with DDQ provides the deep violet **DIAn** in 62% yield. Notably, the synthetic route is possible on moderate scale with 1 g of **3** prepared in a single sequence without chromatography. **DIAn** can be stored as a crystalline solid on the bench top exposed to ambient conditions without degradation. Half-life of a 10^{-6} M solution is approximately 64 days (see Appendix B).

Scheme 3.1. Synthesis of **DIAn**. The synthetic route is rapid and efficient in four steps and 49% overall yield.

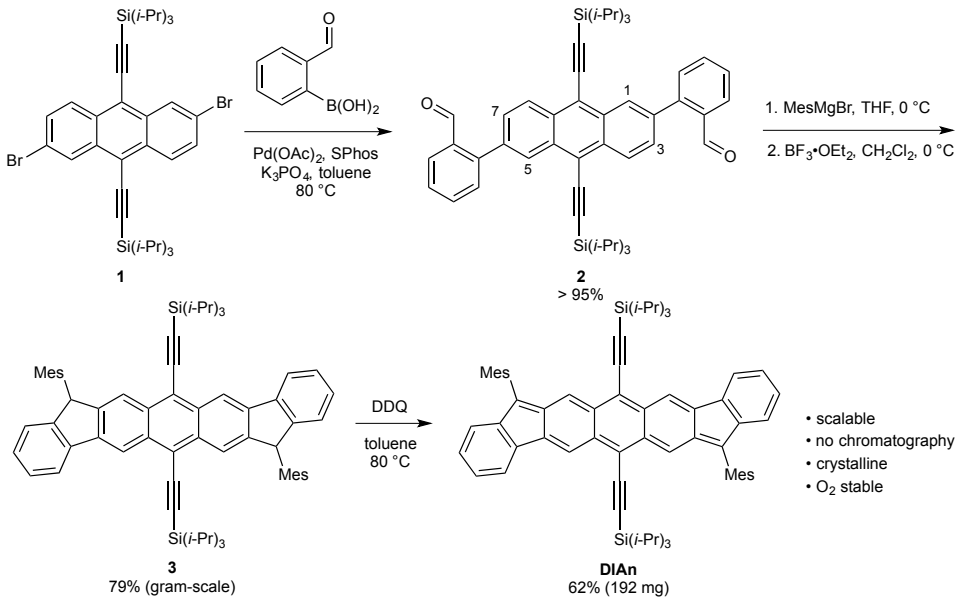

Electronic Absorption Spectra and Cyclic Voltammetry

DIAn exhibits an electronic absorption spectrum similar to other quinoidal PCHs. The deep blue color of **DIAn** in solution can be ascribed to an absorption at 690 nm extending into the green and red regions of the visible spectrum (Figure 3.2a). The λ_{max} is significantly red-shifted by 175 nm compared to the similar indeno[1,2-*b*]fluorene derivative[26]. The strong 690 nm absorption can be assigned to a symmetry allowed $S_0 \rightarrow S_2$ transition with a weak shoulder extending to 900 nm in the near-infrared due to the symmetry forbidden $S_0 \rightarrow S_1$ transition. Cyclic voltammetry (CV) reveals the amphoteric redox character of **DIAn** (Figure 3.2b). Electron-

accepting behavior is evident in two reversible one-electron reductions at –1.28 and –1.67 V versus the ferrocene/ ferrocenium couple (Fc/Fc^+). While the ability of cyclopenta-fused PCHs to accept multiple electrons is established[26,27], **DIAn** is also easily oxidized in two one-electron oxidations at 0.17 and 0.70 V versus Fc/Fc^+. The full CV wave displays striking symmetry between oxidations and reductions, indicating similar electro-kinetic parameters for both anodic and cathodic processes. The highest occupied molecular orbital (HOMO) and lowest unoccupied molecular orbital (LUMO) energies, estimated from electrochemical data, are –5.27 and –3.82 eV, respectively. In conjunction with the 900 nm absorption edge, the HOMO/LUMO energy gap of 1.45 eV represents one of the narrowest values for a PCH bearing no strongly electron-withdrawing groups.

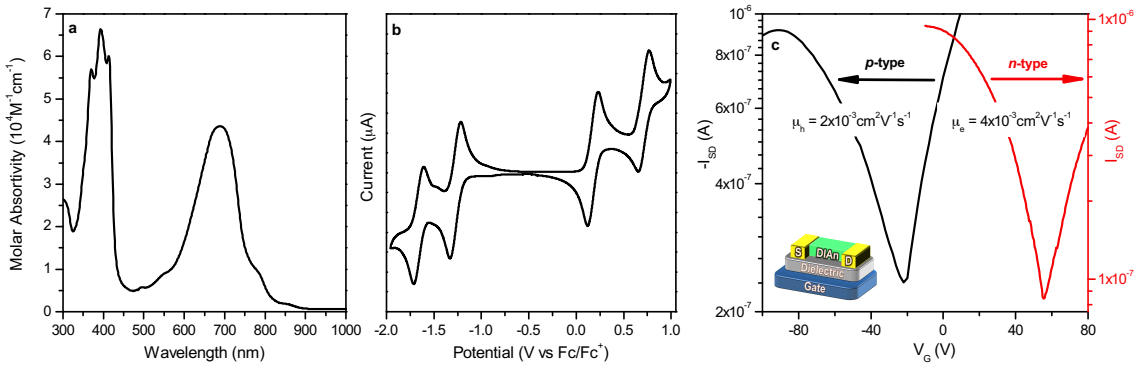

Figure 3.2. Steady-state properties of **DIAn** and OFET device results. (a) Electronic absorption spectrum of **DIAn** in CH_2Cl_2. (b) Cyclic voltammetry of **DIAn** in CH_2Cl_2 shows two reversible one-electron reductions and two reversible one-electron oxidations with a HOMO/LUMO energy gap of 1.45 eV. (c) OFET *p*-channel and *n*-channel transfer characteristics of a vapor-deposited film of **DIAn** exhibiting balanced ambipolar charge transport. V_{SD} was fixed at 80 V and –100 V for positive and negative bias, respectively. Fc/Fc^+, ferrocene/ferrocenium.

Ambipolar OFETs

The amphoteric redox character of **DIAn** has implications for balanced ambipolar charge transport[26]. In fact, organic field-effect transistors (OFETs) fabricated using OTS-treated gate dielectrics by vapour-deposition of **DIAn** gave ambipolar performances with quite balanced

electron and hole mobilities. Analysis of these devices indicates a gradual increase of electron mobility with temperature at the expense of hole mobility; nevertheless, mobilities in the range of 10^{-3}-10^{-2} $cm^2 \bullet V^{-1}s^{-1}$ (Figure 3.2c) are registered for the whole temperature range analyzed (see Appendix B). These values are comparable with the best values previously reported for organic biradicals[28,29]. It should be noted, however, that of the many Kekulé biradicals reported in the literature, only a few are described as electrically active and, of these, a small fraction exhibited ambipolar behavior. Rather, most exhibit mismatched character between hole and electron mobilities, i.e., unbalanced transport. In contrast, OFETs fabricated from **DIAn** result in excellent performance in absolute simultaneous hole/electron mobilities with a unique balanced ambipolar transport. This device performance is aided by the chemical robustness of **DIAn** as the instability of many biradicals deteriorates the electrical response. In addition, the ambipolar behavior can be explained dual pseudo-quinoidal (related to reduction and *n*-type transport) and pseudo-aromatic (related to oxidation and *p*-type transport) structures acting in cooperation (see below).

Single-Crystal X-ray Diffraction

Single-crystal X-ray diffraction (XRD) and bond distance analysis provide insight into the ground state electronic structure of PCHs. Prism-like crystals suitable for XRD were grown by slow diffusion of CH_3CN into a $CHCl_3$ solution of **DIAn**. The molecule is centrosymmetric and planar; RMS deviation from an average plane drawn through the polycyclic core amounts to 0.03 Å. The outer six-membered rings have an average bond distance of 1.40 ± 0.01 Å indicating benzenoid character. In the core of the molecule, significant bond distance alternation is observed as expected for a closed-shell quinoidal structure (Figure 3.3a). The bond distances vary greatly, spanning distances (1.359-1.461 Å) typically seen for C–C double, benzenoid and single bonds. Upon closer inspection of the quinoidal unit, significantly lengthened C–C bonds of 1.406 and 1.399 Å are apparent, suggesting delocalized, partial double bond character rather than distinct double bonds. The bond distance from the apical sp^2 carbon to the anthracene core is 1.406 Å,

whereas the analogous bond distances in the mesityl-substituted indenofluorene isomers range from 1.377 Å (closed shell) and 1.437 Å (open shell), respectively (Figure 3.3b)[30]. The intermediate value in **DIAn** indicates contributions from both pure open-shell and closed-shell structures; thus, the solid-state structure of **DIAn** obtained at 173 K is a resonance hybrid with both forms contributing to the overall ground electronic state (Figure 3.3c).

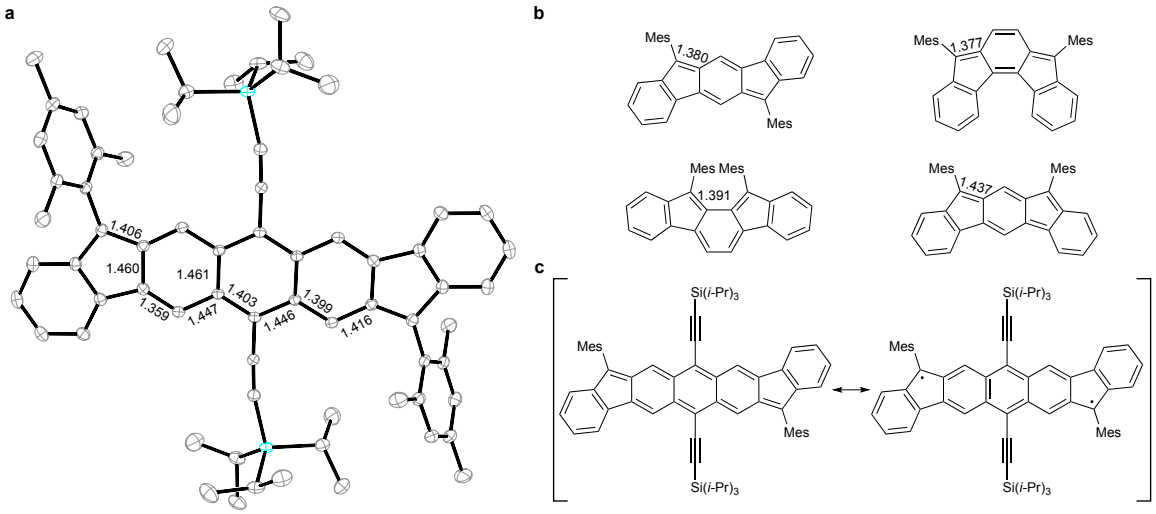

Figure 3.3. Solid-state structure of **DIAn** by single crystal X-ray diffraction. (a) ORTEP image with selected bond distances (Å) of the diindeno[*b*,*i*]anthracene core drawn with 35% thermal ellipsoids, hydrogens are omitted for clarity. (b) In similar indeno-fused compounds, the bond distance from the apical carbon to the acene core is an indication of the degree of biradical character. (c) The ground state of **DIAn** is a resonance hybrid between hypothetical closed-shell (left) and open-shell (right) structures.

Variable-Temperature NMR Experiment

More evidence for the unusual electronic structure of **DIAn** is brought to light by ^{1}H NMR experiments. Slightly broadened resonances are observed at 25 °C (Figure 3.4a). As the temperature is increased to 150 °C in degassed 1,2-dichlorobenzene-d_4 the aromatic resonances broaden and eventually disappear. The signals are recovered to full height when the sample is cooled to 25 °C. Further cooling to –25 °C in CD_2Cl_2 allows complete assignment of the ^{1}H resonances. The variable temperature NMR studies suggest that a thermally accessible triplet state is responsible for the signal broadening. Interestingly, the presence of oxygen broadens the NMR spectra of **DIAn** (see Appendix B). It can be inferred that $^3O_2$ promotes reversible spin-

crossover rather than engaging **DIAn** in an irreversible reaction[31]. This behavior is in sharp contrast to most biradical PCHs that readily decompose when heated or exposed to oxygen.

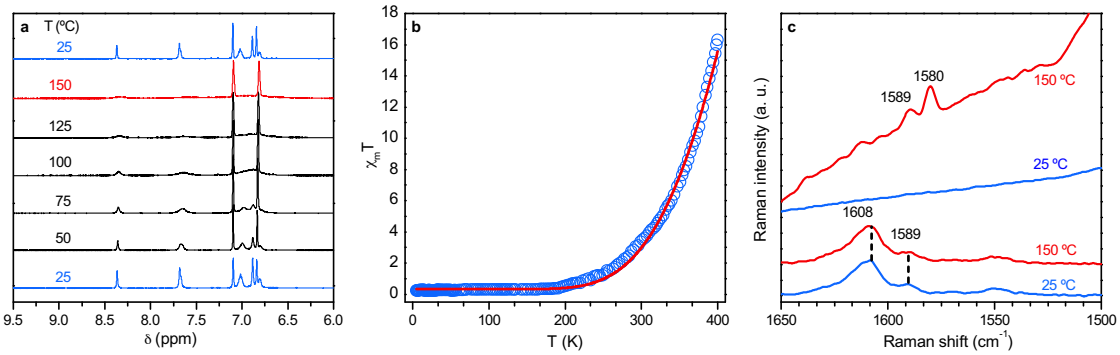

Figure 3.4. Temperature-dependent properties of **DIAn.** (a) Variable temperature ^{1}H NMR experiment (500 MHz, 1,2-dichlorobenzene-d_4) shows broadening of the aromatic proton resonances with increasing temperature and the return of the original spectrum when cooled. (b) SQUID measurements (blue circles) of the magnetic susceptibility, χT, from 4 to 400 K provides an estimation of $\Delta E(S_0–T_1)$ through fitting (red line) to the Bleaney-Bowers equation. (c) Raman spectra (top: 785 nm, bottom: 633 nm) of **DIAn** from 25 to 150 °C shows the formation of a new anthracene-like feature at elevated temperature.

SQUID and ESR Experiments

The magnetic properties of **DIAn** were studied by superconducting quantum interference device (SQUID) magnetometry and electron-spin resonance (ESR) spectroscopy. Figure 3.4b displays the SQUID magnetic response of **DIAn** (χ_mT) from 4 to 400 K, which reveals a continuous increase of the whole magnetic molar susceptibility. The data can be fitted to the Bleaney-Bowers equation[32] yielding a low- to high-spin energy gap, $\Delta E(S_0–T_1)$, of 4.18 kcal mol^{-1}. This magnetic behaviour is also associated with a weak Q-band ESR absorption at g ~2.012 that decreases with cooling (see Appendix B for details). Quantum chemical calculations using the spin-flip TD-PBE50 method with non-collinear kernel[33] on the model **DIAn-a** (*vide infra*) gives a $\Delta E(S_0–T_1)$ of 4.9 kcal mol^{-1}, in good agreement with SQUID and ESR measurements (See Appendix B). Taken together, this behaviour indicates antiferromagnetic coupling in the ground electronic state and a thermally activated ferromagnetic interaction between the π-electrons, a

triplet species, populated by heating from the singlet ground state *via* singlet-triplet intersystem crossing.

Variable-Temperature Raman Spectroscopy

To investigate the transformation in molecular structure from singlet to triplet upon heating, we turned to Raman spectroscopy[34,35]. The 1064 nm Raman spectrum, which is very simple despite being recorded in non-resonant conditions, is dominated by two bands at 1610 and 1592 cm^{-1} that arise from C–C stretching vibrations of conjugated systems (see Appendix B for details). The appearance of two ν(C=C) bands separated by ~20 cm^{-1} describes a situation of two separate parts in the conjugated core in line with the solid-state structure of the singlet ground electronic state (Figure 3.4c). Conversely, the 785 nm Raman spectrum at room temperature is featureless; however, with heating, a new band appears at 1580 cm^{-1}, a value typical of anthracene derivatives[36]. Raman spectra of PCHs at temperatures above 50 °C are often strongly interfered by thermal effects on signal quality, provoking the full disappearance of vibrational Raman bands. For **DIAn** we observe the opposite effect, a fact that can be addressed by considering the formation of an electronic state at high temperature at the expense of a low temperature configuration. The rather small $\Delta E(S_0–T_1)$ = 4.18 kcal mol^{-1} implies a thermal population for the triplet species at 150 °C of 2%, justifying the detection by highly sensitive SQUID and EPR techniques. However, as this is also the case for the weak Raman signal, the phenomenon of Raman resonance must be invoked by which we observe the excited state electronic absorptions of the triplet in the 785 nm spectrum at 150 °C[37]. Aside from a strict discussion of the magnitude of $\Delta E(S_0–T_1)$ in **DIAn**, it is clear that the process of populating the triplet state from the singlet state is statistically favorable, or entropy-driven, an aspect already considered in the triply degenerate states in the Boltzmann equation. Indeed, entropy-driven effects have been invoked in singlet exciton fission to justify the fast singlet-triplet conversion

under optical pumping of the excited electronic states in tetracene and pentacene[38]. It is interesting to consider that this situation in **DIAn** can be likened to an intramolecular entropy-driven singlet-triplet process. This may be viewed as a simplified situation in acene-like molecules of the more complex singlet exciton fission process in which two neighboring triplets are involved. Therefore, the fast singlet-triplet intersystem crossing in **DIAn** is fueled by the favourable entropic conditions and by the small $\Delta E(S_0–T_1)$ due to the similarity of the singlet and triplet structures.

Computational Assessment

Quantum chemical calculations are a powerful tool to analyse the fragmental contributions to the π-electron structure of open-shell PCHs. To explore the properties of **DIAn** in more detail, we optimized two model compounds at the B3LYP/6-311G(d) level[39–41] (Figure 3.5a). In **DIAn-a** the large Si(*i*-Pr)$_3$ group is replaced with $SiMe_3$, and the Mes group is reduced slightly by one methyl, whereas all substituents are omitted in **DIAn-b**. Calculations of the model systems confirm that **DIAn** has an open-shell singlet biradical ground state with the closed-shell singlet solution a modest 1.07 (**DIAn-b**) to 1.44 (**DIAn-a**) kcal mol^{-1} higher in energy. Calculations performed at the PUHF level on **DIAn-a** support this conclusion with y = 0.62, a value indicative of moderate biradical character in the ground state[42]. As noted above, the greater stability of the singlet state compared to the triplet state is due to the mechanism of double spin polarization that preferentially stabilizes the singlet over the triplet solution[6]. Figure 3.5b shows the odd-electron density, a visualization of the biradical character index y, for the singlet open-shell state in which we observe densities primarily delocalized on the carbon atoms that link the outer benzenoid rings to the inner anthracene.

The ACID method[43] is used to examine the ring currents at the CSGT-LC-UBLYP-6-311+G(d,p) level[44-47] in **DIAn-a** (Figure 3.5c). Three well-differentiated diatropic (aromatic) circuits exist for the singlet open-shell ground state, the strongest in the external benzenoid rings

and a weaker anthracenic core, which is consistent with moderate open-shell character. The ACID plot for the triplet (See Appendix B for details) reveals a markedly aromatic anthracene moiety, a prediction that justifies the appearance of the new Raman band at 1580 cm^{-1} in the excited triplet state at lower frequencies (i.e. 1590 cm^{-1}) compared to the weakly aromatized anthracene moiety in the singlet ground state.

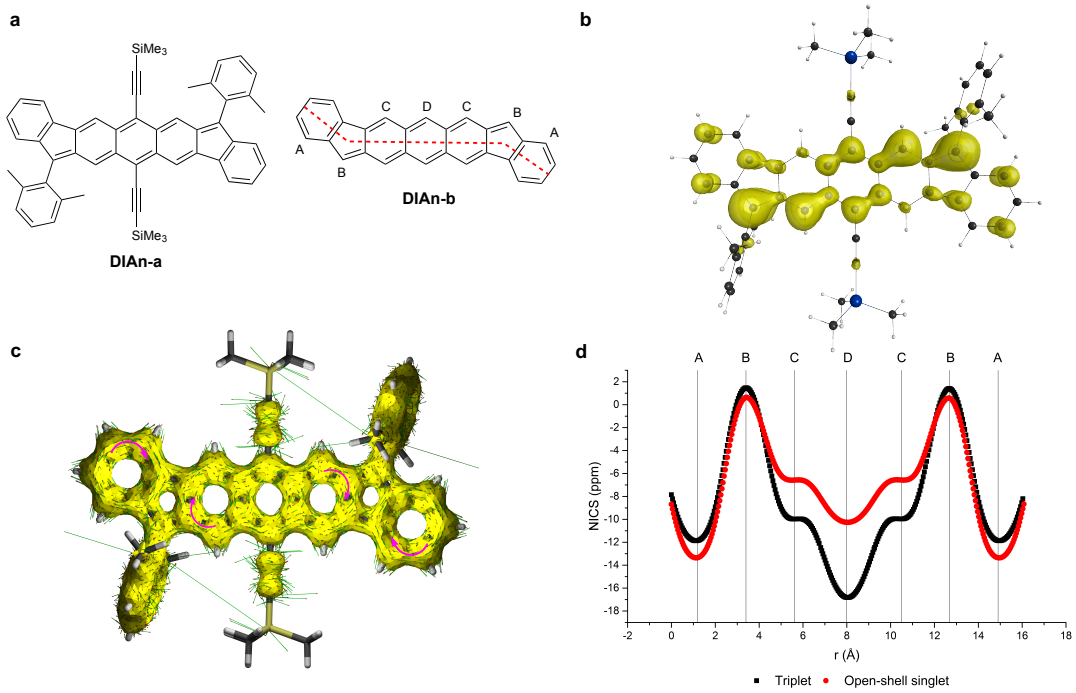

Figure 3.5. Theoretical assessment of **DIAn**. (a**)** Chemical structures of model systems **DIAn-a** and **DIAn-b**. (b) The singlet biradical character of **DIAn-a** is visualized by the odd-electron density plot at 0.001 a.u. isosurface value at the LC-UBLYP/6-311+G(d,p) level of theory. (c) Isosurface (yellow) and current density vectors (green arrows) calculated by ACID for the open-shell singlet state of **DIAn-a**. General aromatic current is indicated by superimposed clockwise magenta arrows. **d**, NICS-XY scan of the open-shell singlet and triplet states of **DIAn-b** shows an increase in aromaticity for the thermally accessible triplet state. Capital letters (top) refer to rings in the model structure.

The NICS-XY scan (Figure 3.5d) of **DIAn-b** visually discloses the evolution of the NICS values along the different fragments of the molecular scaffold[48]. The GIAO-LC-UBLYP/6-311+G(d,p)[49] NICS values are taken 1.7 Å above the molecular plane and employ the σ-only model[50] in order to consider only π−contributions. The three minima correspond to the three aromatic parts of the molecule, the two external benzenes and the central anthracene, with higher

NICS values indicating less aromatic character. The open-shell singlet shows aromatic outer benzenoid rings and a somewhat aromatic anthracene core. In the triplet state the external benzenoid rings remain aromatic while the aromaticity of the central anthracene is accentuated. The two five-membered rings in both singlet and triplet states are non-aromatic and contain the sites of highest odd-electron density, further supporting the resonance structures depicted in Figure 3.3c.

Conclusions

In conclusion, we have reported a new heptacene-like PCH that is segmented by two five-membered rings, thus creating a central dearomatized anthracene. The diindenoanthracene is able to develop biradical character by the aromatization of a closed-shell, non-aromatic, quinoidal structure. The significant results from this study are: (i) whereas acenes and related PCHs express biradical character and concomitantly acquire great reactivity and chemical instability, **DIAn** combines moderate biradical character with a chemical robustness even in the presence of oxygen and at elevated temperatures; (ii) the synthesis is concise, straightforward and multi-gram scalable, providing a versatile way to overcome a critical limitation of many biradical PCH syntheses. Undoubtedly, these are crucial aspects Chemistry must solve for future use of these molecules in market-competitive applications. Complete characterization of the **DIAn** molecule is provided by single-crystal XRD, cyclic voltammetry, optical and vibrational spectroscopies, magnetic measurements and quantum chemical calculations. We provide evidence for the singlet biradical ground electronic state with a thermally accessible triplet excited state. The rather small 4.18 kcal mol^{-1} singlet-triplet gap is significant as the low value implies the ability of switching on and off the magnetic response in a reversible heating-cooling cycle. We have computationally scrutinized the electronic structure of **DIAn** and explained the thermal behavior as a result of efficient intersystem crossing in a heavy-atom free all-carbon molecule. The preparation of **DIAn** opens the way for a new family of five-membered ring intercalated acenes in which chemical

stability and biradical character are realized in concert. Based on these properties, and preliminary OFET devices yielding balanced, ambipolar charge transport behavior, **DIAn** thus substantiates a strategy to optimize chemical design and engineering applications, providing the foundation for the future use of these multifunctional molecules. We are now developing diindeno-fused tetracene and pentacene derivatives that will constitute the next step in the progress of organic materials for potential applications.

Experimental Section

Synthesis of Compound 2 by Suzuki-Miyaura Reaction.

To a 100 ml unregulated pressure vessel equipped with a magnetic stir bar was added compound **1** (1.50 g, 2.15 mmol), 2-formylbenzeneboronic acid (0.81 g, 5.38 mmol, 2.50 equiv.), K_3PO_4 (1.25 g, 6.5 mmol, 3.00 equiv.) and toluene (25 ml). The mixture was sparged with N_2 for twenty minutes then palladium(II) diacetate (10 mg, 0.043 mmol, 2 mol%) and SPhos (35 mg, 0.086 mmol, 4 mol%) were added and the mixture was sparged with N_2 for ten minutes. The vessel was sealed with a PTFE cap and stirred at 80 °C for 18 h. Upon cooling to room temperature, the reaction mixture was diluted with diethyl ether (50 mL) and washed with water (100 mL) then brine (100 mL). The organic phase was dried over anhydrous magnesium sulfate and filtered. Removal of volatiles under reduced pressure afforded **2** as an orange solid (1.60 g, >95%); melting point (m.p.), 226-227 °C; ^{1}H NMR (500 MHz, $CDCl_3$, 25 °C), δ (ppm) 10.18 (d, J = 0.8 Hz, 2H), 8.77 – 8.72 (m, 4H), 8.15 (dd, J = 7.9, 1.4 Hz, 2H), 7.77 – 7.70 (m, 4H), 7.67 (dd, J = 7.7, 1.2 Hz, 2H), 7.61 (t, J = 7.7 Hz, 2H), 1.24 (br s, 42H); ^{13}C NMR (126 MHz, CDCl3, 25 °C), δ (ppm) 191.94, 145.38, 136.61, 133.83, 133.62, 132.36, 131.98, 131.06, 129.44, 128.77, 128.20, 128.03, 127.56, 119.19, 106.27, 102.68, 18.87, 11.45; high-resolution mass spectroscopy (HRMS) (ES+) (*m/z*), calculated for $C_{50}H_{59}O_2Si_2$ $(M+H)^+$ 747.4048, found 747.4034; elemental analysis (EA) calculated for $C_{50}H_{59}O_2Si_2$ C 80.37%, H 7.82%, found C 80.38%, H 7.78%.

Synthesis of Dihydro-DIAn (Compound 3).

An oven-dried 100 ml flask equipped with a stir bar was charged with 2 (1.00 g, 1.34 mmol) and dry tetrahydrofuran (THF, 50 ml). The flask was cooled to 0 °C then a THF solution of 2-mesitylmagnesium bromide (1M, 5.4 ml, 4.00 equiv.) was added via syringe. After stirring for one hour, the reaction was quenched with saturated aqueous NH_4Cl solution (25 ml) and diluted with diethyl ether (50 ml). The organic phase was dried over anhydrous magnesium sulfate and filtered. Volatiles were removed under reduced pressure. The crude diol was dissolved in dry dichloromethane (150 ml) and cooled to 0 °C. Boron trifluoride diethyl etherate (0.66 ml, 5.4 mmol, 4.00 equiv.) was added dropwise and the dark solution was stirred for five minutes. With vigorous stirring, the excess catalyst was quenched by addition of saturated aqueous $NaHCO_3$ solution (25 ml). The organic phase was concentrated under reduced pressure to 25 ml then ethanol (25 ml) was added. The mixture was filtered and washed with water to provide **3** as a yellow solid (1.01 g, 79%); m.p., decomposition >330 °C; ^{1}H NMR (600 MHz, $CDCl_3$, 25 °C), δ (ppm) 9.03 (s, 2H), 8.41 (d, *J* = 1.6 Hz, 2H), 7.97 (d, *J* = 7.6 Hz, 2H), 7.47 (t, *J* = 7.4 Hz, 2H), 7.35 (t, *J* = 7.3 Hz, 2H), 7.31 (d, *J* = 7.5 Hz, 2H), 7.05 (d, *J* = 2.0 Hz, 2H), 6.67 (s, 2H), 5.81 (s, 2H), 2.74 (s, 6H), 2.32 (s, 6H), 1.22 (br s, 42H), 1.18 (s, 6H); ^{13}C NMR (151 MHz, $CDCl_3$, 25 °C), δ (ppm) 148.39, 146.67, 140.78, 140.03, 137.65, 137.44, 136.17, 134.31, 132.48, 132.16, 130.58, 128.87, 128.61, 127.20, 124.53, 121.42, 121.04, 118.27, 117.04, 104.25, 104.17, 49.28, 21.80, 20.88, 19.34, 18.86, 11.55; HRMS (ES+) (*m*/*z*), calculated for $C_{68}H_{79}Si_2$ $(M+H)^+$ 951.5720, found 951.5726; EA calculated for $C_{68}H_{78}Si_2$ C 85.83%, H 8.26%, found C 85.69%, H 8.18%.

Synthesis of DIAn.

To a 250 ml flask with a stir bar was added 3 (310 mg, 0.26 mmol) and dry toluene (75 ml). The mixture was sparged with N_2 for ten minutes then brought to 80 °C. Upon dissolution of 3, DDQ (89 mg, 0.39 mmol, 1.50 equiv.) in toluene (5 ml) was added dropwise via syringe. After

stirring for three hours the deep blue solution was cooled then passed through a plug of basic alumina (4 x 8 cm), eluting with a 1:1 mixture of dichloromethane and hexanes. Volatiles were removed under reduced pressure. The crude material was dissolved in chloroform and an equal volume of acetonitrile was carefully layered above. Dark violet blades of **DIAn** were collected by filtration (192 mg, 62%); m.p., decomposition >260 °C; ^{1}H NMR (600 MHz, CD_2Cl_2, –25 °C), δ (ppm) 8.41 (s, 2H), 7.72 (d, J = 6.3 Hz, 2H), 7.65 (s, 2H), 7.25 – 7.19 (m, 4H), 7.02 (s, 4H), 6.97 (d, J = 6.3 Hz, 2H), 2.39 (s, 6H), 2.09 (s, 12H), 1.11 (br s, 42H); ^{13}C NMR (151 MHz, CD_2Cl_2, –25 °C), δ (ppm) 143.87, 141.89, 138.94, 137.54, 136.85, 136.46, 135.37, 132.54, 130.31, 129.78, 128.73, 128.38, 126.77, 123.54, 123.06, 122.06, 121.58, 121.18, 105.80, 102.34, 21.08, 20.20, 18.53, 11.28; HRMS (ES+) (*m*/*z*), calculated for $C_{68}H_{77}Si_2$ $(M+H)^+$ 949.5564, found 949.5536; EA calculated for $C_{68}H_{76}Si_2$ C 86.02%, H 8.07%, found C 86.06%, H 8.03%.

Bridge to Chapter IV

Chapter III describes the synthesis and characterization of a singlet biradical diindenoanthracene derivative. Chapter IV explores the redox properties of the same compound.

CHAPTER IV

AMPHOTERIC REDOX PROPERTIES OF AN OPEN-SHELL DIINDENOANTHRACENE

This chapter was written by Gabriel Rudebusch and contains results from several research groups. José L. Zafra acquired and, along with Juan Casado, interpreted Raman and UV-vis-NIR spectroelectrochemical data and co-wrote the manuscript; Sarah Spisak and Zheng Wei synthesized and characterized the reduced species and co-wrote the paper; Kotaro Fukuda performed and with Masayoshi Nakano interpreted quantum chemical computations; Erik J. Leonhart provided synthetic support; Marina A. Petrukhina and Michael M. Haley provided editorial and material support. This work is in preparation for publication in the *Journal of the American Chemical Society*.

Introduction

The reduced and oxidized states of an open-shell diindeno[*b,i*]anthracene (**DIAn**) derivative have been investigated by experimental and theoretical techniques. As a result of significant biradical character in cooperation with the ability of cyclopenta-fused scaffolds to stabilize both positive and negative charges, **DIAn** exhibits rich redox chemistry resulting in four observable and isolable states. Structural and electronic properties are brought to light by UV-vis-NIR and Raman spectroelectrochemistry. Aromatization of the **DIAn** scaffold upon successive single electron injections is revealed through single-crystal X-ray diffraction of radical anion and dianion salts. We present a unique case where the pseudo-aromatic/quinoidal ground state of a neutral biradical PCH leads to a stable 5-state redox-active system.

Polycyclic hydrocarbons (PCHs) very often exhibit rich redox chemistry in addition to their unique electronic and optical properties. The exploration of the charge distribution, magnetism, electronic structure and solid-state morphology of redox-active PCHs are well-engrained areas of research.[1-3] The practical application of redox active PCHs and related

materials has seen considerable growth in recent years as the limits of traditional inorganic based materials are approached. First, organic radical batteries based on stable nitroxyl radical polymers or trioxotriangulene systems are attractive alternatives to the current generation of metal ion batteries because of their charging speed, cycling stability and environmental sustainability.[4,5] The storage of information using redox-active organic compounds as memory elements is another potentially fruitful area of research as a single molecule could, in principle, represent the physically smallest bit of information.[6] A remarkable recent example was reported in a homocatenane with six configurable and air-stable charged states. The interlocked molecule was shown to switch between diamagnetic and paramagnetic forms as a function of oxidation state.[7] The ability to stabilize both negative and positive charges, as well as metal-like electron delocalization in the solid-state, has been exploited in ambipolar OFETs based on redox amphoteric small molecules.[8,9] Koike and co-authors demonstrated highly coherent band transport in thin films based on an indacenodiphenalene derivative (Figure 3.1). The excellent performance of the OFETs is likely due to the intimate π-π contacts and multi-center bonding between molecules.[10]

We have recently reported a dimesityl diindeno[*b,i*]anthracene (**DIAn**) derivative as an air- and temperature-stable biradical compound.[11] In connection with a frontier orbital energy gap

Scheme 4.1. Redox processes of **DIAn**. The ground state is a resonance hybrid of quinoidal (acceptor) (top left) and aromatic (donor) (bottom left) structures. Single electron reduction and oxidation events lead to radical cation/anion and dianion/dication species. R = (triisopropylsilyl)ethynyl.

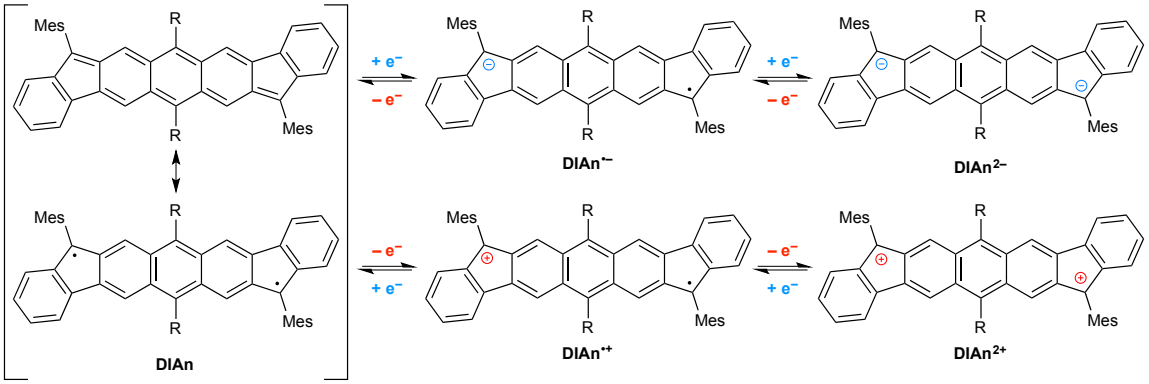

of 1.45 eV and moderate singlet biradical character in the ground state, two reversible one-electron reductions and two reversible one-electron oxidations were observed in the cyclic voltammetry (CV) experiment (Figure 3.3b). The symmetry between all four redox waves, indicating similar electro-kinetic parameters, and good resolution between each wave (ΔE_{red} = 0.39 V, ΔE_{ox} = 0.53 V), led to the hypothesis that each species could be accessed and characterized independently (Scheme 4.1). Here, we investigate the reduced and oxidized states of DIAn and the transformation of molecular structure and properties along all four redox events. Our results provide a clearer understanding of the nature of charge carriers in the ambipolar OFETs and serves as a platform for further modulation of the **DIAn** scaffold.

Results and Discussion

Spectroelectrochemistry

The redox processes examined in solution cyclic voltammetry (Figure 3.3b) were studied by UV-vis-NIR spectroelectrochemistry (Figure 4.1). In the anodic branch, the first one-electron oxidation gives rise to a spectrum with two main bands at 867 nm and 1945 nm (Figure 4.1, top). Interestingly, the 867 nm peak is also observed when **DIAn** is heated to 135 °C in 1,1,2,2-tetrachloroethane (Figure C.1) with the intensity showing a decrease upon cooling to 25 °C. This could be due to a reversible redox process with oxygen or the solvent. The low energy absorbance (1945 nm, 0.65 eV) is typical of a PCH radical cation and can be assigned to a SOMO→LUMO singly excited transition[12,13] while the 867 nm absorbance has major contributions from the HOMO→SOMO transition (See Appendix C).

Increasing the anodic potential further yields two new bands centered at 744 nm and 1026 nm, presumably due to **DIAn^{2+}**. The one-electron reduction process shows disappearance of the neutral absorption at 690 nm and the emergence of two groups of bands centered at 1600–1700 nm and at 400 nm (Figure 4.1, bottom). The low energy (~0.75 eV) absorbance can be attributed

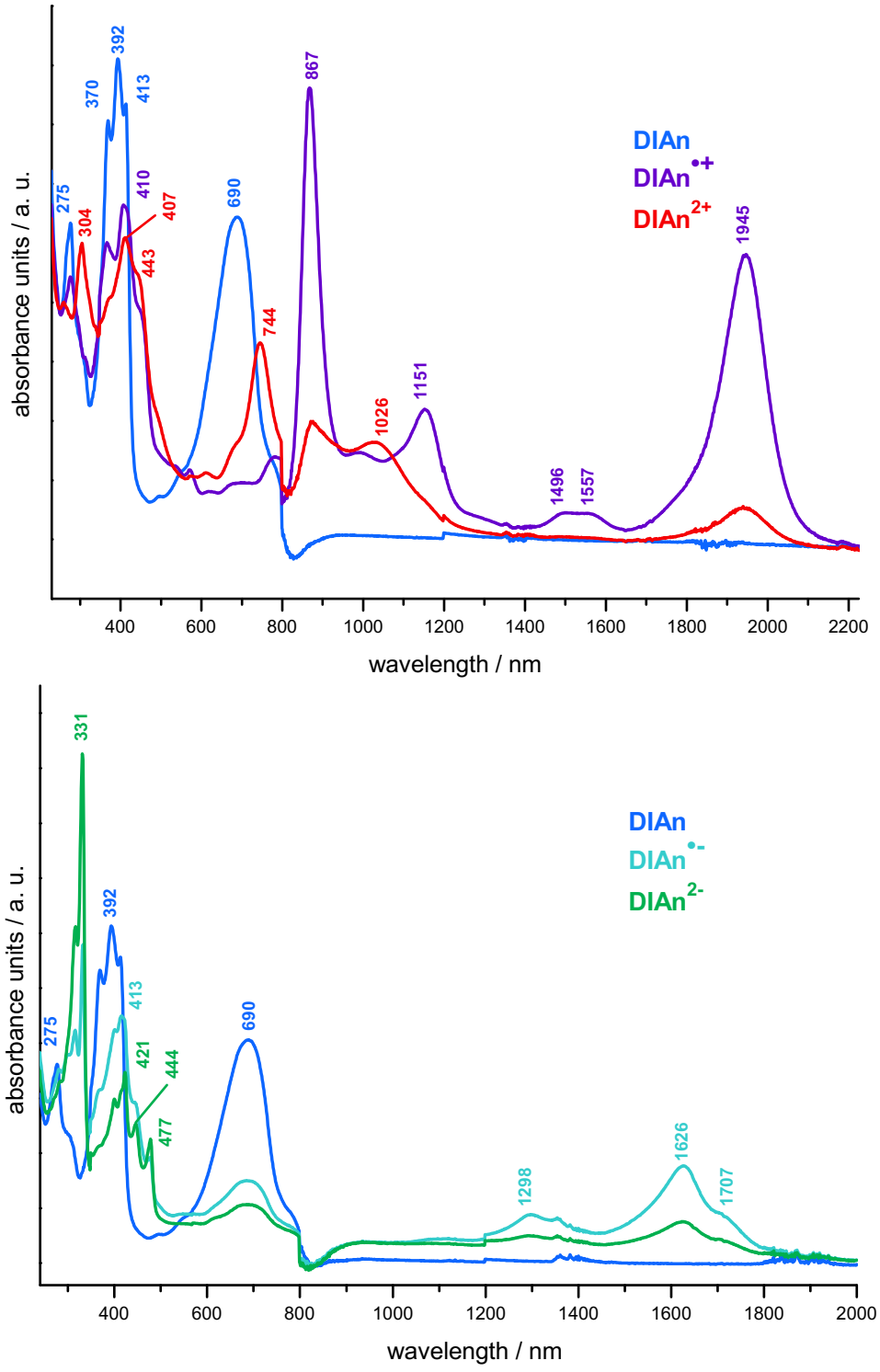

Figure 4.1. The oxidation (top) and reduction (bottom) of **DIAn** followed by UV-vis-NIR spectroelectrochemistry. Conditions: CH_2Cl_2, 0.1 M [*n*-Bu_4N][PF_6].

to

a HOMO→SOMO singly excited transition (See Appendix C). Again, this is typical of a

quinoidal PCH radical anion where the skeletal backbone has regained partial aromaticity.[14]

With increasing cathodic potential, a clear progression to $DIAn^{2-}$ is observed with new peaks at 330 nm and vibronic features from 440 to 470 nm. These anthracene-like vibronic features are in good agreement with a dihydro-DIAn that also contains an aromatic anthracene core appended by saturated indeno fragments (Figure C.4). In parallel with the spectroelectrochemical experiment, chemical reduction and oxidation with K metal and $NOBF_4$, respectively, gave similar absorption spectra, thus confirming the assignment of the UV-vis-NIR electrolysis experiments (Figure C.2 and C.3).

Raman spectroelectrochemical measurements were carried out to investigate the change in molecular structure with each redox event. The Raman spectra of **DIAn** during electrolysis is shown in Figure 4.2. We focus our analysis to the 1600–1550 cm^{-1} spectral range where the structurally relevant C=C stretching vibrations of PCH backbones appear. The Raman spectrum of neutral **DIAn** shows a band at 1589 cm^{-1} due to the characteristic (C=C) stretching mode of the pseudo-aromatic biradical anthracene structure (Scheme 4.1, left). One electron oxidation produces $\mathbf{DIAn^{\bullet+}}$ with a pair of bands at 1587 cm^{-1} and 1581 cm^{-1}. Interestingly, the Raman spectrum of **DIAn** upon one-electron reduction is also characterized by a band at 1580 cm^{-1}. After the second one electron oxidation to $\mathbf{DIAn^{2+}}$ the spectrum is simplified to a single band at 1580 cm^{-1}. In the cathodic branch, a second one-electron reduction to $\mathbf{DIAn^{2-}}$ yields a similar Raman spectrum with a single band at 1582 cm^{-1}. What is significant among the different spectra is that either redox process results in Raman absorption with main skeletal (C=C) bands appearing

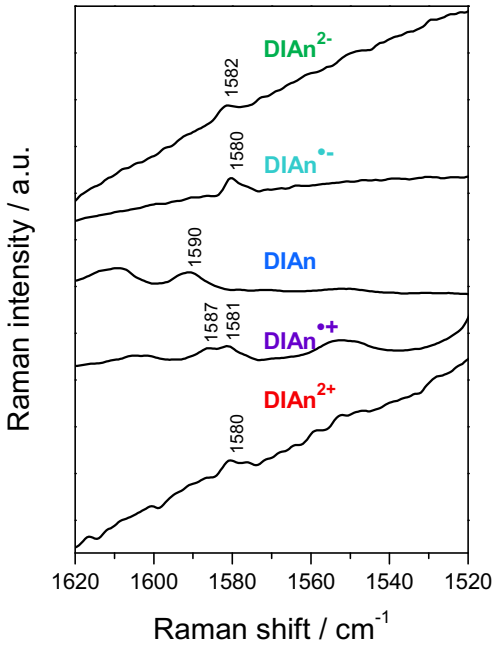

Figure 4.2. Raman spectroelectrochemical experiment of **DIAn** excited at 785 nm. Neutral spectrum is taken at 633 nm. Conditions: 10^{-3} M with 0.1 M [*n*-Bu_4N][PF_6] in CH_2Cl_2.

within a small range of frequencies; there is a structural resemblance between the doubly charged species independent of sign. We can assign the 1580 cm^{-1} band of triplet **DIAn** (Figure 3.5c) to the gain of aromatic character in the thermally accessible triplet excited state. Therefore, the appearance of (C=C) bands in the charged species near 1580 cm^{-1} is an indicator of the recovery of aromaticity in the anthracene core. It can be inferred that the accumulation of aromatic character during redox events is the most efficient mode of stabilizing charges of different sign. From a structural viewpoint, this can be an explanation for the mirror-like reduction and oxidation events in the CV experiment (Figure 3.3b). Further, the ability to stabilize both radical anions and cations has implications in describing the microscopic charge carriers and ambipolar charge transport properties previously shown in OFETs fabricated from **DIAn**.

Solid-State Structure of Reduced DIAn Species

To gain insight into the structural changes upon one and two electron reductions we sought to prepare and characterize salts of $\mathbf{DIAn}^{\bullet-}$ and $\mathbf{DIAn}^{2-}$ in the solid-state. Brief exposure of neutral **DIAn** to K metal in the presence of 18-crown-6 ether provides the solvent-separated radical anion salt **1** (Scheme 4.2). Full reduction to the dianion **2** was possible with longer exposure to K metal. In similar reducing conditions, but with the omission of 18-crown-6 ether and the use of diglyme, the contact-ion complex **3** is obtained. The pair of $[(diglyme)K(THF)]^+$ ions are disordered over two positions of the core with short K···π-contacts of 2.91 Å (η^5) and 3.26 (η^6) (See Figure C.9). Notably, **1** and **2** lack any ion–π interactions; the $[(18\text{-crown-}6)K(THF)_2]^+$ ions are located 5.67 Å (**1**) and 6.24 Å (**2**) from the polycyclic core. This permits meaningful comparison of bond distances between the neutral ligand and "naked" reduced species.[15]

Scheme 4.2. Synthesis of radical anion (**1**) and dianion salts (**2**, **3**) of **DIAn** by dissolving metal reduction. Conditions: **a**, K metal, 18-crown-6, THF, 10 min. **b**, K metal, 18-crown-6, THF, 2 h. **c**, K metal, THF, 10 h, then diglyme/hexanes layer. All H omitted for clarity.

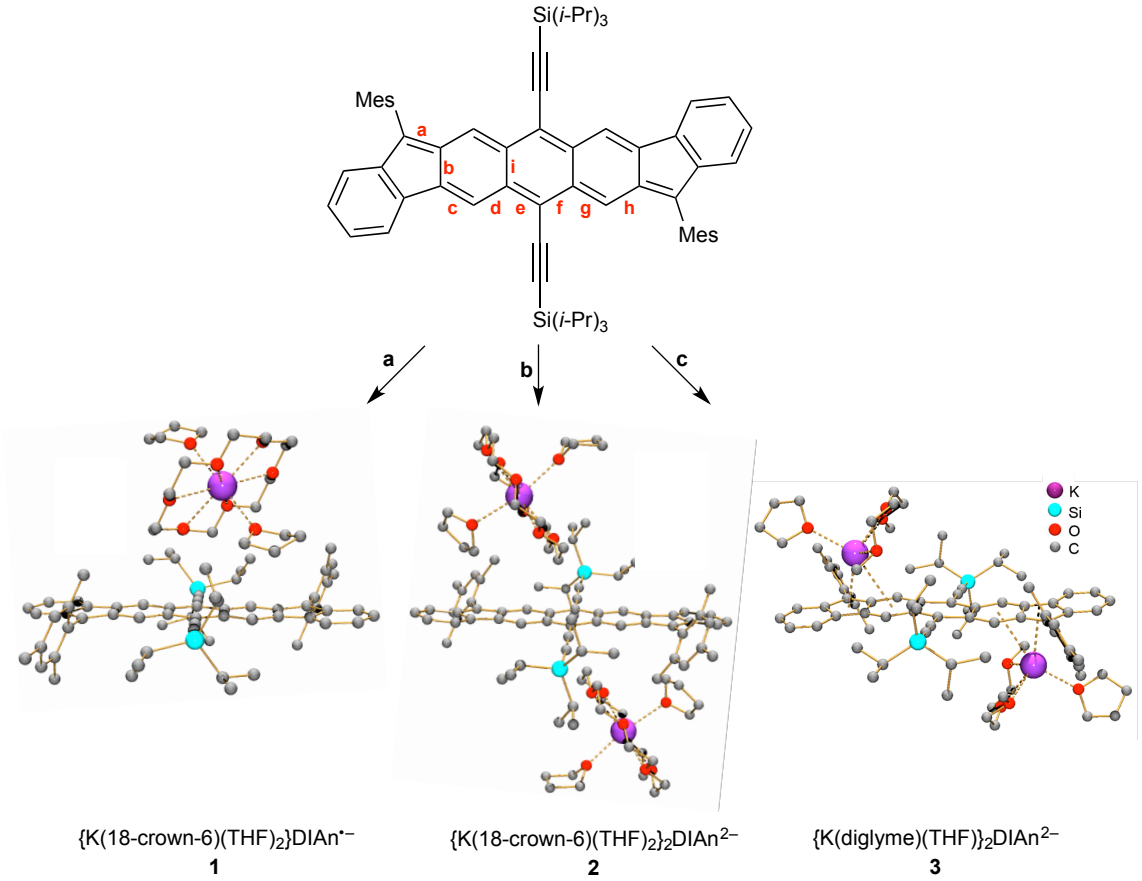

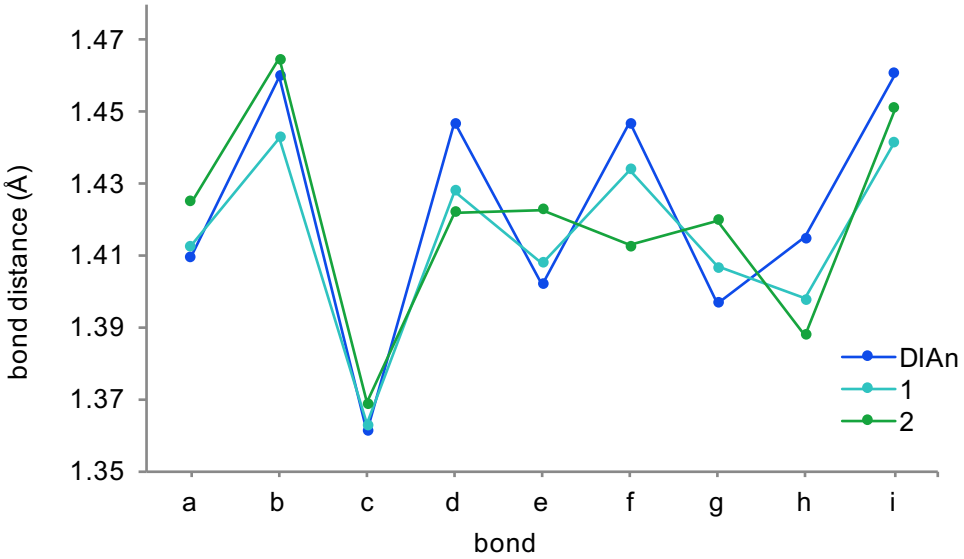

Figure 4.3. Single-crystal X-ray diffraction of neutral **DIAn** (blue), radical anion (**1**, teal) and dianion (**2**, green) discloses aromatization of the core upon reduction. See bond lettering in Scheme 4.2.

Analysis of the bond distances of the non-contact ion pair complexes **1** and **2** reveals aromatization of the anthracene core (Figure 4.3). In the first reduction event, bonds b, d, f, h, and i show an average contraction of 0.017 Å.

These bonds were previously ascribed partial single bond character in neutral **DIAn**. Double bonds throughout the core remain unaffected with average elongation of 0.006 Å (c, e, g). The structure of **1** preserves the bond distance alternation of the neutral ligand, but, as a result of an electron in a previously non-bonding orbital there is contraction of bond distances in the core.[16,17] The next single-electron reduction to dianion **2** shows the homogenization of central bonds d, e, f, and g to 1.420 (± 0.005) Å, a value indicative of a delocalized anthracene-like structure. In fact, comparison of **2** to the structure of a similar saturated system gives excellent agreement (Figure C.11). From the solid-state structure of **1** we observe that the first reduction results in constricted bond distances but overall retention of the quinoidal bonding pattern. The second reduction towards **2** completes the aromatization of the anthracene core. Considering the η^5 coordination of K in the contact-ion pair **3**, we can infer that the negative charges are predominantly localized on the five-membered rings giving two cyclopentadienyl-like anions that straddle the central anthracene (Scheme 4.1).

Computational Assessment

Quantum chemical calculations were carried out to further scrutinize the neutral, reduced and oxidized states of **DIAn**. For computational ease, the Si(*i*-Pr)$_3$ and mesityl groups were simplified to $SiMe_3$ and 2,6-dimethylphenyl, respectively. HOMO and LUMO density plots are shown in Figures 4.4a and 4.4b, respectively. In both plots, the orbital density is largely delocalized over the 5-6-6-6-5 core of **DIAn** with some density on the outer benzenoid rings. For the singly reduced and oxidized states the UB3LYP/6-311G* level of theory was chosen as it has been previously confirmed to provide reasonable estimations of geometries and excitation

energies for charged PCHs[18]. The SOMO density plots for **DIAn**$^{\bullet+}$ and **DIAn**$^{\bullet-}$ in their doublet states are depicted in Figures 4.4c and 4.4d, respectively. At first glance there is a strong resemblance between the neutral HOMO density plot and radical cation SOMO density plot. A similar relationship is evident between the neutral LUMO density plot and radical anion SOMO density plots. We rationalize this by recognizing that in the first oxidation process an electron is removed from the HOMO, creating a SOMO state of similar orbital density and symmetry. A similar explanation can be made to explain orbital density distribution and symmetry between the monoanion SOMO and neutral LUMO. This explanation is supported by the similarity between the solid-state structures of **DIAn** and **2** (Figure 4.3).

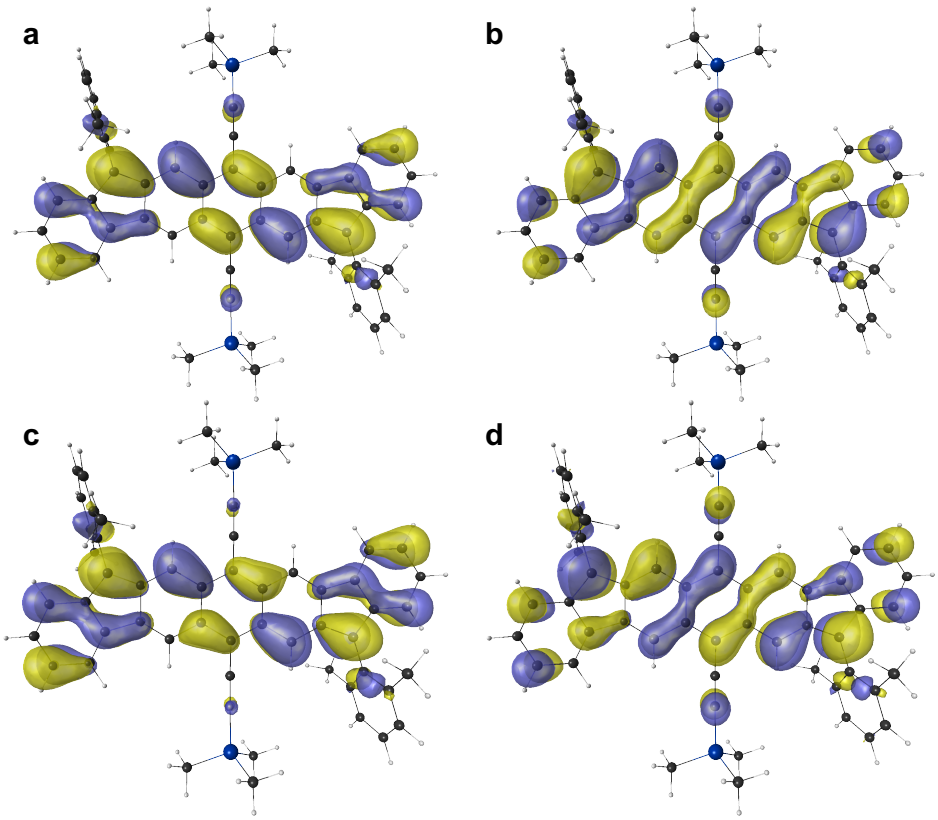

Figure 4.4. (a) HOMO and (b) LUMO density plots of the neutral model **DIAn** in the singlet state at the LC-RBLYP/6-311+G** level of theory. SOMO density plots for the (c) radical cation and (d) radical anion doublet states at the LC-UBLYP/6-311+G** level of theory. Each plotted at 0.02 a.u. isosurface values.

Electrostatic potential maps were calculated at the LC-UBLYP/6-311+G** on the **DIAn** model system and the two diionic states. For the neutral species we observe marginal charge on the core and substituents, as expected for a neutral species (Figure 4.5a). In the **DIAn**$^{2-}$ model, regions of negative charge are localized near the five-membered ring and adjacent ring on the anthracene core (Figure 4.5b). The central benzenoid ring and ethynyl substituents show a distinct lack of charge. Moving to the **DIAn**$^{2+}$ model a similar distribution of charge is apparent with the five-membered rings containing the most electropositive regions (Figure 4.5c). Along with the electrostatic potential maps, a Hirshfeld charge analysis indicates that charges in both diionic states are greatest on the apical carbons connecting the outer benzenoid rings and the inner anthracene. Considering the position of K ions in the solid-state structures of dianions **2** and **3**, this localization of negative charge is in excellent agreement. An alternate explanation could be that these are also the most accessible sites on the DIAn core owing to the bulkiness of Si(*i*-Pr)$_3$ and Mes substituents. Nevertheless, computational studies are in good agreement with experimental data and the redox processes outlined above (Scheme 4.1).

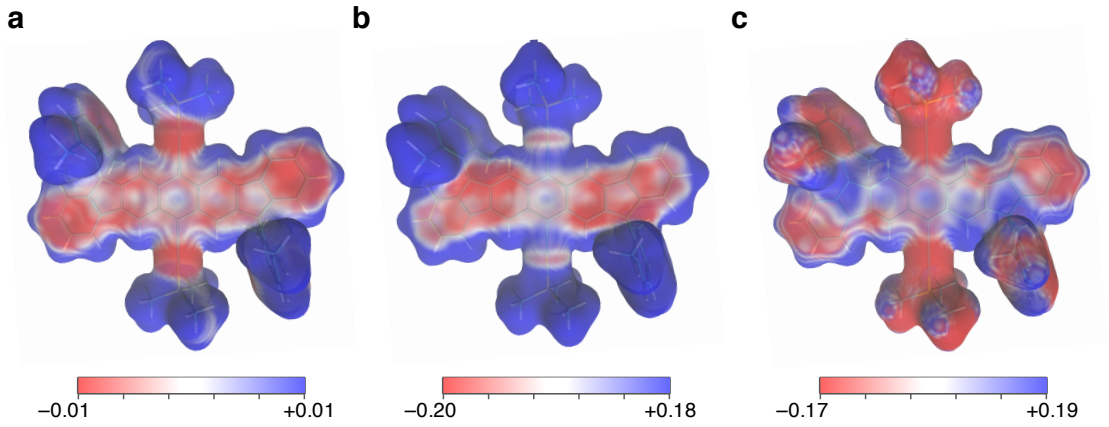

Figure 4.5. Electrostatic potential maps for the model **DIAn** in the (a) neutal, (b) dianionic and (c) dicationic states. Red and blue regions represent negative and positive charges, respectively.

Conclusions

We have shown that **DIAn** is a cyclopenta-fused PCH that can accept or donate electrons reversibly with charges primarily localized on the five-membered rings. As a result of the biradical character and the resonance between quinoidal (acceptor) and aromatic (donor) structures in the ground state, **DIAn** is able to stabilize both negative and positive charges. Through spectroelectrochemical experiments we identified low energy absorptions (ca. 0.7 eV) in the monoradical states and assigned these transitions to HOMO→SOMO for $\mathbf{DIAn}^{\bullet-}$ and SOMO→LUMO for $\mathbf{DIAn}^{\bullet+}$ by TD-DFT methods. Raman spectroscopy in conjunction with *in situ* electrolysis indicated that the structures of all redox states are quite similar. This translates to a minimal change in geometry upon exciton formation, an appealing feature for organic electronic applications as large structural reorganization typically hampers electronic performance. Investigation of the non-contact crown-ether potassium salts of $\mathbf{DIAn}^{\bullet-}$ and $\mathbf{DIAn}^{2-}$ through X-ray crystallography provided a clear picture of the structural consequences of successive single-electron charging. Finally, a quantum chemical computational study supported our experimental results and detailed the localization of charge on the polycyclic core. From multiple experiments and spectroscopic techniques we conclude that the cyclopenta-fused rings are the predominant sites of the rich redox chemistry observed in **DIAn**, in accord with the sites of highest odd-electron density in the ground state. This study represents a unique case where the stability of a neutral open-shell compound allows for the thorough characterization and structural analysis across four redox states. Future work will focus on tuning the solid-state packing and electronic properties of diindeno[*b*,*i*]anthracene system in addition to π-expansion of the central acene core.

Experimental Section

[{K(18-crown-6)(THF)$_2$}DIAn$^{\bullet-}$] • 2THF (Compound 1)

THF (3 mL) was added to a closed system containing **DIAn** (~2 mg) and an excess of K metal and 18-crown-6. The initial color of the mixture was blue-green (neutral parent ligand). After being stirred at room temperature for 10 minutes, the reaction solution turned deep green. The mixture was stirred at room temperature until brown swirls were seen coming off the K metal (indication of the dianion beginning to form). The mixture was then filtered and the green filtrate was layered with hexanes (3.1 mL) and cooled to 0 °C. After 5 d, dark brown plates of **1** were formed in moderate yield (*ca*. 40 %). Crystals were collected, washed with hexanes (3 × 2 mL) and dried before measurements.

[{K(18-crown-6)(THF)$_2$}$_2$DIAn^{2-}] • 4THF (Compound 2)

THF (3 mL) was added to a closed system containing **DIAn** (~3 mg) and excess of K metal and 18-crown-6. The initial color of the mixture was blue-green. After being stirred at room temperature for 10 min, the reaction solution turned deep green. The mixture was stirred for an additional 2 h resulting in a brown suspension. After stirring at room temperature for a total of 10 h, the deep brown mixture was filtered and the orange-brown filtrate was layered with hexanes (2.7 mL) and cooled to 10 °C. Red-brown plate shaped crystals of **2** had formed in high yield (*ca*. 70 %) after 3 d. Crystals were collected, washed with hexanes (3 × 2 mL) and dried before measurements.

[{K(diglyme)(THF)}$_2$DIAn^{2-}] • 2THF (Compound 3)

THF (3 mL) was added to a closed system containing **DIAn** (~2 mg) and an excess of K metal. The initial color of the mixture was blue-green. After being stirred at room temperature for 10 min, the reaction solution turned deep green. The mixture was stirred for an additional 2 h

resulting in a brown suspension. After stirring at room temperature for a total of 10 h, the deep brown mixture was filtered and the brown filtrate was layered with diglyme:hexanes (1:20, 1.4 mL). The ampoule was placed at 0 °C. After 4 d, orange-brown plate-shaped crystals of **3** had formed in moderate yield (*ca*. 35 %). Crystals were collected, washed with hexanes (3 × 2 mL) and dried.

Bridge to Chapter V

Chapter IV explored the redox chemistry of a diindenoanthracene derivative both computationally and by spectroscopic techniques. In Chapter V I describe the challenges associated with derivatizing the diindenoanthracene core and present a new, potentially versatile synthetic intermediate.

CHAPTER V

DIINDENOANTHRACENE-DIONE

This chapter was written by Gabriel Rudebusch. Conerd K. Frederickson performed the CV experiments; Victoria M. Stanfill provided synthetic assistance; and Michael M. Haley provided guidance and editorial support. This work is in preparation for publication in the *Journal of Organic Chemistry*.

Introduction

Biradical polycyclic hydrocarbons (PCHs) are an emerging class of functional organic materials.[1-3] In essence, a C–C double bond is formally dissociated across the PCH framework with partial occupation of a formerly unoccupied molecular orbital. These systems have been shown to possess narrow energy gaps, strong absorption in the vis-near-IR, rich redox amphoterism and large two-photon absorption cross sections. In a previous report we investigated the electronic structure of **1** (Figure 5.1). Through a combined experimental and computational effort including single-crystal X-ray diffraction, variable temperature techniques and a quantum chemical assessment, it was found that **1** exhibits a singlet biradical ground state with a low lying triplet excited state. Associated with the biradical nature is an exceptionally low frontier orbital energy gap (~1.45 eV) and redox amphoterism. These properties were exploited in preliminary organic field effect transistors (OFETs) with **1** as the active layer. Balanced hole and electron mobilities were measured; however, the values (10^{-3} $cm^2V^{-1}s^{-1}$) fell short of the range typically cited for useful organic transistors (1–10 $cm^2V^{-1}s^{-1}$). Strategies to improve the electrical performance of OFETs

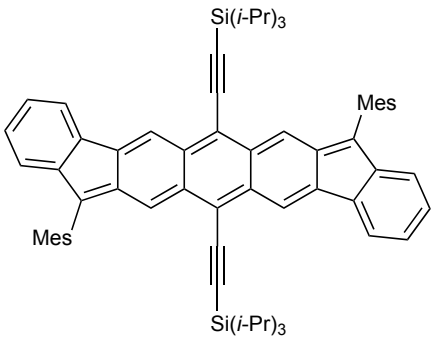

1

Figure 5.1. Structure of the first diindeno[*b*,*i*]anthracene (DIAn) derivative **1**. Mes = 2,4,6-trimethylphenyl.

involve optimization of both device fabrication and molecular structure through synthesis. The preparation of additional DIAn derivatives is desirable to modulate the solid-state packing as more intimate π-π contacts typically translate to better device results[4-6]. In addition to control of the solid-state morphology, a survey of electronically diverse aryl groups could provide interesting results as most biradical systems lack stability towards ambient conditions and opportunities for late-stage functionalization. Further, the effects of donor/acceptor character on open-shell PCHs is relatively unexplored[7,8] and could offer new insight.

The initial synthesis of **1** was efficient and possible on the gram-scale in four steps from a known dibromoanthracene precursor. A drawback of the original route was the dependence on bulky aryl groups that directed the Friedel-Crafts reaction away from the otherwise more reactive[9] positions on anthracene. Further, while use of mesityl substituents proved critical for solution stability, allowing for full characterization at elevated temperature, the same groups were responsible for prohibiting the close intermolecular contacts essential for organic electronic applications. Here, we report the synthesis and characterization of a DIAn dione derivative that represents the next step towards the practical application of a stable organic biradical.

Results and Discussion

Synthesis

Initial attempts at the synthesis of new DIAn derivatives began from the dialdehyde **2**, an intermediate in the reported synthesis of **1**. The pentafluorophenyl diol was prepared in excellent yield from **2** by the Grignard reagent. An attempt at the Friedel-Crafts alkylation with BF_3•OEt_2 resulted in no reaction and the starting diol was recovered in excellent yield. Presumably, the secondary carbocation-like intermediate is too stabilized to undergo the desired electrophilic aromatic substitution reaction. Moving towards less substituted aryl substituents also proved unfruitful. The phenyl-substituted secondary alcohol underwent Friedel-Crafts alkylation to the more hindered, yet electronically preferred, C(1) and C(5) positions on the anthracene core

despite the steric bulk of the Si(*i*-Pr)$_3$ groups (Scheme 5.1). The structure of the unexpected diphenyl dihydro isomer **3** was confirmed by single-crystal X-ray diffraction. The compound was found to be distorted from planarity with a RMS deviation of 0.09 Å from an average plane drawn through the core and the Si atoms displaced 1.622 Å above the molecular plane. Subjection of **3** to DDQ oxidation at elevated temperatures resulted in no reaction as the Si(*i*-Pr)$_3$ groups likely block the tertiary C–H groups from approach by the oxidant.

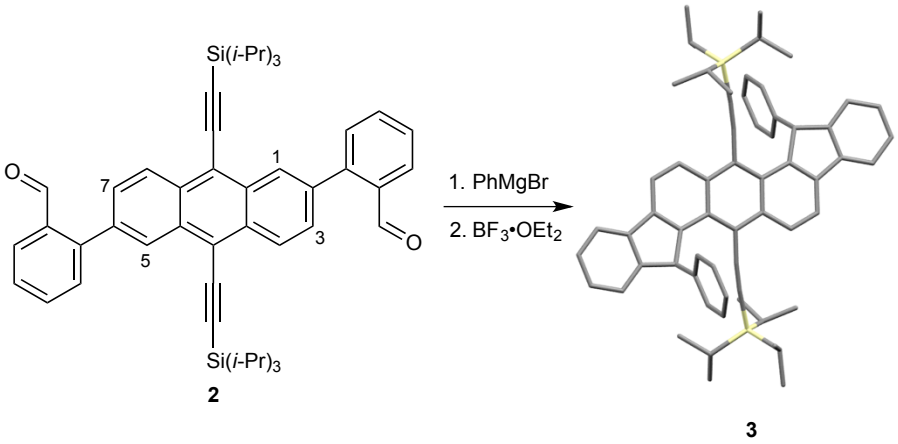

Scheme 5.1. Unexpected formation of the diindeno[*a*,*h*]anthracene **3** and the molecular structure illustrating the strained phenyl–Si(*i*-Pr)$_3$ interaction. All H atoms are omitted for clarity.

To overcome the constraints with the previously established synthetic route to the DIAn core, in particular the limited scope of the "outside-in" Friedel-Crafts alkylation, we initiated synthesis towards **4**. In brief, an "inside-out" acylation strategy was adopted to append the indenone groups to the anthracene core (Scheme 5.2). Ensuing steps from the dione **4** consist of the addition of an aryl nucleophile then $SnCl_2$ reduction to give the substituted DIAn derivative. It has been shown previously that the $SnCl_2$ conditions are applicable to both electron rich or electron deficient aryl groups.[10]

To begin the synthesis, we took inspiration from Wudl's preparation of a substituted heptacene derivative.[11] Owing to the directing ability of the Si(*i*-Pr)$_3$-ethynyl groups, the C(3) and C(7) positions on dibromoanthracene **5** can be selectively deprotonated by an excess of LiTMP at –78 °C (Scheme 5.2). Quenching the dilithio species at –78°C with dry CO_2 followed by an acidic workup gives the dibromo diacid **6** in 84% yield. Use of LiTMP is critical as the bulkiness of the amine byproduct precludes addition to any adventitiously produced benzyne-like elimination products.[12] Next, a palladium-catalyzed Suzuki-Miyaura reaction furnishes the diphenyl diacid **7** that is moved forward without purification. The polar solvent system of toluene/ethanol was found to be necessary for solubilizing the bromocarboxylic acid. Direct cross-coupling to the

Scheme 5.2. Synthesis of DIAn-dione **4** in 74% overall yield over four steps.

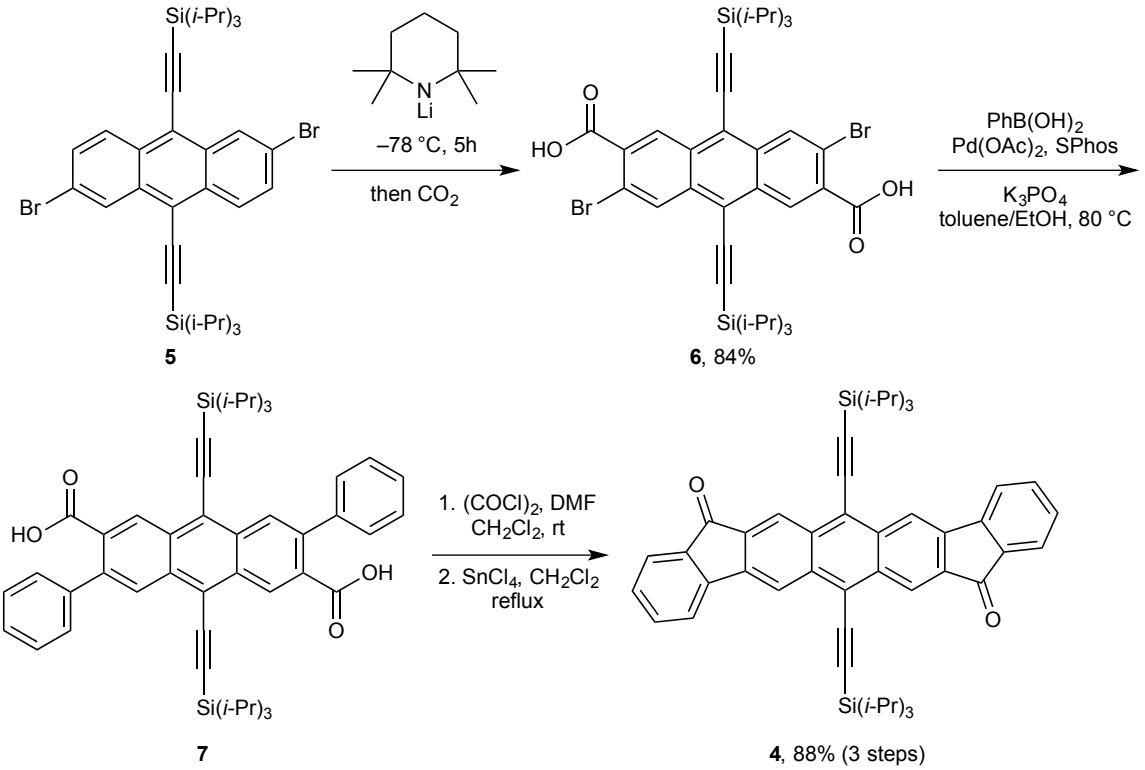

5 **6**, 84%

7 **4**, 88% (3 steps)

free acid is attractive as it avoids wasteful esterification and saponification steps. Conversion to the acid chloride by oxalyl chloride followed by $SnCl_4$ mediated Friedel-Crafts acylation provides the DIAn-dione **4** in 88% yield from **5**. Careful selection of Lewis acid in the acylation reaction was critical as $AlCl_3$ gave complex mixtures of byproducts and BF_3•OEt_2 resulted in no reaction.

The synthesis can be performed without chromatography on the multi-gram scale. Future work stemming from this synthetic route will pursue more diverse arylboronic acids in the Suzuki reaction to further modify the DIAn core. In addition, since the bulkiness of LiTMP most likely directs the sites of deprotonation on **5**, the trialkylsilyl group could be varied to include the smaller triethylsilyl or *n*-octyldi(isopropyl)silyl to further modify the solid-state packing.

Solid-State Structure

The structure of dione **4** was confirmed through single-crystal X-ray diffraction. The compound is centrosymmetric and planar; RMS deviation from an average plane drawn through the fused core is 0.01Å. **4** was found to arrange into a 1D slipped stack that is typical for the C_2

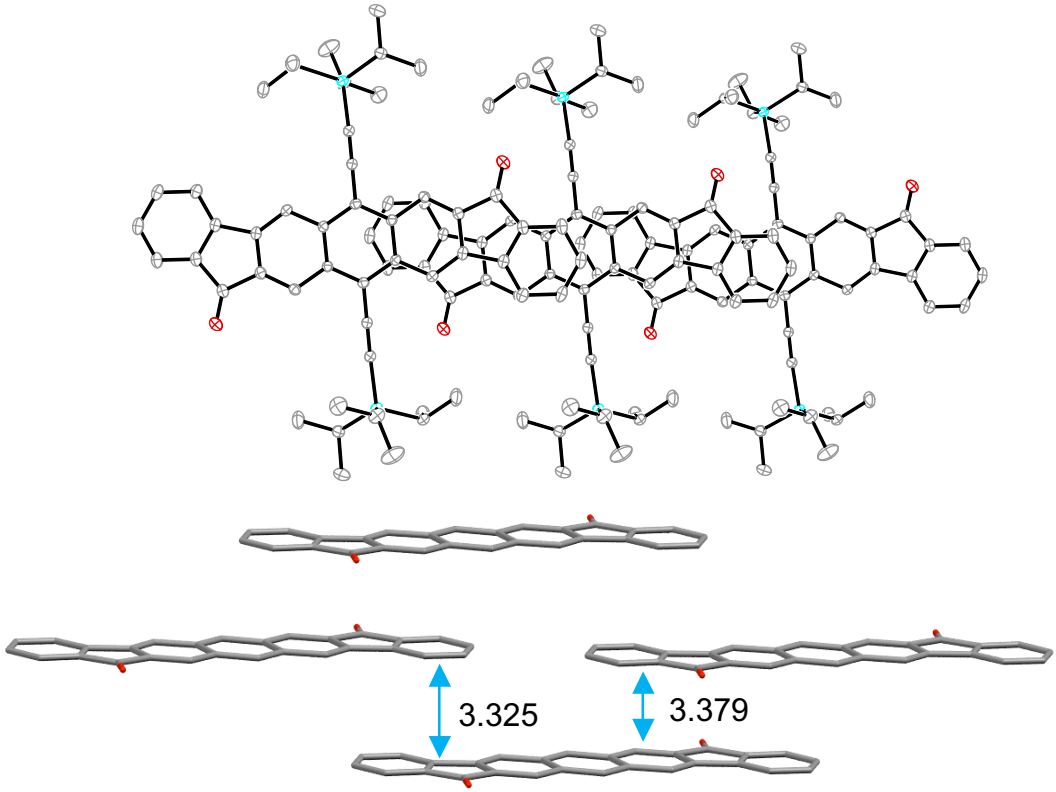

Figure 5.2. Single-crystal X-ray diffraction of DIAn-dione **4** shows the 1D slipped stack (top). Close interactions with an adjacent 1D stack gives a pseudo-2D brickwork (bottom). Interplanar distances in Å are shown with blue arrows. H atoms and Si(*i*-Pr)$_3$-ethynyl groups are omitted for clarity.

symmetric diindenoacene family (Figure 5.2, top).[13,14] Average planes drawn through the

polycyclic core are separated by 3.379 Å. Overlapping with an adjacent 1D stack is observed with an interplanar distance of 3.325 Å. Taken together, the solid-state arrangement is suggestive of a 2D brickwork (Figure 5.2, bottom). However, minimal HOMO/LUMO density on the benzenoid rings, compounded with the lack of constructive close C–C contacts, renders the pseudo-2D brickwork of **4** unfavorable for potential devices.

Absorption and Emission Spectroscopy

The steady-state properties of DIAn-dione **4** were examined through absorption and fluorescence spectroscopy (Figure 5.3, Figure 5.4). The dione exhibits a strong absorption at 364 nm with lower intensity vibronic features at 414 and 439 nm as a result of the rigid anthracene core. In line with the similar indeno[1,2-*b*]fluorene-6,12-diones (IF),[14] low energy absorptions extend to 560 nm and could be related to the $S_0 \rightarrow S_1$ transition. From this lowest energy absorption we observe a strong emission tailing to 700 nm (Figure 5.4). A Stokes shift of 130 cm^{-1} is indicative of a small change in excited state geometry owing to the rigid acene structure of **4**. Photoluminescence quantum yield measurements give a value of 13%, in range of the smaller IF-diones.[15]

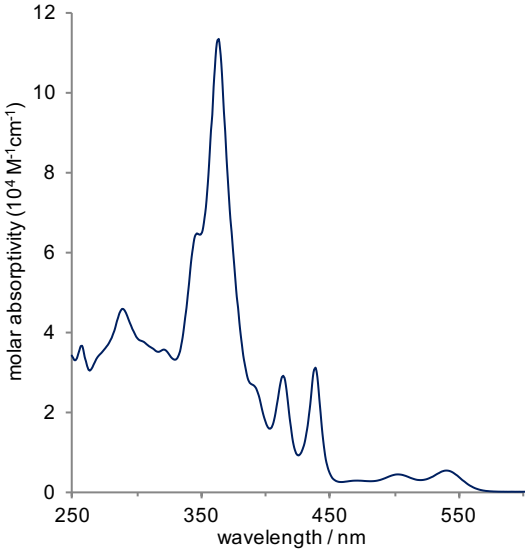

Figure 5.3. Full electronic absorption spectrum of DIAn-dione **4**.

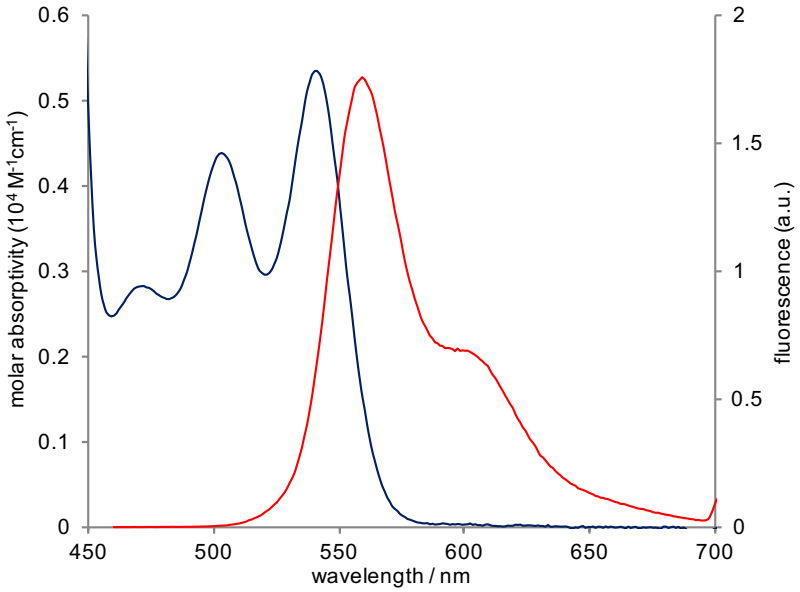

Figure 5.4. Absorption (navy) and normalized fluorescence (350 nm excitation, red) spectra of DIAn-dione **4**.

Cyclic Voltammetry

The CV experiment revealed two one-electron reduction processes at -1.01 and -1.23 vs. SCE (Figure 5.5). In contrast to the smaller IF dione, these reductions arrive at more negative potentials, but the difference between reductions, ΔE_{red} is cut to 0.22 V from 0.42 V. This can be rationalized by considering the alleviation of Coulombic charge repulsion from the increased distance between ketone moieties, the probable site of reductions. One reversible one electron oxidation was observed at 1.51 V vs. SCE, most likely a property gained from the larger acene core. From the solution CV experiment we can estimate the HOMO to be -6.15 eV below the vacuum level and the LUMO at –3.63 eV, giving an energy gap of 2.52 eV.

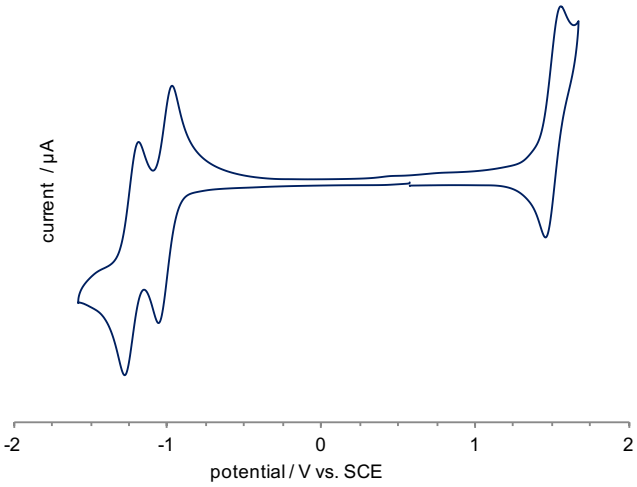

Figure 5.5. Cyclic voltammogram of DIAn-dione **4** shows two reversible one-electron reductions and one reversible one-electron oxidation.

Substrate Scope

To test the feasibility of this new precursor for derivatization of the DIAn scaffold we subjected **4** to excess MesMgBr followed by dehydroxylation with $SnCl_2$ in anhydrous toluene to give **1** in 73% yield (See the Experimental Section). The efficiency of this new route to **1** is comparable to the previously reported oxidative conditions with DDQ. At present, other aryl nucleophiles (i.e. Ph, C_6F_5, 3,5-$(CF_3)_2C_6H_3$) or triisopropylsilylethynyl failed to produce the desired DIAn derivatives. Rather, the formation of several fluorescent and non-polar species was observed. Optimization of reaction conditions and the use other nucleophiles is under current investigation.

Conclusions

We have presented the synthesis of a promising precursor molecule based on the diindenoanthracene-8,16-dione framework. Limitations of the original synthetic route to DIAn were overcome by an "inside-out" acylation strategy through the regiospecific metallation of

dibromoanthracene and use of a milder Lewis acid in the Friedel-Crafts reaction. The steady-state properties of dione **4** were analyzed by absorption and emission spectroscopy and in the solid-state by single-crystal X-ray diffraction. A pseudo-2D brickwork arrangement was observed due to the lack of steric bulk on the outer rings. Future work involves derivatization of this intermediate dione as well as modifications in the newly developed synthetic route.

Experimental Section

Synthesis of 3,7-dibromo-9,10-bis(triisopropylsilyl)ethynyl)anthracene-2,6-dicarboxylic acid (Compound 6)

To an oven dried 250 mL 3-necked flask equipped with a magnetic stir bar, nitrogen inlet, rubber septum and 50 mL pressure equalizing addition funnel was added 2,2,6,6-tetramethylpiperidine (TMP, 1.8 mL, 8.6 mmol, 6.00 equiv.) and THF (50 mL). Under nitrogen flow, compound **5** (1.20 g, 1.7 mmol, 1.00 equiv.) and THF (40 mL) were added to the addition funnel. The flask was cooled to 0 °C and *n*-butyllithium (8.6 mmol, 2.5 M in hexanes, 5.00 equiv) was added dropwise to the TMP solution. The flask was cooled to –78 °C and the solution of **5** was added dropwise to the stirred LiTMP solution. After 5 h at –78 °C, a nitrogen purged straight addition funnel was quick-switched to the spare neck. A kim-wipe followed by anhydrous $MgSO_4$ (10 g) were added to the funnel. The addition funnel was charged with dry ice and CO_2 was sublimed into the lower reaction flask head space. With gentle shaking, the dark orange dilithio species was replaced by the deep green fluorescence of the title compound. The reaction was quenched by careful addition of 10% H_2SO_4 (20 mL) at –78 °C. Upon warming to room temperature, water (50 mL) and diethyl ether (100 mL) were added. The organic phase was dried over $MgSO_4$ and evaporated under reduced pressure. Compound **6** was collected by filtration and washed with hexanes to give an orange solid (1.14 g, 84%); ^{1}H NMR (600 MHz, DMSO-d_6, 25 °C), δ (ppm) 13.82 (br s, 2H), 9.03 (s, 2H), 8.81 (s, 2H), 1.24 (br s, 42H); ^{13}C NMR (151 MHz,

DMSO-d_6) δ (ppm) 166.75, 133.23, 133.08, 132.16, 131.11, 131.05, 119.91, 118.67, 108.49, 101.44, 19.03, 11.26.

Synthesis of 3,7-diphenyl-9,10-bis(triisopropylsilyl)ethynyl)anthracene-2,6-dicarboxylic acid (Compound 7)

To a 50 mL unregulated pressure vessel equipped with a magnetic stir bar was charged with compound **6** (0.750 g, 0.96 mmol, 1.00 equiv.), phenylboronic acid (0.466 g, 3.83 mmol, 4.00 equiv.), K_3PO_4 (1.20 g, 5.73 mmol, 6.00 equiv.), toluene (15 mL) and ethanol (15 mL). The mixture was sparged with N_2 for twenty minutes then palladium(II) diacetate (9 mg, 0.038 mmol, 4 mol%) and SPhos (31 mg, 0.076 mmol, 8 mol%) were added and the mixture was sparged with N_2 for ten minutes. The vessel was sealed with a PTFE cap and stirred at 80 °C for 18 h. Upon cooling to room temperature, the reaction mixture was diluted with ethanol (50 mL) and filtered. Volatiles were removed under reduced pressure and suspended in diethyl ether (50 mL). The mixture was filtered and washed with water (100 mL) then cold acetone (20 mL) to provide **7** as a yellow solid that was carried on without further purification.

Synthesis of 6,14-bis((triisopropylsilyl)ethynyl)diindeno[b:i]anthracene-8,16-dione (Compound 4)

To a suspension of compound **7** in CH_2Cl_2 (100 mL) was added 3 drops of DMF followed by oxalyl chloride (0.26 mL, 3.0 mmol, 3.0 equiv.). After 1 h the volatiles were removed under reduced pressure. The crude acid chloride was dissolved in CH_2Cl_2 (100 mL) and $SnCl_4$ in CH_2Cl_2 (4.0 mmol, 1 M, 4.0 equiv.) was added dropwise via syringe. The reaction was refluxed for 4 h then cooled and quenched with water (50 mL) followed by hexanes (50 mL). The organic phase was shaken with 1 M NaOH (50 mL). The organic phase was dried over anhydrous $MgSO_4$, filtered and condensed to a slurry under reduced pressure. Ethanol (50 mL) was added and the solids were filtered to give the title compound as an orange-red solid (0.628 g, 88% from **6**); ^{1}H

NMR (600 MHz, $CDCl_3$) δ (ppm) 9.00 (s, 2H), 8.74 (s, 2H), 7.86 (d, *J* = 7.4 Hz, 2H), 7.78 (d, *J* = 7.5 Hz, 2H), 7.67 (td, *J* = 7.4, 1.1 Hz, 2H), 7.46 (td, *J* = 7.4, 0.9 Hz, 2H), 1.44 – 1.31 (br s, 42H); ^{13}C NMR (151 MHz, $CDCl_3$) δ (ppm) 192.07, 144.51, 138.78, 136.90, 135.52, 135.40, 134.80, 134.25, 129.90, 125.16, 124.65, 123.19, 121.47, 118.32, 107.28, 102.11, 18.94, 11.57.

Synthesis of Compound 1

To a 250 mL round bottom flask was charged **4** (75 mg, 0.10 mmol), THF (25 mL) then cooled to 0 °C. A solution of MesMgBr (0.5 mL, 1M, 5.0 equiv.) was added dropwise and the reaction was allowed to warm to 25 °C. After 1 h, the reaction was quenched with saturated NH_4Cl (25 mL) followed by Et_2O (50 mL). The organic phase was dried over anhydrous $MgSO_4$. Volatiles were removed under reduced pressure, then the crude diol was redissolved in anhydrous toluene (50 mL). Anhydrous $SnCl_2$ (189 mg, 1.0 mmol, 10 equiv.) was added and the reaction mixture was heated to 50 °C. After 1 h the deep blue solution was allowed to cool and filtered through a short plug of silica gel with CH_2Cl_2/hexanes (100 mL, 1:1). Removal of volatiles under reduced pressure gave the title compound as a dark blue solid (69 mg, 73% yield). Spectroscopic data matched previous work.

APPENDIX A

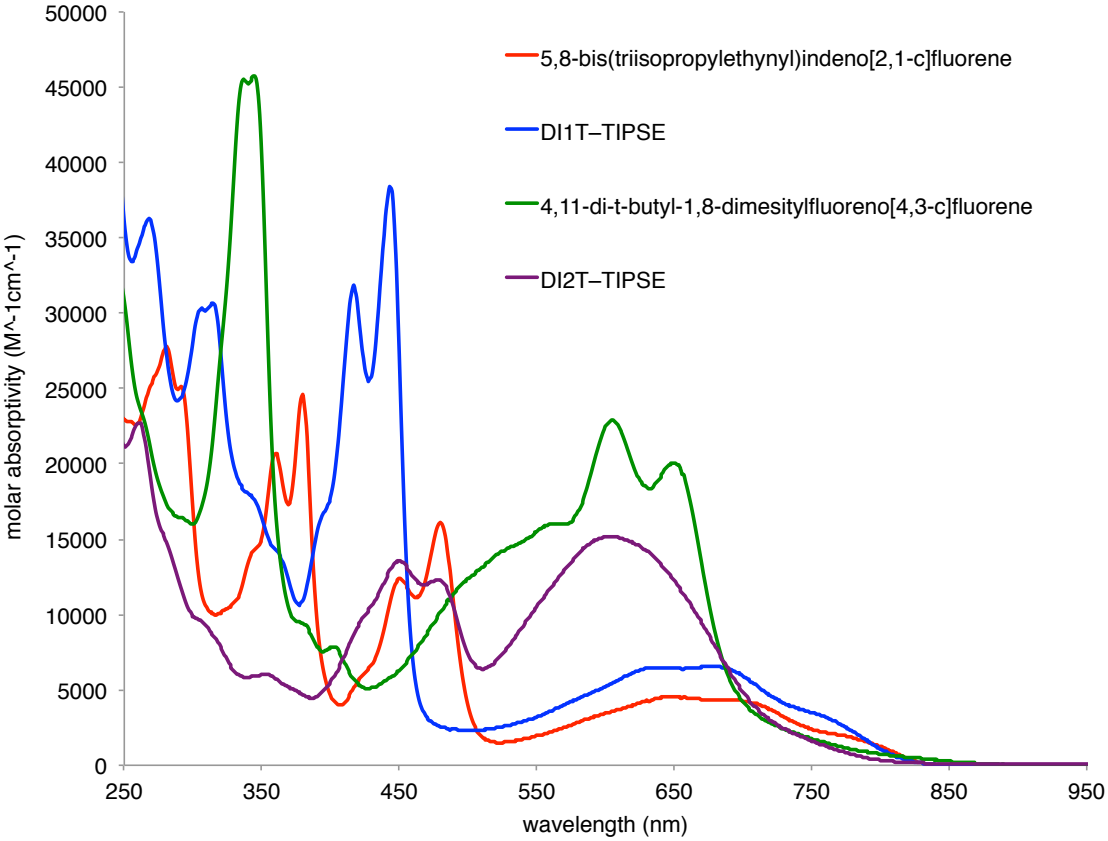

Figure A.1. Absorption spectra of **DI1T-TIPSE** and **DI2T-TIPSE** with indeno[2,1-*c*]fluorene and fluoreno[3,4-*c*]fluorene.

X-ray Crystallography

Diffraction intensities for **DI1T-TIPSE, DI2T, DI1T-TESE** and **DI3T** were collected at 100(2) and 150(2) K, respectively, on a Bruker Apex2 CCD diffractometer with a mirco-focus *IμS* source using CuKα radiation λ= 1.54178 Å. Absorption corrections were applied by SADABS.[1] Structures were solved by direct methods and Fourier techniques and refined on F^2 using full matrix least-squares procedures. All non-H atoms were refined with anisotropic thermal parameters. All H atoms were refined in calculated positions in a rigid group model. The structures of **DI2T** and **DI1T-TESE** have two symmetrically independent molecules. One of terminal –$CHMe_2$ groups in **DI3T** is disordered over two positions in ratio 42/58. X-ray

diffraction from crystals of **MH117** and **MH120** at high angles were very weak and even with a strong Incoatec *IμS* Cu source we could collected data only up to $2\theta_{max}$ = 114.98° and 120.0°, respectively. All calculations were performed by the Bruker SHELXTL (v. 6.10) package.[2]

Crystallographic data for **DI1T-TIPSE**: $C_{40}H_{50}SSi_2$, M = 619.04, 0.25 x 0.12 x 0.02 mm, T = 100 K, Triclinic, space group *P*-1, a = 8.3989(9) Å, b = 12.4017(10) Å, c = 17.7936(19) Å, α = 88.626(6)°, β = 88.890(8)°, γ = 81.912(6)°, V = 1834.2(3) Å^3, Z = 2, D_c = 1.121 Mg/m^3, μ = 1.585 mm^{-1}, F(000) = 668, $2\theta_{max}$ = 135.38°, 22289 reflections, 6439 independent reflections [R_{int} = 0.0405], R1 = 0.0395, wR2 = 0.0997 and GOF = 1.031 for 6439 reflections (388 parameters) with I>2s(I), R1 = 0.0511, wR2 = 0.1071 and GOF = 1.031 for all reflections, max/min residual electron density +0.383/–0.282 eÅ^3. CCDC 1000352.

Crystallographic data for **DI1T-TESE**: $C_{34}H_{38}SSi_2$, M = 534.88, 0.29 x 0.06 x 0.02 mm, T = 100 K, Triclinic, space group *P*-1, a = 7.0866(8) Å, b = 16.2124(19) Å, c = 26.849(3) Å, α = 85.812(10)°, β = 84.502(7)°, γ = 77.978(7)°, V = 2998.7(6) Å^3, Z = 4, Z' = 2, D_c = 1.185 Mg/m^3, μ = 1.866 mm^{-1}, F(000) = 1144, $2\theta_{max}$ = 120.0°, 24784 reflections, 8380 independent reflections [R_{int} = 0.0710], R1 = 0.1233, wR2 = 0.2892 and GOF = 1.130 for 8380 reflections (667 parameters) with I>2s(I), R1 = 0.1495, wR2 = 0.3028 and GOF = 1.130 for all reflections, max/min residual electron density +1.101/–0.687 eÅ^3. CCDC 1000354.

Crystallographic data for **DI2T**: $C_{42}H_{50}S_2Si_2$, M = 675.12, 0.17 x 0.04 x 0.02 mm, T = 100 K, Triclinic, space group *P*-1, a = 7.4177(10) Å, b = 14.5332(16) Å, c = 18.922(2) Å, α = 73.889(8)°, β = 84.135(10)°, γ = 78.229(10)°, V = 1916.2(4) Å^3, Z = 2, D_c = 1.170 Mg/m^3, μ = 2.055 mm^{-1}, F(000) = 724, $2\theta_{max}$ = 114.98°, 12023 reflections, 4765 independent reflections [R_{int} = 0.0398], R1 = 0.0530, wR2 = 0.1247 and GOF = 1.021 for 4765 reflections (415 parameters) with I>2s(I), R1 = 0.0738, wR2 = 0.1356 and GOF = 1.021 for all reflections, max/min residual electron density +0.400/–0.282 eÅ^3. CCDC 1000353.

Crystallographic data for **DI3T**: $C_{44}H_{50}S_3Si_2$, M = 731.20, 0.25 x 0.12 x 0.02 mm, T = 150 K, Triclinic, space group *P*-1, a = 7.5217(4) Å, b = 14.0563(8) Å, c = 20.3360(11) Å, α =

73.188(4)°, β = 81.718(4)°, γ = 82.685(4)°, V = 2028.36(19) Å^3, Z = 2, D_c = 1.197 Mg/m^3, μ = 2.449 mm^{-1}, F(000) = 780, 2θ_{max} = 133.82°, 24367 reflections, 6946 independent reflections [R_{int} = 0.0496], R1 = 0.0493, wR2 = 0.1232 and GOF = 1.014 for 6946 reflections (452 parameters) with I>2s(I), R1 = 0.0642, wR2 = 0.1330 and GOF = 1.026 for all reflections, max/min residual electron density +0.479/–0.559 eÅ^3. CCDC 1000355.

Crystallographic data for **9**: $C_{18}H_8SO_2$, M = 288.30, 0.16 x 0.12 x 0.08 mm, T = 100 K, orthorhombic, space group $Pca2_1$, a = 15.913(6) Å, b = 11.398(4) Å, c = 6.921(2) Å, V = 1255.4(8) Å^3, Z = 4, D_c = 1.525 Mg/m^3, μ = 0.258 mm^{-1}, F(000) = 592, 2θ_{max} = 52.0°, 5496 reflections, 2112 independent reflections [R_{int} = 0.0608], R1 = 0.0529, wR2 = 0.1001 and GOF = 1.038 for 2112 reflections (191 parameters) with I>2s(I), R1 = 0.0960, wR2 = 0.1145 and GOF = 1.038 for all reflections, the Flack parameter is 0.00(15), max/min residual electron density +0.308/–0.434 eÅ^3. CCDC 1003348. Crystallographic data for **13**: $C_{20}H_8O_2S_2$, M = 344.38, 0.18 x 0.04 x 0.02 mm, T = 100 K, monoclinic, space group $P2_1/c$, a = 12.983(4) Å, b = 3.9148(12) Å, c = 14.969(4) Å, β = 111.93(2)°, V = 705.7(4) Å^3, Z = 4, D_c = 1.621 Mg/m^3, μ = 3.500 mm^{-1}, F(000) = 352, 2θ_{max} = 135.36°, 3991 reflections, 1188 independent reflections [R_{int} = 0.0848], R1 = 0.0848, wR2 = 0.2128 and GOF = 1.034 for 1188 reflections (109 parameters) with I>2s(I), R1 = 0.1084, wR2 = 0.2292 and GOF = 1.034 for all reflections, max/min residual electron density +0.536/–0.543 eÅ^3. CCDC 1003349. These data can be obtained free of charge from The Cambridge Crystallographic Data Centre via www.ccdc.cam.ac.uk/data_request/cif.

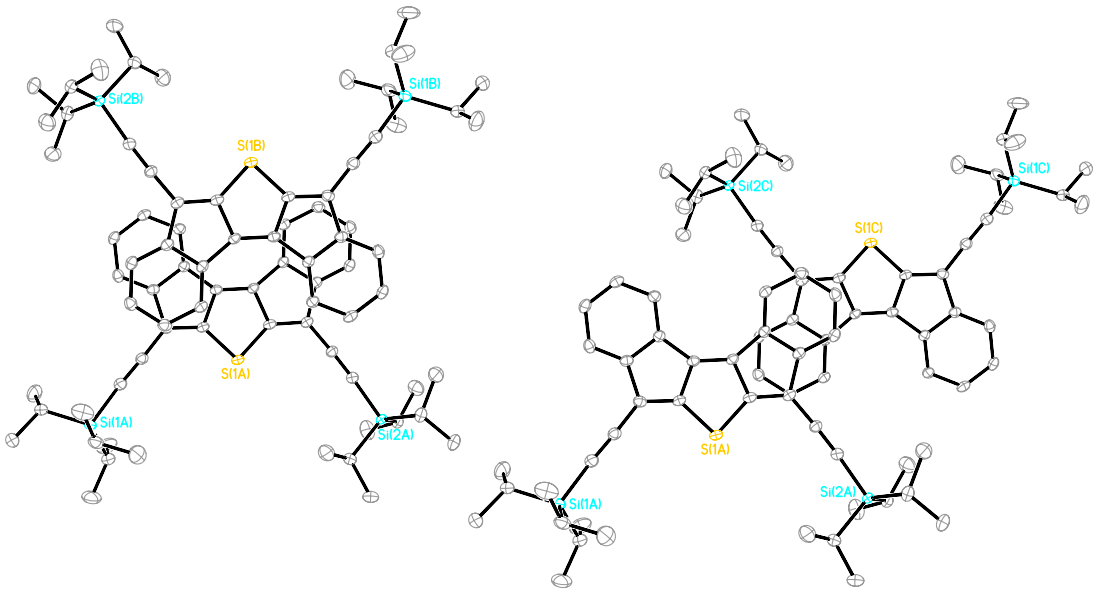

Figure A.2. Additional views of the pairwise arrangement for **DI1T-TIPSE**.

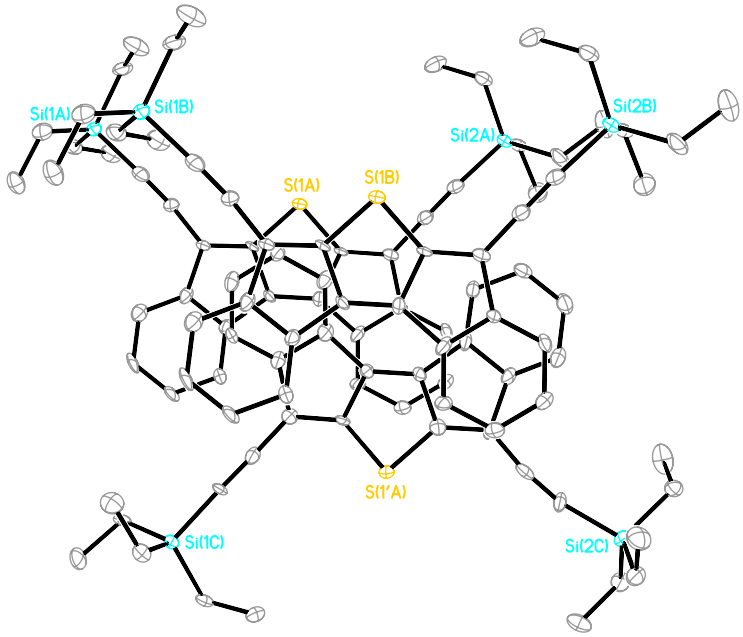

Figure A.3. Pairwise slipped stack of **DI1T-TESE**.

Cyclic Voltammetry

All electrochemical experiments were conducted in a traditional 3-electrode geometry using a Solartron 1287 potentiostat. Electrolyte solutions (0.1 M) were prepared from HPLC-grade CH_2Cl_2 and anhydrous Bu_4NBF_4, and the solutions were freeze-pump-thaw degassed (3x) prior to analysis. Cyclic voltammetry was conducted under a nitrogen atmosphere. The working electrode was a glassy carbon electrode (3-mm diameter), with a Pt-coil counter electrode and Ag wire pseudo reference. The ferrocene/ferrocenium (Fc/Fc^+) couple was used as an internal standard following each experiment. Potential values were re-referenced to SCE using a value of 0.46 (V vs. SCE) for the Fc/Fc^+ couple in CH_2Cl_2. When necessary, potentials were re-referenced to NHE using SCE = –0.24 (V vs. NHE). LUMO and HOMO levels were approximated using SCE = –4.68 eV vs. vacuum.[3] Cyclic voltammetry experiments were conducted at sweep rates of 50 (reported), 75, 100 and 125 mVs^{-1}. All scan rates show quasi-reversible kinetics with no alteration of peak splitting with scan rate. $E_{1/2}$ values were calculated assuming $E_{1/2} \approx E^{o\prime}=(E_{anodic} + E_{cathodic})/2$ based on these observations for reversible couples; for irreversible couples the $E^{o\prime}$ value is estimated as the potential at peak current. The $E_{a,c}$ peak splitting of the Fc/Fc^+ couple was similar to that of the analyte (~100 mV). The anodic peak current increases linearly with the square root of the scan rate in the range 50 to 125 mV s^{-1}, indicating a diffusion-controlled process. Analyte concentrations were ca. 1-5 mM.

Electronic Paramagnetic Resonance

An apparatus (Figure A.4) was constructed from borosilicate glass and dried in a 100 °C oven. The apparatus was then cooled to room temperature under nitrogen and approximately 0.05 mg of DI[*n*]T was collected on a melting point capillary that was open on both ends and deposited at point A. Potassium metal was added at point B and then opening C was sealed with an oxygen/natural gas torch. Vacuum was pulled (approx. 10^{-6} torr) and potassium metal was sublimed with a Bunsen burner, resulting in a metal mirror inside D. The apparatus was then

sealed at point E. Dry THF (approx. 1 mL) from a NaK still was directly distilled through the vacuum system to A and the apparatus was sealed at point F. Controlled exposure to the potassium mirror resulted in formation of DI[n]T anion, from which the EPR spectra in Figure A.5, Figure A.6 and Figure A.7 were obtained. The EPR spectra were collected on a Bruker EMX-080.

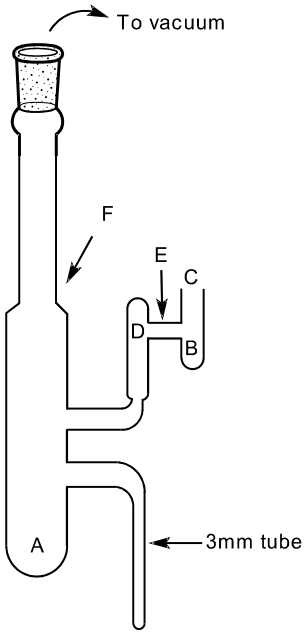

Figure A.4. Apparatus used for generation of anion radical.

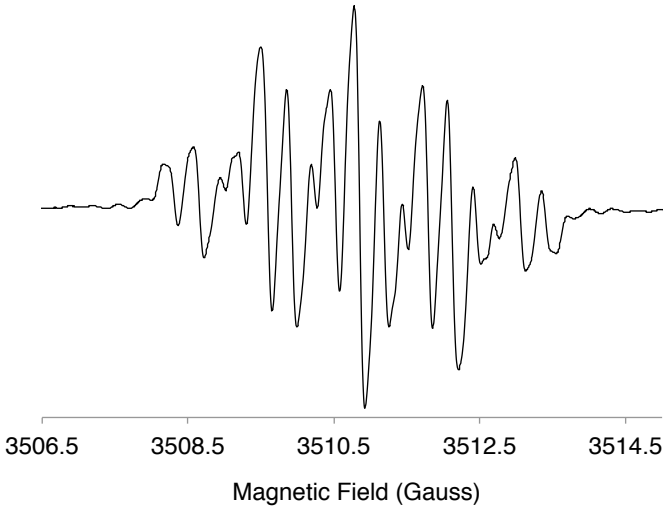

Figure A.5. EPR spectrum of **DI1T**.

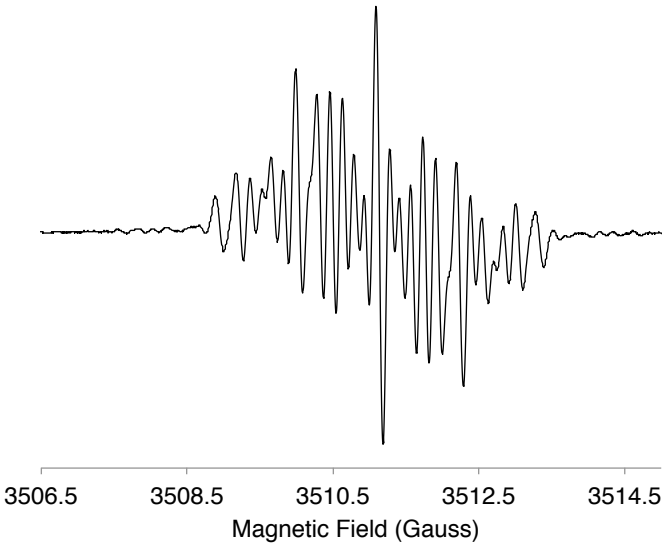

Figure A.6. EPR spectrum of **DI2T**.

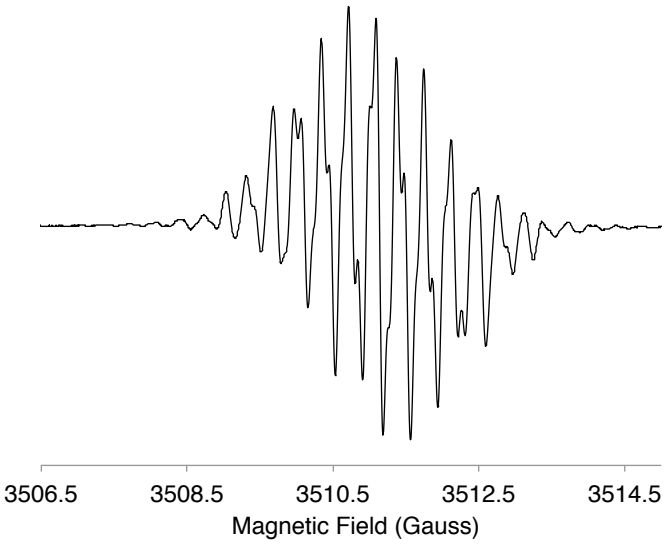

Figure A.7. EPR spectrum of **DI3T**.

EPR Computational Details

In order to determine the hyperfine coupling constants for the hydrogen and silicon nuclei coupled with the anion radical, the EPR spectra were simulated with the EasySpin[4] package utilizing MATLAB code.[5] DFT calculations were performed for the gas phase molecules using Gaussian09 Revision C.01[6] and the results were used to assign the HFCC and carbon spin density locations. These computations were carried out at the UB3W91/6-311++G(2df,2pd)//UCAM-B3LYP/6-31++G(d,p) level of theory.

Geometry Computations

DFT calculations were performed for gas phase molecules using the Gaussian09 Revision C.01.[6] Harmonic frequency analyses, performed at the same level of theory as the minimization, were used to confirm minimized structures.

Cartesian Coordinates

DI1T Neutral

UCAM-B3LYP/6-31G(d,p)

Zero-point correction=	0.448804 (Hartree/Particle)
Thermal correction to Energy=	0.481967
Thermal correction to Enthalpy=	0.482911
Thermal correction to Gibbs Free Energy=	0.379259
Sum of electronic and zero-point Energies=	-2058.703728
Sum of electronic and thermal Energies=	-2058.670565
Sum of electronic and thermal Enthalpies=	-2058.669621
Sum of electronic and thermal Free Energies=	-2058.773273

NIMAG = 0

C	1.93558	4.11556	-0.00060
C	1.82260	2.73673	0.00025
C	3.21007	4.68787	-0.00134
C	2.98224	1.92787	0.00039
C	4.24123	2.49387	-0.00043
C	4.34546	3.88761	-0.00129
H	5.12629	1.86635	-0.00056
H	5.32724	4.34978	-0.00197
H	1.05689	4.74990	-0.00074
H	3.31141	5.76782	-0.00203
C	2.58279	0.49782	0.00128
C	0.67455	1.82696	0.00094
C	1.22605	0.46961	0.00151
C	3.48230	-0.59110	0.00156
S	-0.00314	-0.78434	0.00212
C	-1.23106	0.47082	0.00153
C	-0.67827	1.82761	0.00099
C	-1.82548	2.73845	0.00041
C	-2.58779	0.50027	0.00113
C	-2.98589	1.93067	0.00049
C	-1.93713	4.11738	-0.00020
C	-4.24428	2.49795	-0.00002
C	-3.21106	4.69094	-0.00073
C	-4.34721	3.89178	-0.00064
H	-1.05782	4.75087	-0.00025
H	-3.31135	5.77098	-0.00121
H	-5.12994	1.87126	0.00010
H	-5.32855	4.35489	-0.00105
C	-3.48759	-0.5882	0.00093
C	4.26800	1.51855	0.00153
Si	5.44268	2.93551	-0.00042
C	-4.27192	-1.51704	0.00060
Si	-5.43894	-2.94056	-0.00053
C	-6.63740	-2.73204	1.43019
C	-4.44445	-4.51988	0.20022
C	-6.36728	-2.95221	-1.63294
C	4.87476	-4.17921	-1.28695

C	5.44532	-3.71522	1.70780
C	7.15304	-2.28615	-0.42501
H	-3.88452	-4.51898	1.13918
H	-3.72743	-4.64272	-0.61587
H	-5.10247	-5.39445	0.20288
H	-6.11060	-2.70409	2.38770
H	-7.34853	-3.56343	1.46294
H	-7.21065	-1.80570	1.33711
H	3.86916	-4.54664	-1.06559
H	5.54809	-5.04165	-1.31499
H	4.85564	-3.73611	-2.28617
H	4.45105	-4.08030	1.97859
H	5.75677	-2.99762	2.47150
H	6.13549	-4.56399	1.74364
H	7.16412	-1.81134	-1.40976
H	7.88358	-3.10100	-0.43824
H	7.49054	-1.54744	0.30704
H	-6.93524	-2.02873	-1.77418
H	-7.07292	-3.78810	-1.67030
H	-5.68142	-3.05482	-2.47804

DI1T Anion

UCAM-B3LYP/6-31++G(d,p)

Zero-point correction=	0.444806 (Hartree/Particle)
Thermal correction to Energy=	0.478102
Thermal correction to Enthalpy=	0.479046
Thermal correction to Gibbs Free Energy=	0.375054
Sum of electronic and zero-point Energies=	-2058.828161
Sum of electronic and thermal Energies=	-2058.794866
Sum of electronic and thermal Enthalpies=	-2058.793921
Sum of electronic and thermal Free Energies=	-2058.897913

NIMAG = 0

C	1.94799	4.11942	0.00310
C	1.83308	2.73021	0.00100
C	3.21242	4.70462	0.00361
C	3.01300	1.92490	-0.00045
C	4.27089	2.52068	-0.00017
C	4.36507	3.91079	0.00198
H	5.16532	1.90406	-0.00199
H	5.34346	4.38340	0.00221
H	1.06232	4.74584	0.00427
H	3.30306	5.78712	0.00523
C	2.62682	0.51601	-0.00248
C	0.70015	1.82703	-0.00023
C	1.23578	0.50367	-0.00224
C	3.50917	-0.57731	-0.00251
S	0.00000	-0.74381	-0.00407
C	-1.23578	0.50367	-0.00223
C	-0.70015	1.82703	-0.00023
C	-1.83308	2.73021	0.00101

C	-2.62682	0.51601	-0.00246
C	-3.01300	1.92490	-0.00043
C	-1.94799	4.11942	0.00311
C	-4.27088	2.52067	-0.00015
C	-3.21241	4.70462	0.00363
C	-4.36507	3.91079	0.00201
H	-1.06232	4.74584	0.00428
H	-3.30306	5.78711	0.00525
H	-5.16532	1.90406	-0.00196
H	-5.34345	4.38340	0.00224
C	-3.50917	-0.57731	-0.00250
C	4.28847	-1.52013	-0.00336
Si	5.42442	-2.93673	0.00093
C	-4.28847	-1.52012	-0.00335
Si	-5.42442	-2.93673	0.00093
C	-5.70944	-3.54927	1.76173
C	-4.69630	-4.34160	-1.02205
C	-7.08060	-2.42031	-0.73782
C	4.69622	-4.34167	-1.02191
C	5.70953	-3.54918	1.76176
C	7.08056	-2.42037	-0.73794
H	-3.72561	-4.65081	-0.62244
H	-4.54105	-4.02936	-2.05921
H	-5.35811	-5.21507	-1.02284
H	-4.76626	-3.85770	2.22313
H	-6.39345	-4.40553	1.77888
H	-6.13788	-2.75819	2.38493
H	3.72557	-4.65085	-0.62221
H	5.35804	-5.21514	-1.02270
H	4.54089	-4.02948	-2.05908
H	4.76637	-3.85757	2.22323
H	6.13802	-2.75806	2.38489
H	6.39354	-4.40544	1.77892
H	6.95664	-2.07507	-1.76888
H	7.78968	-3.25584	-0.74047
H	7.52492	-1.60041	-0.16514
H	-7.52495	-1.60041	-0.16493
H	-7.78971	-3.25579	-0.74040
H	-6.95674	-2.07492	-1.76874

DI1T Dianion

UCAM-B3LYP/6-31++G(d,p)

Zero-point correction=	0.442213 (Hartree/Particle)
Thermal correction to Energy=	0.475713
Thermal correction to Enthalpy=	0.476657
Thermal correction to Gibbs Free Energy=	0.372411
Sum of electronic and zero-point Energies=	-2058.797119
Sum of electronic and thermal Energies=	-2058.763620
Sum of electronic and thermal Enthalpies=	-2058.762676
Sum of electronic and thermal Free Energies=	-2058.866921

NIMAG = 0

C	-1.96138	4.10054	0.01211
C	-1.84371	2.70439	0.00652
C	-3.21726	4.69851	0.01847
C	-3.04402	1.90052	0.00746
C	-4.29859	2.52313	0.01394
C	-4.38387	3.91054	0.01938
H	-5.20058	1.91486	0.01461
H	-5.36013	4.39176	0.02441
H	-1.06942	4.72052	0.01145
H	-3.29776	5.78361	0.02274
C	-2.67242	0.50957	0.00102
C	-0.72161	1.80756	-0.00055
C	-1.24168	0.51219	-0.00370
C	-3.54520	-0.57112	-0.00026
S	0.00252	-0.72847	-0.01276
C	1.24609	0.51285	-0.01205
C	0.72540	1.80793	-0.00535
C	1.84709	2.70530	-0.00535
C	2.67682	0.51087	-0.01663
C	3.04781	1.90205	-0.01225
C	1.96399	4.10152	-0.00014
C	4.30196	2.52549	-0.01386
C	3.21951	4.70024	-0.00180
C	4.38655	3.91291	-0.00865
H	1.07167	4.72096	0.00517
H	3.29943	5.78537	0.00220
H	5.20432	1.91777	-0.01967
H	5.36254	4.39469	-0.01005
C	3.54968	-0.56971	-0.02105
C	-4.33915	-1.51613	-0.00131
Si	-5.47090	-2.89818	-0.00313
C	4.34126	-1.51671	-0.02839
Si	5.46945	-2.90140	0.00762
C	6.97412	-2.59983	-1.10675
C	4.61708	-4.48486	-0.58232
C	6.15385	-3.25367	1.74296
C	-5.25356	-4.01577	1.51347
C	-5.25297	-4.01171	-1.52255
C	-7.26553	-2.28942	-0.00239
H	4.26668	-4.37379	-1.61323
H	3.74198	-4.70303	0.03801
H	5.29410	-5.34677	-0.53729
H	6.66070	-2.46141	-2.14636
H	7.68083	-3.43812	-1.06633
H	7.50346	-1.69155	-0.80001
H	-4.22906	-4.39879	1.56319
H	-5.93945	-4.87200	1.48701
H	-5.43698	-3.45376	2.43487
H	-4.22832	-4.39419	-1.57322
H	-5.43653	-3.44738	-2.44250

H	-5.93853	-4.86825	-1.49835
H	-7.46419	-1.67427	0.88113
H	-7.97161	-3.12884	-0.00306
H	-7.46436	-1.67267	-0.88475
H	6.68105	-2.37674	2.13321
H	6.85063	-4.10176	1.74123
H	5.33797	-3.47963	2.43715

DI2T Neutral

UCAM-B3LYP/6-31G(d,p)

Zero-point correction=	0.463062 (Hartree/Particle)
Thermal correction to Energy=	0.498623
Thermal correction to Enthalpy=	0.499567
Thermal correction to Gibbs Free Energy=	0.389852
Sum of electronic and zero-point Energies=	-2533.040684
Sum of electronic and thermal Energies=	-2533.005123
Sum of electronic and thermal Enthalpies=	-2533.004179
Sum of electronic and thermal Free Energies=	-2533.113894

NIMAG = 0

C	4.07561	3.49564	-0.11229
C	3.20184	2.42553	-0.07788
C	1.80398	2.63860	-0.08716
C	1.28393	3.92068	-0.13100
C	1.18186	1.32102	-0.04381
C	2.17037	4.99840	-0.16571
H	0.21176	4.08979	-0.13835
C	3.54523	4.78691	-0.15638
H	1.78196	6.01058	-0.20021
H	4.21720	5.63849	-0.18375
H	5.14807	3.33146	-0.10499
C	3.47382	0.96806	-0.02864
C	2.26383	0.34784	-0.00955
C	4.75780	0.38065	-0.00730
S	1.69141	-1.31324	0.04584
C	0.03465	-0.72812	0.02395
C	-0.03348	0.73074	-0.02549
S	-1.69023	1.31584	-0.04716
C	-2.26267	-0.34524	0.00830
C	-1.18069	-1.31841	0.04249
C	-1.80276	-2.63600	0.08627
C	-3.20062	-2.42295	0.07732
C	-1.28270	-3.91807	0.13045
C	-3.47262	-0.96550	0.02768
C	-4.07444	-3.49300	0.11253
C	-4.75682	-0.37858	0.00620
C	-2.16916	-4.99576	0.16585
H	-0.21054	-4.08720	0.13761
C	-3.54403	-4.78425	0.15694
H	-5.14691	-3.32878	0.10588
H	-1.78075	-6.00792	0.20066

H	-4.21599	-5.63582	0.18502
C	5.86787	-0.11460	0.01072
Si	7.54086	-0.88138	0.03869
C	7.35853	-2.68171	0.53848
C	8.59984	0.04180	1.28481
C	8.28952	-0.75030	-1.67858
H	7.67699	-1.27178	-2.41887
H	9.29024	-1.19324	-1.69931
H	8.37893	0.29253	-1.99449
H	8.16859	-0.01122	2.28800
H	8.69798	1.09772	1.01872
H	9.60609	-0.38647	1.32941
H	6.90672	-2.77443	1.52967
H	8.33457	-3.17600	0.56758
H	6.72821	-3.22759	-0.16863
C	-5.86751	0.11525	-0.01154
Si	-7.54251	0.87760	-0.03825
C	-7.47622	2.49142	0.91892
C	-8.75046	-0.31375	0.76682
C	-8.02979	1.19393	-1.82393
H	-7.17916	2.32397	1.95761
H	-8.45629	2.97862	0.92488
H	-6.75957	3.18732	0.47460
H	-7.32683	1.87389	-2.31248
H	-9.02566	1.64477	-1.87897
H	-8.05049	0.26505	-2.40012
H	-8.46854	-0.52677	1.80141
H	-8.78962	-1.26437	0.22808
H	-9.76070	0.10721	0.77492

DI2T Anion

UCAM-B3LYP/6-31++G(d,p)

Zero-point correction=	0.459072 (Hartree/Particle)
Thermal correction to Energy=	0.494818
Thermal correction to Enthalpy=	0.495763
Thermal correction to Gibbs Free Energy=	0.385295
Sum of electronic and zero-point Energies=	-2533.175198
Sum of electronic and thermal Energies=	-2533.139451
Sum of electronic and thermal Enthalpies=	-2533.138507
Sum of electronic and thermal Free Energies=	-2533.248975

NIMAG = 0

C	-4.21159	-3.38926	-0.00394
C	-3.31638	-2.32209	-0.00479
C	-1.91111	-2.57068	-0.00592
C	-1.42996	-3.87850	-0.00620
C	-1.25784	-1.28240	-0.00644
C	-2.33681	-4.93529	-0.00538
H	-0.36109	-4.07301	-0.00706
C	-3.71594	-4.69068	-0.00424
H	-1.97135	-5.95801	-0.00561

H	-4.40836	-5.52791	-0.00363
H	-5.28185	-3.20355	-0.00314
C	-3.54674	-0.87917	-0.00471
C	-2.28392	-0.29342	-0.00581
C	-4.80016	-0.24338	-0.00226
S	-1.64880	1.34103	-0.00591
C	-0.00921	0.70770	-0.00633
C	0.00920	-0.70771	-0.00660
S	1.64880	-1.34104	-0.00635
C	2.28391	0.29341	-0.00559
C	1.25784	1.28239	-0.00590
C	1.91111	2.57067	-0.00485
C	3.31637	2.32209	-0.00376
C	1.42996	3.87849	-0.00465
C	3.54674	0.87917	-0.00422
C	4.21158	3.38925	-0.00246
C	4.80016	0.24338	-0.00195
C	2.33681	4.93528	-0.00339
H	0.36108	4.07300	-0.00549
C	3.71593	4.69067	-0.00229
H	5.28184	3.20354	-0.00169
H	1.97134	5.95800	-0.00325
H	4.40835	5.52790	-0.00132
C	-5.89532	0.30046	0.00009
Si	-7.51188	1.13178	0.00846
C	-7.25687	2.99101	-0.14876
C	-8.42389	0.76311	1.61691
C	-8.55965	0.52167	-1.43529
H	-8.06651	0.73011	-2.38961
H	-9.54154	1.00827	-1.44483
H	-8.71772	-0.55963	-1.37436
H	-7.84865	1.11356	2.47929
H	-8.57984	-0.31324	1.73958
H	-9.40395	1.25313	1.63854
H	-6.65148	3.37340	0.67866
H	-8.21506	3.52251	-0.14385
H	-6.73625	3.23630	-1.07939
C	5.89532	-0.30046	0.00024
Si	7.51189	-1.13177	0.00841
C	7.25690	-2.99096	-0.14934
C	8.42385	-0.76353	1.61699
C	8.55969	-0.52124	-1.43514
H	6.65151	-3.37359	0.67796
H	8.21510	-3.52244	-0.14457
H	6.73630	-3.23599	-1.08004
H	8.06659	-0.72942	-2.38953
H	9.54159	-1.00782	-1.44479
H	8.71774	0.56005	-1.37391
H	7.84860	-1.11425	2.47925
H	8.57977	0.31278	1.73998
H	9.40393	-1.25353	1.63850

DI2T Dianion

UCAM-B3LYP/6-31++G(d,p)

Zero-point correction=	0.456790 (Hartree/Particle)
Thermal correction to Energy=	0.492717
Thermal correction to Enthalpy=	0.493661
Thermal correction to Gibbs Free Energy=	0.383872
Sum of electronic and zero-point Energies=	-2533.159282
Sum of electronic and thermal Energies=	-2533.123355
Sum of electronic and thermal Enthalpies=	-2533.122411
Sum of electronic and thermal Free Energies=	-2533.232201

NIMAG = 0

C	4.26785	3.38184	-0.01673
C	3.37813	2.29933	-0.01833
C	1.95863	2.55021	-0.02045
C	1.48655	3.86803	-0.02107
C	1.30352	1.27556	-0.02133
C	2.38848	4.92602	-0.01961
H	0.41642	4.06204	-0.02268
C	3.77505	4.68087	-0.01742
H	2.02113	5.94968	-0.02012
H	4.46863	5.51933	-0.01630
H	5.33993	3.19867	-0.01518
C	3.60419	0.87589	-0.01804
C	2.29996	0.29414	-0.02008
C	4.84110	0.23817	-0.01184
S	1.64345	-1.33004	-0.02079
C	0.00295	-0.68926	-0.02210
C	-0.00294	0.68926	-0.02217
S	-1.64345	1.33004	-0.02095
C	-2.29996	-0.29414	-0.02011
C	-1.30351	-1.27556	-0.02123
C	-1.95863	-2.55021	-0.02025
C	-3.37813	-2.29933	-0.01817
C	-1.48654	-3.86802	-0.02073
C	-3.60418	-0.87588	-0.01803
C	-4.26785	-3.38184	-0.01648
C	-4.84110	-0.23817	-0.01190
C	-2.38847	-4.92601	-0.01917
H	-0.41641	-4.06203	-0.02230
C	-3.77505	-4.68087	-0.01703
H	-5.33993	-3.19866	-0.01496
H	-2.02113	-5.94967	-0.01958
H	-4.46863	-5.51933	-0.01583
C	5.94404	-0.31148	-0.00690
Si	7.53776	-1.12707	0.03143
C	7.33030	-2.99939	-0.12974
C	8.47601	-0.78915	1.64397
C	8.66210	-0.54360	-1.37868
H	8.20645	-0.76314	-2.34944

H	9.64427	-1.03093	-1.33945
H	8.81583	0.53934	-1.32618
H	7.90266	-1.14967	2.50394
H	8.63034	0.28624	1.78130
H	9.45725	-1.28012	1.65278
H	6.70855	-3.39030	0.68175
H	8.29894	-3.51276	-0.09911
H	6.83564	-3.25378	-1.07230
C	-5.94404	0.31148	-0.00703
Si	-7.53776	1.12706	0.03139
C	-7.33050	2.99918	-0.13247
C	-8.47485	0.79134	1.64505
C	-8.66307	0.54160	-1.37712
H	-6.70809	3.39120	0.67798
H	-8.29912	3.51256	-0.10172
H	-6.83662	3.25232	-1.07578
H	-8.20817	0.75989	-2.34851
H	-9.64526	1.02889	-1.33780
H	-8.81666	-0.54128	-1.32306
H	-7.90087	1.15302	2.50412
H	-8.62909	-0.28386	1.78395
H	-9.45608	1.28234	1.65392

DI3T Neutral

UCAM-B3LYP/6-31G(d,p)

Zero-point correction=	0.476970 (Hartree/Particle)
Thermal correction to Energy=	0.515018
Thermal correction to Enthalpy=	0.515962
Thermal correction to Gibbs Free Energy=	0.400435
Sum of electronic and zero-point Energies=	-3007.373585
Sum of electronic and thermal Energies=	-3007.335538
Sum of electronic and thermal Enthalpies=	-3007.334594
Sum of electronic and thermal Free Energies=	-3007.450121

NIMAG = 0

C	-6.14426	-2.29908	0.00174
C	-4.89363	-1.70945	0.00162
C	-6.22368	-3.69286	0.00177
C	-5.07472	-4.47804	0.00164
C	-3.72473	-2.50607	0.00140
C	-3.81027	-3.88826	0.00143
C	-4.51073	-0.27776	0.00156
C	-2.59609	-1.58565	0.00107
C	-3.15007	-0.24067	0.00119
C	-5.41514	0.80620	0.00162
S	-1.91719	1.01190	0.00067
C	-1.24379	-1.57253	0.00053
C	-0.67621	-0.23443	0.00028
C	0.67622	-0.23443	-0.00029
C	1.24379	-1.57254	-0.00054
S	0.00000	-2.81411	-0.00001

C	2.59609	-1.58565	-0.00107
C	3.15007	-0.24068	-0.00120
S	1.91720	1.01190	-0.00068
C	3.72473	-2.50607	-0.00140
C	4.89364	-1.70946	-0.00161
C	4.51073	-0.27776	-0.00155
C	5.41514	0.80619	-0.00161
H	-2.91685	-4.50493	0.00128
H	-5.16182	-5.55922	0.00167
H	-7.04067	-1.68783	0.00168
H	-7.19764	-4.17128	0.00184
C	3.81027	-3.88826	-0.00143
C	5.07472	-4.47804	-0.00164
C	6.22368	-3.69287	-0.00175
C	6.14426	-2.29909	-0.00172
H	2.91685	-4.50494	-0.00128
H	5.16182	-5.55922	-0.00166
H	7.19764	-4.17128	-0.00182
H	7.04067	-1.68784	-0.00166
C	6.20350	1.73175	-0.00134
Si	7.38808	3.13985	0.00115
C	-6.20350	1.73175	0.00136
Si	-7.38810	3.13984	-0.00115
C	6.82671	4.39115	1.28349
C	7.40236	3.91793	-1.70792
C	9.09226	2.47852	0.43185
C	-7.40305	3.91739	1.70815
C	-9.09209	2.47863	-0.43275
C	-6.82621	4.39155	-1.28286
H	9.09687	2.00532	1.41742
H	9.82886	3.28788	0.44578
H	9.42627	1.73598	-0.29790
H	5.82513	4.76729	1.05846
H	7.50744	5.24775	1.31167
H	6.80089	3.95047	2.28363
H	8.09990	4.76071	-1.74261
H	6.41219	4.29148	-1.98226
H	7.70993	3.19690	-2.46996
H	-5.82470	4.76758	-1.05732
H	-7.50689	5.24820	-1.31099
H	-6.80003	3.95123	-2.28315
H	-7.71084	3.19612	2.46988
H	-8.10064	4.76013	1.74286
H	-6.41299	4.29091	1.98296
H	-9.42642	1.73590	0.29667
H	-9.09626	2.00567	-1.41844
H	-9.82868	3.28799	-0.44680

DI3T Anion

UCAM-B3LYP/6-31++G(d,p)

Zero-point correction= 0.473045 (Hartree/Particle)

Thermal correction to Energy=	0.511285
Thermal correction to Enthalpy=	0.512229
Thermal correction to Gibbs Free Energy=	0.396153
Sum of electronic and zero-point Energies=	-3007.518003
Sum of electronic and thermal Energies=	-3007.479764
Sum of electronic and thermal Enthalpies=	-3007.478820
Sum of electronic and thermal Free Energies=	-3007.594896

NIMAG = 0

C	6.18998	-2.32068	0.00125
C	4.93936	-1.70687	0.00111
C	6.26311	-3.71100	0.00113
C	5.10098	-4.49305	0.00088
C	3.75533	-2.50307	0.00084
C	3.84434	-3.89396	0.00074
C	4.56729	-0.29403	0.00106
C	2.63834	-1.58870	0.00071
C	3.17681	-0.26837	0.00089
C	5.45642	0.79531	0.00115
S	1.93882	0.97404	0.00072
C	1.24775	-1.57160	0.00044
C	0.69588	-0.26928	0.00049
C	-0.69229	-0.26898	0.00021
C	-1.24477	-1.57104	-0.00018
S	0.00121	-2.80299	-0.00006
C	-2.63538	-1.58750	-0.00052
C	-3.17328	-0.26694	-0.00026
S	-1.93469	0.97487	0.00027
C	-3.75276	-2.50143	-0.00104
C	-4.93643	-1.70473	-0.00104
C	-4.56377	-0.29204	-0.00052
C	-5.45289	0.79728	-0.00016
H	2.94626	-4.50545	0.00053
H	5.18084	-5.57607	0.00078
H	7.09342	-1.71772	0.00131
H	7.23494	-4.19651	0.00120
C	-3.84241	-3.89226	-0.00154
C	-5.09936	-4.49073	-0.00204
C	-6.26113	-3.70815	-0.00203
C	-6.18740	-2.31784	-0.00153
H	-2.94463	-4.50419	-0.00156
H	-5.17972	-5.57372	-0.00244
H	-7.23318	-4.19321	-0.00243
H	-7.09058	-1.71446	-0.00153
C	-6.23505	1.73653	0.00022
Si	-7.38483	3.14656	0.00125
C	6.23663	1.73618	0.00086
Si	7.38182	3.15018	-0.00096
C	-7.10643	4.20854	-1.52998
C	-7.11081	4.20277	1.53725
C	-9.15536	2.50131	-0.00245

C	8.59216	2.99190	-1.43703
C	8.35441	3.19731	1.61291
C	6.39797	4.74511	-0.18300
H	-9.34573	1.88620	-0.88730
H	-9.87491	3.32761	-0.00199
H	-9.34825	1.88303	0.87963
H	-6.07977	4.58606	-1.56149
H	-7.78528	5.06869	-1.54290
H	-7.27297	3.62882	-2.44297
H	-6.08427	4.58025	1.57305
H	-7.27980	3.61954	2.44756
H	-7.78979	5.06278	1.55160
H	5.82900	4.74885	-1.11761
H	7.05952	5.61851	-0.18338
H	5.68434	4.85983	0.63850
H	9.17031	2.06575	-1.36058
H	9.29665	3.83109	-1.45523
H	8.06123	2.97196	-2.39359
H	8.92847	2.27570	1.75039
H	7.68187	3.29827	2.47015
H	9.05536	4.03957	1.62828

DI3T Dianion

UCAM-B3LYP/6-31++G(d,p)

Zero-point correction=	0.471050 (Hartree/Particle)
Thermal correction to Energy=	0.509493
Thermal correction to Enthalpy=	0.510437
Thermal correction to Gibbs Free Energy=	0.394727
Sum of electronic and zero-point Energies=	-3007.516246
Sum of electronic and thermal Energies=	-3007.477803
Sum of electronic and thermal Enthalpies=	-3007.476858
Sum of electronic and thermal Free Energies=	-3007.592569

NIMAG = 0

C	6.23630	2.32246	-0.00002
C	4.98782	1.68616	-0.00002
C	6.30279	3.70966	-0.00001
C	5.12980	4.48844	-0.00001
C	3.78808	2.48293	-0.00002
C	3.88060	3.87977	-0.00001
C	4.62741	0.29019	-0.00003
C	2.68036	1.57474	-0.00002
C	3.20379	0.27583	-0.00003
C	5.50715	-0.79130	-0.00002
S	1.95893	-0.95867	-0.00003
C	1.25122	1.55585	-0.00002
C	0.71212	0.28281	-0.00003
C	-0.71215	0.28281	-0.00002
C	-1.25125	1.55585	-0.00001

S	-0.00001	2.78121	-0.00001
C	-2.68039	1.57475	-0.00001
C	-3.20383	0.27585	-0.00002
S	-1.95897	-0.95866	-0.00003
C	-3.78810	2.48295	0.00002
C	-4.98785	1.68618	0.00002
C	-4.62745	0.29021	-0.00000
C	-5.50719	-0.79127	-0.00001
H	2.97771	4.48603	-0.00001
H	5.20237	5.57337	-0.00001
H	7.14565	1.72614	-0.00002
H	7.27315	4.20151	-0.00001
C	-3.88062	3.87979	0.00003
C	-5.12982	4.48847	0.00005
C	-6.30281	3.70969	0.00005
C	-6.23632	2.32249	0.00004
H	-2.97773	4.48604	0.00003
H	-5.20238	5.57339	0.00006
H	-7.27316	4.20154	0.00007
H	-7.14568	1.72617	0.00004
C	-6.29781	-1.73430	-0.00001
Si	-7.43862	-3.11928	-0.00000
C	6.29778	-1.73432	-0.00002
Si	7.43866	-3.11923	0.00003
C	-7.21031	-4.22179	1.52162
C	-7.21154	-4.22085	-1.52249
C	-9.22451	-2.49378	0.00088
C	7.21083	-4.22142	1.52195
C	9.22451	-2.49359	0.00035
C	7.21131	-4.22115	-1.52216
H	-9.41826	-1.87689	0.88414
H	-9.93767	-3.32673	0.00097
H	-9.41899	-1.87645	-0.88191
H	-6.18709	-4.60834	1.56708
H	-7.89854	-5.07579	1.50656
H	-7.38621	-3.65321	2.44028
H	-7.89976	-5.07487	-1.50742
H	-6.18836	-4.60736	-1.56903
H	-7.38819	-3.65170	-2.44065
H	6.18813	-4.60771	-1.56841
H	7.89956	-5.07514	-1.50703
H	7.38775	-3.65221	-2.44050
H	7.38699	-3.65264	2.44044
H	7.89908	-5.07541	1.50688
H	6.18764	-4.60799	1.56781
H	9.41844	-1.87654	0.88345
H	9.41871	-1.87640	-0.88259
H	9.93774	-3.32649	0.00040

Table A.1. Bond distances (Å) for **DI1T-TMSE**

bond #	neutral	radical anion	dianion
1	1.3570	1.3910	1.4310
2	1.4560	1.4280	1.3960
3	1.3530	1.4000	1.4470

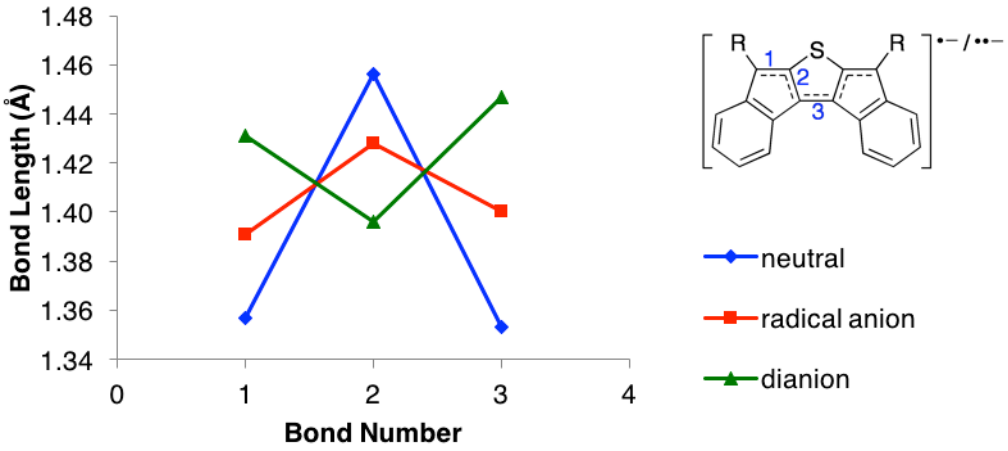

Figure A.8. Calculated bond distances upon reduction of **DI1T**, R = TMSE.

Table A.2. Bond distances (Å) for **DI2T-TMSE**

bond #	neutral	radical anion	dianion
1	1.3819	1.393	1.401
2	1.3966	1.393	1.389
3	1.391	1.401	1.408
4	1.396	1.393	1.39
5	1.384	1.394	1.4
6	1.414	1.427	1.442
7	1.483	1.461	1.441
8	1.36	1.392	1.428
9	1.456	1.425	1.399
10	1.458	1.444	1.433
11	1.351	1.391	1.432
12	1.461	1.416	1.379

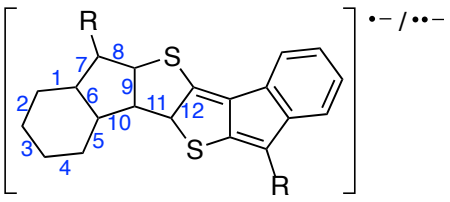

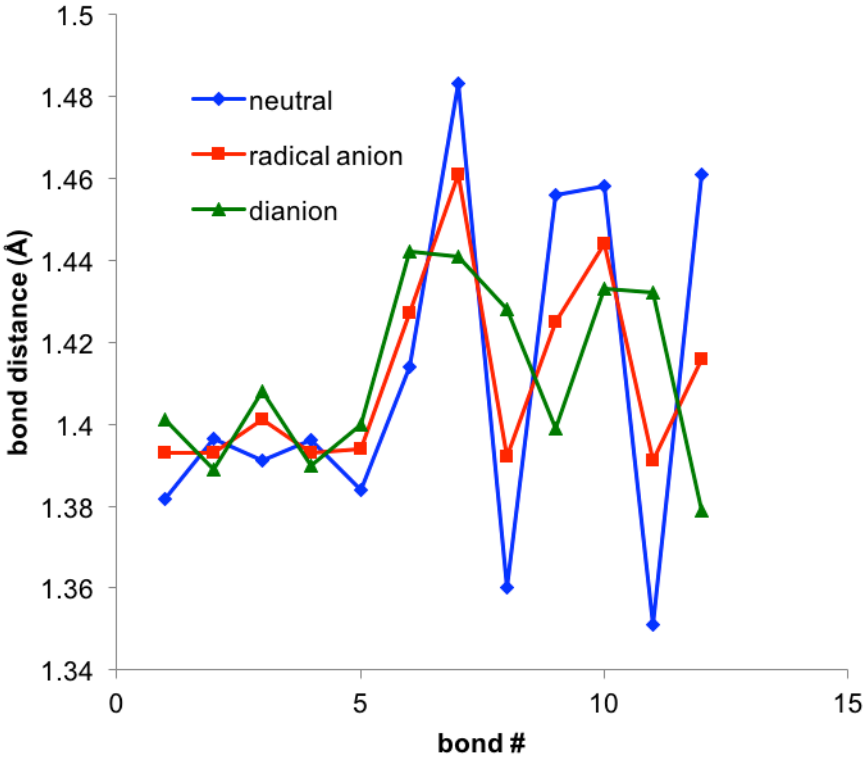

Figure A.9. Calculated bond distances upon reduction of **DI2T**, R = TMSE.

Table A.3. Bond distances (Å) for **DI3T-TMSE**

bond #	neutral	radical anion	dianion
1	1.361	1.391	1.424
2	1.455	1.4260	1.400
3	1.352	1.3910	1.429
4	1.454	1.414	1.382
5	1.352	1.388	1.424

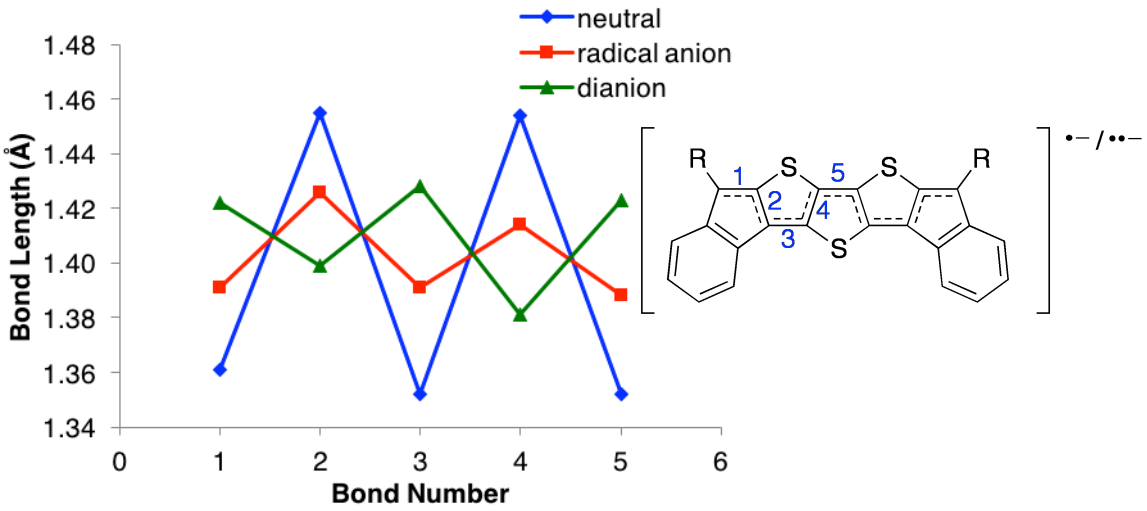

Figure A.10. Calculated bond distances upon reduction of **DI3T**, R = TMSE.

APPENDIX B

Stability studies of DIAn

Quartz cuvette exposed to ambient light

A single crystal of **DIAn** was dissolved in HPLC grade CH_2Cl_2 open to atmosphere. The cuvette was sealed with a Teflon cap and kept on the bench top.

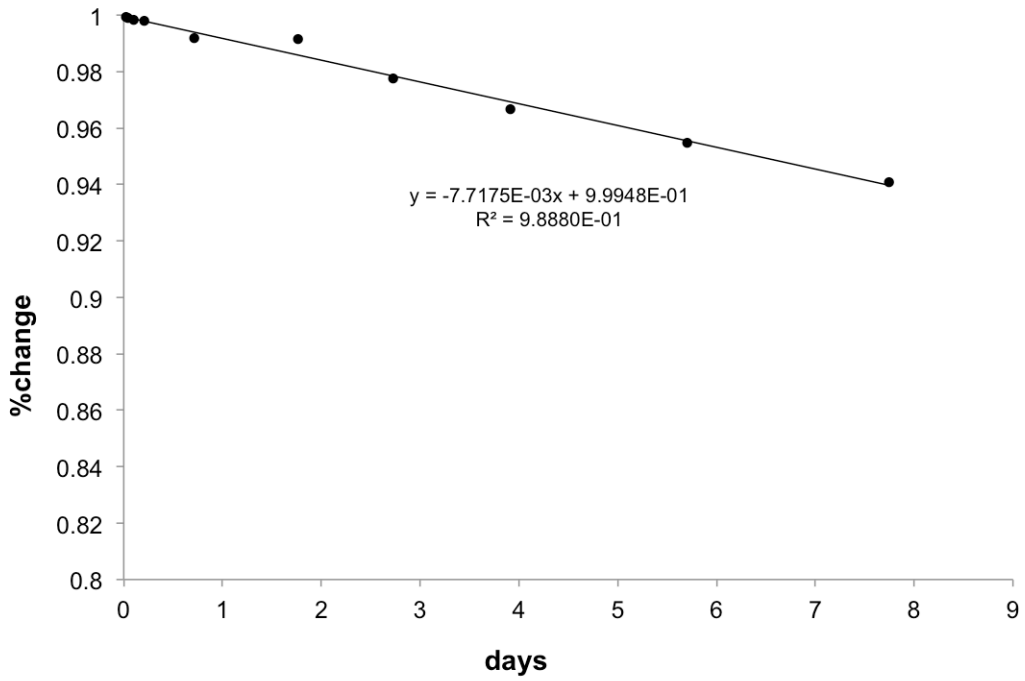

Figure B.1. Ambient light stability test of DIAn. Linear regression and extrapolation to % change = 0.50 gives a half-life of 64 days.

NMR experiment under oxygen

To a J-young tube was added approx. 10 mg **DIAn**, approx. 5 mg 1,3,5-trimethoxybenzene as an internal standard and 0.6 ml $CDCl_3$. The solution was degassed by repeated freeze-pump-thaw cycles. The cap was removed and two balloons of oxygen were sparged through the solution. The tube was resealed and shaken vigorously.

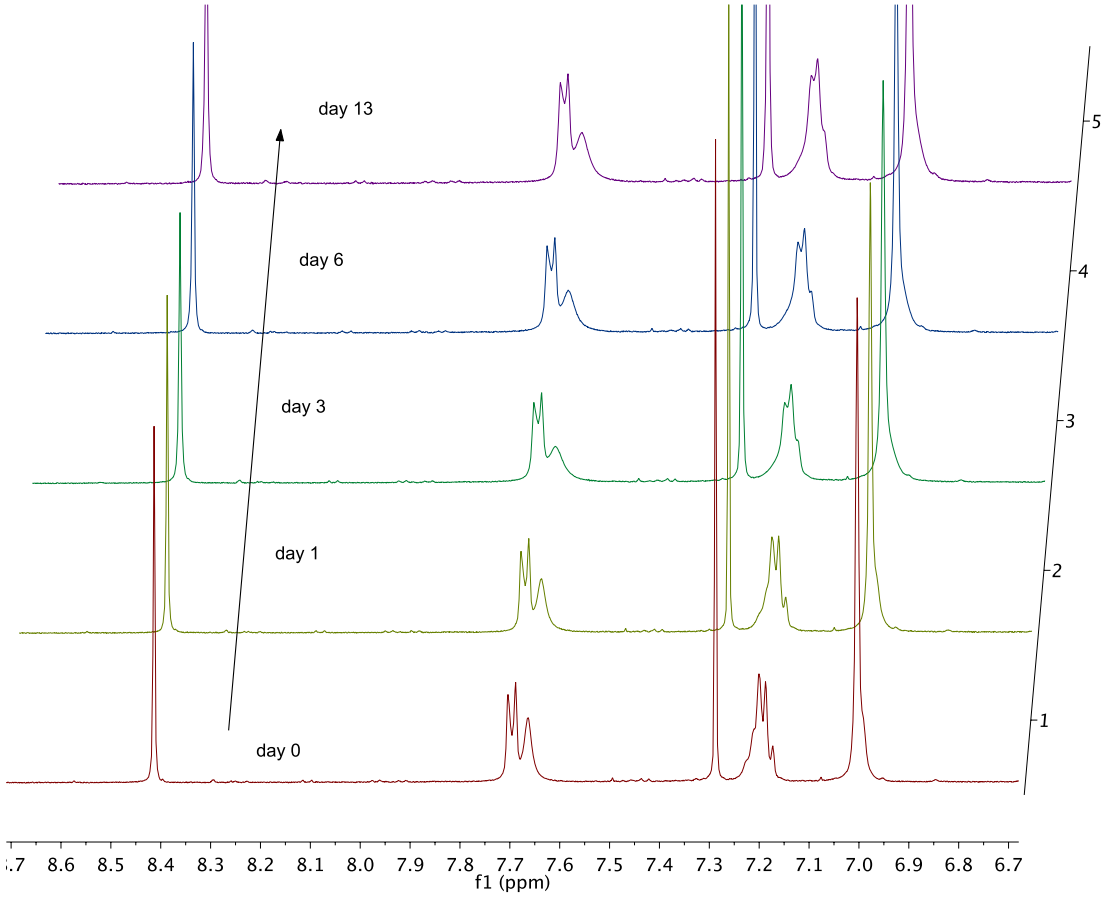

Figure B.2. NMR experiment under oxygen atmosphere. Broadening of the **DIAn** aromatic resonances is observed after 13 days. Integration to the internal standard shows no decomposition.

Thermogravimetric analysis

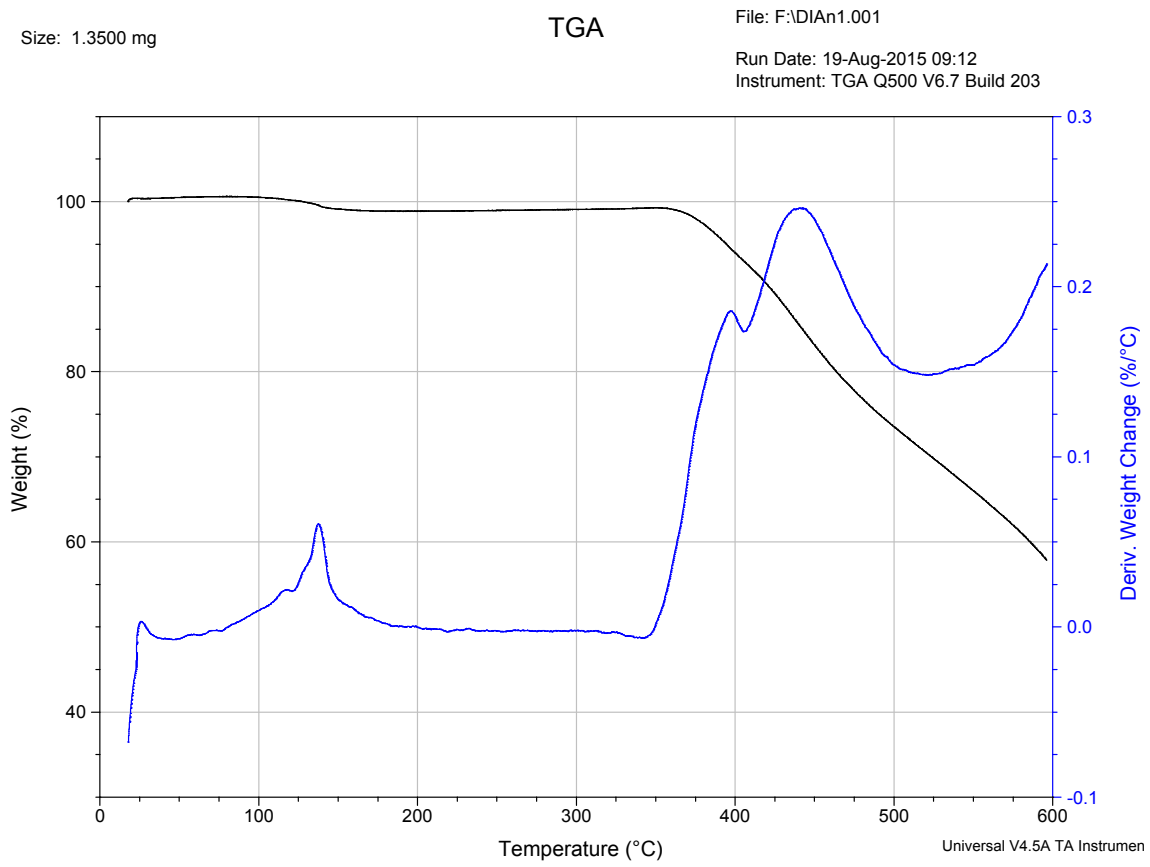

Figure B.3. TGA of **DIAn** under nitrogen shows negligible decomposition before 350 °C.

Cyclic voltammetry

All electrochemical experiments were conducted in a traditional 3-electrode geometry using a Biologic SP-50 potentiostat. Electrolyte solutions (0.1 M) were prepared from HPLC grade DCM and anhydrous Bu_4NBF_4, and the solutions were degassed via freeze-pump-thaw (3×) prior to analysis. The working electrode was a glassy carbon electrode (3 mm diameter) with a Pt-coil counter electrode and Ag wire pseudo reference. The ferrocene/ferrocenium (Fc/Fc^+) couple was used as an internal standard following each experiment. Potential values were re-referenced to SCE using a value of 0.46 (V vs. SCE) for the Fc/Fc^+ couple in CH_2Cl_2. When necessary, potentials were re-referenced to NHE using SCE = –0.24 (V vs. NHE). LUMO and HOMO levels were approximated using SCE = –4.68 eV vs. vacuum.[2] Cyclic voltammetry experiments were conducted in a nitrogen-filled drybox at sweep rates of 50 (reported), 75, 100, 125 and 150 mV s^{-1}. All scan rates show quasi-reversible kinetics with no alteration of peak splitting with scan rate. $E_{1/2}$ values were calculated assuming $E^{o'} \approx E_{1/2} = (E_{anodic} + E_{cathodic})/2$ based on these observations for reversible couples. The $E_{a,c}$ peak splitting of the Fc/Fc^+ couple was similar to that of the analyte (~100 mV). The anodic peak current increases linearly with the square root of the scan rate in the range 50 to 150 mV s^{-1}, indicating a diffusion-controlled process. Analyte concentrations were ca. 1–5 mM.

General X-Ray data collection

Diffraction intensities were collected at 173 K on a Bruker Apex2 CCD diffractometer using MoKα radiation, λ= 0.71073 Å. Space group was determined based on systematic absences. Absorption correction was applied by SADABS.[3] Structure was solved by direct methods and Fourier techniques and refined on F^2 using full matrix least-squares procedures. All non-H atoms were refined with anisotropic thermal parameters. H atoms were treated in calculated positions. Diffraction data were collected up to $2\theta_{max} = 56.0°$ and have been used in the final refinement. All calculations were performed by the SHELXL-2013 package.[4]

Crystallographic Data for **DIAn**: $C_{68}H_{76}Si_2$, M = 949.46, 0.19 × 0.19 × 0.13 mm, T = 173 K, Monoclinic, space group $P2_1/c$, a = 12.3601(12) Å, b = 14.0292(13) Å, c = 16.6209(16) Å, β = 97.754(3)°, V = 2855.8(5) Å^3, Z = 2, Z' = 0.5, D_c = 1.104 Mg/m^3, μ(Mo) = 0.102 mm^{-1}, F(000) = 1024, $2\theta_{max} = 56.0°$, 32693 reflections, 6932 independent reflections [R_{int} = 0.0503], R1 = 0.0515, wR2 = 0.1315 and GOF = 1.054 for 6932 reflections (316 parameters) with I>2σ(I), R1 = 0.0917, wR2 = 0.1584 and GOF = 1.054 for all reflections, max/min residual electron density +0.400/–0.270 eÅ^3. CCDC-1426708 contains the supplementary crystallographic data for this compound. The data can be obtained free of charge from the Cambridge Crystallographic Data Centre via www.ccdc.cam.ac.uk/data_request/cif.

Solid-state arrangement of DIAn

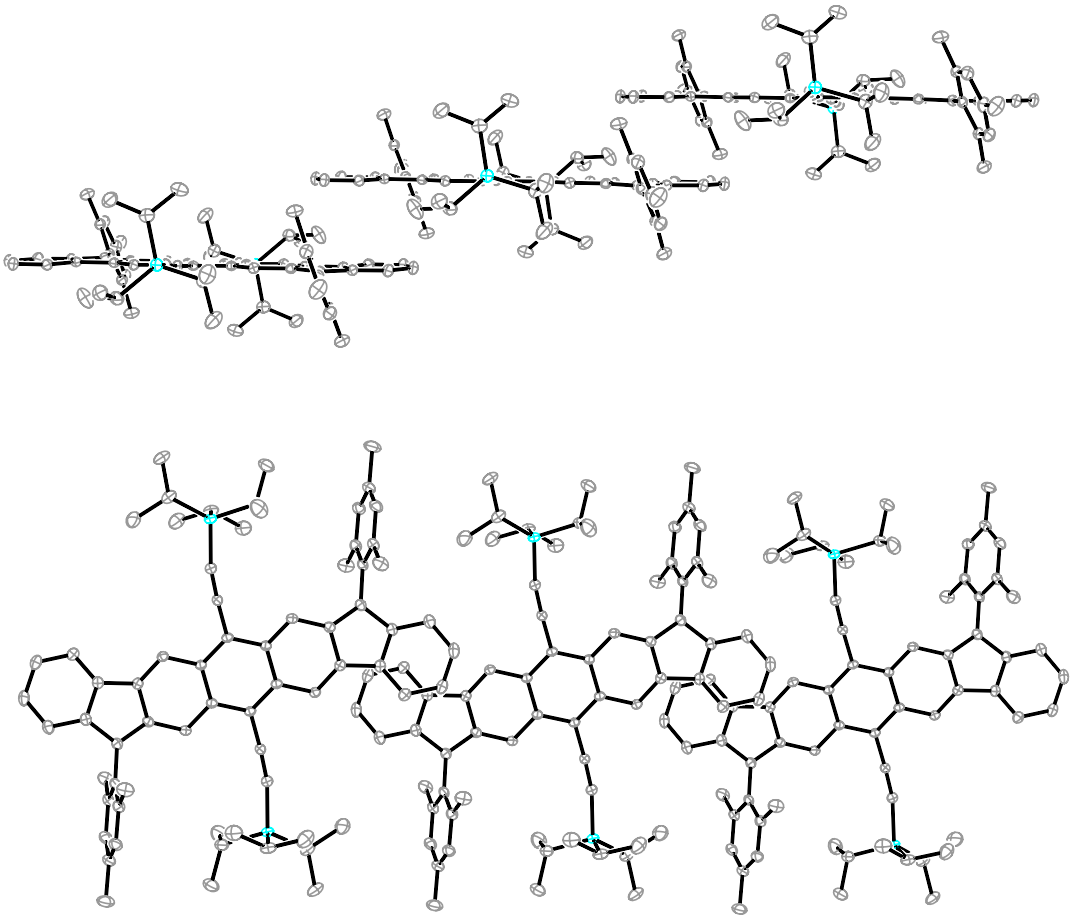

Figure B.4. ORTEP images showing the solid state packing of **DIAn** drawn with 35% thermal ellipsoids, hydrogens are omitted for clarity.

Variable-temperature NMR experiment

Approximately 10 mg of **DIAn** was dissolved in 1,2-dichlorobenzene-d_4 and transferred to a J-Young tube. The solution was degassed by 4 freeze-pump-thaw cycles. Spectra were acquired in a Varian Inova 500MHz spectrometer that was heated to 50, 75, 100, 125, 150, then 25 °C.

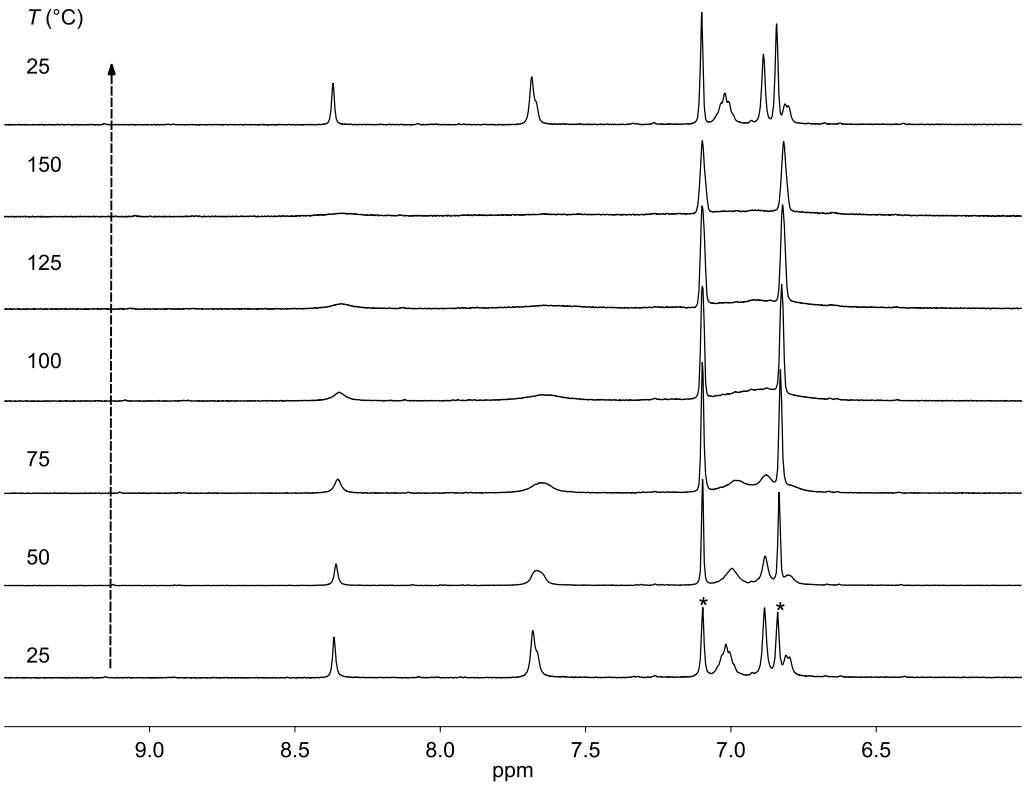

Figure B.5. VT ^{1}H NMR spectra of the aromatic region of **DIAn** in 1,2-dichlorobezene-d_4, residual non-deuterated ODCB solvent (*).

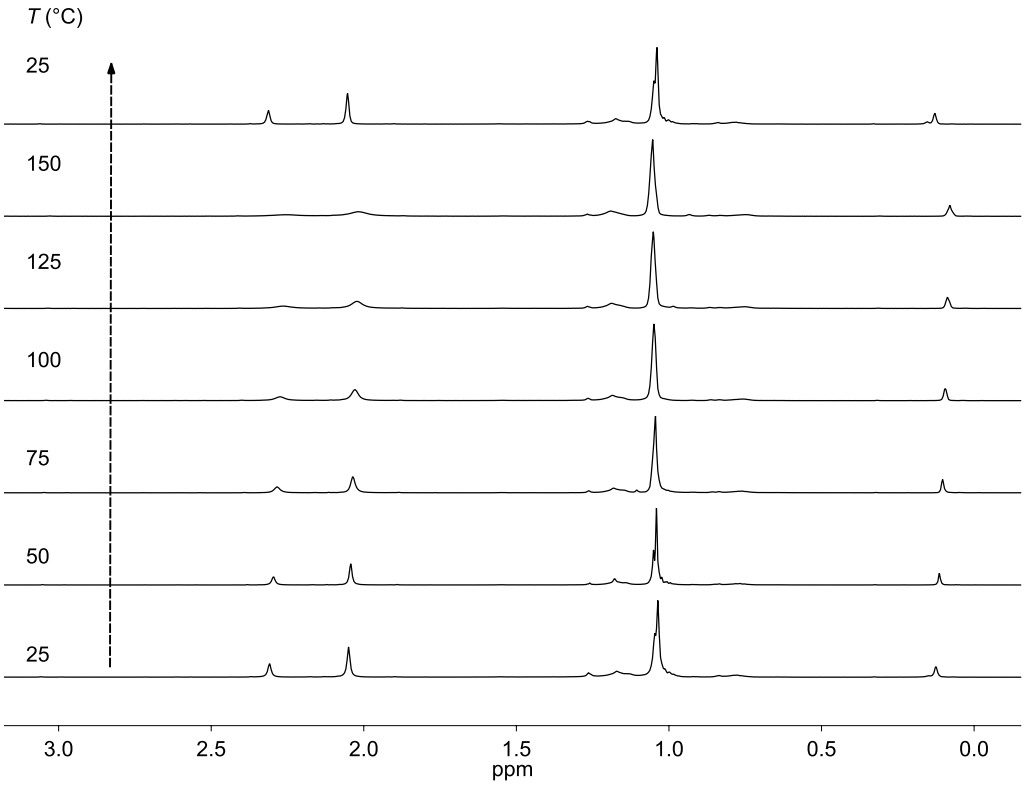

Figure B.6. VT ^{1}H NMR spectra of the aliphatic region of **DIAn** in 1,2-dichlorobezene-d_4.

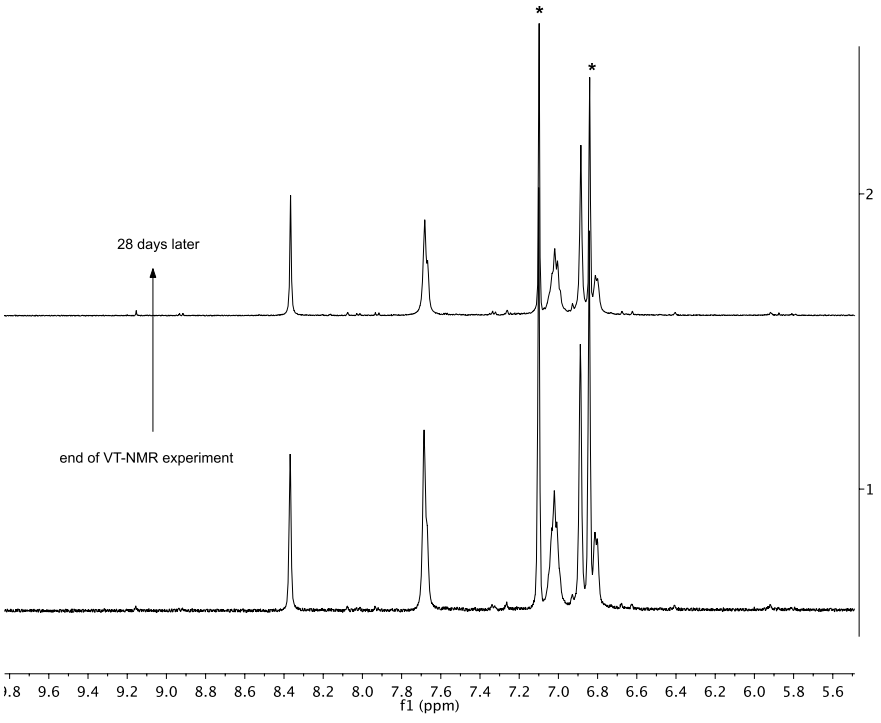

Figure B.7. Proton NMR spectrum of the high-temperature experiment 28 days later showing negligible decomposition.

Raman spectroscopy general details

Raman spectra were recorded in the solid state in off- or on-resonance conditions depending on the excitation wavelength used, either 785 or 633 nm. The measurements were carried out in the 1 × 1 camera of a Bruker Senterra Raman microscope by averaging spectra during 50 min with a resolution of 3–5 cm^{-1}. A CCD camera operating at –50 °C was used for detection. Variable temperature Raman measurements were performed in KBr pellets (to assure faster thermal equilibration) in the range between 25 and 150 ºC, by using a Linkam FTIR600 stage cooled by liquid nitrogen and with a temperature stability of <0.1 °C.

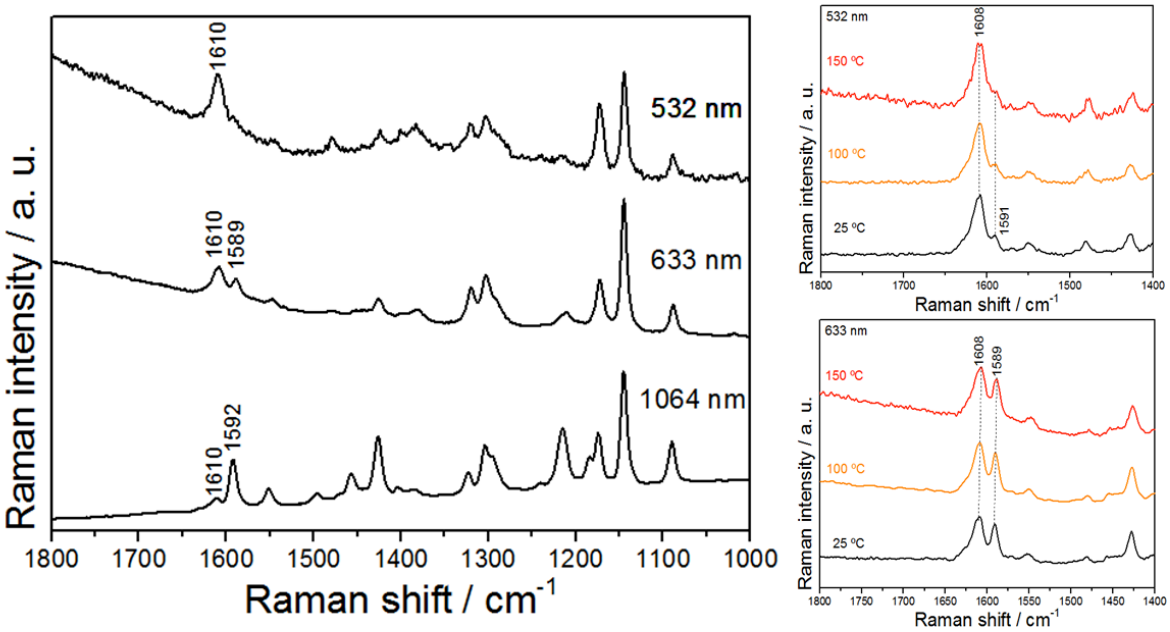

Figure B.8. Raman spectra of solid **DIAn** taken with several Raman excitation wavelengths (left) and VT-Raman spectra of **DIAn** with several Raman excitation wavelengths (right).

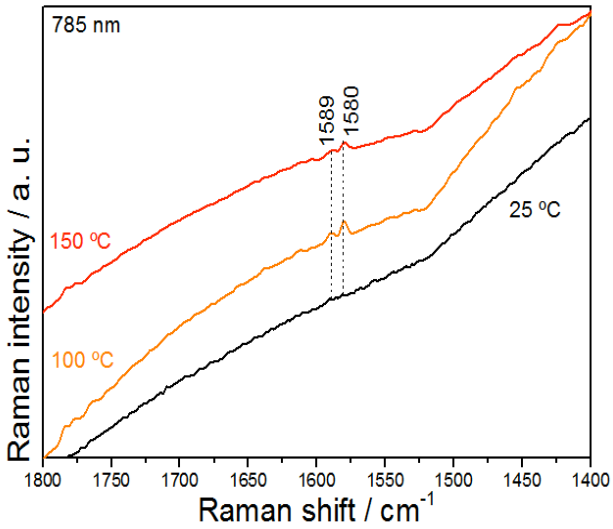

Figure B.9. Expanded region of the VT-Raman experiment where the aromatic/quinoidal C=C stretching frequencies in the 1800-1400 cm^{-1} range is shown; spectra taken with the 785 nm Raman excitation wavelength at different temperatures.

Comparison between Raman spectra of DIAn and its corresponding dihydrogenated presursor

Figure B.10 displays the Raman spectra of **DIAn** in its singlet open-shell pseudo-aromatic state and in its low energy lying aromatized triplet excited state (recorded at 150 ºC) together with the Raman spectrum of the dihydrogenated precursor, **DIAn-H_2** (compound **3**), also in the solid state. This precursor (see chemical structure in Figure B.11 below) contains a fully aromatized anthracene moiety with the external benzenes partially decoupled from the anthracene core. Hence, **DIAn-H_2** can be used as a reference compound to address the effect or degree of aromatization in the central core of **DIAn**. In **DIAn-H_2**, there are two neat bands at 1580 cm^{-1} which is due to the CC stretching vibration of the central anthracene core; thus, it can be considered as typical of an aromatized structure. At higher frequencies, 1606 cm^{-1}, the second band appears which is due to the CC stretching of the external benzene rings. Therefore, the band at 1580 cm^{-1} in the spectrum of the triplet excited state corroborates its aromatic character in the central anthracene. On the other hand, the 1589 cm^{-1} band in the singlet ground electronic state of **DIAn** due to the CC stretching of the central core corroborates its partial aromatized character in contrast with the more accentauted character of the aromatic shape in the triplet.

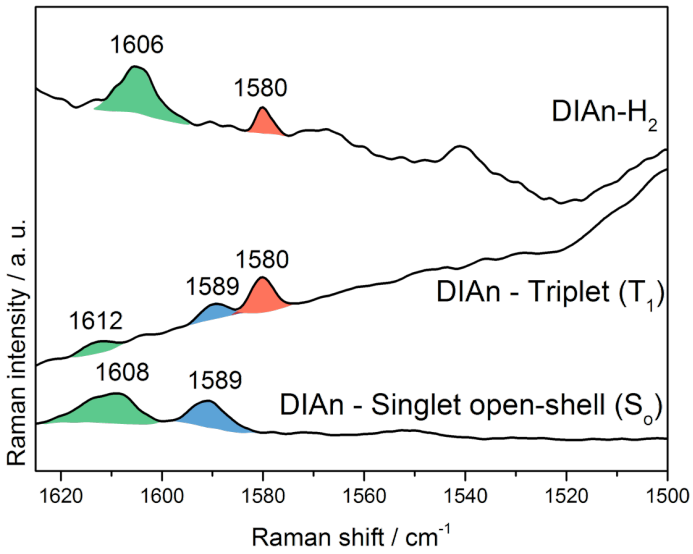

Figure B.10. Comparison between Raman spectra of DIAn and its corresponding dihydrogenated presursor. Bottom: solid-state Raman spectrum of **DIAn** (633 nm, 25 °C). Middle: solid-state Raman spectrum of **DIAn** (785 nm, 150 °C). Top: solid-state Raman spectrum of **DIAn-H_2** (785 nm, 25 °C).

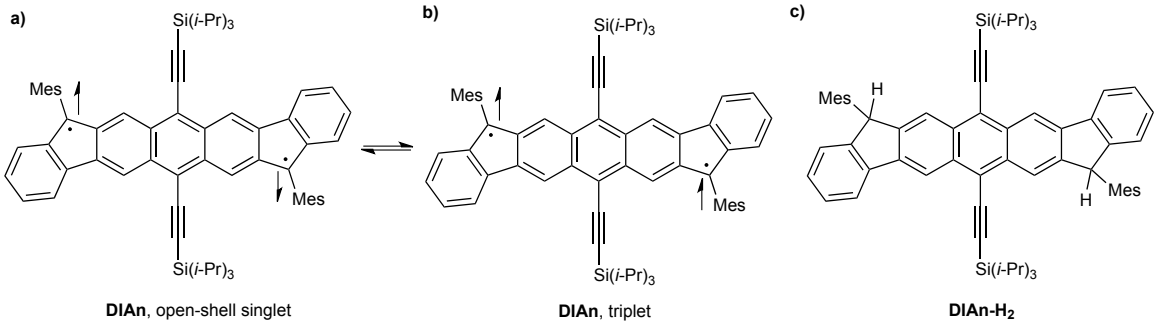

Figure B.11. Resonance structures of **DIAn**: a) open-shell singlet and b) triplet. c) Chemical structure of **DIAn-H_2** (compound **3**).

ESR measurements

The X-band ESR measurements were performed on a polycrystalline powder sample in the 4.2-300 K temperature range with a Q-band (34.0 GHz) Bruker ELEXSYS E580 Spectrometer equipped with a helium cryostat (Figure B.12a). The spin susceptibility (proportional to the area of the signal) was obtained by integrating the area of the signal at each temperature. In this way it was possible to obtain a qualitative variation of the spin susceptibility with temperature (Figure B.12b). As expected, this thermal variation can also be reproduced with the classical Bleaney-Bowers model although, given the qualitative character of these measurements, the obtained J value is lower than the one obtained from the SQUID measurements.

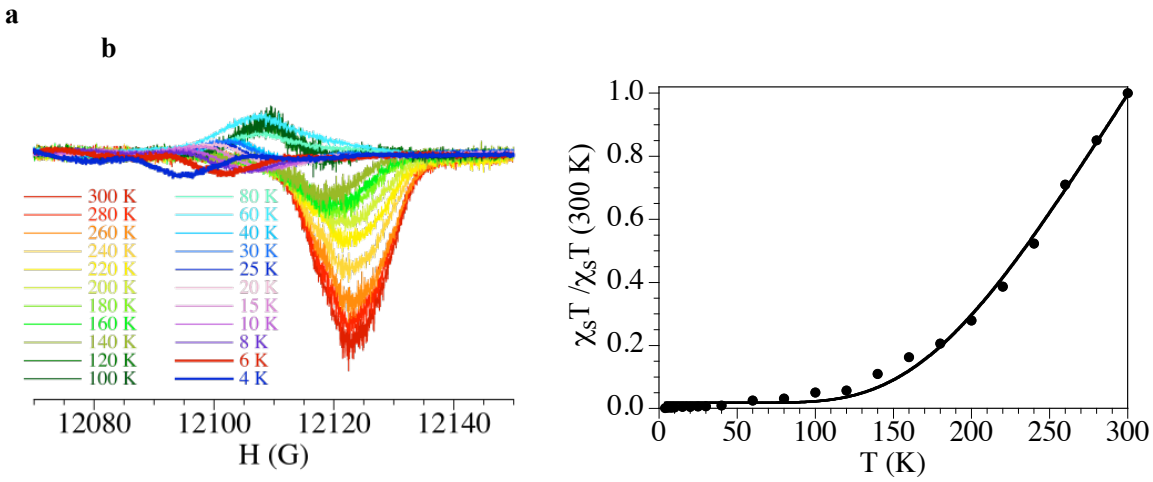

Figure B.12. a, Solid-state ESR spectra taken from 300K to 4K. **b**, Thermal variation of the normalized product of the EPR spin susceptibility times the temperature for the title compound. Solid line is the best fit to the Bleaney-Bowers model.

SQUID measurements

The magnetic susceptibility measurements were carried out in the temperature range 2–400 K with an applied magnetic field of 0.1 T on a polycrystalline sample of the title compound (with a mass of 9.88 mg) with a Quantum Design MPMS-XL-5 SQUID susceptometer. The susceptibility data were corrected for the sample holder previously measured using the same conditions and for the diamagnetic contribution of the compound as deduced by using Pascal's constant tables. The experimental data (X_mT vs. T) were fit using the classical Bleaney-Bowers model for an antiferromagentic S = ½ dimer:[5]

$$\chi_m = \frac{2Ng^2\beta^2}{k_BT}\frac{1}{3 + exp\ (\text{-}J/k_BT)}$$

Computational details

Geometry optimization

To perfom the computational investigation of the synthesized **DIAn** derivative, we adopted two model systems, **DIAn-a** and **DIAn-b** (Figure B.13). For all the calculations, the 6-311G(d) basis set is applied. Gaussian 09 program package is applied for all the calculations except for the spin-flip TD-DFT calculations.[6] GAMESS and Q-CHEM program packages are applied for the calculation of spin-flip calculation with the collinear and the non-collinear kernels, respectively.[7,8]

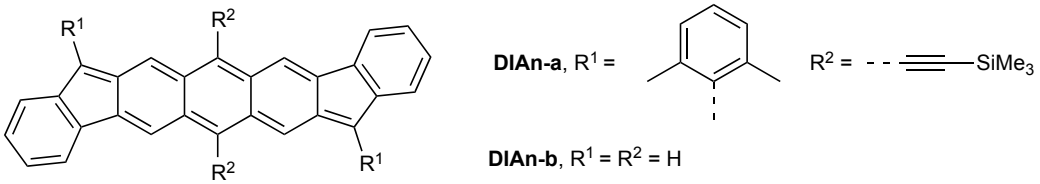

Figure B.13. Model structures used in computations.

For the geometry optimization of the model systems, restricted and unrestricted B3LYP method for both the model systems and spin-flip TD-BHHLYP for only **DIAn-b** have been adopted and the obtained geometries were compared to the experimentally obtained X-ray crystallographic data. All the optimized geometries were confirmed to be at the potential energy local minima by the hessian calculation. Figure B.14 shows the numbering scheme of the bonds in π-conjugated framework and the bond length alternation is shown in Figure B.15 for the singlet states and in Figure B.16 for the triplet states.

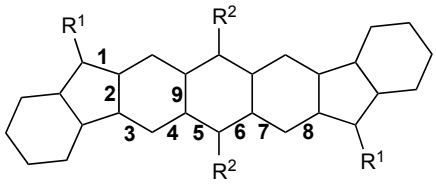

Figure B.14. DIAn model system numbering scheme.

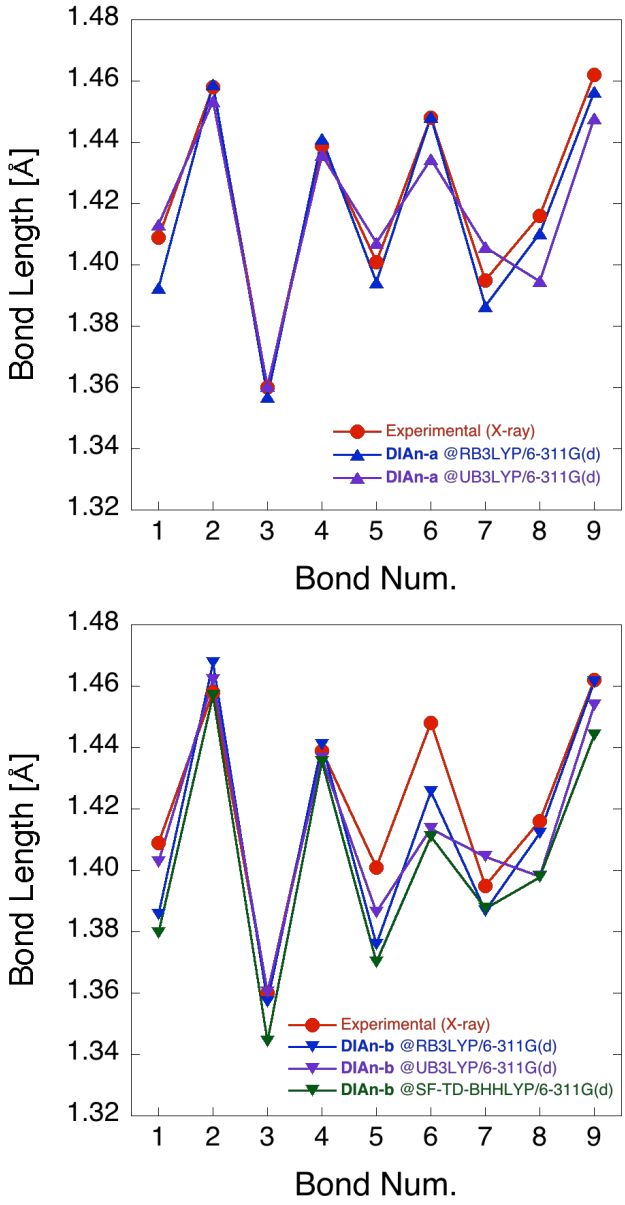

Figure B.15. Bond length alternation of the π-conjugated framework in the singlet states.

The **DIAn-a** geometry optimized at RB3LYP/6-311G(d) level of theory reproduces the bond length and also the alternation of the experimental data quite well. Also, the smaller **DIAn-b** optimized at RB3LYP semi-qualitatively agrees well though the bonds 5 and 6 are shorter than those of **DIAn-a**, the differences of which originate from the existence/absence of the bulky substituents. The validity of the optimization at RB3LYP method is also confirmed with the fact

the bond length alternation is in semi-quantitatively well agreement with the optimized geometry of **DIAn-b** at the spin-flip TD-BHHLYP method, which is known to well reproduce the geometries of diradical species.[9] On the other hand, the UB3LYP method fails to reproduce the bond length alternation of the singlet species even in qualitative manner for both the model systems though the method is often adopted for the calculations of open-shell species (see bond 7 to 8). This is probably because of the spin contamination error of the unrestricted wavefunctions. In fact, this tendency of the optimized geometry that the bond 7 is shorter than that of the bond 8 is the tendency observed in the triplet states even at the spin-flip TD-BHHLYP method (Figure B.16). For the triplet geometry, the UB3LYP method well reproduces that of the spin-flip TD-BHHLYP method for the **DIAn-b**. **DIAn-a** in the triplet state optimized at UB3LYP method agrees well with that of the **DIAn-b** except for the bonds 5 and 6, which is lengthened by the substitution groups. The reason why the triplet geometry of the spin-flip TD-BHHLYP method is well reproduced by the UB3LYP method would be the negligible spin contamination of the unrestricted wavefunction in the triplet state. From these observations, we adopt the **DIAn-a** structure optimized at RB3LYP method for the singlet state and UB3LYP method for the triplet state for the further investigations.

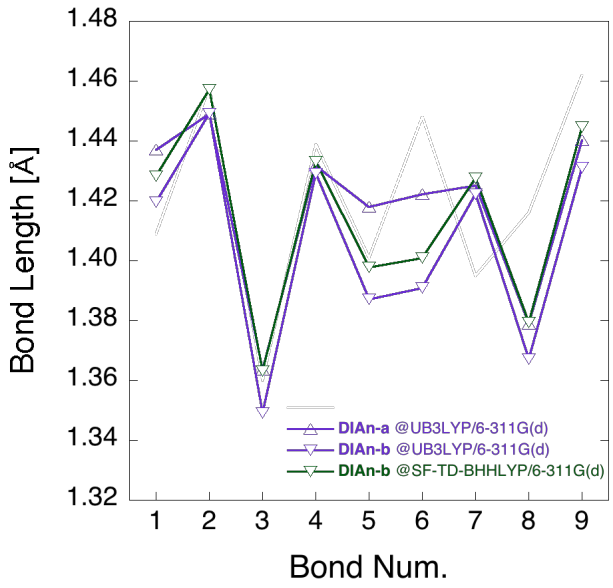

Figure B.16. Bond length alternation of the π-conjugated framework in the triplet states.

The open-shell singlet solution is the lowest energy state of **DIAn**; however, unrestricted DFT calculations sometimes cause severe problem on the geometry optimization because of the spin contamination error. The validity of the optimized geometry is confirmed above by the comparison with the X-ray data but also with the higher level of theory with negligible spin contamination error, spin-flip TD-DFT method. The energies of open-shell (singlet in unrestricted), closed-shell (singlet in restricted) and triplet (triplet in unrestricted) at B3LYP/6-311G(d) level of theory using the RB3LYP/6-311(d)-optimized geometry are given in Table B.1.

Table B.1. Relative energy (kcal mol^{-1}) of **DIAn-a** and **DIAn-b** at B3LYP/6-311G(d) level of theory using the singlet optimized geometry by the RB3LYP/6-311G(d) method.

	DIAn-a	**DIAn-b**
open-shell singlet, unrestricted	(set as 0)	(set as 0)
open-shell triplet, unrestricted	8.30	9.50
closed-shell singlet, restricted	1.44	1.07

Singlet-triplet energy gap and biradical character index, y, calculation

The singlet–triplet energy gap (ST gap) accompanied with the geometry relaxation is calculated using the zero point vibration energy at the same level of theory as the optimization and the electronic energy of each optimized geometry calculated at the spin-flip TD-PBE50 method with the non-collinear kernel.[10] The calculated ST gap is 4.9 kcal mol^{-1} including the difference of the zero-point vibration energies of 0.9 kcal mol^{-1}. The result quite well agrees with the experimentally determined ST gap, 4.18 kcal mol^{-1}.

The open-shell character of the present system is characterized with the spin-projected unrestricted hartree-fock (PUHF) method, which well reproduces the variation in the diradical character of H_2 dissociation calculated at the full configuration interaction method.[11] Within the PUHF method, the diradical character is expressed as the following equation:

$$y = 1 - \frac{2T}{1+T^2},$$

where T indicates the orbital overlap between the highest occupied natural orbital (HONO) and the lowest unoccupied natural orbital (LUNO). Using the occupation numbers of UHF natural orbitals (UNO), the overlap T is calculated as follows:

$$T = \frac{n_{\mathrm{HONO}} - n_{\mathrm{LUNO}}}{2},$$

Since the diradical character is not an observable and is an index of "the degree" of the open-shell singlet character, the absolute value varies with the calculation method, but once the calculation method is determined, the y value can be compared each other. In this regard, one should be careful on which calculation method is used for the determination of the diradical character when comparing y with some other one calculated at the other study. Therefore, to compare the diradical character of the present system with the previously synthesized open-shell systems, we have recalculated the four simplified model systems of the reported open-shell singlet systems, indeno[2,1-*b*]fluorene, indacenodiphenalene, octazethrene and teranthene, at the method applied in the present study. The result shows that the diradical character of these systems is in the range between 0.504 and 0.737 (Figure B.17).

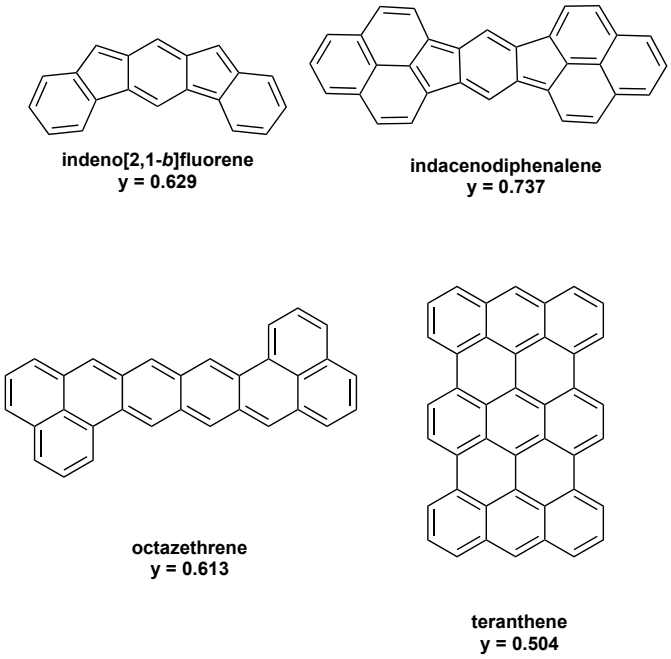

Figure B.17. Comparison of open-shell PCHs with calculated biradical character index y.

The spatial distribution of the open-shell character is expressed with the odd-electron density distribution;[12]

$$\rho^{\mathrm{odd}} = y \times \left\{ \left| \phi_{\mathrm{HONO}} \right|^2 + \left| \phi_{\mathrm{LUNO}} \right|^2 \right\}.$$

Since in the present case, we apply LC-UBLYP method for the calculation of the odd-electron density, the applied y in the above equation is calculated without spin-projection scheme. Namely, we apply the occupation number of LUNO in the LC-UBLYP method as y for the calculation of the odd-electron density distribution.

NICS-XY scans and ACID plots calculations

The NICS-XY scans[13] were performed using Gaussian09 Rev. D.01 and Aroma 1.0.[14] We used the B3LYP[15] functional as well as LC-BLYP combining the BLYP functional[16] with the long-range correction of Hirao[17], both together with the 6-311+G(d,p) basis set.[18] For the LC

scheme a "ω" value of 0.33 was employed by specifying the following keywords in Gaussian09: "iop(3/107=0330000000,3/108=0330000000)". The GIAO[19] procedure was employed for the calculation of the NICS values at 1.7 Å above the molecular plane and the -only model[20] was used to remove the influence of the system. Minima with substantially negative NICS values in the NICS-XY scan represent aromatic rings, while maxima with substantially positive values represent antiaromatic rings. NICS values around zero correspond to non-aromatic rings. For benzene, the minimum NICS value at 1.7 Å distance above the ring plane is –16 ppm with the -only model, while the maximum value for D_{2h} cyclobutadiene is ca. +20 ppm.[13]

The ACID[21] plots were generated with Gaussian09 using the CSGT method[22] and AICD 2.0.0. ACID is a method to visualize conjugation and ring currents in molecules. Clockwise ring currents correspond to aromatic systems and counter-clockwise ring currents to antiaromatic systems. Systems with no evident ring current are considered non-aromatic. The following keywords were used in Gaussian09 to control the grid size for the GIAO and CSGT calculations: "cphf=grid=fine" and "integral=grid=ultrafine".

The NICS-XY scan for **DIAn-b** with B3LYP is presented in Figure B.18. The LC-UBLYP ACID plot for the T_1 state of **DIAn-a** is presented in Figure B.19, while the ACID plots for S_0 and T_1 with B3LYP are found in Figures B.20 and B.21, respectively. The results with B3LYP and LC-UBLYP are in general agreement, although LC-UBLYP ascribes a larger open-shell character to the singlet state. It has previously been shown that LC-UBLYP better reproduces optical response properties of open-shell species as compared to B3LYP.[23]

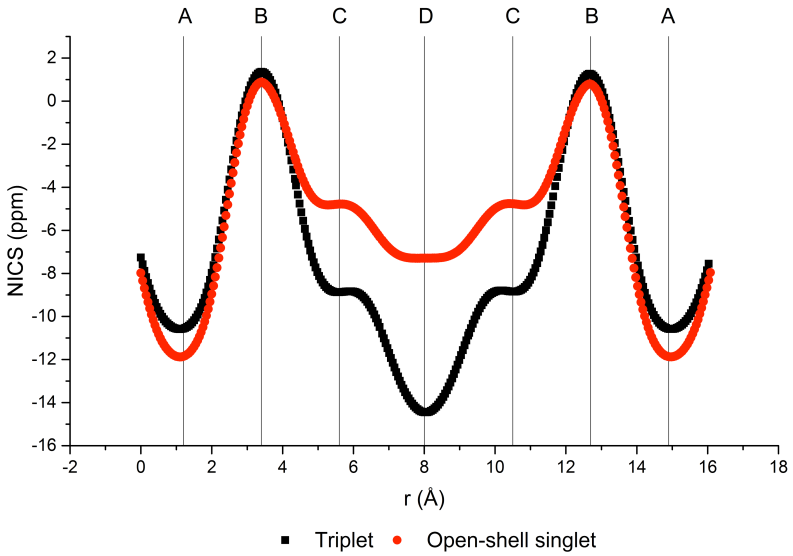

Figure B.18. GIAO-UB3LYP/6-311+G(d,p) NICS-XY scan comparing open-shell singlet and triplet states of **DIAn-b**.

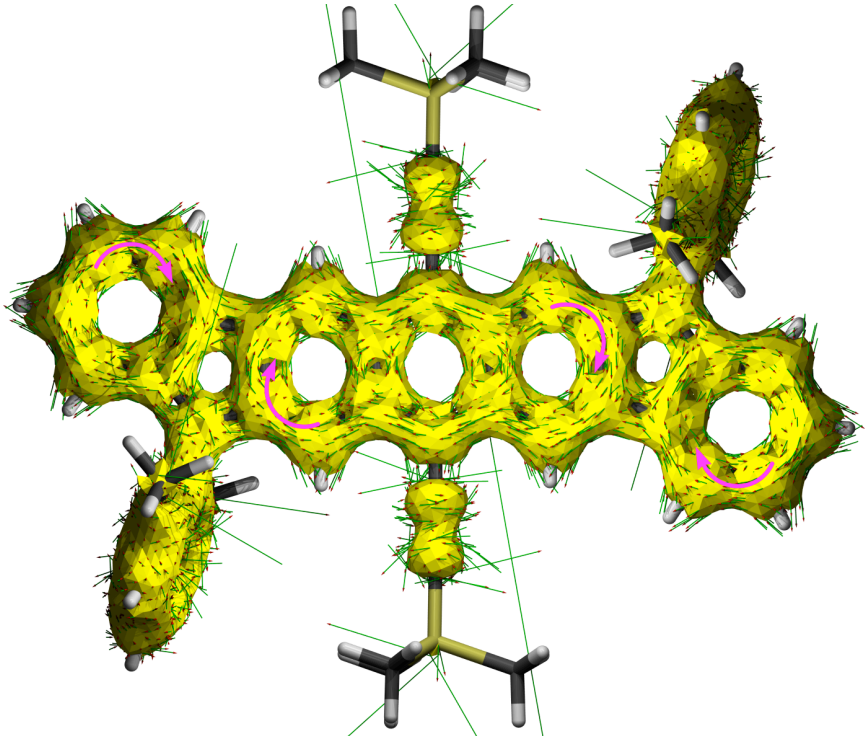

Figure B.19. ACID plot in T_1 at the LC-UBLYP/6-311+G(d,p) level of **DIAn-a**.

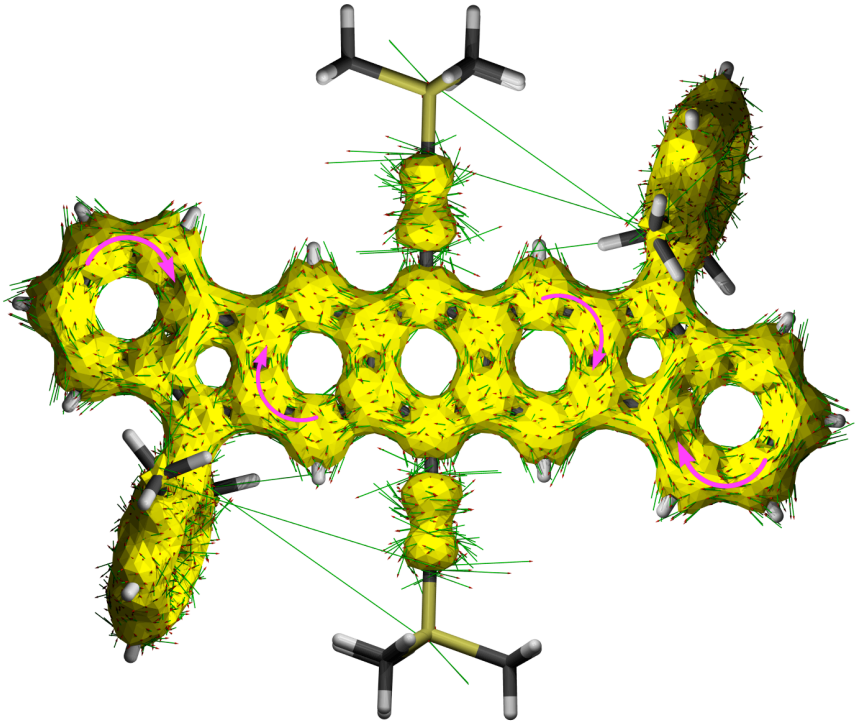

Figure B.20. ACID plot in S_0 at the UB3LYP/6-311+G(d,p) level of **DIAn-a**.

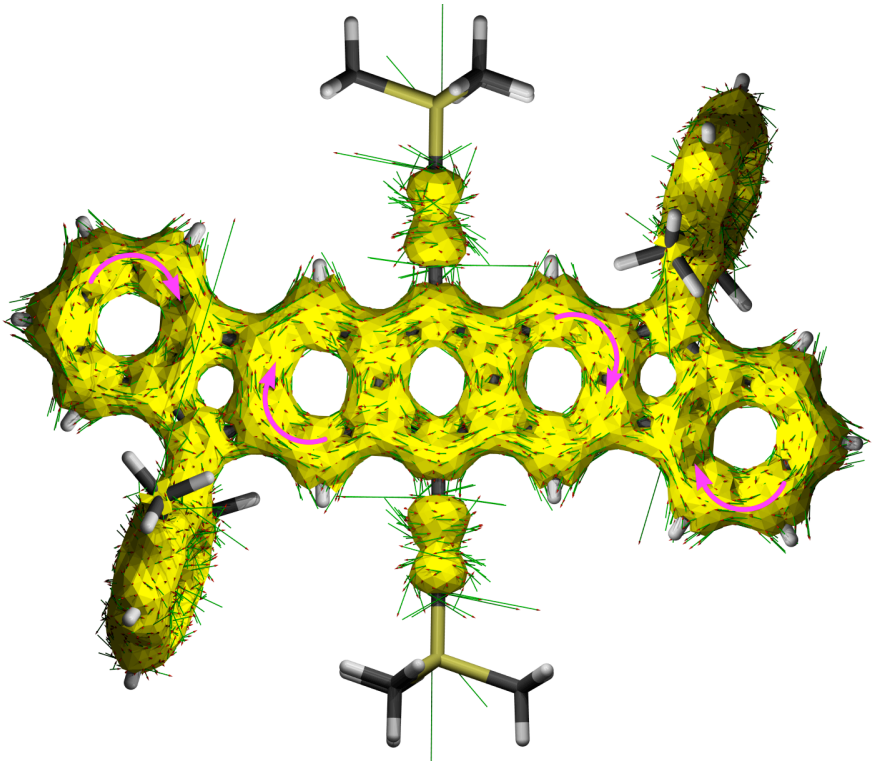

Figure B.21. ACID plot in T_1 at the UB3LYP/6-311+G(d,p) level of **DIAn-a**.

Cartesian coordinates

Table B.2. Cartesian coordinate of **DIAn-a** in singlet state optimized at RB3LYP/6-311G(d) level of theory.

atom	x	y	z
C	1.198133	0.785288	0.100175
C	2.377084	1.608252	0.198490
H	3.341749	1.114431	0.231178
C	2.274909	2.960386	0.247085
C	3.269581	4.026014	0.343470
C	4.655646	4.012597	0.424720
H	5.206309	3.076690	0.420415
C	5.340055	5.228112	0.514378
H	6.423301	5.231145	0.578123
C	4.643307	6.441923	0.524961
H	5.195506	7.373549	0.597842
C	3.251935	6.470616	0.445213
H	2.716862	7.414896	0.458185
C	2.556757	5.261053	0.351022
C	1.131548	4.989137	0.262524
C	0.968246	3.607671	0.200980
C	-0.193186	2.814132	0.099815
H	-1.166251	3.289455	0.057640
C	-0.106375	1.431300	0.050442
C	0.056982	6.012734	0.245491
C	-0.635760	6.323854	1.434364
C	-1.644837	7.290158	1.396094
H	-2.177079	7.537558	2.309971
C	-1.968011	7.940093	0.210239
C	-1.280041	7.630677	-0.957774
H	-1.532881	8.138062	-1.884217
C	-0.263850	6.671754	-0.960196

H	0.770590	5.698546	2.960723
H	-2.753408	8.689543	0.196981
Si	-5.256027	2.694990	-0.203814
C	-1.291355	0.604916	-0.051136
C	-2.561012	1.242307	-0.099653
C	-3.635816	1.811868	-0.140546
C	-6.631963	1.406348	-0.227186
H	-6.553065	0.750927	-1.099179
H	-6.605790	0.774995	0.665440
H	-7.616211	1.884197	-0.263328
C	-5.398866	3.788052	1.324331
H	-4.599901	4.533854	1.358170
H	-5.342161	3.200950	2.245068
H	-6.352819	4.325319	1.332541
C	-5.303314	3.741656	-1.769933
H	-6.254284	4.277794	-1.853243
H	-5.190202	3.127358	-2.667407
H	-4.502863	4.486529	-1.776940
C	-0.297732	5.636431	2.736790
H	-0.551688	4.572764	2.711625
H	-0.842289	6.087606	3.568716
C	0.461453	6.340971	-2.243447
H	0.069186	6.927300	-3.076752
H	0.359884	5.282812	-2.500593
H	1.533600	6.543136	-2.168014
C	-1.198133	-0.785288	-0.100175
C	-2.377084	-1.608252	-0.198490
H	-3.341749	-1.114431	-0.231178
C	-2.274909	-2.960386	-0.247085
C	-3.269581	-4.026014	-0.343470
C	-4.655646	-4.012597	-0.424720

H	-5.206309	-3.076690	-0.420415
C	-5.340055	-5.228112	-0.514378
H	-6.423301	-5.231145	-0.578123
C	-4.643307	-6.441923	-0.524961
H	-5.195506	-7.373549	-0.597842
C	-3.251935	-6.470616	-0.445213
H	-2.716862	-7.414896	-0.458185
C	-2.556757	-5.261053	-0.351022
C	-1.131548	-4.989137	-0.262524
C	-0.968246	-3.607671	-0.200980
C	0.193186	-2.814132	-0.099815
H	1.166251	-3.289455	-0.057640
C	0.106375	-1.431300	-0.050442
C	-0.056982	-6.012734	-0.245491
C	0.635760	-6.323854	-1.434364
C	1.644837	-7.290158	-1.396094
H	2.177079	-7.537558	-2.309971
C	1.968011	-7.940093	-0.210239
C	1.280041	-7.630677	0.957774
H	1.532881	-8.138062	1.884217
C	0.263850	-6.671754	0.960196
H	-0.770590	-5.698546	-2.960723
H	2.753408	-8.689543	-0.196981
Si	5.256027	-2.694990	0.203814
C	1.291355	-0.604916	0.051136
C	2.561012	-1.242307	0.099653
C	3.635816	-1.811868	0.140546
C	6.631963	-1.406348	0.227186
H	6.553065	-0.750927	1.099179
H	6.605790	-0.774995	-0.665440
H	7.616211	-1.884197	0.263328

C	5.398866	-3.788052	-1.324331
H	4.599901	-4.533854	-1.358170
H	5.342161	-3.200950	-2.245068
H	6.352819	-4.325319	-1.332541
C	5.303314	-3.741656	1.769933
H	6.254284	-4.277794	1.853243
H	5.190202	-3.127358	2.667407
H	4.502863	-4.486529	1.776940
C	0.297732	-5.636431	-2.736790
H	0.551688	-4.572764	-2.711625
H	0.842289	-6.087606	-3.568716
C	-0.461453	-6.340971	2.243447
H	-0.069186	-6.927300	3.076752
H	-0.359884	-5.282812	2.500593
H	-1.533600	-6.543136	2.168014

Table B.3. Cartesian coordinate of **DIAn-a** in triplet state optimized at UB3LYP/6-311G(d) level of theory.

atom	x	y	z
C	1.187148	0.789719	0.102820
C	2.361849	1.601956	0.203980
H	3.326376	1.108351	0.236612
C	2.260485	2.960699	0.255662
C	3.260242	4.022357	0.353298
C	4.645506	3.994070	0.433517
H	5.185207	3.051951	0.428596
C	5.345182	5.201520	0.522598
H	6.428396	5.190479	0.585559
C	4.664344	6.427364	0.533396
H	5.230317	7.350654	0.605505
C	3.276731	6.474817	0.454861

H	2.753222	7.425465	0.467480
C	2.560073	5.270773	0.361497
C	1.147694	5.027482	0.274414
C	0.962740	3.603899	0.209027
C	-0.184789	2.846335	0.106962
H	-1.158046	3.320326	0.064694
C	-0.104798	1.424408	0.052807
C	0.074128	6.049472	0.253596
C	-0.612806	6.369486	1.443556
C	-1.626462	7.330373	1.401605
H	-2.154795	7.584313	2.315927
C	-1.960266	7.965649	0.210576
C	-1.279224	7.646253	-0.958768
H	-1.541410	8.141485	-1.889162
C	-0.258932	6.691689	-0.957582
H	0.800310	5.820917	2.991997
H	-2.749858	8.710586	0.194117
Si	-5.261339	2.669733	-0.206679
C	-1.276177	0.624462	-0.049756
C	-2.548465	1.255040	-0.099423
C	-3.632264	1.808020	-0.141670
C	-6.622928	1.365168	-0.229739
H	-6.536099	0.710451	-1.101558
H	-6.589094	0.734448	0.663117
H	-7.612820	1.831260	-0.266045
C	-5.423290	3.763893	1.319425
H	-4.632955	4.518825	1.354946
H	-5.362385	3.178755	2.241176
H	-6.383386	4.290218	1.323954
C	-5.325973	3.716215	-1.772936
H	-6.283663	4.240597	-1.854629

H	-5.206625	3.103251	-2.670550
H	-4.534673	4.470865	-1.781701
C	-0.259005	5.697588	2.749621
H	-0.450569	4.621304	2.716209
H	-0.841624	6.113555	3.573957
C	0.460835	6.349708	-2.241113
H	0.043735	6.905016	-3.083529
H	0.385196	5.283447	-2.472547
H	1.527788	6.583360	-2.183066
C	-1.187148	-0.789719	-0.102820
C	-2.361849	-1.601956	-0.203980
H	-3.326376	-1.108351	-0.236612
C	-2.260485	-2.960699	-0.255662
C	-3.260242	-4.022357	-0.353298
C	-4.645506	-3.994070	-0.433517
H	-5.185207	-3.051951	-0.428596
C	-5.345182	-5.201520	-0.522598
H	-6.428396	-5.190479	-0.585559
C	-4.664344	-6.427364	-0.533396
H	-5.230317	-7.350654	-0.605505
C	-3.276731	-6.474817	-0.454861
H	-2.753222	-7.425465	-0.467480
C	-2.560073	-5.270773	-0.361497
C	-1.147694	-5.027482	-0.274414
C	-0.962740	-3.603899	-0.209027
C	0.184789	-2.846335	-0.106962
H	1.158046	-3.320326	-0.064694
C	0.104798	-1.424408	-0.052807
C	-0.074128	-6.049472	-0.253596
C	0.612806	-6.369486	-1.443556
C	1.626462	-7.330373	-1.401605

H	2.154795	-7.584313	-2.315927
C	1.960266	-7.965649	-0.210576
C	1.279224	-7.646253	0.958768
H	1.541410	-8.141485	1.889162
C	0.258932	-6.691689	0.957582
H	-0.800310	-5.820917	-2.991997
H	2.749858	-8.710586	-0.194117
Si	5.261339	-2.669733	0.206679
C	1.276177	-0.624462	0.049756
C	2.548465	-1.255040	0.099423
C	3.632264	-1.808020	0.141670
C	6.622928	-1.365168	0.229739
H	6.536099	-0.710451	1.101558
H	6.589094	-0.734448	-0.663117
H	7.612820	-1.831260	0.266045
C	5.423290	-3.763893	-1.319425
H	4.632955	-4.518825	-1.354946
H	5.362385	-3.178755	-2.241176
H	6.383386	-4.290218	-1.323954
C	5.325973	-3.716215	1.772936
H	6.283663	-4.240597	1.854629
H	5.206625	-3.103251	2.670550
H	4.534673	-4.470865	1.781701
C	0.259005	-5.697588	-2.749621
H	0.450569	-4.621304	-2.716209
H	0.841624	-6.113555	-3.573957
C	-0.460835	-6.349708	2.241113
H	-0.043735	-6.905016	3.083529
H	-0.385196	-5.283447	2.472547
H	-1.527788	-6.583360	2.183066

Table B.4. Cartesian coordinate of **DIAn-b** in singlet state optimized at RB3LYP/6-311G(d) level of theory.

atom	x	y	z
C	0.552243	-1.319486	0.000000
C	1.069783	-2.664222	0.000000
H	2.148193	-2.800254	0.000000
C	0.223550	-3.725300	0.000000
C	0.444850	-5.169052	0.000000
C	1.599611	-5.941625	0.000000
H	2.582204	-5.479005	0.000000
C	1.483085	-7.333470	0.000000
H	2.377745	-7.947491	0.000000
C	0.223550	-7.946411	0.000000
H	0.157896	-9.029836	0.000000
C	-0.942752	-7.186067	0.000000
H	-1.914368	-7.670719	0.000000
C	-0.841208	-5.790297	0.000000
C	-1.851093	-4.761448	0.000000
C	-1.230033	-3.522781	0.000000
C	-1.748221	-2.209383	0.000000
H	-2.823251	-2.049984	0.000000
C	-0.894866	-1.116434	0.000000
H	-2.919995	-4.937017	0.000000
C	-1.382934	0.222900	0.000000
H	-2.459683	0.374100	0.000000
C	-0.552243	1.319486	0.000000
C	-1.069783	2.664222	0.000000
H	-2.148193	2.800254	0.000000
C	-0.223550	3.725300	0.000000
C	-0.444850	5.169052	0.000000
C	-1.599611	5.941625	0.000000
H	-2.582204	5.479005	0.000000
C	-1.483085	7.333470	0.000000
H	-2.377745	7.947491	0.000000
C	-0.223550	7.946411	0.000000
H	-0.157896	9.029836	0.000000
C	0.942752	7.186067	0.000000
H	1.914368	7.670719	0.000000

C	0.841208	5.790297	0.000000
C	1.851093	4.761448	0.000000
C	1.230033	3.522781	0.000000
C	1.748221	2.209383	0.000000
H	2.823251	2.049984	0.000000
C	0.894866	1.116434	0.000000
H	2.919995	4.937017	0.000000
C	1.382934	-0.222900	0.000000
H	2.459683	-0.374100	0.000000

Table B.5. Cartesian coordinate of **DIAn-b** in triplet state optimized at UB3LYP/6-311G(d) level of theory.

atom	x	y	z
C	0.547957	-1.312926	0.000000
C	1.073905	-2.646148	0.000000
H	2.152700	-2.777290	0.000000
C	0.231037	-3.717357	0.000000
C	0.468982	-5.160452	0.000000
C	1.635012	-5.912927	0.000000
H	2.609319	-5.433394	0.000000
C	1.543738	-7.308303	0.000000
H	2.449934	-7.905145	0.000000
C	0.295052	-7.947378	0.000000
H	0.251686	-9.031832	0.000000
C	-0.883348	-7.210944	0.000000
H	-1.846210	-7.712595	0.000000
C	-0.810297	-5.807712	0.000000
C	-1.831653	-4.813458	0.000000
C	-1.213544	-3.525831	0.000000
C	-1.746237	-2.253451	0.000000
H	-2.821527	-2.098649	0.000000
C	-0.883348	-1.116050	0.000000
H	-2.897884	-5.001559	0.000000

C	-1.383622	0.192382	0.000000
H	-2.460443	0.340932	0.000000
C	-0.547957	1.312926	0.000000
C	-1.073905	2.646148	0.000000
H	-2.152700	2.777290	0.000000
C	-0.231037	3.717357	0.000000
C	-0.468982	5.160452	0.000000
C	-1.635012	5.912927	0.000000
H	-2.609319	5.433394	0.000000
C	-1.543738	7.308303	0.000000
H	-2.449934	7.905145	0.000000
C	-0.295052	7.947378	0.000000
H	-0.251686	9.031832	0.000000
C	0.883348	7.210944	0.000000
H	1.846210	7.712595	0.000000
C	0.810297	5.807712	0.000000
C	1.831653	4.813458	0.000000
C	1.213544	3.525831	0.000000
C	1.746237	2.253451	0.000000
H	2.821527	2.098649	0.000000
C	0.883348	1.116050	0.000000
H	2.897884	5.001559	0.000000
C	1.383622	-0.192382	0.000000
H	2.460443	-0.340932	0.000000

OFET Fabrication and Characterization

Field-effect transistors were fabricated by vapour deposition of ~50 nm thick layers of the semiconductors at preselected temperatures (~6 x 10^{-6} torr, 0.2 Å s^{-1}) on p-doped Si (001) wafers with a 300 nm thermally grown SiO_2 dielectric layer. The SiO_2 substrate was heated at 150 °C and the DIAn source was heated 160–201 °C. Prior to deposition, the wafers were cleaned by rinsing twice with EtOH followed by a 5 min plasma cleaning in a Harrick PDC-32G Plasma Cleaner/Sterilizer. A self-assembled monolayer (SAM) of either hexamethyldisilazane (HMDS) or octadecyltrichlorosilane (OTS) was then deposited to reduce charge trapping and thus enhance mobility. Treatment with HMDS was carried out by exposing the cleaned silicon wafers to HMDS vapour at room temperature in a closed air-free container under argon, whereas treatment with OTS was performed by immersing the silicon wafers in a 3.0 mM humidity-exposed OTS-hexane solution for 1 hour, as previously described.

Solution-processed OFETs were fabricated either by spin-coating of a 7 mg ml^{-1} solution in $CHCl_3$ or by drop-casting of a 5 mg ml^{-1} solution in $CHCl_3$. Due to the hydrophobicity of the substrates, spreading of the solutions with the tip of the pipette helped to achieve a homogenous deposition.

Top contact OFETs were fabricated by vapour deposition of Au electrodes (~10^{-7} torr, 0.2 Å s^{-1}, ~50 nm thick) onto the semiconductor thin films through a shadow mask to obtain devices with deliberately varied channel widths and lengths. The capacitance of the 300 nm SiO_2 gate insulator is 1 x 10^{-8} F cm^{-2}. Characterization of the devices was performed under vacuum in a customized high-vacuum probe station (~10^{-6} torr) and in ambient atmosphere using an EB-4 Everbeing probe station with a 4200-SCS/C Keithley semiconductor characterization system.

Table B.6 shows the electrical performance parameters of OFETs fabricated by vapour-deposition of the semiconductor. The corresponding output I-V_{SD} plots are shown in Figure B.22. Note that performances of devices with no SAM treatment or treated with HMDS are only

modest. Recently, it has been found a similar behavior for a biradical organic semiconductor, where HMDS treatment rendered non-active devices, whereas trichlorosilane-derived SAM-treated devices showed ambipolar characteristics.[24] On the contrary, devices fabricated using OTS-treated gate dielectrics give ambipolar performances with quite balanced electron and hole mobilities (Table B.6). During vapour-deposition the substrates were preheated at different temperatures in order to improve film morphology and crystallinity. Analysis of these devices indicates a gradual increase of electron mobility with temperature at the expense of the hole mobility. Nevertheless, mobilities in the range of $10^{-3} - 10^{-2}$ cm^2 V^{-1} s^{-1} are registered for the whole temperature range analyzed. These values are comparable with previously reported for organic biradicals.[24,25] It should be noted that under ambient conditions, **DIAn** behaves solely as a p-type semiconductor, with mobilities as high as 4.5×10^{-2} cm^2 V^{-1} s^{-1}.

Table B.6. OFET electrical data for vapour-deposited films of the material deposited on untreated, HMDS-treated and OTS-treated gate dielectrics. Measurements were carried out in vacuum and in ambient conditions.

		Vaccuum						Air		
		μ_h [cm^{2}V^{-1}s^{-1}]	V_T [V]	Ion/Ioff	μ_e [cm^{2}V^{-1}s^{-1}]	V_T [V]	Ion/Ioff	μ_h [cm^{2}V^{-1}s^{-1}]	V_T [V]	Ion/Ioff
OTS	**150**	2,28E-03	22	5,E+00	3,97E-03	32	5,E+00	2,18E-02	-4	2,E+04
	100	5,19E-03	18	3,E+00	1,22E-03	76	2,E+00	4,53E-02	-2	5,E+04
	Tamb	7,41E-03	8	1,E+01	1,78E-03	27	4,E+00	3,09E-05	10	1,E+04
HMDS	**150**	1,41E-05	15	6,E+00				5,27E-05	-16	4,E+03
	Tamb	3,64E-06	28	3,E+00				8,20E-05	-3	7,E+03
Sintto	**150**	1,10E-05	-11	2,E+03				1,29E-05	-53	4,E+02
	100	1,21E-03	-15	6,E+02				4,06E-05	5	6,E+03
	Tamb	2,68E-04	-18	8,E+02				4,38E-05	3	1,E+03

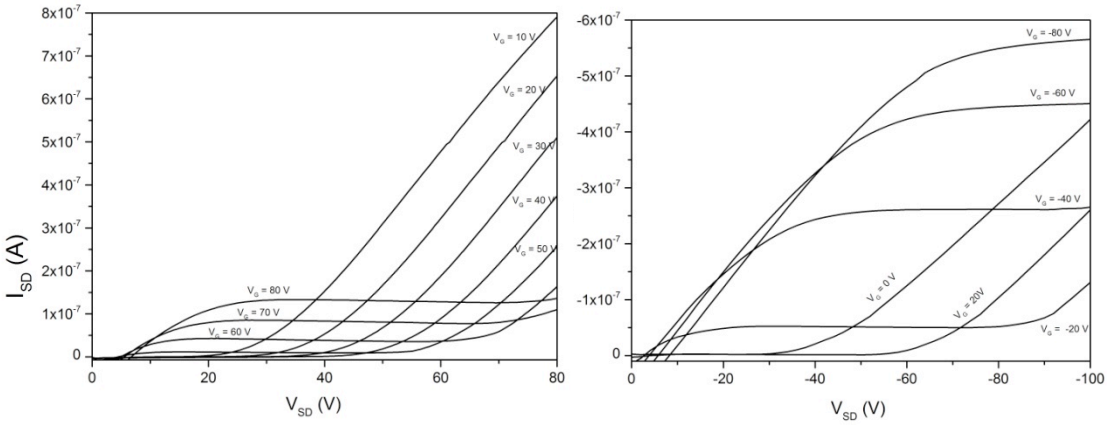

Figure B.22. Selected output plot data for vapour-deposited films grown on OTS-treated Si/SiO_2 substrates: (left) Electron-transport characteristics for films deposited on substrates pre-heated at 150 ºC. (right) Hole-transport characteristics for films deposited at 25 ºC.

Table B.7 shows the electrical performances of solution-processed films. Under these conditions the semiconductor only behaves as a p-type material both under vacuum or ambient environments, showing similar field-effect mobilities to the vapour-deposited devices. Additional improvements are underway to optimize these conditions.

Table B.7. OFET electrical data for solution-processed films of the material deposited on HMDS-treated and OTS-treated gate dielectrics. Measurements were carried out in vacuum and in ambient conditions.

		Vaccuum			Air		
		μ_h [$cm^2V^{-1}s^{-1}$]	V_T [V]	Ion/Ioff	μ_h [$cm^2V^{-1}s^{-1}$]	V_T [V]	Ion/Ioff
OTS [a]	**100**	3,38E-03	-11	5,45E+02	3,32E-03	-19	4,40E+04
	Tamb	1,27E-03	-6	7,53E+02	2,19E-03	-18	4,28E+04
HMDS [b]	**Tamb**	3,18E-06	-20	8,46E+01	2,46E-06	16	3,41E+02

[a]: spin-coating
[b]: drop-casting

APPENDIX C

Variable temperature UV-vis spectroscopy

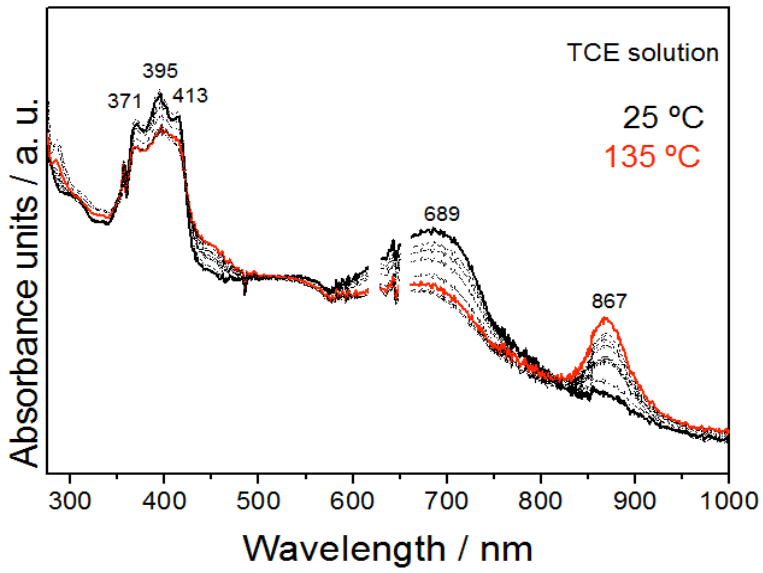

Figure C.1. DIAn in tetrachloroethane from 25 °C to 135 °C. The 689 nm peak corresponding to neutral **DIAn** is fully recovered upon cooling to 25 °C.

Spectroelectrochemistry

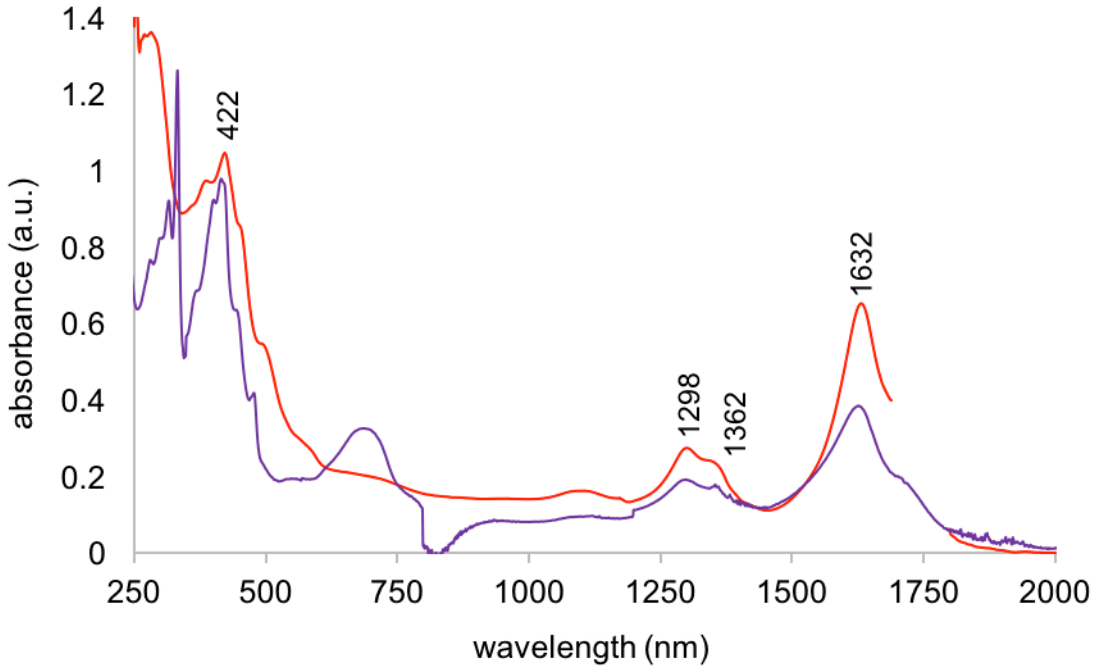

Figure C.2. Comparison of **DIAn**$^{\bullet-}$ (red) generated by contact with K metal in THF and by electrolysis (violet).

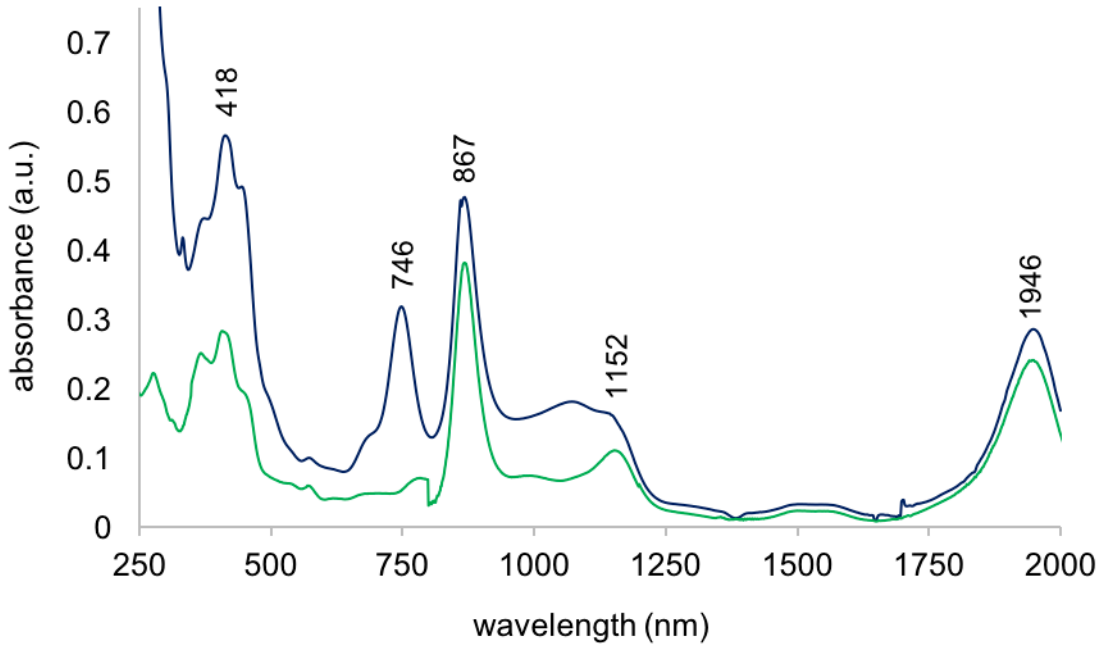

Figure C.3. Comparison of **DIAn**$^{\bullet+}$ (blue) generated by $NOBF_4$ in CH_2Cl_2 and by electrolysis (green). The absorbance at 746 could be due to overoxidation towards **DIAn**$^{2+}$.

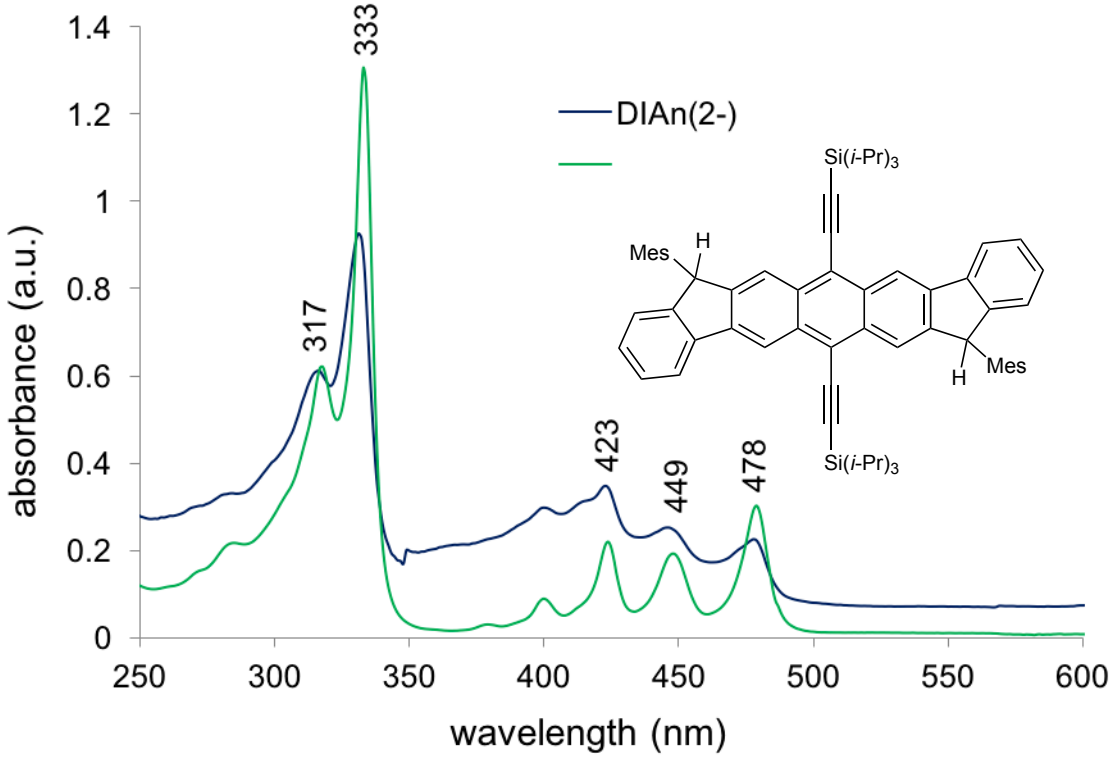

Figure C.4. Comparison of **DIAn**$^{2-}$ prepared by electrolysis (navy) and the **DIAn** precursor (green).

Experimental Details

All manipulations were carried out using break-and-seal[1] and glove-box techniques under an atmosphere of Ar. THF and hexanes were dried over Na/benzophenone and distilled prior to use. THF-d_8 and diglyme were dried over Na/K alloy and distilled prior to use. Potassium was purchased from Strem Chemicals. Crown ether, 18-crown-6 ether, was purchased from Sigma Aldrich and dried over P_2O_5 *in vacuo* for 24 hours. **DIAn** was prepared as described previously.[2] The UV-vis spectra were recorded on a PerkinElmer Lambda 35 spectrometer. The ^{1}H NMR spectra were measured on a Bruker AC-400 spectrometer at 400 MHz and were referenced to the resonances of the corresponding solvent used.

X-ray crystallography

Data collections for **1**, **2**, and **3** were performed on a Bruker D8 VENTURE X-ray diffractometer with PHOTON 100 CMOS detector and mirror-monochromated Cu-Kα radiation (λ= 1.54178 Å) at T = 100(2) K. Data were corrected for absorption effects using the empirical method SADABS.[3] The structures were solved by direct methods and refined using the Bruker SHELXTL (Version 6.14) software package.[4] All non-hydrogen atoms were refined anisotropically. All H-atoms were included at calculated positions and refined as riders, with U_{iso}(H) = 1.2 U_{eq}(C) and U_{iso}(H) = 1.5 U_{eq}(C) for methyl groups. In **1**, two of three isopropyl groups connected to the silicon atom were disordered. The disorder was modelled with two orientations having relative occupancies of 0.70:0.30 and 0.53:0.47 for the two parts. The geometries of the disordered parts were restrained to be similar. The anisotropic displacement parameters of the disordered molecules in the direction of the bonds were restrained to be equal with a standard uncertainty of 0.01 Å^2. They were also restrained to have the same U_{ij} components, with a standard uncertainty of 0.04 Å^2. Two severely disordered solvent THF molecules in the unit cell were removed by the SQUEEZE routine in PLATON. In **2**, one of two

THF molecules coordinated to Na cation was disordered. The disorder was modelled with two orientations having relative occupancies of 0.65:0.35 for the two parts. The geometries of the disordered parts were restrained to be similar. The anisotropic displacement parameters of the disordered molecules in the direction of the bonds were restrained to be equal with a standard uncertainty of 0.01 $Å^2$. They were also restrained to have the same U_{ij} components, with a standard uncertainty of 0.04 $Å^2$. The severely disordered solvent THF molecules were removed by the SQUEEZE routine in PLATON.[5] In **3**, the whole molecule was found to be disordered. The disorder was modelled with two orientations having relative occupancies of 0.50:0.50 for the two parts. The geometries of the disordered parts were restrained to be similar. The anisotropic displacement parameters of the disordered molecules in the direction of the bonds were restrained to be equal with a standard uncertainty of 0.01 $Å^2$. They were also restrained to have the same U_{ij} components, with a standard uncertainty of 0.04 $Å^2$. Two severely disordered solvent THF molecules in the unit cell were removed by the SQUEEZE routine in PLATON.

Table C.1. Crystallographic data for **1**, **2**, and **3**.

Parameter	**1**	**2**	**3**
Empirical formula	$C_{88}H_{116}KO_8Si_2$	$C_{108}H_{156}K_2O_{20}Si_2$	$C_{88}H_{120}K_2O_8Si_2$
M_r	1397.09	1844.71	1440.22
Crystal system	Triclinic	Monoclinic	Triclinic
Space group	*P*-1	$P2_1/c$	*P*-1
a (Å)	11.1538 (4)	14.2971 (6)	9.1690 (4)
b (Å)	18.6855 (7)	31.7860 (15)	15.4719 (7)
c (Å)	20.8179 (7)	13.0756 (6)	17.6353 (7)
α (°)	89.264 (2)	90	66.240 (2)
β (°)	88.812 (2)	94.512 (3)	84.584 (1)
γ (°)	86.356 (2)	90	81.803 (2)
V ($Å^3$)	4328.8 (3)	5923.8 (5)	2264.45 (17)
Z	2	2	1
ρ_{calcd} [$g \cdot cm^{-3}$]	1.424	1.034	1.056
μ [mm^{-1}]	3.39	1.33	1.55
2θ-range [deg]	8.5-148.7	6.2-149.2	5.5-150.0

Reflections collected	82735	196398	51467
no. unique data, R_{int}	16789, 0.084	12111, 0.096	9027,0.046
no. obsd data [$I \geq 2\sigma(I)$]	12509	9254	6705
R_1[a]	0.060	0.076	0.059
wR_2[b]	0.145	0.199	0.151
Data/restraints/parameters	16789/900/1198	12111/151/632	9027/1528/856
Quality-of-fit[c]	1.05	1.09	1.04
peak/hole [e·Å^{-3}]	1.21/-0.80	0.50/-0.46	0.33/-0.25

[a] $R_1 = \Sigma||F_o|-|F_c||/\Sigma|F_o|$. [b] $wR_2 = [\Sigma[w(F_o^2-F_c^2)^2]/\Sigma[w(F_o^2)^2]]^{½}$. [c] Quality-of-fit = $[\Sigma[w(F_o^2-F_c^2)^2]/(N_{obs}-N_{params})]^{½}$, based on all data.

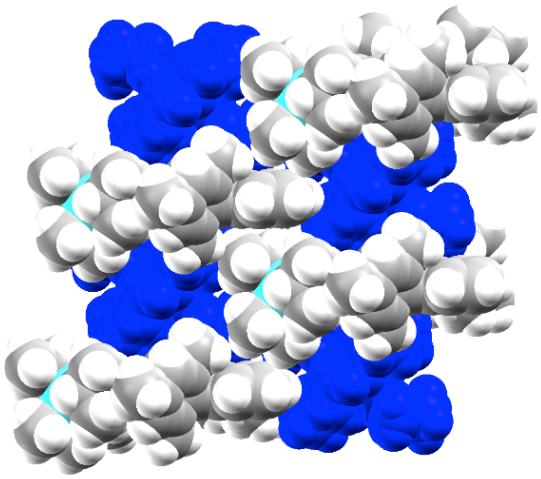

Figure C.5. Solid-state packing of **1**, space-filling model. The $[\{K(18\text{-crown-6})(THF)_2\}]^+$ cations are shown in dark blue.

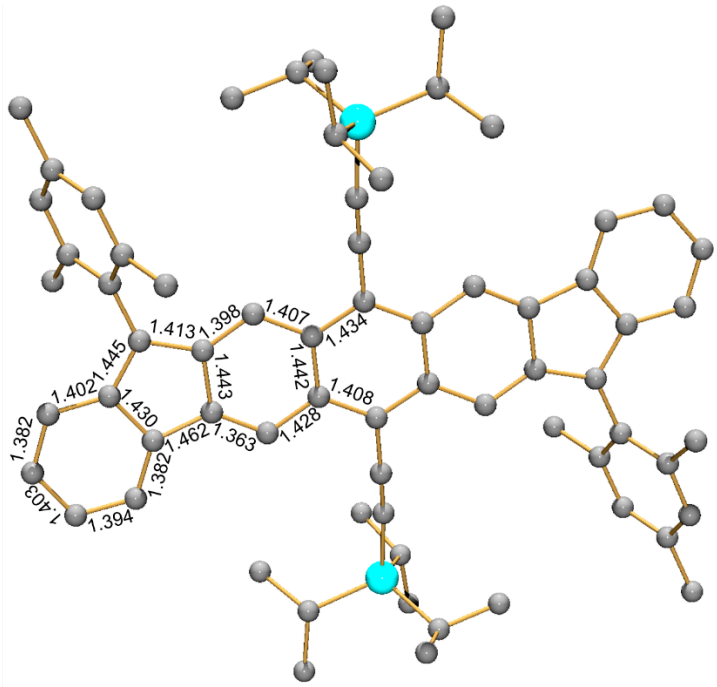

Figure C.6. Key bond distances (Å) in the core of [{K(18-crown-6)(THF)$_2$}DIAn$^{\bullet-}$] (**1**).

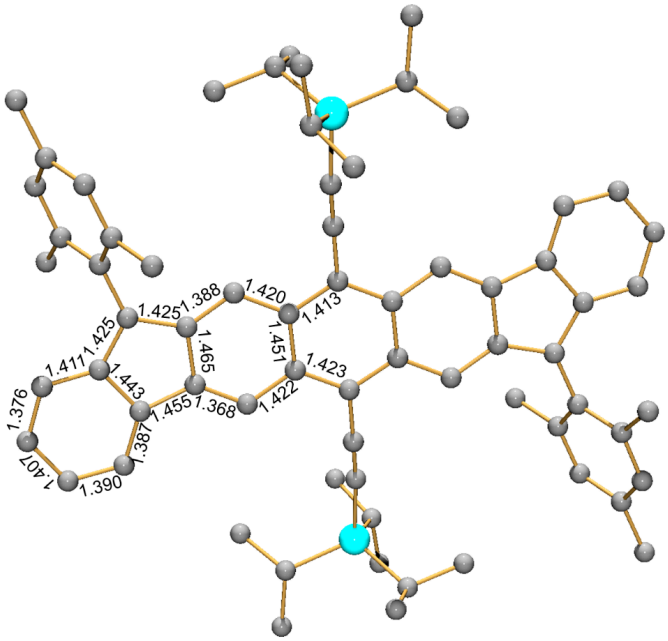

Figure C.7. Key bond distances (Å) in the core of [{K(18-crown-6)(THF)$_2$}$_2$DIAn^{2-}] (**2**).

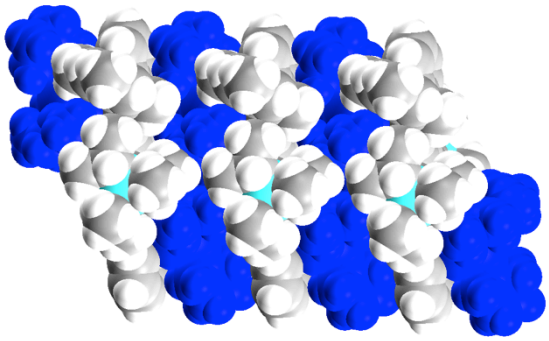

Figure C.8. Solid-state packing of **3**. The [{K(diglyme)(THF)}]$^{+}$ cations are shown in dark blue.

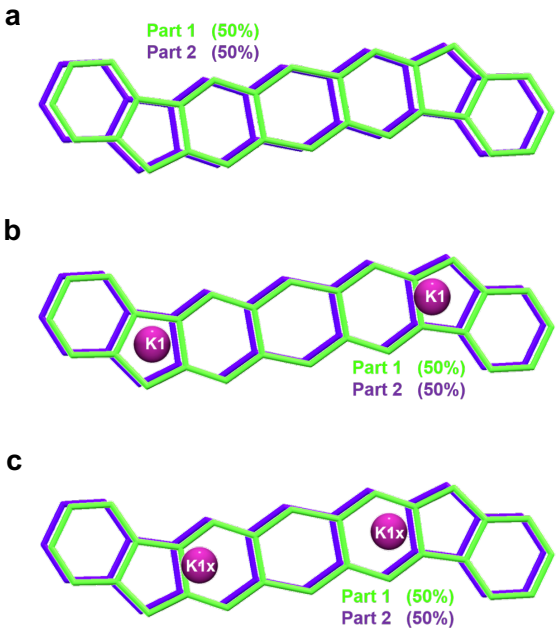

Figure C.9. The anion and K ion are disordered over two orientations in **3**, which were resolved as part 1 and part 2. Disorder of the **DIAn**$^{2-}$ core (a), and binding of K ions (b and c).

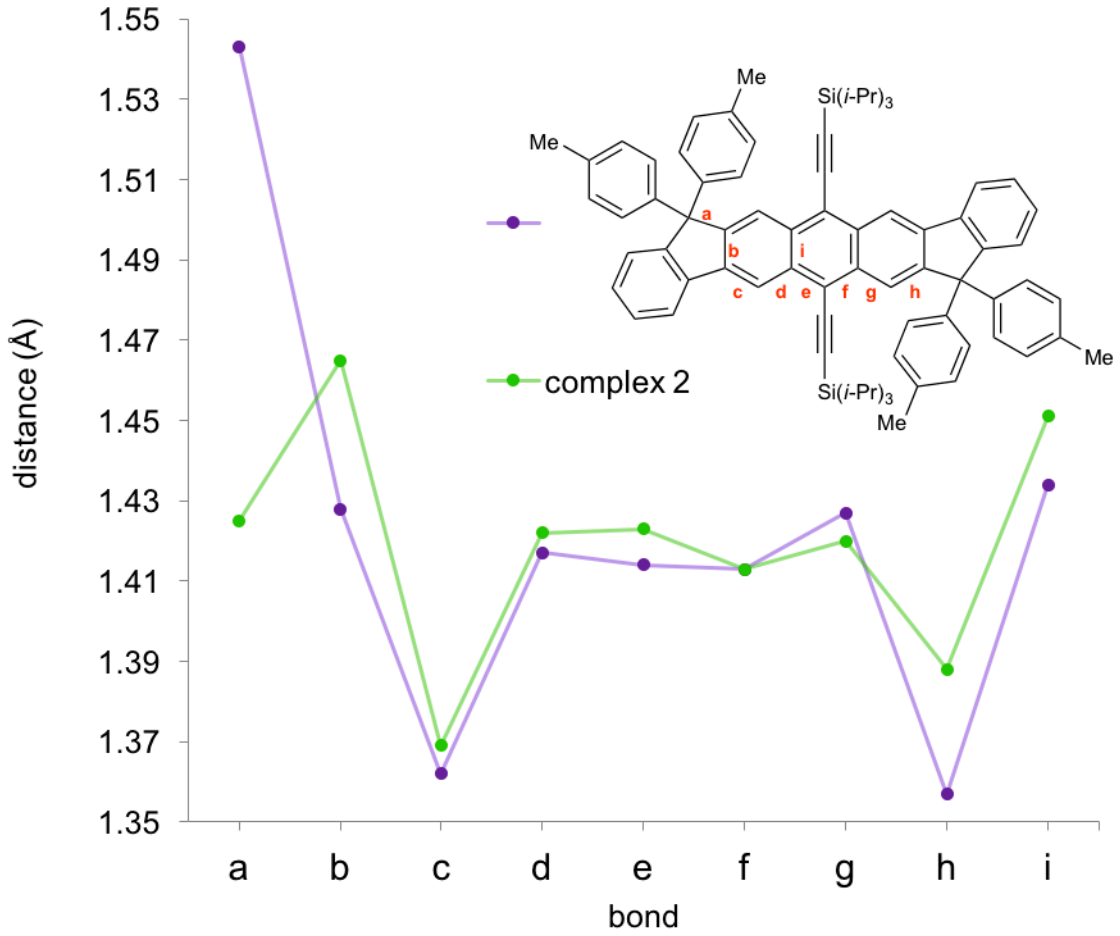

Figure C.10. Comparison of the solid-state structures of the non-contact ion pair **2** (green) and a tetrakis-*p*-tolyl **DIAn** derivative (violet). Bond lettering shown in red.

Computational Section

Table C.2. TD-UB3LYP/6-311+G** result of low lying states with non-zero f in neutral state.

state	configuration	E	f
2	H-1a => La (0.43) Ha => La (-0.28) Ha => L+1a (0.46) H-1a => Lb (-0.43) Hb => Lb (0.28) Hb => L+1b (0.46)	1.5490 eV (800.43 nm)	0.0950
3	H-1a => La (-0.14) H-1a => L+1a (0.13) Ha => La (-0.62) Ha => L+1a (-0.27) H-1b => Lb (0.14) H-1b => L+1b (0.13) Hb => Lb (0.62) Hb => L+1b (-0.27)	1.7264 eV (718.17 nm)	0.5228

Table C.3. TD-UB3LYP/6-311+G** result of low lying states with non-zero f in mono-anionic state.

state	configuration	E	f
1	H-1a=>La (-0.10) Sa=>La (0.51) Hb=>Sb (0.84)	0.8595 eV (1442.58 nm)	0.1841
2	H-1a=>La (0.17) Sa=>La (0.84) H-2b=>Lb (0.11) Hb=>Sb (-0.49)	1.0229 eV (1212.05 nm)	0.2244

Table C.4. TD-U(R)B3LYP/6-311+G** result of low lying states with non-zero f in dianionic state [restricted wavefunction]

state	configuration	E	f
2	Ha=>La (0.71) Hb=>Lb (-0.71)	0.9589 eV (1293.00 nm)	0.0785

Table C.5. TD-UB3LYP/6-311+G** result of low lying states with non-zero f in mono-cationic state

state	configuration	E	f
1	Sa=>La (0.90) H-1b=>Sb (-0.13) Hb=>Sb (0.39) Hb=>L+1b (-0.12)	0.8524 eV (1454.59 nm)	0.1663
3	Sa=>La (-0.31) H-6b=>Lb (-0.12) H-3b=>Sb (-0.20) H-1b=>Sb (-0.30) Hb=>Sb (0.87)	1.3178 eV (940.87 nm)	0.1183

Table C.6. TD-U(R)B3LYP/6-311+G** result of low lying states with non-zero f in dicationic state [restricted wavefunction]

state	configuration	E	f
2	Ha=>La (0.68) Hb=>Lb (0.68) H-3a=>La (0.19) H-3b=>Lb (0.19)	1.0894 eV (1138.13 nm)	0.1811

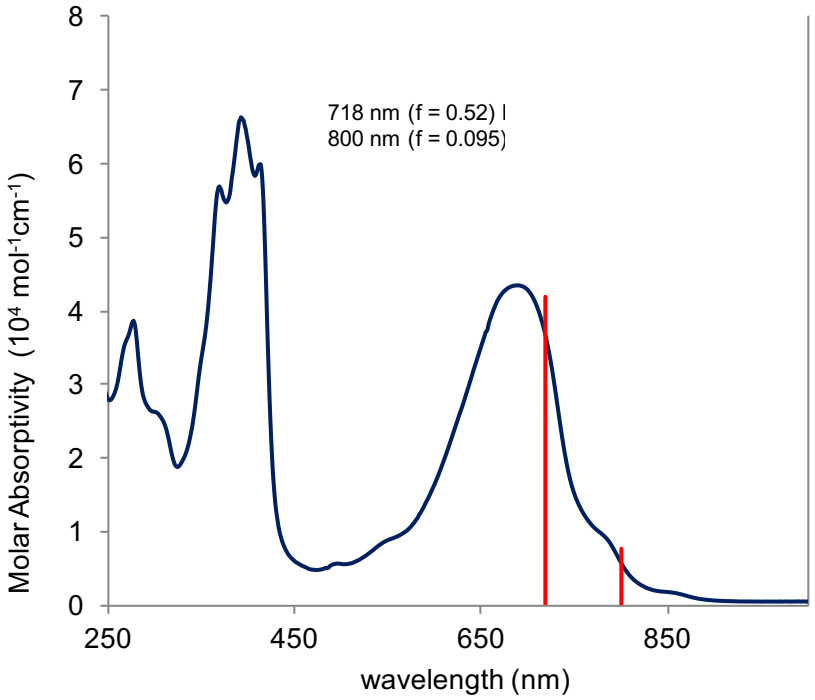

Figure C.11. Electronic absorption spectra of neutal **DIAn** and and electronic transitions from TD-DFT calculation.

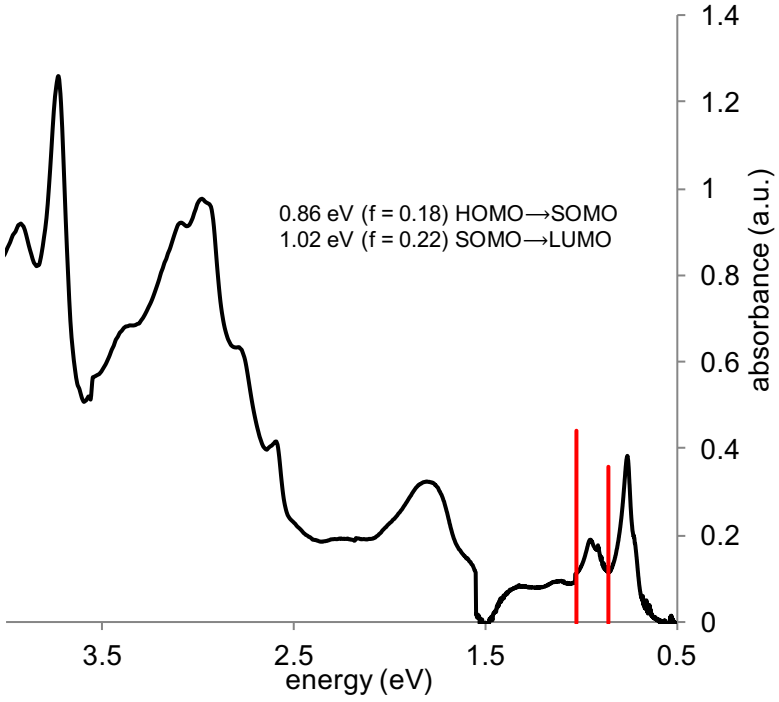

Figure C.12. DIAn$^{\bullet-}$ generated by electrolysis and electronic transitions from TD-DFT calculation.

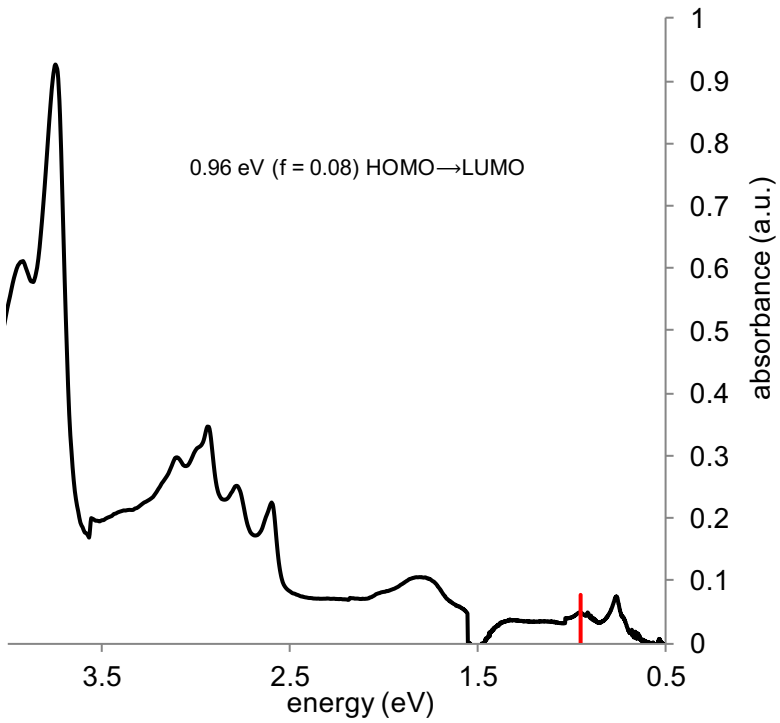

Figure C.13. $DIAn^{2-}$ generated by electrolysis and electronic transitions from TD-DFT calculation.

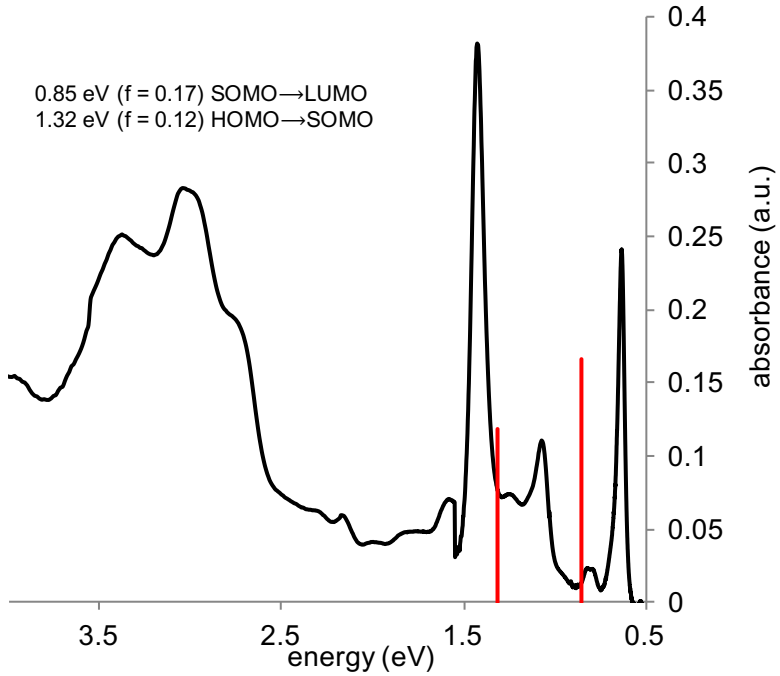

Figure C.14. $DIAn^{\bullet+}$ generated by electrolysis and electronic transitions from TD-DFT calculation.

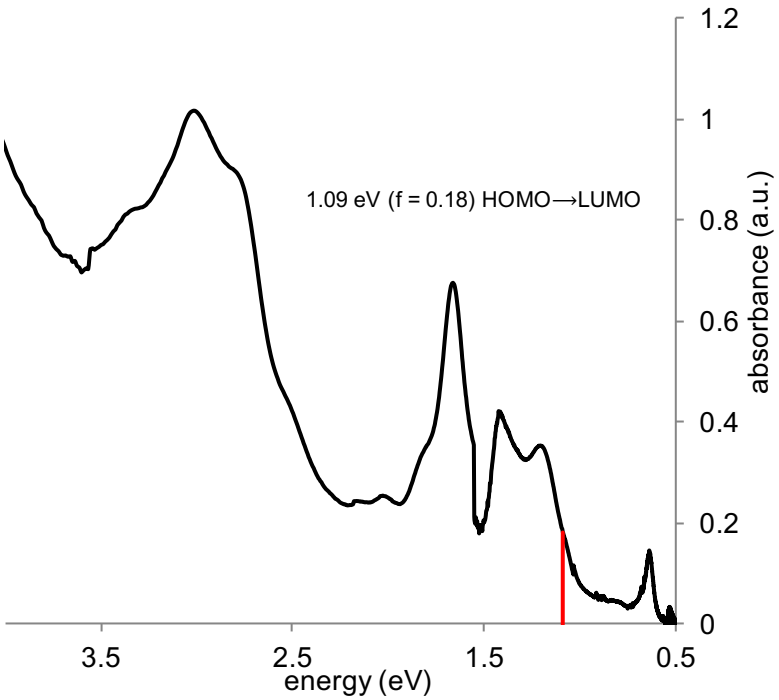

Figure C.15. $DIAn^{2+}$ generated by electrolysis and electronic transitions from TD-DFT calculation.

REFERENCES CITED

Chapter I

1) Barth, W. E.; Lawton, R. G. *J. Am. Chem. Soc.* **1966**, *88*, 380–381.

2) Scott, L. T.; Boorum, M. M.; McMahon, B. J.; Hagen, S.; Mack, J.; Blank, J.; Wegner, H.; de Meijere, A. *Science* **2002**, *295*, 1500–1503.

3) Scott, L. T.; Jackson, E. A.; Zhang, Q.; Steinberg, B. D.; Bancu, M.; Li, B. *J. Am. Chem. Soc.* **2012**, *134*, 107–110.

4) Sanchez-Valencia, J. R.; Dienel, T.; Gröning, O.; Shorubalko, I.; Mueller, A.; Jansen, M.; Amsharov, K.; Ruffieux, P.; Fasel, R. *Nature* **2014**, *512*, 61–64.

5) Bendikov, M.; Wudl, F.; Perepichka, D. F. *Chem. Rev.* **2004**, *104*, 4891–4946.

6) Anthony, J. E. *Chem. Rev.* **2006**, *106*, 5028–5048.

7) Anthony, J. E. *Angew. Chem. Int. Ed.* **2008**, *47*, 452–483.

8) Harvey, R. G. Polycyclic Aromatic Hydrocarbons; Wiley-VCH: Weinheim, Germany, 1997.

9) Minsky, A.; Meyer, A. Y.; Hafner, K.; Rabinovitz, M. *J. Am. Chem. Soc.* **1983**, *105*, 3975–3981.

10) Randić, M. *Chem. Rev.* **2003**, *103*, 3449–3606.

11) Trost, B.; Bright, G. *J. Am. Chem. Soc.* **1968**, *90*, 2732–2732.

12) Trost, B. M.; Bright, G. M.; Frihart, C.; Brittelli, D. *J. Am. Chem. Soc.* **1971**, *93*, 737–745.

13) Diogo, H. P.; Kiyobayashi, T.; Minas da Piedade, M. E.; Burlak, N.; Rogers, D. W.; McMasters, D.; Persy, G.; Wirz, J.; Liebman, J. F. *J. Am. Chem. Soc.* **2002**, *124*, 2065–2072.

14) Dang, H.; Garcia-Garibay, M. A. *J. Am. Chem. Soc.* **2001**, *123*, 355–356.

15) Dang, H.; Levitus, M.; Garcia-Garibay, M. A. *J. Am. Chem. Soc.* **2002**, *124*, 136–143.

16) Wood, J. D.; Jellison, J. L.; Finke, A. D.; Wang, L.; Plunkett, K. N. *J. Am. Chem. Soc.* **2012**, *134*, 15783–15789.

17) Wegner, H. A.; Scott, L. T.; de Meijere, A. *J. Org. Chem.* **2003**, *68*, 883–887.

18) Kung, Y.-H.; Cheng, Y.-S.; Tai, C.-C.; Liu, W.-S.; Shin, C.-C.; Ma, C.-C.; Tsai, Y.-C.; Wu, T.-C.; Kuo, M.-Y.; Wu, Y.-T. *Chem. Eur. J.* **2010**, *16*, 5909–5919.

19) Lee, Y.-H.; Wu, T.-C.; Liaw, C.-W.; Wen, T.-C.; Guo, T.-F.; Wu, Y.-T. *J. Mater. Chem.* **2012**, *22*, 11032.

20) Lee, Y.-H.; Wu, T.-C.; Liaw, C.-W.; Wen, T.-C.; Feng, S.-W.; Lee, J.-J.; Wu, Y.-T.; Guo, T.-F. *Org. Electron.* **2013**, *14*, 1064–1072.

21) Amsharov, K. Y.; Kabdulov, M. A.; Jansen, M. *Angew. Chem. Int. Ed.* **2012**, *51*, 4594–4597.

22) Jellison, J. L.; Lee, C.-H.; Zhu, X.; Wood, J. D.; Plunkett, K. N. *Angew. Chem. Int. Ed.* **2012**, *51*, 12321–12324.

23) Xia, H.; Liu, D.; Xu, X.; Miao, Q. *Chem. Commun.* **2013**, *49*, 4301.

24) Lütke Eversloh, C.; Avlasevich, Y.; Li, C.; Müllen, K. *Chem. Eur. J.* **2011**, *17*, 12756–12762.

25) Lee, C.-H.; Plunkett, K. N. *Org. Lett.* **2013**, *15*, 1202–1205.

26) Takeya, J.; Yamagishi, M.; Tominari, Y.; Hirahara, R.; Nakazawa, Y.; Nishikawa, T.; Kawase, T.; Shimoda, T.; Ogawa, S. *Appl. Phys. Lett.* **2007**, *90*, 102120-

27) Reese, C.; Bao, Z. *J. Mater. Chem.* **2006**, *16*, 329–333.

28) Gu, X.; Luhman, W. A.; Yagodkin, E.; Holmes, R. J.; Douglas, C. J. *Org. Lett.* **2012**, *14*, 1390–1393.

29) Lee, H.; Zhang, Y.; Zhang, L.; Mirabito, T.; Burnett, E. K.; Trahan, S.; Mohebbi, A. R.; Mannsfeld, S. C. B.; Wudl, F.; Briseno, A. L. *J. Mater. Chem. C* **2014**, *2*, 3361.

30) Brand, K. *Ber.* **1912**, *45*, 3071–3077.

31) Blood, C. T.; Linstead, R. P. *J. Chem. Soc.* **1952**, 2263.

32) Hopf, H. *Angew. Chem. Int. Ed.* **2013**, *52*, 12224–12226.

33) Bally, T.; Chai, S.; Neuenschwander, M.; Zhu, Z. *J. Am. Chem. Soc.* **1997**, *119*, 1869–1875.

34) Le Goff, E. *J. Am. Chem. Soc.* **1962**, *84*, 3975–3976.

35) Hafner, K.; Süss, H. U. *Angew. Chem. Int. Ed. Engl.* **1973**, *12*, 575–577.

36) Chuen, C. C.; Fenton, S. W. *J. Org. Chem.* **1958**, *23*, 1538–1539.

37) Chakraborty, M.; Tessier, C. A.; Youngs, W. J. *J. Org. Chem.* **1999**, *64*, 2947–2949.

38) Babu, G.; Orita, A.; Otera, J. *Chem. Lett.* **2008**, *37*, 1296–1297.

39) Xu, F.; Peng, L.; Orita, A.; Otera, J. *Org. Lett.* **2012**, *14*, 3970–3973.

40) Kawase, T.; Konishi, A.; Hirao, Y.; Matsumoto, K.; Kurata, H.; Kubo, T. *Chem. Eur. J.* **2009**, *15*, 2653–2661.

41) Zhang, H.; Karasawa, T.; Yamada, H.; Wakamiya, A.; Yamaguchi, S. *Org. Lett.* **2009**, *11*, 3076–3079.

42) Saito, M.; Nakamura, M.; Tajima, T.; Yoshioka, M. *Angew. Chem. Int. Ed.* **2007**, *46*, 1504–1507.

43) Saito, M.; Nakamura, M.; Tajima, T. *Chem. Eur. J.* **2008**, *14*, 6062–6068.

44) Kuwabara, T.; Ishimura, K.; Sasamori, T.; Tokitoh, N.; Saito, M. *Chem. Eur. J.* **2014**, *20*, 7571–7575.

45) Levi, Z. U.; Tilley, T. D. *J. Am. Chem. Soc.* **2009**, *131*, 2796–2797.

46) Jeffrey, J. L.; Sarpong, R. *Tetrahedron Lett.* **2009**, *50*, 1969–1972.

47) Levi, Z. U.; Tilley, T. D. *J. Am. Chem. Soc.* **2010**, *132*, 11012–11014.

48) Hashmi, A. S. K.; Wieteck, M.; Braun, I.; Nösel, P.; Jongbloed, L.; Rudolph, M.; Rominger, F. *Adv. Synth. Catal.* **2012**, *354*, 555–562.

49) Maekawa, T.; Segawa, Y.; Itami, K. *Chem. Sci.* **2013**, *4*, 2369–2373.

50) Zhao, J.; Oniwa, K.; Asao, N.; Yamamoto, Y.; Jin, T. *J. Am. Chem. Soc.* **2013**, *135*, 10222–10225.

51) Shen, J.; Yuan, D.; Qiao, Y.; Shen, X.; Zhang, Z.; Zhong, Y.; Yi, Y.; Zhu, X. *Org. Lett.* **2014**, *16*, 4924–4927.

52) Subramanian, S.; Park, S. K.; Parkin, S. R.; Podzorov, V.; Jackson, T. N.; Anthony, J. E. *J. Am. Chem. Soc.* **2008**, *130*, 2706–2707.

53) Cho, D. M.; Parkin, S. R.; Watson, M. D. *Org. Lett.* **2005**, *7*, 1067–1068.

54) Li, H.; Wang, X.-Y.; Wei, B.; Xu, L.; Zhang, W.-X.; Pei, J.; Xi, Z. *Nat. Commun.* **2014**, *5*, 4508.

55) Kawase, T.; Fujiwara, T.; Kitamura, C.; Konishi, A.; Hirao, Y.; Matsumoto, K.; Kurata, H.; Kubo, T.; Shinamura, S.; Mori, H.; Miyazaki, E.; Takimiya, K. *Angew. Chem. Int. Ed.* **2010**, *49*, 7728–7732.

56) Yamamoto, T.; Shinamura, S.; Miyazaki, E.; Takimiya, K. *Bull. Chem. Soc. Jpn.* **2010**, *83*, 120–130.Nakano, M.; Osaka, I.; Takimiya, K.; Koganezawa, T. *J. Mater. Chem. C* **2014**, *2*, 64–70.

57) Fix, A. G.; Chase, D. T.; Haley, M. M. *Topics in Current Chemistry (Polyarenes I), Volume 349*; Siegel, J. S., Wu, Y.-T., Eds.; Springer: Berlin, Germany, **2014**, pp 159-195.

58) Wang, Z.; Kim, C.; Facchetti, A.; Marks, T. J. *J. Am. Chem. Soc.* **2007**, *129*, 13362–13363.

59) Mei, J.; Diao, Y.; Appleton, A. L.; Fang, L.; Bao, Z. *J. Am. Chem. Soc.* **2013**, *135*, 6724–6746.

60) Zhao, Y.; Guo, Y.; Liu, Y. *Adv. Mater.* **2013**, *25*, 5372–5391.

61) Ito, S.; Minami, T.; Nakano, M. *J. Phys. Chem. C* **2012**, *116*, 19729–19736.

62) Sun, Z.; Ye, Q.; Chi, C.; Wu, J. *Chem. Soc. Rev.* **2012**, *41*, 7857–7889.

63) Abe, M. *Chem. Rev.* **2013**, *113*, 7011–7088.

64) Fabian, J.; Nakazumi, H.; Matsuoka, M. *Chem. Rev.* **1992**, *92*, 1197–1226.

65) Morita, Y.; Suzuki, S.; Sato, K.; Takui, T. *Nat. Chem.* **2011**, *3*, 197–204.

66) Chase, D. T.; Rose, B. D.; McClintock, S. P.; Zakharov, L. N.; Haley, M. M. *Angew. Chem. Int. Ed.* **2011**, *50*, 1127–1130.

67) Zhou, Q.; Carroll, P. J.; Swager, T. M. *J. Org. Chem.* **1994**, *59*, 1294–1301.

68) Chase, D. T.; Fix, A. G.; Rose, B. D.; Weber, C. D.; Nobusue, S.; Stockwell, C. E.; Zakharov, L. N.; Lonergan, M. C.; Haley, M. M. *Angew. Chem. Int. Ed.* **2011**, *50*, 11103–11106.

69) Chase, D. T.; Fix, A. G.; Kang, S. J.; Rose, B. D.; Weber, C. D.; Zhong, Y.; Zakharov, L. N.; Lonergan, M. C.; Nuckolls, C.; Haley, M. M. *J. Am. Chem. Soc.* **2012**, *134*, 10349–10352.

70) Reisch, H.; Wiesler, U.; Scherf, U.; Tuytuylkov, N. *Macromolecules* **1996**, *29*, 8204–8210.

71) Nishida, J.-I.; Tsukaguchi, S.; Yamashita, Y. *Chem. Eur. J.* **2012**, *18*, 8964–8970.

72) Shimizu, A.; Tobe, Y. *Angew. Chem. Int. Ed.* **2011**, *50*, 6906–6910.

73) Miyoshi, H.; Nobusue, S.; Shimizu, A.; Hisaki, I.; Miyata, M.; Tobe, Y. *Chem. Sci.* **2014**, *5*, 163–168.

74) Shimizu, A.; Kishi, R.; Nakano, M.; Shiomi, D.; Sato, K.; Takui, T.; Hisaki, I.; Miyata, M.; Tobe, Y. *Angew. Chem. Int. Ed.* **2013**, *52*, 6076–6079.

75) Pansare, V. J.; Hejazi, S.; Faenza, W. J.; Prud'homme, R. K. *Chem. Mater.* **2012**, *24*, 812–827.

76) Fix, A. G.; Deal, P. E.; Vonnegut, C. L.; Rose, B. D.; Zakharov, L. N.; Haley, M. M. *Org. Lett.* **2013**, *15*, 1362–1365.

77) Paudel, K.; Johnson, B.; Thieme, M.; Haley, M. M.; Payne, M. M.; Anthony, J. E.; Ostroverkhova, O. *Appl. Phys. Lett.* **2014**, *105*, 043301-1–043301-4

78) Rose, B. D.; Vonnegut, C. L.; Zakharov, L. N.; Haley, M. M. *Org. Lett.* **2012**, *14*, 2426–2429.

79) Preis, E.; Scherf, U. *Macromol. Rapid Commun.* **2006**, *27*, 1105–1109.

80) Kamada, K.; Ohta, K.; Shimizu, A.; Kubo, T.; Kishi, R.; Takahashi, H.; Botek, E.; Champagne, B.; Nakano, M. *J. Phys. Chem. Lett.* **2010**, *1*, 937–940.

81) Rose, B. D.; Shoer, L. E.; Wasielewski, M. R.; Haley, M. M. *Chem. Phys. Lett.* **2014**, *616-617*, 137–141.

82) de Oteyza, D. G.; Gorman, P.; Chen, Y. C.; Wickenburg, S.; Riss, A.; Mowbray, D. J.; Etkin, G.; Pedramrazi, Z.; Tsai, H. Z.; Rubio, A.; Crommie, M. F.; Fischer, F. R. *Science* **2013**, *340*, 1434–1437.

83) Gundlach, D. J.; Royer, J. E.; Park, S. K.; Subramanian, S.; Jurchescu, O. D.; Hamadani, B. H.; Moad, A. J.; Kline, R. J.; Teague, L. C.; Kirillov, O.; Richter, C. A.; Kushmerick, J. G.; Richter, L. J.; Parkin, S. R.; Jackson, T. N.; Anthony, J. E. *Nat. Mater.* **2008**, *7*, 216–221.

84) Roncali, J. *Chem. Rev.* **1997**, *97*, 173–206.

85) Briseno, A. L.; Miao, Q.; Ling, M.-M.; Reese, C.; Meng, H.; Bao, Z.; Wudl, F. *J. Am. Chem. Soc.* **2006**, *128*, 15576–15577.

86) Payne, M. M.; Odom, S. A.; Parkin, S. R.; Anthony, J. E. *Org. Lett.* **2004**, *6*, 3325–3328.

87) Payne, M. M.; Parkin, S. R.; Anthony, J. E.; Kuo, C.-C.; Jackson, T. N. *J. Am. Chem. Soc.* **2005**, *127*, 4986–4987.

88) Rudebusch, G. E.; Fix, A. G.; Henthorn, H. A.; Vonnegut, C. L.; Zakharov, L. N.; Haley, M. M. *Chem. Sci.* **2014**, *5*, 3627–3633.

89) Shi, X.; Burrezo, P. M.; Lee, S.; Zhang, W.; Zheng, B.; Dai, G.; Chang, J.; López Navarrete, J. T.; Huang, K.-W.; Kim, D.; Casado, J.; Chi, C. *Chem. Sci.* **2014**, *5*, 4490–4503.

Chapter II

1) Casado, J.; Ponce Ortiz, R.; López Navarrete, J. T. *Chem. Soc. Rev.*, **2012**, *41*, 5672–5686.

2) Pappenfus, T. M.; Chesterfield, R. J.; Frisbie, C. D.; Mann, K. R.; Casado, J.; Raff, J. D.; and Miller, L. L.; *J. Am. Chem. Soc.*, **2002**, *124*, 4184–4185.

3) Chesterfield, R. J.; Newman, C. R.; Pappenfus, T. M.; Ewbank, P. C.; Haukaas, M. H.; Mann, K. R.; Miller, L. L.; Frisbie, C. D. *Adv. Mater.* **2003**, *15* (15), 1278.

4) Takahashi, T.; Matsuoka, K.-I.; Takimiya, K.; Otsubo, T.; Aso, Y. *J. Am. Chem. Soc.* **2005**, *127*, 8928.

5) Ponce Ortiz, R.; Casado, J.; Hernández, V.; López Navarrete, J. T.; Viruela, P. M.; Ortí, E.; Takimiya, K.; Otsubo, T. *Angew. Chem. Int. Ed.* **2007**, *46*, 9057.

6) Handa, S.; Miyazaki, E.; Takimiya, K.; Kunugi, Y. *J. Am. Chem. Soc.* **2007**, *129*, 11684.

7) Wu, Q.; Li, R.; Hong, W.; Li, H.; Gao, X.; Zhu, D. *Chem. Mater.* **2011**, *23*, 3138.

8) (*a*) Lanata, M.; Bertarelli, C.; Gallazzi, M. C.; Bianco, A.; Del Zoppo, M.; Zerbi, G. *Synthetic Metals* **2003**, *138* (1-2), 357–362; (*b*) Raymond, J. E.; Casado, J.; López Navarrete, J. T.; Takimiya, K.; Goodson, T., III. *J. Phys. Chem. Lett.* **2011**, *2*, 2179.

9) (*a*) Paci, I.; Johnson, J. C.; Chen, X.; Rana, G.; Popović, D.; David, D. E.; Nozik, A. J.; Ratner, M. A.; Michl, J. *J. Am. Chem. Soc.* **2006**, *128*, 16546–16553; (*b*) Minami, T.; Nakano, M. *J. Phys. Chem. Lett.* **2012**, *3*, 145–150.

10) Fix, A. G.; Chase, D. T.; Haley, M. M. *Topics in Current Chemistry (Polyarenes I), Volume 349*; Siegel, J. S., Wu, Y.-T., Eds.; Springer: Berlin, Germany, **2014**, pp 159-195.

11) (*a*) Chase, D. T.; Rose, B. D.; McClintock, S. P.; Zakharov, L. N.; Haley, M. M. *Angew. Chem. Int. Ed. Engl.* **2011**, *50*, 1127-1130; (*b*) Chase, D. T.; Fix, A. G.; Rose, B. D.; Weber, C. D.; Nobusue, S.; Stockwell, C. E.; Zakharov, L. N.; Lonergan, M. C.; Haley, M. M. *Angew. Chem. Int. Ed.* **2011**, *50*, 11103–11106; (*c*) Chase, D. T.; Fix, A. G.; Kang, S. J.; Rose, B. D.; Weber, C. D.; Zhong, Y.; Zakharov, L. N.; Lonergan, M. C.; Nuckolls, C.; Haley, M. M. *J. Am. Chem. Soc.* **2012**, *134*, 10349–10352.

12) Fix, A. G.; Deal, P. E.; Vonnegut, C. L.; Rose, B. D.; Zakharov, L. N.; Haley, M. M. *Org. Lett.* **2013**, *15*, 1362–1365.

13) Rose, B. D.; Vonnegut, C. L.; Zakharov, L. N.; Haley, M. M. *Org. Lett.* **2012**, *14*, 2426–2429.

14) Young, B. S.; Chase, D. T.; Marshall, J. L.; Vonnegut, C. L.; Zakharov, L. N.; Haley, M. M. *Chem. Sci.* **2014**, *5*, 1008–1014.

15) (*a*) Payne, M. M.; Odom, S. A.; Parkin, S. R.; Anthony, J. E. *Org. Lett.* **2004**, *6*, 3325–3328; (*b*) Payne, M. M.; Parkin, S. R.; Anthony, J. E.; Kuo, C.-C.; Jackson, T. N. *J. Am. Chem. Soc.* **2005**, *127*, 4986–4987; (*c*) Takimiya, K.; Shinamura, S.; Osaka, I.; Miyazaki, E. *Adv. Mater.* **2011**, *23*, 4347–4370; (*d*) Briseno, A. L.; Miao, Q.; Ling, M.-M.; Reese, C.; Meng, H.; Bao, Z.; Wudl, F. *J. Am. Chem. Soc.* **2006**, *128*, 15576–15577.

16) (*a*) Anthony, J. E.; Brooks, J. S.; Eaton, D. L.; Parkin, S. R. *J. Am. Chem. Soc.* **2001**, *123*, 9482–9483; (*b*) Anthony, J. E. *Chem. Rev.* **2006**, *106*, 5028–5048.

17) (*a*) Barder, T. E.; Walker, S. D.; Martinelli, J. R.; Buchwald, S. L. *J. Am. Chem. Soc.* **2005**, *127*, 4685–4696; (*b*) Nicolaus, N.; Franke, P. T.; Lautens, M. *Org. Lett.* **2011**, *13*, 4236–4239.

18) Fuller, L. S.; Iddon, B.; Smith, K. A. *J. Chem. Soc., Perkin Trans. 1* **1997**, No. 22, 3465–3470.

19) Henssler, J. T.; Matzger, A. J. *Org. Lett.* **2009**, *11*, 3144–3147.

20) Reiss, H.; Heller, A. *J. Phys. Chem.*, **1985**, *89*, 4207–4213.

21) Yui, K.; Ishida, H.; Aso, Y.; Otsubo, T.; Ogura, F.; Kawamoto, A.; Tanaka, J. *Bull. Chem. Soc. Jpn.* **1989**, *62*, 1547–1555.

22) Rose, B. D.; Sumner, N. J.; Filatov, A. S.; Peters, S. J.; Zakharov, L. N.; Petrukhina, M. A.; Haley, M. M. *J. Am. Chem. Soc.* **2014**, *136*, 9181–9189.

23) Yui, K.; Ishida, H.; Aso, Y.; Otsubo, T.; Ogura, F.; Kawamoto, A.; Tanaka, J. *Bull. Chem. Soc. Jpn.* **1989**, *62*, 1547–1555.

24) Frey, J.; Bond, A. D.; Holmes, A. B. *Chem. Commun.* **2002**, 2424–2425.

Chapter III

1) Tschitschibabin, A. E. *Chem. Ber.* **1907**, *40*, 1810–1819.

2) Montgomery, L. K.; Huffman, J. C.; Jurczak, E. A.; Grendze, M. P. *J. Am. Chem. Soc.* **1986**, *108*, 6004–6011.

3) Doehnert, D.; Koutecky, J. *J. Am. Chem. Soc.* **1980**, *102*, 1789–1796.

4) Yamaguchi, K.; Kawakami, T.; Takano, Y.; Kitagawa, Y.; Yamashita, Y.; Fujita, H. *Int. J. Quantum Chem.* **2002**, *90*, 370–385.

5) Abe, M. *Chem. Rev.* **2013**, *113*, 7011–7088.

6) Karafiloglou, P. *J. Chem. Educ.* **1989**, *66*, 816–818.

7) Shimizu, A.; Kishi, R.; Nakano, M.; Shiomi, D.; Sato, K.; Takui, T.; Hisaki, I.; Miyata, M.; Tobe, Y. *Angew. Chem. Int. Ed.* **2013**, *52*, 6076–6079.

8) Kubo, T.; Shimizu, A.; Sakamoto, M.; Uruichi, M.; Yakushi, K.; Nakano, M.; Shiomi, D.; Sato, K.; Takui, T.; Morita, Y.; Nakasuji, K. *Angew. Chem. Int. Ed.* **2005**, *44*, 6564–6568.

9) Li, Y.; Heng, W.-K.; Lee, B. S.; Aratani, N.; Zafra, J. L.; Bao, N.; Lee, R.; Sung, Y. M.; Sun, Z.; Huang, K.-W.; Webster, R. D.; López Navarrete, J. T.; Kim, D.; Osuka, A.; Casado, J.; Ding, J.; Wu, J. *J. Am. Chem. Soc.* **2012**, *134*, 14913–14922.

10) Konishi, A.; Hirao, Y.; Nakano, M.; Shimizu, A.; Botek, E.; Champagne, B.; Shiomi, D.; Sato, K.; Takui, T.; Matsumoto, K.; Kurata, H.; Kubo, T. *J. Am. Chem. Soc.* **2010**, *132*, 11021–11023.

11) Sun, Z.; Ye, Q.; Chi, C.; Wu, J. *Chem. Soc. Rev.* **2012**, *41*, 7857–7889.

12) Nakano, M.; Kishi, R.; Nitta, T.; Kubo, T.; Nakasuji, K.; Kamada, K.; Ohta, K.; Champagne, B.; Botek, E.; Yamaguchi, K. *J. Phys. Chem. A* **2005**, *109*, 885–891.

13) Motomura, S.; Nakano, M.; Fukui, H.; Yoneda, K.; Kubo, T.; Carion, R.; Champagne, B. *Phys. Chem. Chem. Phys.* **2011**, *13*, 20575–20583.

14) Nakano, M.; Kishi, R.; Ohta, S.; Takahashi, H.; Kubo, T.; Kamada, K.; Ohta, K.; Botek, E.; Champagne, B. *Phys. Rev. Lett.* **2007**, *99*, 033001.

15) Nakano, M.; Champagne, B. *J. Phys. Chem. Lett.* **2015**, *6*, 3236–3256.

16) Kamada, K.; Ohta, K.; Kubo, T.; Shimizu, A.; Morita, Y.; Nakasuji, K.; Kishi, R.; Ohta, S.; Furukawa, S.-I.; Takahashi, H.; Nakano, M. *Angew. Chem. Int. Ed.* **2007**, *46*, 3544–3546.

17) Zeng, Z.; Shi, X.; Chi, C.; López Navarrete, J. T.; Casado, J.; Wu, J. *Chem. Soc. Rev.* **2015**, *44*, 6578–6596.

18) Morita, Y.; Suzuki, S.; Sato, K.; Takui, T. *Nat. Chem.* **2011**, *3*, 197–204.

19) Ito, S.; Minami, T.; Nakano, M. *J. Phys. Chem. C* **2012**, *116*, 19729–19736.

20) Smith, M. B.; Michl, J. *Annu. Rev. Phys. Chem.* **2013**, *64*, 361–386.

21) Varnavski, O.; Abeyasinghe, N.; Aragó, J.; Serrano-Pérez, J. J.; Ortí, E.; López Navarrete, J. T.; Takimiya, K.; Casanova, D.; Casado, J.; Goodson, T., III. *J. Phys. Chem. Lett.* **2015**, *6*, 1375–1384.

22) Thorley, K. J.; Anthony, J. E. *Isr. J. Chem.* **2014**, *13*, 642–649.

23) Anthony, J. E.; Brooks, J. S.; Eaton, D. L.; Parkin, S. R. *J. Am. Chem. Soc.* **2001**, *123*, 9482–9483.

24) Fudickar, W.; Linker, T. *J. Am. Chem. Soc.* **2012**, *134*, 15071–15082.

25) Park, J.-H.; Chung, D. S.; Park, J. W.; Ahn, T.; Kong, H.; Jung, Y. K.; Lee, J.; Yi, M. H.; Park, C. E.; Kwon, S.-K.; Shim, H.-K. *Org. Lett.* **2007**, *9*, 2573–2576.

26) Chase, D. T.; Fix, A. G.; Kang, S. J.; Rose, B. D.; Weber, C. D.; Zhong, Y.; Zakharov, L. N.; Lonergan, M. C.; Nuckolls, C.; Haley, M. M. *J. Am. Chem. Soc.* **2012**, *134*, 10349–10352.

27) Wood, J. D.; Jellison, J. L.; Finke, A. D.; Wang, L.; Plunkett, K. N. *J. Am. Chem. Soc.* **2012**, *134*, 15783–15789.

28) Chikamatsu, M.; Mikami, T.; Chisaka, J.; Yoshida, Y.; Azumi, R.; Yase, K.; Shimizu, A.; Kubo, T.; Morita, Y.; Nakasuji, K.; *Appl. Phys. Lett.* **2007**, *91*, 043506-1–043506-3.

29) Koike, H.; Chikamatsu, M.; Azumi, R.; Tsutsumi, J.; Ogawa, K.; Yamane, W.; Nishiuchi, T.; Kubo, T.; Hasegawa, T.; Kanai, K. *Adv. Funct. Mater.* **2016**, *26*, 277–283.

30) Marshall, J. L.; Haley, M. M. *Organic Redox Systems: Synthesis, Properties and Applications;* Nishinaga, T., Ed.; Wiley-VCH: New York, 2016; pp. 311–358.

31) Turro, N. J.; Ramamurthy, V.; Scaiano, J. C. *Principles of Molecular Photochemistry: An Introduction;* University Science Books: Sausalito, CA, 2009.

32) Bleaney, B.; Bowers, K. D. *Proc. R. Soc. Lond. A.* **1952**, *214*, 451–465.

33) Bernard, Y. A.; Shao, Y.; Krylov, A. I. *J. Chem. Phys.* **2012**, *136*, 204103–1–17.

34) Casado, J. Patchkovskii, S.; Zgierski, M. Z.; Hermosilla, L.; Sieiro, C.; Moreno Oliva, M.; López Navarrete, J. T. *Angew. Chem. Int. Ed.* **2008**, *47***,** 1443–1446.

35) Casado, J.; Ponce Ortiz, R.; López Navarrete, J. T. *Chem. Soc. Rev.* **2012**, *41*, 5672–5686.

36) Casado, J.; Moreno Oliva, M.; Ruiz Delgado, M. C.; López Navarrete, J. T.; Sánchez, L.; Martín, N.; Andreu, R.; Carrasquer, L.; Garín, J.; Orduna, J. *J. Chem. Phys.* **2007**, *126*, 074701-1–074701-8.

37) Albrecht, A. C. *J. Chem. Phys.* **1961**, *34*, 1476.

38) Burdett, J. J.; Bardeen, C. J. *J. Am. Chem. Soc.* **2012***, 134*, 8597–8607.

39) Frisch, M. J.; Trucks, G. W.; Schlegel, H. B.; Scuseria, G. E.; Robb, M. A.; Cheeseman, J. R.; Scalmani, G.; Barone, V.; Mennucci, B.; Petersson, G. A.; Nakatsuji, H.; Caricato, M.; Li, X.; Hratchian, H. P.; Izmaylov, A. F.; Bloino, J.; Zheng, G.; Sonnenberg, J. L.; Hada, M.; Ehara, M.; Toyota, K.; Fukuda, R.; Hasegawa, J.; Ishida, M.; Nakajima, T.; Honda, Y.; Kitao, O.; Nakai, H.; Vreven, T.; Montgomery, J. A., Jr.; Peralta, J. E.; Ogliaro, F.; Bearpark, M.; Heyd, J. J.; Brothers, E.; Kudin, K. N.; Staroverov, V. N.; Kobayashi, R.; Normand, J.; Raghavachari, K.; Rendell, A.; Burant, J. C.; Iyengar, S. S.; Tomasi, J.; Cossi, M.; Rega, N.; Millam, N. J.; Klene, M.; Knox, J. E.; Cross, J. B.; Bakken, V.; Adamo, C.; Jaramillo, J.; Gomperts, R.; Stratmann, R. E.; Yazyev, O.; Austin, A. J.; Cammi, R.; Pomelli, C.; Ochterski, J. W.; Martin, R. L.; Morokuma, K.; Zakrzewski, V. G.; Voth, G. A.; Salvador, P.; Dannenberg, J. J.; Dapprich, S.; Daniels, A. D.; Farkas, Ö.; Foresman, J. B.; Ortiz, J. V.; Cioslowski, J.; Fox, D. J. *Gaussian* 09, Revision C.01; Gaussian Inc.: Wallingford, CT, 2010.

40) Stephens, P. J.; Devlin, F. J.; Chabalowski, C. F.; Frisch, M. J. *J. Phys. Chem.* **1994**, *98*, 11623–11627.

41) Krishnan, R.; Binkley, J. S.; Seeger, R.; Pople, J. A. *J. Chem. Phys.* **1980**, *72*, 650–654.

42) Yamaguchi, K. In *Self-Consistent Field: Theory and Applications;* Carbó, R. & Klobukowski, M.; Eds.; Elsevier: Philadelphia, PA, 1990; pp. 727–828.

43) Herges, R.; Geuenich, D. *J. Phys. Chem. A* **2001**, *105*, 3214–3220.

44) Keith, T. A.; Bader, R. F. W. *Chem. Phys. Lett.* **1993**, *210*, 223–231.

45) Becke, A. D. *Phys. Rev. A* **1988**, *38*, 3098–3100.

46) Lee, C.; Yang, W.; Parr, R. G. *Phys. Rev. B* **1988**, *37*, 785–789.

47) Iikura, H.; Tsuneda, T.; Yanai, T.; Hirao, K. *J. Chem. Phys.* **2001**, *115*, 3540–3544.

48) Gershoni-Poranna, R.; Stanger, A. *Chem. Eur. J.* **2014**, *20*, 5673–5688.

49) Wolinski, K.; Hinton, J. F.; Pulay, P. *J. Am. Chem. Soc.* **1990**, *112*, 8251–8260.

50) Stanger, A. *J. Org. Chem.* **2010**, *75*, 2281–2288.

Chapter IV

1) Müllen, K. *Chem. Rev.* **1984**, *84*, 603–684.

2) Benshafrut, R.; Shabtai, E.; Rabinovitz, M.; Scott, L. T.; *Eur. J. Org. Chem.* **2000**, 1091–1106.

3) Sternfeld, T. & Rabinovitz, M. In "Carbon Rich Compounds: from Molecules to Materials", Haley, M. M. & Tykwinski R.; Eds.; Wiley-VCH: Weinheim, Germany, 2006; pp. 566–624.

4) Morita, Y.; Nishida, S.; Murata, T.; Moriguchi, M.; Ueda, A.; Satoh, M.; Arifuku, K.; Sato, K.; Takui, T. *Nat. Mater.* **2011**, *10*, 947–951.

5) Janoschka, T.; Hager, M. D.; Schubert, U. S. *Adv. Mater.* **2012**, *24*, 6397–6409.

6) Lee, J.; Lee, E.; Kim, S.; Bang, G. S.; Shultz, D. A.; Schmidt, R. D.; Forbes, M. D. E.; Lee, H. *Angew. Chem. Int. Ed.* **2011**, *50*, 4414–4418.

7) Barnes, J. C.; Fahrenbach, A. C.; Cao, D.; Dyar, S. M.; Frasconi, M.; Giesener, M. A.; Benitez, D.; Tkatchouk, E.; Chernyashevskyy, O.; Shin, W. H.; Li, H.; Sampath, S.; Stern, C. L.; Sarjeant, A. A.; Hartlieb, K. J.; Liu, Z.; Carmieli, R.; Botros, Y. Y.; Choi, J. W.; Slawin, A. M. Z.; Ketterson, J. B.; Wasielewski, M. R.; Goddard, W. A.; Stoddart, J. F. *Science* **2013**, *339*, 429–433.

8) Chase, D. T.; Fix, A. G.; Kang, S. J.; Rose, B. D.; Weber, C. D.; Zhong, Y.; Zakharov, L. N.; Lonergan, M. C.; Nuckolls, C.; Haley, M. M. *J. Am. Chem. Soc.* **2012**, *134*, 10349–10352.

9) Koike, H.; Chikamatsu, M.; Azumi, R.; Tsutsumi, J.; Ogawa, K.; Yamane, W.; Nishiuchi, T.; Kubo, T.; Hasegawa, T.; Kanai, K. *Adv. Funct. Mater.* **2015**, *26*, 277–283.

10) Kubo, T.; Shimizu, A.; Sakamoto, M.; Uruichi, M.; Yakushi, K.; Nakano, M.; Shiomi, D.; Sato, K.; Takui, T.; Morita, Y.; Nakasuji, K. *Angew. Chem. Int. Ed.* **2005**, *44*, 6564–6568.

11) Rudebusch, G. E.; Zafra, J. L.; Jorner, K.; Fukuda, K.; Marshall, J. L.; Arrechea- Marcos, I.; Espejo, G. L.; Ortiz, R. P.; Gómez-García, C. J.; Zakharov, L. N.; Nakano, M.; Ottosson, H.; Casado, J.; Haley, M. M. *Nat. Chem.* **2016**, *8*, in press.

12) Mondal, R.; Tönshoff, C.; Khon, D.; Neckers, D. C.; Bettinger, H. F. *J. Am. Chem. Soc.* **2009**, *131*, 14281–14289.

13) Cataldo, F.; Iglesias-Groth, S.; Manchado, A. *Spectrochim. Acta A* **2010**, *77*, 998–1004.

14) Ohashi, K.; Kubo, T.; Masui, T.; Yamamoto, K.; Nakasuji, K.; Takui, T.; Kai, Y.; Murata, I. *J. Am. Chem. Soc.* **1998**, *120*, 2018–2027.

15) Zabula, A. V.; Spisak, S. N.; Filatov, A. S.; Grigoryants, V. M.; Petrukhina, M. A. *Chem. Eur. J.* **2012**, *18*, 6476–6484.

16) Casado, J.; Miller, L. L.; Mann, K. R.; Pappenfus, T. M.; Higuchi, H.; Ortí, E.; Milián, B.; Pou-Amérigo, R.; Hernández, V.; López Navarrete, J. T. *J. Am. Chem. Soc.* **2002**, *124*, 12380–12388.

17) Rudebusch, G. E.; Fix, A. G.; Henthorn, H. A.; Vonnegut, C. L.; Zakharov, L. N.; Haley, M. M. *Chem. Sci.* **2014**, *5*, 3627–3633.

18) Rose, B. D.; Sumner, N. J.; Filatov, A. S.; Peters, S. J.; Zakharov, L. N.; Petrukhina, M. A.; Haley, M. M. *J. Am. Chem. Soc.* **2014**, *136*, 9181–9189.

Chapter V

1) Abe, M. *Chem. Rev.* **2013**, *113*, 7011–7088.

2) Zeng, Z.; Shi, X.; Chi, C.; Navarrete, J. T. L. X. P.; Casado, J.; Wu, J. *Chem. Soc. Rev.* **2015**, *44*, 6578–6596.

3) Kubo, T. *Chem. Lett.* **2015**, *44*, 111–122.

4) Rudebusch, G. E.; Zafra, J. L.; Jorner, K.; Fukuda, K.; Marshall, J. L.; Arrechea- Marcos, I.; Espejo, G. L.; Ortiz, R. P.; Gómez-García, C. J.; Zakharov, L. N.; Nakano, M.; Ottosson, H.; Casado, J.; Haley, M. M. *Nat. Chem.* **2016**, *8*, in press.

5) Bredas, J. L.; Calbert, J. P.; da Silva Filho, D. A.; Cornil, J. *Proc. Natl. Acad. Sci.* **2002**, *99*, 5804–5809.

6) Anthony, J. E. *Chem. Rev.* **2006**, *106*, 5028–5048.

7) Mei, J.; Diao, Y.; Appleton, A. L.; Fang, L.; Bao, Z. *J. Am. Chem. Soc.* **2013**, *135*, 6724–6746.

8) Marco, A. B.; Andreu, R.; Franco, S.; Garín, J.; Orduna, J.; Villacampa, B.; Diosdado, B. E.; López Navarrete, J. T.; Casado, J. *Org. Biomol. Chem.* **2013**, *11*, 6338–6349.

9) Zeng, Z.; Lee, S.; Son, M.; Fukuda, K.; Burrezo, P. M.; Zhu, X.; Qi, Q.; Li, R.-W.; Navarrete, J. T. L.; Ding, J.; Casado, J.; Nakano, M.; Kim, D.; Wu, J. *J. Am. Chem. Soc.* **2015**, *137*, 8572–8583.

10) Rao, M. R.; Desmecht, A.; Perepichka, D. F. *Chem. Eur. J.* **2015**, *21*, 6193–6201.

11) Chase, D. T.; Fix, A. G.; Kang, S. J.; Rose, B. D.; Weber, C. D.; Zhong, Y.; Zakharov, L. N.; Lonergan, M. C.; Nuckolls, C.; Haley, M. M. *J. Am. Chem. Soc.* **2012**, *134*, 10349–10352.

12) Chun, D.; Cheng, Y.; Wudl, F. *Angew. Chem. Int. Ed.* **2008**, *47*, 8380–8385.

13) Fitzgerald, J. J.; Drysdale, N. E.; Olofson, R. A. *J. Org. Chem.* **1992**, *57*, 7122–7126.

14) Rudebusch, G. E.; Fix, A. G.; Henthorn, H. A.; Vonnegut, C. L.; Zakharov, L. N.; Haley, M. M. *Chem. Sci.* **2014**, *5*, 3627–3633.

15) Rose, B. D.; Santa Maria, P. J.; Fix, A. G.; Vonnegut, C. L.; Zakharov, L. N.; Parkin, S. R.; Haley, M. M. *Beilstein J. Org. Chem.* **2014**, *10*, 2122–2130.

16) Rose, B. D.; Chase, D. T.; Weber, C. D.; Zakharov, L. N.; Lonergan, M. C.; Haley, M. M. *Org. Lett.* **2011**, *13*, 2106–2109.

17) Park, J.-H.; Chung, D. S.; Park, J. W.; Ahn, T.; Kong, H.; Jung, Y. K.; Lee, J.; Yi, M. H.; Park, C. E.; Kwon, S.-K.; Shim, H.-K. *Org. Lett.* **2007**, *9*, 2573–2576.

Appendix A

1) G. M. Sheldrick, *Bruker/Siemens Area Detector Absorption Correction Program*, Bruker AXS, Madison, WI, 1998.

2) SHELXTL-6.10 "Program for Structure Solution, Refinement and Presentation" BRUKER AXS Inc., 5465 East Cheryl Parkway, Madison, WI 53711-5373 USA

3) Reiss, H.; Heller, A. *J. Phys. Chem.* **1985**, *89*, 4207–4213.

4) Stoll, S.; Schweiger, A. *J. Magnet. Res.* **2006**, *178*, 42–55.

5) *MATLAB*; The Mathworks, Inc.

6) Frisch, M. J.; Trucks, G. W.; Schlegel, H. B.; Scuseria, G. E.; Robb, M. A.; Cheeseman, J. R.; Scalmani, G.; Barone, V.; Mennucci, B.; Petersson, G. A.; Nakatsuji, H.; Caricato, M.; Li, X.; Hratchian, H. P.; Izmaylov, A. F.; Bloino, J.; Zheng, G.; Sonnenberg, J. L.; Hada, M.; Ehara, M.; Toyota, K.; Fukuda, R.; Hasegawa, J.; Ishida, M.; Nakajima, T.; Honda, Y.; Kitao, O.; Nakai, H.; Vreven, T.; Montgomery, Jr., J. A.; Peralta, J. E.; Ogliaro, F.; Bearpark, M.; Heyd, J. J.; Brothers, E.; Kudin, K. N.; Staroverov, V. N.; Kobayashi, R.; Normand, J.; Raghavachari, K.; Rendell, A.; Burant, J. C.; Iyengar, S. S.; Tomasi, J.; Cossi, M.; Rega, N.; Millam, N. J.; Klene, M.; Knox, J. E.; Cross, J. B.;

Bakken, V.; Adamo, C.; Jaramillo, J.; Gomperts, R.; Stratmann, R. E.; Yazyev, O.; Austin, A. J.; Cammi, R.; Pomelli, C.; Ochterski, J. W.; Martin, R. L.; Morokuma, K.; Zakrzewski, V. G.; Voth, G. A.; Salvador, P.; Dannenberg, J. J.; Dapprich, S.; Daniels, A. D.; Farkas, Ö.; Foresman, J. B.; Ortiz, J. V.; Cioslowski, J.; Fox, D. J. *Gaussian 09*; 2010.

Appendix B

1) Park, J.-H.; Chung, D. S.; Park, J. W.; Ahn, T.; Kong, H.; Jung, Y. K.; Lee, J.; Yi, M. H.; Park, C. E.; Kwon, S.-K.; Shim, H-K. *Org. Lett.* **2007**, *9*, 2573–2576.

2) Reiss, H.; Heller, A. *J. Phys. Chem.* **1985**, *89*, 4207–4213.

3) Sheldrick, G. M. *Bruker/Siemens Area Detector Absorption Correction Program*, Bruker AXS, Madison, WI, 1998.

4) Sheldrick, G. M. *Acta Cryst.* **2008**, *A64*, 112–122.

5) Bleaney, B.; Bowers, K. D. *Proc. R. Soc. Lond. A.* **1952**, *214*, 451–465.

6) Gaussian 09, Revision A.02, Frisch, M. J.; Trucks, G. W.; Schlegel, H. B.; Scuseria, G. E.; Robb, M. A.; Cheeseman, J. R.; Scalmani, G.; Barone, V.; Mennucci, B.; Petersson, G. A.; Nakatsuji, H.; Caricato, M.; Li, X.; Hratchian, H. P.; Izmaylov, A. F.; Bloino, J.; Zheng, G.; Sonnenberg, J. L.; Hada, M.; Ehara, M.; Toyota, K.; Fukuda, R.; Hasegawa, J.; Ishida, M.; Nakajima, T.; Honda, Y.; Kitao, O.; Nakai, H.; Vreven, T.; Montgomery, Jr., J. A.; Peralta, J. E.; Ogliaro, F.; Bearpark, M.;. Heyd, J. J; Brothers, E.; Kudin, K. N.; Staroverov, V. N.; Kobayashi, R.; Normand, J.; Raghavachari, K.; Rendell, A.; Burant, J. C.; Iyengar, S. S.; Tomasi, J.; Cossi, M.; Rega, N.; Millam, J. M.; Klene, M.; Knox, J. E.; Cross, J. B.; Bakken, V.; Adamo, C.; Jaramillo, J.; Gomperts, R.; Stratmann, R. E.; Yazyev, O.; Austin, A. J.; Cammi, R.; Pomelli, C.; Ochterski, J. W.; Martin, R. L.; Morokuma, K.; Zakrzewski, V. G.; Voth, G. A.; Salvador, P.; Dannenberg, J. J.; Dapprich, S.; Daniels, A. D.; Farkas, O.; Foresman, J. B.; Ortiz, J. V.; Cioslowski, J.; Fox, D. J.; Gaussian, Inc., Wallingford CT, 2009.

7) Schmidt, M. W.; Baldridge, K. K.; Boatz, J. A.; Elbert, S. T.; Gordon, M. S.; Jensen, J. H.; Koseki, S.; Matsunaga, H.; Nguyen, K. A.; Su, S.; Windus, T. L.; Dupuis, M.; Montgomery, Jr. J. A. *J. Comput. Chem.* **2003**, *14*, 1347–1363.

8) Shao, Y.; Fusti-Molnar, L.; Jung, Y.; Kussmann, J.; Ochsenfeld, C.; Brown, S. T.; Gilbert, A. T. B.; Slipchenko, L. V.; Levchenko, S. V.; O'Neill, D. P. et. al. Q-CHEM, version 4.1; Q- Chem. Inc.: Pittsburgh, PA, 2008.

9) Shao, Y.; Head-Gordon, M.; Krylov, A. I. *J. Chem. Phys.* **2003**, *118*, 4807–4818.

10) Y. A. Bernard, Y. Shao and A. I. Krylov. *J. Chem. Phys.* **2012**, *136*, 204103–1–17.

11) Fukui, H.; Nakano, M.; Shigeta, Y.; Champagne, B. *J. Phys. Chem. Lett.* **2011**, *2*, 2063–2066.

12) (*a*) Head-Gordon, M. *Chem. Phys. Lett.* **2003**, *372*, 508-511. (*b*) Nakano, M.; Fukui, H.; Minami, T.; Yoneda, K.; Shigeta, Y.; Kishi, R.; Champagne, B.; Botek, E.; Kubo, T.; Ohta, K.; Kamada, K. *Theoret. Chem. Acc.* **2011**, *130*, 711-724; *erratum* **2011**, *130*, 725. (*c*) Takatsuka, K.; Fueno, T.; Yamaguchi, K. *Theoret. Chim. Acta (Berl.)* **1978**, *48*, 175-183.

13) Gershoni-Poranne, R.; Stanger, A. *Chem. Eur. J.* **2014**, *20*, 5673–5688.

14) Rahalkar, A.; Stanger, A. "Aroma", http://schulich.technion.ac.il/Amnon_Stanger.htm

15) Stephens, P. J.; Devlin, F. J.; Chabalowski, C. F.; Frisch M. J. *J. Phys. Chem.* **1994**, *98*, 11623–11627.

16) (*a*) Becke, A. D. *Phys. Rev. A* **1988**, *38*, 3098–3100. (*b*) Lee, C.; Yang, W.; Parr, R. G. *Phys. Rev. B* **1988**, *37*, 785–789.

17) Iikura, H.; Tsuneda, T.; Yanai, T.; Hirao, K. *J. Chem. Phys.* **2001**, *115*, 3540–3544.

18) Krishnan, R.; Binkley, J. S.; Seeger, R.; Pople, J. A. *J. Chem. Phys.* **1980**, *72*, 650–654.

19) Wolinski, K.; Hinton, J. F.; Pulay, P. *J. Am. Chem. Soc.* **1990**, *112*, 8251–8260.

20) Stanger, A. *J. Org. Chem.* **2010**, *75*, 2281–2288.

21) (*a*) Herges, R.; Geuenich, D. *J. Phys. Chem. A* **2001**, *105*, 3214–3220. (*b*) Geuenich, D.; Hess, K.; Kohler, F.; Herges, R. *Chem. Rev.* **2005**, *105*, 3758–3772.

22) Keith, T. A.; Bader, R. F. W. *Chem. Phys. Lett.* **1993**, *210*, 223–231.

23) Kishi, R.; Bonness, S.; Yoneda, K.; Takahashi, H.; Nakano, M.; Botek, E.; Champagne, B.; Kubo, T.; Kamada, K.; Ohta, K.; Tsuneda, T. *J. Chem. Phys.* **2010**, *132*, 094107-1-11.

24) Koike, H.; Chikamatsu, M.; Azumi, R.; Tsutsumi, J. y.; Ogawa, K.; Yamane, W.; Nishiuchi, T.; Kubo, T.; Hasegawa, T.; Kanai, K. *Adv. Funct. Mater.* **2015**, *26*, 277–283.

25) Chikamatsu, M.; Mikami, T.; Chisaka, J.; Yoshida, Y.; Azumi, R.; Yase, K.; Shimizu, A.; Kubo, T.; Morita, Y.; Nakasuji, K. *Appl. Phys. Lett.* **2007**, *91*, 043506-1–043506-3.

Appendix C

1) N. V. Kozhemyakina, J. Nuss, M. Jansen, *Z. Anorg. Allg. Chem.* **2009**, *635*, 1355.

2) Rudebusch, G. E.; Zafra, J. L.; Jorner, K.; Fukuda, K.; Marshall, J. L.; Arrechea-Marcos, I.; Espejo, G. L.; Ortiz, R. P.; Gómez-García, C. J.; Zakharov, L. N.; Nakano, M.; Ottosson, H.; Casado, J.; Haley, M. M. *Nat. Chem.* **2016**, *8*, in press.

3) *SADABS, Bruker AXS*. **2001**.

4) G. M. Sheldrick, *SHELXTL, Version 6.14, University of Göttingen, Germany* **2000**.

5) A. L. Spek, *Acta Cryst*. **2009**, *D65*, 148.